UNIVERSITÀ DEGLI STUDI DI PADOVA

UNIVERSITÀ DEGLI STUDI DI PADOVA

DIPARTIMENTO DI FISICA "GALILEO GALILEI"

SCUOLA DI DOTTORATO DI RICERCA IN FISICA

CICLO XXIII

A MULTI-DISCIPLINARY APPROACH TO DARK MATTER SEARCHES

Direttore della Scuola:

Ch.mo Prof. Attilio Stella

Supervisore:

Ch.mo Prof. Antonio Masiero

Dottorando: Miguel Figueiredo Vaz Pato

Acknowledgements

First of all, it is a pleasure to thank both my supervisors, Prof. Antonio Masiero and Prof. Gianfranco Bertone, for the full support throughout my thesis and the much I have learned from them. I especially thank Gianfranco for the constant attention. The work presented in this thesis benefited a lot from fruitful discussions with several colleagues and collaborators. I would like to mention in particular Laura Baudis, Fernando Barão, Marco Cirelli, Mattia Fornasa, Nicolao Fornengo, Michael Gustafsson, Dan Hooper, Fabio Iocco, Lidia Pieri, Antje Putze, Marco Taoso and Roberto Trotta. I am greatly indebted to Prof. Mário Pimenta and Laboratório de Instrumentação e Física Experimental de Partículas for introducing me to the field of astroparticle physics and for the tremendous support. Moreover, the hospitality of the Institut d'Astrophysique de Paris, the Fermi National Accelerator Laboratory and the Institute for Theoretical Physics at the University of Zürich are warmly acknowledged. I would also like to acknowledge my PhD scholarship financed by Fundação para a Ciência e Tecnologia (Portuguese Ministry of Science, Technology and Higher Education) as well as the International Doctorate on AstroParticle Physics (IDAPP). A truly sincere thanks goes to my friends, in special Stefano. To my parents, brother and sister for the unconditional support, enthusiasm and understanding. And to Larissa.

Riassunto

Una gran parte dell'Universo è composta da un tipo non luminoso di materia, che è intrinsecamente distinto da tutta la materia nota. Le prove d'esistenza di questa cosiddetta Materia Oscura si estendono da scale sotto-galattiche a scale cosmologiche e suggeriscono che la Materia Oscura contribuisca per circa l'80-85% alla materia totale nel nostro Universo. Comprendere la natura della Materia Oscura e individuarne le proprietà è uno dei problemi più importanti della fisica moderna. Interfacciando fisica delle particelle, cosmologia e astrofisica, la ricerca della Materia Oscura mette insieme aree di competenza tradizionalmente distanti, come ad esempio la ricerca di nuova fisica agli acceleratori di particelle, la fisica dei raggi cosmici, l'astronomia dei raggi γ e rilevatori sotteranei a basso background. Negli ultimi anni, numerosi risultati sperimentali rilevanti per la ricerca della Materia Oscura sono stati resi noti innescando un grande entusiasmo nel campo. Una grande quantità di dati è inoltre prevista per il prossimo futuro, soprattutto con i risultati del Large Hadron Collider, il lancio del rivelatore di raggi cosmici Alpha Magnetic Spectrometer AMS-02 e l'avvento di una nuova generazione di esperimenti sotterranei. In questo contesto, diversi candidati per la Materia Oscura proposti vari anni fa, come ad esempio le particelle massive di interazione debole (WIMPs, in inglese), saranno messi alla prova.

Questa tesi si propone di collegare dei modelli di Materia Oscura alle loro evidenze sperimentali nei rivelatori attuali e futuri. Per quanto riguarda la rivelazione diretta, un'attenzione speciale è riservata all'eccesso di elettroni/positroni recentemente riportato, che può in linea di principio essere spiegato con annichilazioni di Materia Oscura nella nostra Galassia. Al fine di verificare questa possibilità si è sviluppata un'analisi multi-messenger combinando i vincoli forniti da diversi canali astrofisici come gli antiprotoni, i raggi γ e i segnali radio. Un notevole miglioramento rispetto ai lavori precedenti consiste nell'inclusione autoconsistente della sottostruttura galattica secondo i risultati delle ultime simulazioni numeriche. Viene anche redatto un ampio insieme di vincoli fenomenologici sulla sezione d'urto di annichilazione di Materia Oscura per porre dei limiti sull'espansione precedente alla Big Bang Nucleosintesi. Inoltre, vengono analizzate le possibilità di differenziare un'interpretazione dell'eccesso di elettroni/positroni in termini di Materia Oscura da un'interpretazione astrofisica in termini di pulsar nel quadro del Alpha Magnetic Spectrometer AMS-02.

Le incertezze che entrano nel calcolo dei segnali di Materia Oscura sono molto significative e limitano la nostra capacità di estrarne le proprietà in caso di scoperta. Pertanto, valutare tutte le incertezze è cruciale, e una grande porzione di questa tesi è dedicata a tale argomento. In particolare, proviamo a capire quali siano le prospettive di misurare i parametri di propagazione dei raggi cosmici con AMS-02. Oltre ad essere un oggetto di estrema rilevanza astrofisica *per se*, la propagazione svolge un ruolo centrale nell'interpretazione degli eccessi di raggi cosmici, come accade nella frazione di positroni. Un'altra quantità importante che non si conosce attualmente con esattezza è la densità locale di Materia Oscura; la corrispondente incertezza sistematica è stimata facendo uso di recentissime simulazioni numeriche di galassie spirali. La densità locale e la forma sconosciuta della distribuzione di velocità nella vicinanza del sole si traducono in grandi incertezze sul tasso di dispersione della stessa su esperimenti di rivelazione diretta. Facendo uso di possibilità sperimentali realistiche, si valuta come tali incertezze influenzino la ricostruzione della massa di Materia Oscura e sezioni d'urto di diffusione e si quantifica la complementarità tra diversi materiali-bersaglio, come ad esempio xenon, argon e germanio.

Parole chiave: Materia Oscura, raggi cosmici

Summary

A large portion of the present Universe is composed of a non-luminous kind of matter, which is intrinsically distinct from all mass constituents known to exist. The evidence for this so-called Dark Matter spans sub-galactic to cosmological scales, and strongly suggests that it contributes around 80-85% of the matter content in our Universe. To understand the nature of Dark Matter and pinpoint its properties rests as one of the most exciting problems of modern physics. Lying at the interface between particle physics, cosmology and astrophysics, the quest for Dark Matter brings together areas of expertise traditionally far apart, including for instance the search for new physics at particle colliders, cosmic-ray physics, $\gamma-$ray astronomy and low-background underground detectors. Over the past years, numerous experimental results relevant for Dark Matter searches have been released, triggering a great deal of excitement in the field. Moreover, plenty of data are expected in the near future, especially with the results from the Large Hadron Collider, the launch of the cosmic-ray detector Alpha Magnetic Spectrometer AMS-02 and the onset of a new generation of underground experiments. In this data-driven context, several Dark Matter candidates proposed long ago, such as Weakly Interacting Massive Particles, will be severely put to test.

This thesis aims at linking Dark Matter models and their experimental signatures in current and upcoming detectors. As far as indirect Dark Matter detection is concerned, special attention is paid to the recently reported electron/positron excess in cosmic rays, which can in principle be explained by Dark Matter annihilations in our Galaxy. In order to test this possibility we perform a multi-messenger analysis combining the constraints from different astrophysical channels such as antiprotons, $\gamma-$rays and radio signals. A considerable improvement upon earlier works is the self-consistent inclusion of galactic substructure according to the findings of the latest high-resolution numerical simulations. An extensive picture of phenomenological constraints on Dark Matter annihilation cross-sections is also drawn and used to place limits on the pre-Big Bang Nucleosynthesis expansion of the Universe. Furthermore, we thoroughly analyse the prospects for discriminating a Dark Matter interpretation of the electron/positron excess against an astrophysical interpretation in terms of pulsars with the upcoming Alpha Magnetic Spectrometer AMS-02.

The uncertainties entering the computation of Dark Matter signatures are very significant and ultimately limit our ability to extract the properties of Dark Matter in case of discovery. Therefore, to assess and forecast all relevant uncertainties is crucial, and a large portion of this thesis is devoted to that topic. In particular, we try to understand the prospects for pinpointing cosmic-ray propagation with AMS-02. Besides being a subject of extreme astrophysical relevance *per se*, propagation plays a central role in the interpretation of cosmic-ray excesses such as the rise in the positron fraction. Another important quantity that is not accurately known as of today is the local Dark Matter density; the corresponding systematic uncertainties are estimated here by making use of very recent high-resolution numerical simulations of spiral galaxies. The poorly constrained local density and the unknown shape of the velocity distribution in the solar neighbourhood translate into large uncertainties on the Dark Matter scattering rate on direct detection experiments. Focusing on realistic upcoming experimental capabilities, we evaluate how such uncertainties affect the reconstruction of the Dark Matter mass and spin-independent scattering cross-section and quantify the complementarity between different target materials, namely xenon, argon and germanium.

Keywords: Dark Matter, cosmic rays

Résumé

Une grande partie de notre Univers consiste en un type de matière non-lumineuse intrinsèquement différente de tous les types de matière connus. A ce jour, cette "Matière Noire" a été mise en évidence aux échelles sous-galactiques jusqu'aux échelles cosmologiques. Les preuves expérimentales suggèrent fortement qu'elle contribue à environ 80-85% de la matiére de l'Univers. Sa compréhension ainsi que l'identification de ses propriétés est un sujet très important de la physique moderne. Située à l'intersection de la physique des particules, de la cosmologie et de l'astrophysique, la recherche en Matière Noire réunit plusieurs domaines traditionellement séparés l'un de l'autre, tels que la physique des grands collisionneurs de particules, l'astronomie des rayons cosmiques et gamma ou encore les détecteurs souterrains. Ces dernières années, de nombreux résultats expérimentaux concernant la Matière Noire ont été publiés, faisant de ce domaine de recherche un des plus excitants. Beaucoup de données sont également attendues dans un avenir proche, notamment celles du Large Hadron Collider (LHC), ainsi que le lancement du détecteur de rayons cosmiques Alpha Magnetic Spectrometer AMS-02 et la construction d'une nouvelle génération d'expériences souterraines. Plusieurs candidats de Matière Noire, en particulier les particules massives interagissant faiblement (WIMPs en anglais), proposés depuis assez longtemps, seront donc enfin mis à l'épreuve.

Le but de cette thèse est d'établir le lien entre certains modèles de Matière Noire et leurs signatures expérimentales visibles dans les détecteurs actuels ou futurs. L'exposé est organisé de la façon suivante:

- Au **Chapitre 1** nous établissons le cadre général de la phénoménologie de la Matière Noire en mettant l'accent sur les WIMPs. Il existe des preuves extrêmement convaincantes que la Matière Noire domine largement la matière baryonique dans notre Univers, mais sa nature nous est à ce jour inconnue. L'existence d'importantes quantités de Matière Noire avait déjà été proposée par l'astronome suisse Fritz Zwicky en 1933 qui fonda cette suggestion sur des mesures dynamiques des galaxies dans l'amas de Coma. A l'époque, cette proposition était accueillie sans enthousiasme, et ce n'est que plusieurs décennies plus tard – après l'observation des courbes de rotation plates dans les galaxies spirales – que l'existence de la Matière Noire fut discutée serieusement. Pendant les années 1980, travaillant sur des questions comme la stabilité du proton ou encore la grande unification des forces, les physiciens des particules construisirent le cadre théorique sous-jacent: en tant que produits secondaires, ces théories prédisent d'excellents candidats pour la Matière Noire, notamment des WIMPs. Cette classe de particules s'est rapidement établie comme le plus populaire des candidats de Matière Noire et a fourni une base trés féconde pour une étroite collaboration entre la physique des particules, la cosmologie et l'astrophysique. Prédisant à la fois des signatures directes, indirectes ainsi que des signaux aux collisionneurs, les WIMPs se trouvent aujourd'hui au centre d'un énorme effort expérimental dédié à leur détection. Après des décennies de spéculation et à la veille des premiers résultats du LHC, les expériences commencent enfin à sonder une partie importante des théories de la physique des particules aux hautes énergies.

- Le **Chapitre 2** présente une analyse detaillée de la distribution de la Matière Noire. La densité local, le profil et la distribution de vitesses dans la Voie Lactée sont au

cœur de cette étude. La Section 2.4 contient la publication [1], dans laquelle *les incertitudes systématiques affectant la détermination de la densité locale de la Matière Noire* sont examinées à l'aide des simulations numériques récentes des galaxies spirales. Nous constatons que, les baryons provoquent un aplatissement significatif du halo dans la direction perpendiculaire au disque stellaire. Cela produit une surdensité dans le disque pouvant atteindre 41% par rapport à la valeur sphérique moyenne. Ce résultat a des conséquences importantes pour la détermination de la densité locale de la Matière Noire.

- Le **Chapitre 3** décrit l'état actuel de la détection directe de la Matière Noire en tenant compte des aspects théoriques et expérimentaux. Nous nous concentrons sur les recherches indépendantes du spin. Vers la fin de ce Chapitre, la Section 3.3 est dédiée à l'étude de la *complémentarité entre les materiaux employés par les experiences de détection directe* [2]. Nous étudions l'influence de l'incertitude des paramètres astrophysiques sur la reconstruction de la masse de la Matière Noire et de la section efficace indépendante du spin. Pour un candidat WIMP d'une masse de 50 GeV, les incertitudes astrophysiques diminuent la précision de la reconstruction de la masse jusqu'à un facteur ~ 4 pour le xénon et le germanium. Cependant, si les resultats obtenus avec l'argon, le germanium et le xénon sont combinés, la précision augmente d'un facteur ~ 2 par rapport au germanium ou au xénon employés seuls. Nous montrons que les futurs expériences de détection directe pourront déterminer certains paramètres astrophysiques. Ils seront aussi capables de mesurer la masse du WIMP en utilisant un minimum de contraintes astrophysiques extérieures.

- Au **Chapitre 4** nous traitons la phénoménologie des rayons cosmiques aux hautes énergies. Après une introduction aux processus pertinents liés à la propagation des rayons cosmiques à travers le milieu galactique (noyaux, protons, antiprotons, électrons et positrons), ce Chapitre présente le cadre théorique général ainsi que l'état actuel des expériences. Ensuite, la Section 4.5 est dédiée aux *perspectives pour l'Alpha Magnetic Spectrometer AMS-02 de determiner la propagation des rayons cosmiques*, qui fait l'objet de l'article [3]. Nous constatons que dans le contexte des modèles de propagation relativement simples, tous les paramètres peuvent être déterminés avec une grande précision en utilisant les données attendues de AMS-02. Toutefois, ces mesures sont moins contraignantes pour des scénarios plus complexes.

- Le **Chapitre 5** est consacré à la détection indirecte de Matière Noire. Un formalisme détaillé est présenté pour les photons, les électrons/positrons et les antiprotons. Trois publications sont exposées à la fin de ce Chapitre:

  - *Contraintes multi-messenger sur l'interprétation de la fraction de positrons en termes de l'annihilation de la Matière Noire* [4] (Section 5.6). Nous effectuons une analyse multi-longueur d'onde et "multi-messenger", qui combine d'une manière cohérente les contraintes découlant des différentes observations astrophysiques. Nous montrons que, si quelques hypothèses standards sont faites pour la distribution de la Matière Noire et la propagation des rayons cosmiques, la plupart des modèles ne peuvent pas expliquer le flux de positrons observé sans dépasser les flux observés des antiprotons, rayons γ ou signaux radio.
  - *La discrimination de la source d'électrons et de positrons de haute énergie avec AMS-02* [5] (Section 5.7). Nous constatons qu'il est toujours possible d'imiter

un signal de Matière Noire avec des pulsars. Nous montrons également que, si l'excès de positrons est dû à un pulsar seul, il est toujours possible de trouver un candidat de Matière Noire qui fournit un bon ajustement aux données prédites pour AMS-02. Pour discriminer ces deux scénarios, il faudrait donc une meilleure connaissance des sources sous-jacentes, ou des données complémentaires.

- *Les contraintes sur les cosmologies non-standards découlant des limites astrophysiques sur la section efficace de l'annihilation de la Matière Noire* [6] (Section 5.8). Nous dérivons des contraintes astrophysiques sur l'annihilation de la Matière Noire et nous les utilisons pour contraindre des cosmologies alternatives dans l'époque précédent la Big Bang Nucleosynthesis. Nous déterminons également les caractéristiques de ces cosmologies alternatives afin de fournir la valeur correcte de l'abondance d'une relique thermique ayant une séction efficace suffisamment grande pour expliquer les résultats de l'expérience PAMELA. Ainsi nous expliquons la fraction de positrons observée par PAMELA en offrant une solution cosmologique à ces données.

- Le **Chapitre 6** présente nos conclusions principales.

La recherche sur la Matière Noire est aujourd'hui un domaine en plein essor. Aprés une longue attente, des données précises seront recueillies bientôt par plusieurs expériences, permettant de vérifier les concepts théoriques développés depuis plusieurs décennies. En particulier, les données du LHC, les mesures des rayons cosmiques de AMS-02 et les résultats en détection directe de la prochaine génération de détecteurs souterrains sont attendus avec impatience. A l'avenir, les études de Matière Noire devront adopter une approche "multi-messenger" pour exploiter les synergies entre signaux directs, indirects et venant des collisionneurs sans négliger les incertitudes sous-jacentes. Il semble aujourd'hui fortement probable que la découverte de la Matière Noire sera basée sur plusieurs signatures provenant d'expériences différentes.

Mots clé: Matière Noire, rayons cosmiques

Contents

Abbreviations

Aq	Aquarius simulation
BAO	Baryonic Acoustic Oscillations
BBN	Big Bang Nucleosynthesis
CMB	Cosmic Microwave Background
CR	Cosmic Rays
DM	Dark Matter
GC	Galactic Centre
GZK	Greisen-Zatsepin-Kuzmin
IB	Internal Bremsstrahlung
ICS	Inverse Compton Scattering
ISM	Interstellar Medium
KK	Kaluza Klein
LHC	Large Hadron Collider
LSP	Lightest Supersymmetric Particle
MW	Milky Way
NFW	Navarro-Frenk-White
SD	Spin-dependent
SI	Spin-independent
SM	Standard Model
SN	Supernova
SNR	Supernova Remnant
SUSY	Supersymmetry
VL2	Via Lactea II simulation
WIMP	Weakly Interacting Massive Particle
WMAP	Wilkinson Microwave Anisotropy Probe

Chapter 1

Overview: the case for Dark Matter

Dark Matter (DM) is a long-standing open question in modern astrophysics and a subject of intense research nowadays. Extremely compelling and varied evidence indicates that Dark Matter is the dominant mass component of our Universe, but its nature remains elusive. The first to suggest the existence of significant amounts of Dark Matter was the Swiss astronomer Fritz Zwicky in 1933 based on galaxy measurements in the Coma cluster. The reaction to this proposal was far from enthusiastic, and it was not until several decades later – with the observation of flat rotation curves in spiral galaxies – that the case for Dark Matter built up. Meanwhile, in the 1980s particle physicists were striving to tackle questions such as the stability of the proton or the grand unification of forces, and constructed theoretical frameworks where those issues were addressed. Very interesting by-products of such theories are neutral, massive particles with weak-scale couplings that provide excellent Dark Matter candidates. These Weakly Interacting Massive Particles (WIMPs) quickly became one of the most popular classes of Dark Matter candidates and set the foundations of a highly prolific interface between particle physics, cosmology and astrophysics. Given that WIMPs generally predict rather exciting direct, indirect and collider signatures, there has been since then a tremendous experimental effort in trying to detect such particles. Today, after decades of speculation and with the advent of the Large Hadron Collider (LHC), experiments are finally starting to probe a significant fraction of the parameter space of the most studied particle physics frameworks. We live therefore in a special time with hosts of data already, or about to be, available. The work presented in this thesis aims at connecting Dark Matter models and current or upcoming data. A multi-messenger approach is extensively adopted and special attention is paid to the role of astrophysical uncertainties on the computation of DM signatures.

This Chapter is devoted to delineate a general and up-to-date framework of Dark Matter phenomenology with particular focus on WIMPs. Chapters 2 to 5 are divided into a few introductory Sections where the relevant theoretical and experimental points are addressed, and the final Section(s) where the original contributions of this thesis are presented. In particular,

- **Chapter 2** analyses in detail the distribution of Dark Matter with special emphasis on the local density, velocity distribution and profile in the Milky Way. Section 2.4 presents the paper [1], where the *systematic uncertainties affecting the determination of the local Dark Matter density* are adressed in light of very recent numerical simulations of spiral galaxies.

- **Chapter 3** outlines the present theoretical and experimental status of direct Dark

Matter detection, focusing mainly on spin-independent searches. At the end of this Chapter, Section 3.3 is dedicated to the study of the *complementarity between Dark Matter direct detection targets* presented in the original contribution [2]. In that Section the role of astrophysical uncertainties is thoroughly analysed.

- **Chapter 4** addresses the phenomenology of galactic high-energy cosmic rays. Besides detailing the relevant processes controlling the propagation of cosmic-ray nuclei, protons, antiprotons, electrons and positrons through the galactic medium, this Chapter draws a general theoretical framework and experimental status of galactic cosmic rays. Then, Section 4.5 focus on the *prospects for the Alpha Magnetic Spectrometer AMS-02 to pinpoint cosmic-ray propagation*, which is the subject of the article [3].

- **Chapter 5** is dedicated to indirect Dark Matter detection. A detailed formalism is outlined for photons, electrons/positrons and antiprotons. Three original contributions are presented at the end of this Chapter: *multi-messenger constraints on the annihilating Dark Matter interpretation of the positron fraction* [4] (Section 5.6), *the ability for AMS-02 to discriminate the source of high-energy electrons and positrons* [5] (Section 5.7) and finally *the constraints on non-standard cosmologies arising from astrophysical bounds on Dark Matter annihilation cross-sections* [6] (Section 5.8).

Finally, the main conclusions are presented in Chapter 6.

1.1 The Standard Model of particle physics

To better understand the problematic of Dark Matter it is convenient to introduce the Standard Model (SM) of particle physics as a starting point – excellent introductions can be found in Refs. [7, 8, 9, 10]. The Standard Model is the gauge theory that naturally explains electromagnetic, weak and strong interactions. It is perhaps the most finely tested scientific theory, describing with remarkable success the building blocks of matter and all known fundamental interactions besides gravity. The particle content of the SM consists of *quarks* and *leptons* – the elementary fermions that compose all known matter – and *gauge bosons* – the mediators of the different interactions. Each of these particles is characterised by a mass and a set of quantum numbers that define how the particle behaves under the symmetry structure of the theory, $SU(3)_C \otimes SU(2)_L \otimes U(1)_Y$. For example, the colour C is the quantum number associated to the Quantum Chromodynamics (QCD) sector $SU(3)_C$, while the weak hypercharge Y, weak isospin T_3 and electric charge Q (in units of the electron charge $|e|$) are related by $Q = T_3 + Y/2$ and control electroweak interactions. Other quantum numbers include the spin s (in units of $\hbar$, the reduced Planck constant), the baryon number B and the lepton number L. Table 1.1 summarises the particle content of the Standard Model.

Now, quarks and leptons are organised into three families of $SU(2)_L$ left-handed doublets and right-handed singlets, see Table 1.1. Whereas quarks feel both strong and electroweak interactions, leptons only respond to the latter. A remarkable property of quarks is that they mix in the sense that the weak flavour eigenstates presented in Table 1.1 differ from the corresponding mass eigenstates $\tilde{d}$, $\tilde{s}$, $\tilde{t}$: $(d, s, t)^T = V_{CKM}(\tilde{d}, \tilde{s}, \tilde{t})^T$, where V_{CKM} is the well-known *Cabibbo-Kobayashi-Maskawa (CKM) matrix* (for numerical values of the CKM coefficients see [11]). In other words, this means that in electroweak

Standard Model particles				s	C	Y	T_3	Q	B	L
Fermions	$\binom{\nu_e}{e^-}_L$	$\binom{\nu_\mu}{\mu^-}_L$	$\binom{\nu_\tau}{\tau^-}_L$	$\binom{1/2}{1/2}$	$\binom{-}{-}$	$\binom{-1}{-1}$	$\binom{1/2}{-1/2}$	$\binom{0}{-1}$	$\binom{0}{0}$	$\binom{1}{1}$
	$\nu_{e,R}$	$\nu_{\mu,R}$	$\nu_{\tau,R}$	$1/2$	$-$	0	0	0	0	1
	e^-_R	μ^-_R	τ^-_R	$1/2$	$-$	-2	0	-1	0	1
	$\binom{u}{d}_L$	$\binom{c}{s}_L$	$\binom{t}{b}_L$	$\binom{1/2}{1/2}$	$\binom{r,g,b}{r,g,b}$	$\binom{1/3}{1/3}$	$\binom{1/2}{-1/2}$	$\binom{2/3}{-1/3}$	$\binom{1/3}{1/3}$	$\binom{0}{0}$
	u_R	c_R	t_R	$1/2$	r,g,b	$4/3$	0	$2/3$	$1/3$	0
	d_R	s_R	b_R	$1/2$	r,g,b	$-2/3$	0	$-1/3$	$1/3$	0
Bosons	γ			1	$-$	0	0	0	0	0
	$W^\pm$			1	$-$	0	±1	±1	0	0
	Z^0			1	$-$	0	0	0	0	0
	gluons			1	$c_1\bar{c}_2$	0	0	0	0	0
	H^0			0	$-$	-1	$1/2$	0	0	0

Table 1.1: The particle content of the Standard Model of particle physics. The different columns show the quantum numbers of the different particles: the spin s, the colour C ("r", "g" and "b" correspond to "red", "blue" and "green"), hypercharge Y, weak isospin T_3, electric charge Q, baryon number B and lepton number L. Notice that quarks carry a single colour, while gluons carry a colour and an anticolour (that is what $c_1\bar{c}_2$ stands for). Antiparticles are omitted for simplicity.

interactions quarks do not obey a strict family hierarchy. The same was experimentally verified for neutrinos in what was one of the most striking results of the last decades. In fact, the observation of *neutrino oscillations* strongly suggests that neutrinos are massive and hence there exist right-handed neutrino singlets in the fundamental theory as opposed to the original versions of the SM[1]. This is one of the strongest indications that a theory beyond the SM should exist.

As for bosons, the SM includes $W^\pm$, Z^0 and γ (the mediators of the electroweak force), eight different types of coloured gluons (that control the strong interaction) and the Higgs boson H^0 (responsible for giving mass to the different particles as briefly explained below).

In studying the early stages of the Universe a quantity that turns out to be of particular importance is the total *number of degrees of freedom* within elementary particles. In general, a given particle of spin s presents $g = 2s + 1$ degrees of freedom. The notable exception to this thumb rule occurs when the particle is massless as in the case of the photon or the gluons: both have $s = 1$ but $g = 2$. Using Table 1.1 it is easy to compute the degrees of freedom corresponding to one family of quarks and leptons: adding the contribution of the neutrino, charged lepton and quark doublet (each quark flavour can have three colours), $g_{family} = (1 + 2 + 2 \times 2 \times 3) \times 2 = 30$, where the last factor 2 accounts for antiparticles. Therefore, the fermionic degrees of freedom of the Standard Model amount to $g_{fermions} = 3 \times g_{family} = 90$. Instead, the counting of the gauge bosons (γ, 8 gluons, $W^\pm$, Z^0, H^0) gives $g_{bosons} = 2 + 8 \times 2 + 2 \times 3 + 3 + 1 = 28$.

As hinted in the previous paragraphs, the gauge structure of the SM is $SU(3)_C \otimes SU(2)_L \otimes U(1)_Y$, where $SU(3)_C$ pertains QCD and $SU(2)_L \otimes U(1)_Y$ is the symmetry of electroweak interactions. However, the fact that the $W^\pm$ and Z^0 bosons – that mediate weak interactions – are massive is best explained in light of a spontaneous symmetry breaking $SU(2)_L \otimes U(1)_Y \rightarrow U(1)_Q$. Such is the essence of the so-called *Higgs mechanism*. The Standard Model features the Higgs field ϕ, a (complex) scalar field whose potential can be written as

$$V(|\phi|) = b|\phi|^2 + \lambda|\phi|^4 + K \quad ,$$

where b, λ and K are real constants and $\lambda > 0$ in order to avoid $V \rightarrow -\infty$. In the case that $b < 0$, the ground state for ϕ (i.e. the state that globally minimises V) obeys $|\phi|^2 =$

[1]For completeness, Table 1.1 includes the right-handed neutrino singlets.

$-\frac{b}{2\lambda} > 0$, as opposed to $|\phi| = 0$ if $b > 0$. Consequently, in particle physics terminology, it is said that the field acquires a non-zero expectation value, which is precisely the necessary ingredient to give mass to the $W^{\pm}$ and Z^0 bosons. The very same mechanism naturally gives mass to quarks and leptons, and thus the Higgs particle rests as the missing, undiscovered piece of the Standard Model of particle physics.

As extensively discussed along the last decades, the SM is an incomplete theory and represents perhaps the low-energy limit of a more complete underlying formalism. Apart from the neutrino mass problem emphasised above, there are at least two other problems in the SM. Firstly, it is not clear how the gravitational interaction can be included self-consistently. Secondly, the unification of electromagnetic, weak and strong couplings occurs at the grand unification scale $M_{GUT}c^2 \sim 10^{16}$ GeV, while the Higgs mass should lie below the TeV scale. This discrepancy of so many orders of magnitude, usually known as the hierarchy problem, is difficult to understand since one would expect large corrections to the Higgs mass due to the grand unification scale. Either these corrections are extremely fine-tuned or some other mechanism is at play. Over the years several extensions of the SM (e.g. Supersymmetry) have been put forward to deal with these and other problems. Interestingly enough, a bonus of many such theories of new physics is to provide excellent Dark Matter candidates as we shall see in Section 1.4.

1.2 The early Universe

The Universe as we know it today is believed to have expanded from an extremely hot and dense initial patch. Such is the driving idea of the standard understanding of cosmology, the so-called *hot big bang model*. This framework – built upon the theory of General Relativity – enjoys strong observational evidence. The expansion of the Universe, for instance, has been established since the early studies of Edwin Hubble on redshifted light from nearby galaxies. Furthermore, the remarkable large scale uniformity of the Cosmic Microwave Background (CMB) temperature $T_0 = 2.73$ K supports the concept of an isotropic and homogeneous Universe. Other pieces of evidence include the abundance of primordial light elements, large scale structure and the age of the Universe. In the present Section we shall briefly review the main features of the hot big bang model as well as its shortcomings. Technical details may be found elsewhere [10, 12, 13, 14].

1.2.1 Notions of standard cosmology

Despite being inhomogeneous on small scales, our Universe is highly isotropic and homogeneous on large scales. There exists a coordinate system in which the cosmic fluid is at rest: the comoving coordinate system. The physical distance between any two comoving observers, however, can change over time according to an overall homogeneous scale factor $a(t)$. Such an Universe with a four-dimensional space-time is described by the *Friedmann-Lemaître-Robertson-Walker (FLRW) metric*[2]:

$$ds^2 = g_{\mu\nu}dx^\mu dx^\nu = c^2dt^2 - a^2(t)\left[\frac{dr^2}{1-kr^2} + r^2d\theta^2 + r^2\sin^2\theta\, d\varphi^2\right] \quad , \qquad (1.1)$$

[2]Throughout the introductory Sections SI units are used, while in the body of the thesis equations are usually written in natural units with $c = \hbar = k_B = 1$.

where $g_{\mu\nu}$ is the metric tensor with signature $(+,-,-,-)$, $x^\mu = (ct, \vec{x})$ and $\mu, \nu = 0, 1, 2, 3$. In the above formula, (r, θ, φ) are dimensionless comoving coordinates, whereas the scale factor a has dimensions of length. The quantity k parameterises the curvature of the space: $k = -1, 0, +1$ for open, flat and closed geometries, respectively. To picture the different curvatures it suffices to imagine in two spatial dimensions a saddle (open), an Euclidean plane (flat) and a spherical shell (closed).

The above-described framework represents an idealised (but very accurate) way to model an expanding Universe, where $a(t)$ plays a central role in all dynamical processes. Another important concept in cosmology is that of *redshift* z. Suppose that a distant source located at (comoving) coordinate $r = r_s$ emits an electromagnetic signal of period $\delta t_s = \lambda_s/c$ at $t = t_s$. The electromagnetic wave will follow a geodesic trajectory $ds = 0$ until arriving to the observer at $r = 0$. The first wave front (emitted at t_s) will arrive at t_0, the second (emitted at $t_s + \delta t_s$) will arrive $t_0 + \delta t_0$, and so on. Choosing, without loss of generality, a geodesic of constant θ and φ, $ds = 0$ implies

$$\int_{t_s}^{t_0} \frac{c\,dt}{a} = \int_0^{r_s} \frac{dr}{\sqrt{1-kr^2}} = \int_{t_s+\delta t_s}^{t_0+\delta t_0} \frac{c\,dt}{a} \quad .$$

Equating the two time integrals and assuming $\delta t_0, \delta t_s \ll a/\dot{a}$, one obtains $\frac{\delta t_s}{a(t_s)} = \frac{\delta t_0}{a(t_0)}$, or

$$1 + z \equiv \frac{\lambda_0}{\lambda_s} = \frac{a(t_0)}{a(t_s)} \quad .$$

In words, this result states that an electromagnetic wave propagating in an expanding Universe stretches its wavelength – "redshifts" – or, equivalently, the photons lose momentum. An imploding Universe would cause blueshifts, instead. The observation of numerous redshifted galaxy spectra is thus a solid piece of evidence for an expanding cosmos. The first to determine how fast such expansion is proceeding was Edwin Hubble. To this effect he established the linearity between redshift z and luminosity distance d_L of galaxies, also known as the Hubble law: $z = H_0 d_L/c$, valid for small redshifts $z \ll 1$. The constant of proportionality $H_0 \equiv H(t_0) = \dot{a}(t_0)/a(t_0)$ is the (present) Hubble parameter and measures the expansion rate of the Universe. Taking into account that the recession velocity of objects scales linearly with z for $z \ll 1$ ($v = cz$), one deduces the famous result $v = H_0 d_L$: distant galaxies are recessing faster than closer ones. Now, the Hubble constant is usually parameterised in terms of the reduced Hubble parameter h,

$$H_0 = 100h \text{ km/s/Mpc} \simeq 3h \times 10^{-18} \text{ s}^{-1} \quad ,$$

and it defines a typical distance $cH_0^{-1} \simeq 3h^{-1} \times 10^3$ Mpc and time $H_0^{-1} \simeq 9.8h^{-1}$ Gyr. These will turn out to be closely related to the horizon and age of the Universe. Another question of relevance consists in whether the expansion is currently accelerating or decelerating. This behaviour is regulated by the so-called *deceleration parameter*,

$$q_0 = -\frac{\ddot{a}(t_0)}{a(t_0)H_0^2} \quad , \tag{1.2}$$

that seems to be negative at present indicating an accelerating Universe.

The time evolution of the scale factor $a(t)$ is dictated by the *Einstein field equations*:

$$G_{\mu\nu} \equiv R_{\mu\nu} - \frac{1}{2} R g_{\mu\nu} = \frac{8\pi G}{c^4} T_{\mu\nu} + \Lambda g_{\mu\nu} \quad , \tag{1.3}$$

where $G = \hbar c / M_P^2$ is the gravitational constant, Λ is the cosmological constant, $T_{\mu\nu}$ is the stress-energy tensor while $R_{\mu\nu} = R^{\sigma}_{\mu\sigma\nu}$ [3] is the Ricci tensor and $R = g^{\mu\nu} R_{\mu\nu}$ the Ricci scalar. These equations follow from the minimisation of the Einstein-Hilbert plus matter action. Given that $g_{\mu\nu}$ and $T_{\mu\nu}$ are symmetric tensors, there are 10 independent equations whereas the unknowns are in general the 10+10 components of $g_{\mu\nu}$ and $T_{\mu\nu}$. In any case, the meaning of equation (1.3) is crystal-clear: the geometry of the Universe – encoded in the Einstein tensor $G_{\mu\nu}$ – is shaped by its energy components – represented by $T_{\mu\nu}$. As for the cosmological term $\Lambda g_{\mu\nu}$, it is a geometrical source of gravity (Λ has indeed units of curvature like R) but can also be interpreted as a vacuum component contributing to the energy budget of the Universe such as emphasised in equation (1.3). The historical context of the cosmological constant is a singular one: Einstein used Λ to obtain static solutions and then dropped it after observations confirmed the expansion of the Universe. More recently, however, Λ has been revived in order to explain several measurements including CMB anisotropies and supernova data that point towards an accelerated expansion. In this case a puzzling question for fundamental physics is why the required vacuum energy density $\rho_\Lambda \sim 3c^2 H_0^2/(8\pi G) \sim 10^{-5}$ GeV/cm^3 is so much smaller than the naïve expectation for a gravity-related phenomenon $\rho_G \sim M_P c^2/\ell_P^3 \sim 3 \times 10^{117}$ GeV/cm^3, but not exactly zero. More generally, an accelerated Universe can be explained by a "dark energy" component of which the cosmological constant constitutes simply an example. Another example, discussed in further detail in Section 1.2.4, is a scalar field with time-dependent energy density and pressure.

Let us now specialise the field equations (1.3) to the FLRW metric (1.1). First of all, it is straightforward to verify that the only non-vanishing Ricci tensors are

$$\begin{aligned} R_{00} &= -3\ddot{a}/(c^2 a) \\ R_{ij} &= -g_{ij} \left(2k/a^2 + 2\dot{a}^2/(c^2 a^2) + \ddot{a}/(c^2 a) \right) \end{aligned}$$

with $i, j = 1, 2, 3$, which yield

$$R = -6 \left(k/a^2 + \dot{a}^2/(c^2 a^2) + \ddot{a}/(c^2 a) \right) \quad .$$

Notice that in this scheme R_{00} and R have units of (length)$^{-2}$, R_{ij} and g_{00} are dimensionless and g_{ij} has units of squared length. Secondly, let us consider a generic perfect fluid (with no viscous shear nor heat conduction) embedded in the FLRW geometry. The associated stress-energy tensor is simply (see e.g. [12]) $T^{\mu\nu} = (\rho + p) u^\mu u^\nu - p g^{\mu\nu}$, where ρ is the fluid energy density, p its pressure, u^μ the four-velocity field and $g_{\mu\nu} u^\mu u^\nu = +1$. In the rest frame of the fluid, $u^\mu = (1, 0, 0, 0)$ and $T^\mu_\nu = diag(\rho, -p, -p, -p)$, or $T_{\mu\nu} = g_{\mu\sigma} T^\sigma_\nu$. By simple manipulation of equation (1.3) it is immediate to associate a stress-energy tensor to the vacuum: $(T_\Lambda)_{\mu\nu} = \frac{\Lambda c^4}{8\pi G} g_{\mu\nu}$ and $\rho_\Lambda = \frac{\Lambda c^4}{8\pi G} = -p_\Lambda$. For $\Lambda > 0$, the vacuum behaves indeed as a negative-pressure fluid.

At this point one can write down the $\mu = \nu = 0$ component of Einstein equations (1.3)

[3] $R^\mu_{\nu\alpha\beta} = \partial_\alpha \Gamma^\mu_{\nu\beta} - \partial_\beta \Gamma^\mu_{\nu\alpha} + \Gamma^\mu_{\sigma\alpha} \Gamma^\sigma_{\nu\beta} - \Gamma^\mu_{\sigma\beta} \Gamma^\sigma_{\nu\alpha}$ with $\Gamma^\mu_{\nu\sigma} = \frac{1}{2} g^{\mu\lambda} \left(\partial_\sigma g_{\lambda\nu} + \partial_\nu g_{\lambda\sigma} - \partial_\lambda g_{\nu\sigma} \right)$.

and obtain the so-called *first Friedmann equation*:

$$H^2 \equiv \left(\frac{\dot{a}}{a}\right)^2 = \frac{8\pi G}{3c^2}\rho + \frac{\Lambda c^2}{3} - \frac{kc^2}{a^2} \quad . \tag{1.4}$$

The $\mu = \nu = i$ components yield the *second Friedmann equation*:

$$2\frac{\ddot{a}}{a} + \frac{\dot{a}^2}{a^2} = -\frac{8\pi G}{c^2}p + \Lambda c^2 - \frac{kc^2}{a^2} \quad ,$$

that can be combined with (1.4) to give the more elegant expression

$$\frac{\ddot{a}}{a} = -\frac{4\pi G}{3c^2}(\rho + 3p) + \frac{\Lambda c^2}{3} \quad . \tag{1.5}$$

Once the components of the Universe (ρ, p, Λ) are totally specified, equations (1.4) and (1.5) fix the dynamical evolution of a (at large scales).

To proceed further, the dependencies $\rho(a)$ and $p(a)$ are needed, and these can be deduced from the conservation of energy $T^{\mu\nu}_{;\nu} = 0$ [4]. In fact, $T^{0\nu}_{;\nu} = 0$ results in the first law of thermodynamics: $\frac{d}{dt}(\rho a^3) + p\frac{d}{dt}(a^3) = 0$. This latter equation complemented with the *equation of state* of the fluid, $p = w\rho$, gives (assuming $w = \text{const}$):

$$\rho(a) = \rho_0 \left(\frac{a}{a_0}\right)^{-3(1+w)} = \rho_0(1+z)^{3(1+w)} \quad , \tag{1.6}$$

with $a_0 \equiv a(t_0)$ and $\rho_0 \equiv \rho(t_0)$. Examples of fluids with different equations of state are radiation ($w = 1/3$), non-relativistic matter or dust ($w \simeq 0$) and the cosmological constant ($w = -1$).

Up to now a generic fluid of density ρ and pressure p was considered as the main component of the Universe (besides Λ). Of course, at a given time, the Universe is composed of a mix of different fluids, namely *radiation* (ρ_r), *non-relativistic matter* (usually taken as the sum of a *baryonic* and a *cold non-baryonic* part, $\rho_m = \rho_b + \rho_{cdm}$), *vacuum* ($\rho_\Lambda$) and eventually an unknown component (ρ_X with $p_X = w_X\rho_X$): $\rho_{tot} = \rho_r + \rho_m + \rho_\Lambda + \rho_X$. In particular, since according to equation (1.6) $\rho_r \propto a^{-4}$, $\rho_m \propto a^{-3}$ and $\rho_\Lambda = \text{const}$, there was an epoch in the past when the Universe was matter-dominated and an even earlier period where radiation contributed the largest slice of the energy budget. It is common to express the energy densities of the various fluids normalised to the **critical density** – the density of a flat Universe (cf. equation (1.4)):

$$\rho_c(z) = \frac{3c^2H^2(z)}{8\pi G}$$

with present value

$$\begin{aligned}\rho_c^0 = \frac{3c^2H_0^2}{8\pi G} &\simeq 1.7h^2 \times 10^{-9}\ \mathrm{J/m^3} = h^2 \times 10^{-5}\ \mathrm{GeV/cm^3} \\ &= 1.9h^2 \times 10^{-29}\mathrm{g/cm^3} = 2.8h^2 \times 10^2\ \mathrm{M_\odot/kpc^3} \quad .\end{aligned}$$

[4] $T^{\mu\nu}_{;\nu}$ denotes the covariant derivative and reads $T^{\mu\nu}_{;\nu} = \partial_\nu T^{\mu\nu} + \Gamma^\mu_{\alpha\nu}T^{\alpha\nu} + \Gamma^\nu_{\alpha\nu}T^{\mu\alpha}$.

The **density parameters** are then $\Omega_i(z) = \rho_i(z)/\rho_c(z)$ with $i = tot, r, m, b, cdm, \Lambda, X$, and Ω_i^0 denotes the present value. With these definitions and equation (1.6), the Friedmann equation (1.4) can be recast in the form:

$$H^2(z) = H_0^2 \left(\Omega_r^0 (1+z)^4 + \Omega_m^0 (1+z)^3 + \Omega_\Lambda^0 + \Omega_X^0 (1+z)^{3(1+w_X)} - \frac{kc^2(1+z)^2}{a_0^2 H_0^2} \right) \quad , \tag{1.7}$$

where the curvature may be mathematically (but not physically) interpreted as a fluid of density $\Omega_k^0 = \frac{kc^2}{a_0^2 H_0^2}$ and $w_k = -1/3$. Another enlightening version of Friedmann equation is

$$\frac{kc^2}{a^2 H^2} = \Omega_{tot}(z) - 1 \quad . \tag{1.8}$$

The above expression stresses the direct correspondence between the curvature k and the total energy content of the Universe: open, flat and closed models present $\Omega_{tot} < 1$, $\Omega_{tot} = 1$ and $\Omega_{tot} > 1$, respectively. For a matter plus Λ Universe, this means that the geometry is closed for $\Omega_\Lambda > 1 - \Omega_m$, and vice-versa. Also, notice that in an Universe with radiation ($\rho_r \propto a^{-4}$) and/or matter ($\rho_m \propto a^{-3}$) the curvature is negligible at sufficiently early times.

In addition, it is interesting to know under what circumstances the Universe is accelerating or decelerating. Using Friedmann equation (1.5) to rewrite the parameter q_0 in equation (1.2), one obtains $q_0 = \sum_i \frac{1+3w_i}{2} \Omega_i^0$. In the case of a matter plus Λ Universe, the expansion is accelerating if $q_0 < 0$, i.e. $\Omega_\Lambda^0 > \Omega_m^0/2$, and vice-versa.

Finally, the explicit time evolution of the scale factor is obtained by plugging equation (1.6) into equation (1.4). For $w \neq -1$, $(\dot{a}/a)^2 \propto a^{-3(1+w)}$, or $a \propto t^{\frac{2}{3(1+w)}}$, e.g. $a \propto t^{1/2}$ for a *flat radiation-dominated* phase, $a \propto t^{2/3}$ in a *flat matter-dominated* (Einstein-de Sitter) model or $a \propto t$ in an *open empty* (Milne) Universe. A *flat* Λ*-dominated* model features an exponential growth since $(\dot{a}/a)^2 = \Lambda c^2/3$ or $a \propto e^{\sqrt{\Lambda c^2/3}t}$, while a *closed* Universe reaches eventually a maximum $a = a_{max}$ as evident from Friedmann equation (1.4): $\dot{a} = 0$ for $kc^2/a^2 = 8\pi G\rho/(3c^2)$.

Once the dynamical details are settled, an important quantity to compute is the *expansion age of the Universe*:

$$t_0 = \int_0^{a_0} \frac{da}{\dot{a}} = \int_0^\infty dz\, H^{-1}(z)(1+z)^{-1} \quad ,$$

where $a_0/a = 1 + z$ was used. For instance, an Universe with constant $\dot{a}$ or $H \propto (1+z)$ – as the case of an open empty (Milne) model – features an age equal to the Hubble time, $t_0 = H_0^{-1} \simeq 9.8h^{-1}$ Gyr. A flat radiation- or matter-dominated Universe presents, instead, faster expansion rates at early times (check equation (1.7)). Therefore, the time elapsed until the present epoch is shorter than in the Milne case, namely $t_0 = H_0^{-1}/2$ and $t_0 = 2H_0^{-1}/3$ for flat radiation and matter domination, respectively. Some observations constrain the age of the Universe t_0, and thus can be used to derive constraints on the present-day parameters, in particular h, Ω_m^0 and Ω_Λ^0.

Another useful quantity is the *distance to the horizon* which defines the region of the Universe that could have been in causal contact in the past. The comoving distance travelled by a photon from a (comoving) coordinate r_H until the observer at the origin is $\int_0^{r_H} dr/\sqrt{1-kr^2}$ (if $d\theta = d\varphi = 0$, without loss of generality). Now, using $ds = 0$ one

obtains the proper distance to the horizon,

$$d_H \equiv d_H(t) = a(t) \int_0^t \frac{c dt'}{a(t')} = \frac{c}{1+z} \int_z^\infty dz' \, H^{-1}(z') \quad .$$

It is simple to verify that, for $\Omega^0_{tot} = \Omega^0_r = 1$, $d^0_H = 2ct_0$, and for $\Omega^0_{tot} = \Omega^0_m = 1$, $d^0_H = 3ct_0$.

The cosmological parameters used along the following Sections have been determined to a high degree of accuracy by CMB anisotropy measurements, supernova data, large scale structure and other observations. For reference, the latest results [11] – using 7 years of data from the Wilkinson Microwave Anisotropy Probe (WMAP) satellite [15] – indicate $h = 0.70$, $\Omega^0_r h^2 = 2.47 \times 10^{-5}$, $\Omega^0_m h^2 = 0.135$, $\Omega^0_\Lambda = 0.73$ and $\Omega^0_b h^2 = 0.023$ (see Section 1.3.3 for further details).

1.2.2 Thermodynamics

The early Universe must have been in a hot and dense state with equilibrium thermodynamics driving the main physical processes. Besides photons in the Cosmic Microwave Background, all other fundamental particles known to exist – the building blocks of the Standard Model of particle physics – must have already been present in the primeval plasma. As long as interactions with photons were frequent (i.e. kinetic equilibrium was attained), the number density of a given species was uniform and isotropic, $dn = f(\vec{p}) d^3p = f(E)\, 4\pi p^2 dp$, where $E^2 = m^2c^4 + p^2c^2$. The phase space distribution $f(E)$ (in units of length^{-3}momentum^{-3}) is given by

$$f(E) = (2\pi\hbar)^{-3} \left(\exp\left(\frac{E-\mu}{k_B T} \right) \pm 1 \right)^{-1} \tag{1.9}$$

with k_B the Boltzmann constant and μ the chemical potential of the species. This expression with -1 $(+1)$ in the second factor describes particles obeying to the *Bose-Einstein* (*Fermi-Dirac*) statistics. In the following we shall set $\mu = 0$. The **number density** n, **energy density** ρ and **pressure** p of a gas of particles with mass m and internal degrees of freedom g at temperature T are readily computed making use of equation (1.9):

$$n(T) = g \int f(\vec{p})\, d^3p = \frac{g}{2\pi^2\hbar^3c^3} \int_{mc^2}^\infty dE \, \frac{E(E^2 - m^2c^4)^{1/2}}{\exp(E/(k_BT)) \pm 1} \tag{1.10}$$

$$\rho(T) = g \int E\, f(\vec{p})\, d^3p = \frac{g}{2\pi^2\hbar^3c^3} \int_{mc^2}^\infty dE \, \frac{E^2(E^2 - m^2c^4)^{1/2}}{\exp(E/(k_BT)) \pm 1} \tag{1.11}$$

$$p(T) = g \int \frac{pc^2}{3E} f(\vec{p})\, d^3p = \frac{g}{6\pi^2\hbar^3c^3} \int_{mc^2}^\infty dE \, \frac{(E^2 - m^2c^4)^{3/2}}{\exp(E/(k_BT)) \pm 1} \quad . \tag{1.12}$$

Recall that the number of *internal degrees of freedom* depends upon the type of particle under consideration. For instance, as seen in Section 1.1, massive particles of spin s carry $g = 2s + 1$ degrees of freedom.

There are two regimes of interest for equations (1.10), (1.11), (1.12): relativistic and

non-relativistic species. In the **relativistic** case, $k_BT \gg mc^2$ and

$$n(T) = \frac{\xi_n \zeta(3)}{\pi^2 \hbar^3 c^3} g (k_B T)^3 \tag{1.13}$$

$$\rho(T) = \frac{\xi_\rho \pi^2}{30 \hbar^3 c^3} g (k_B T)^4 \tag{1.14}$$

$$w = p/\rho = 1/3 \tag{1.15}$$

with $\xi_n = 1\,(3/4)$ and $\xi_\rho = 1\,(7/8)$ for Bose-Einstein (Fermi-Dirac) statistics, and $\zeta(x)$ being the Zeta function. A notorious example is of course the CMB fluid that features $T_0 = 2.73$ K, $g_\gamma = 2$ and therefore $n^0_{CMB} \equiv n_\gamma(T_0) \simeq 413\,\mathrm{cm}^{-3}$. It is also interesting to notice that, as expected, the energy per relativistic particle is of order k_BT: $\rho/n \simeq 2.7\,(3.2)\,k_BT$ for Bose-Einstein (Fermi-Dirac) species. In the case of **non-relativistic** particles, i.e. dust, $k_BT \ll mc^2$ and for Bose-Einstein and Fermi-Dirac statistics equations (1.10), (1.11) and (1.12) result in

$$n(T) = \frac{gc}{2\pi^2 \hbar^3} m^2 k_B T \, K_2\left(\frac{mc^2}{k_B T}\right) \to \frac{g}{\hbar^3}\left(\frac{m k_B T}{2\pi}\right)^{3/2} \exp\left(-\frac{mc^2}{k_B T}\right) \tag{1.16}$$

$$\rho(T) \simeq mc^2 n \tag{1.17}$$

$$w = p/\rho = \frac{k_B T}{mc^2} \simeq 0 \quad , \tag{1.18}$$

where $K_n(x)$ is the modified Bessel function of the second kind and order n, the result $\lim_{x\to\infty} K_n(x) = e^{-x}/\sqrt{2\pi x}$ was used for the number density expression, and the energy density was calculated in the zero-momentum limit. For particles on the verge of turning non-relativistic (or vice-versa), $k_BT \sim mc^2$ and the full integrals in equations (1.10), (1.11) and (1.12) must be evaluated.

As evident in equation (1.16), at a given temperature T the number density of non-relativistic particles is exponentially (or Boltzmann) suppressed with respect to radiation. Hence, in the early Universe the equilibrium distribution is dominated by relativistic particles. In full generality one can write the equilibrium energy density and pressure as

$$\rho_r(T) = \sum_i \rho_i(T_i) = \frac{\pi^2}{30\hbar^3 c^3}\, g_*(T)\,(k_B T)^4 \tag{1.19}$$

$$p_r(T) = \sum_i p_i(T_i) = \frac{\pi^2}{90\hbar^3 c^3}\, g_{*p}(T)\,(k_B T)^4 \quad , \tag{1.20}$$

where the sum runs over all particles, ρ_i, p_i refer to equilibrium quantities only, and the temperature T_i may account for a thermal distribution different from that of the photons at temperature T (as in the case of decoupled neutrinos, see below). The **effective degrees of freedom** $g_*(T)$ and $g_{*p}(T)$ may be computed by comparing (1.19) and (1.20) with (1.11) and (1.12). The full integrals of equations (1.11) and (1.12), however, only need to be solved numerically when a particle is changing regime. Since relativistic particles contribute the most to the equilibrium distribution, an useful approximate expression is obtained by comparing (1.19) and (1.20) with (1.14) and (1.15):

$$g_*(T) \simeq g_{*p}(T) \simeq \sum_i \xi^i_\rho g_i (T_i/T)^4 \quad ,$$

with the sum running over relativistic particles at temperature T.

In order to find $g_*(T)$ and $g_{*p}(T)$, one needs as input the fundamental particles of a theory, for instance the Standard Model of particle physics. At the very high temperatures (say $k_BT \gtrsim$ TeV), when all elementary particles are free and relativistic,

$$g_* \simeq g_{*p} \simeq g_{bosons} + \frac{7}{8} g_{fermions} = 106.75 \quad ,$$

where the degrees of freedom counting of Section 1.1 was used. Needless to say, if other particles (as yet undiscovered) exist in the early Universe, their contribution to g_* must be taken into account. Now, the periods when one or more particles turn non-relativistic induce bumps in the temperature evolution of g_* and g_{*p}. Following a chronological order (i.e. with decreasing temperature), at $80 - 90$ GeV the gauge bosons $W^{\pm}$ *and* Z^0 *drop off equilibrium*, while at around $\mathcal{O}(100)$ MeV there is a *quark-hadron transition* which bounds quarks into hadrons and is still a topic of current research. With temperatures of $k_BT \sim m_ec^2 = 511$ keV, it is the turn of *electron-positron pairs* to become non-relativistic and decouple from the photon bath. At later stages, instead, only the CMB photons and relic neutrinos are believed to contribute to g_*.

Let us now turn to another important quantity in the early Universe: the **entropy**. The total entropy in a comoving volume a^3 reads $S \equiv sa^3 = \frac{(\rho_r + p_r)a^3}{T}$, and the entropy density is

$$s(T) = \frac{1}{T} \sum_i \rho_i(T_i) + p_i(T_i) \equiv \frac{2\pi^2}{45\hbar^3c^3}\, g_{*s}(T)\, k_B^4 T^3 = 1.8 k_B\, g_{*s}(T)\, n_\gamma(T) \quad . \qquad (1.21)$$

Again, non-relativistic species are Boltzmann suppressed and their contribution to the entropy of the system is negligible, hence

$$g_{*s}(T) \simeq \sum_i \xi_\rho^i g_i (T_i/T)^3 \quad .$$

The exact behaviour of $g_{*s}(T)$ is found by equating (1.21) and (1.11), (1.12).

Simple thermodynamics arguments [10] may be used to prove that the total entropy in a comoving volume is conserved, $S \equiv sa^3 = \text{const}$, or $s \propto a^{-3}$. The entropy density s traces the (inverse) volume as the Universe expands. This is useful to follow the number of particles of a given species since, in the absence of destruction or creation processes, k_Bn/s is conserved. An example is the *baryon number*: if no baryon violating processes exist, then $k_B(n_b - n_{\bar{b}})/s = (n_b - n_{\bar{b}})/(1.8 g_{*s} n_\gamma)$ remains constant. The ratio $\eta \equiv (n_b - n_{\bar{b}})/n_\gamma$ will turn out to be an important parameter in Big Bang Nucleosynthesis (BBN), and its present value is remarkably small: using $n_{\bar{b}}^0 \simeq 0$ and $n_b^0 \simeq \Omega_b^0 \rho_c^0 / m_p$, $\eta \sim 2.7 \Omega_b h^2 \times 10^{-8}$. In words, the number of photons per baryon is huge in the present epoch.

Because $s \propto a^{-3}$, one can deduce a scale factor-temperature relationship using equation (1.21):

$$T \propto g_{*s}^{-1/3} a^{-1} \quad .$$

For periods when g_{*s} is constant – i.e. when all existing species are either highly relativistic or very non-relativistic – the temperature simply redshifts according to the well-known scaling $T = T_0 a_0 / a = T_0(1 + z)$. Therefore, an expanding Universe like ours must have been extremely hot in the past and the CMB stands as a left over of such early stage.

In order to compute the time evolution of the scale factor, one needs to use the results from the previous Section. In particular, by plugging equation (1.19) in the Friedmann equation (1.4) for a flat, radiation-dominated Universe, the expansion rate is

$$H^2 = \frac{8\pi^3 G}{90\hbar^3 c^5}\, g_*(T)\, (k_B T)^4 \quad , \tag{1.22}$$

and the age reads $t(T) = \frac{1}{2} H^{-1}(T) \simeq 0.8$ s $(10/g_*)^{1/2} (\mathrm{MeV}/(k_B T))^2$.

Up to this point only equilibrium distributions have been used. In fact equations such as (1.10) assume that the different species in the Universe are in equilibrium. This, however, cannot be the end of the story. For example, evaluating the current equilibrium density of non-relativistic protons with equation (1.16) and $T = T_0$ results in a virtually null density, in stark contrast with any galactic or extragalactic observation. At some stage in the past, some species must have left chemical equilibrium – this process is usually referred to as **freeze-out** or **thermal decoupling**. It is reasonable to suppose that in the hot, primeval plasma a species X interacted frequently with the photons through reactions such as $X\gamma \rightarrow X\gamma$ and $X\bar{X} \rightarrow \gamma\gamma$ at a rate per X particle $\Gamma(T)$. Therefore, chemical equilibrium is attained and X and γ share the same temperature. As the Universe expands, the frequency of these interconversions will depend on Γ and the expansion rate H. If $\Gamma > H$, X couples reasonably with the photon bath and its density follows the equilibrium distribution. Instead, if $\Gamma < H$, the expansion is too fast for the X particles to interact with the photons and n_X drops off equilibrium – X freezes-out, or decouples thermally. Equivalently, if the mean free path of the interconversions $\sim c/\Gamma$ is larger than the causal horizon $\sim c/H$, then the interaction between X and γ is rare, and vice-versa. The temperature at which $\Gamma = H$ is usually defined as *freeze-out* or *thermal decoupling temperature*. After freeze-out, the number density n_X simply redshifts, $n_X \propto a^{-3}$, as long as $\Gamma < H$. In this way it is possible to have today relic particles presenting densities much higher than the equilibrium ones. As we shall see, whether the particle is relativistic or non-relativistic at freeze-out has important consequences for its present-day relic density and also for structure formation. Notice that a thermally decoupled species may still be in kinetic equilibrium by changing momentum with the photon bath ($X\gamma \rightarrow X\gamma$). The freezing of these latter reactions is called **kinetic decoupling**, and it usually occurs later than the thermal decoupling.

In light of the processes just described, it is believed that all Standard Model particles were in chemical equilibrium in the early Universe and that at some point thermal decoupling occurred. For instance, weak interactions such as $\nu e \rightarrow \nu e$, $\nu\bar{\nu} \rightarrow e^+ e^-$ or $n \rightarrow p e^- \bar{\nu}$ present cross-sections of order $\sigma_{weak} \sim \frac{G_F^2 \tilde{s}}{\hbar^4 c^4}$ (where $\tilde{s}$ is the squared centre of mass energy and G_F is the Fermi coupling constant), corresponding to the exchange of a massive gauge boson in the limit $\tilde{s} \ll m_W^2 c^4$. Therefore, given that in the primordial plasma the available energy in a relativistic collision was $\tilde{s} \sim k_B^2 T^2$, these interactions were frequent at sufficiently high temperatures. At $k_B T >$ MeV neutrinos and antineutrinos were thus tightly coupled to electrons and positrons that in turn were in equilibrium with the photons. Since the target electrons and positrons were relativistic at these temperatures, their number density reads $n_{e^\pm} \simeq \mathcal{O}(1) \frac{(k_B T)^3}{\hbar^3 c^3}$ and the interaction rate per neutrino is $\Gamma_\nu = n_{e^\pm} \sigma_{weak} v \simeq \mathcal{O}(1) \frac{G_F^2 (k_B T)^5}{\hbar^7 c^6}$, being $v \sim c$ the relative velocity of the relativistic colliding particles. According to the previous paragraph, such reactions *freeze-out* at a temperature given by $\Gamma_\nu = H$, or, using $H \sim \mathcal{O}(1) \frac{G^{1/2} (k_B T)^2}{\hbar^{3/2} c^{5/2}}$, $k_B T_{dec,\nu} = 0.8$ MeV.

At about the same temperature interactions converting neutrons to protons and vice-versa also decouple providing the seed for Big Bang Nucleosynthesis. After $k_BT \sim$ MeV, there are virtually no processes creating or destroying neutrinos: $n_\nu \propto a^{-3}$ which implies $T_\nu \propto a^{-1}$ as long as neutrinos remain relativistic. Instead, the bulk of the radiation plasma redshifts following $T \propto g_{*s}^{-1/3} a^{-1}$. Both behaviours coincide (i.e. $T = T_\nu$) until $k_BT \simeq m_ec^2 = 0.511$ MeV when electron-positron pairs turn non-relativistic producing a drop in g_{*s}. Before the transition $g_{*s}(T_i \gtrsim m_ec^2) = 2 + \frac{7}{8} \times 2 \times 2 = \frac{11}{2}$ (photons, electrons and positrons), while afterwards $g_{*s}(T_f < m_ec^2) = 2$ (photons). Consequently, the photon temperature scales as

$$a_f T_f = \left(\frac{g_{*s}(T_i)}{g_{*s}(T_f)} \right)^{1/3} a_i T_i = \left(\frac{11}{4} \right)^{1/3} a_i T_i \quad ;$$

instead the *temperature of neutrinos* obeys $a_f T_{\nu,f} = a_i T_{\nu,i}$. Since $T_{\nu,i} = T_i$, one has

$$T_\nu = \left(\frac{4}{11} \right)^{1/3} T \simeq 1.95 \text{ K} \, (1+z) \quad ,$$

if evaluated after $T \sim m_ec^2$. Applying this result to 3 species of neutrinos (and antineutrinos), the present-day degrees of freedom are readily computed: $g_*(T_0) = 2 + \frac{7}{8} \times 6 \times \left(\frac{4}{11}\right)^{4/3} = 3.36$, $g_{*s}(T_0) = 2 + \frac{7}{8} \times 6 \times \left(\frac{4}{11}\right) = 3.91$, and $s_0/k_B \simeq 2.9 \times 10^3$ cm^{-3}.

All the above calculations were done assuming a radiation-dominated Universe, which is very reasonable in early Universe processes given that the radiation energy density scales as $\rho_r \propto a^{-4}$ whereas for matter $\rho_m \propto a^{-3}$. Nevertheless, there was a time after which matter dominates the energy budget of the Universe. This period, usually called **matter-radiation equality**, represents the onset of structure formation and is defined by the condition $\rho_m(T_{eq}) = \rho_r(T_{eq})$: $(1 + z_{eq}) = \Omega_m^0 / \Omega_r^0 \sim 5 \times 10^3$, or

$$k_B T_{eq} = k_B T_0 (1 + z_{eq}) \sim \text{eV} \quad .$$

It is shortly after the matter-radiation equality that a number of crucial processes takes place leading to the release of the CMB that we see today. At multi-eV temperatures, protons, electrons, hydrogen atoms and photons are constantly changing energy and interconverting through the reactions $e\gamma \rightarrow e\gamma$ and $pe^- \leftrightarrow H\gamma$. Since chemical equilibrium is attained, the chemical potentials of the species in the latter reaction obey $\mu_p + \mu_e = \mu_H$. This relationship may be used to express the equilibrium density of hydrogen atoms as

$$n_H = \frac{g_H}{g_e g_p} n_e n_p \left(\frac{2\pi\hbar^2}{m_e k_B T} \right)^{3/2} \exp\left(\frac{E_b}{k_B T} \right) \quad , \tag{1.23}$$

where $m_p \simeq m_H$, $E_b = (m_p + m_e - m_H)c^2 = 13.6$ eV is the binding energy of hydrogen, and the equilibrium densities n_i ($i = H, e, p$) are given by equation (1.16) with an additional factor $\exp(\mu_i/(k_BT))$ in the right hand side to account for the chemical potentials. Let us now define the *ionisation fraction* as $X_e \equiv n_p/(n_b - n_{\bar{b}}) \simeq n_p/(n_H + n_p)$. This represents the fraction of free protons, i.e. protons not bound in atoms. If the Universe is assumed neutral, $n_p \simeq n_e$ and X_e also represents the fraction of free electrons. Using $n_b - n_{\bar{b}} = \eta n_\gamma$

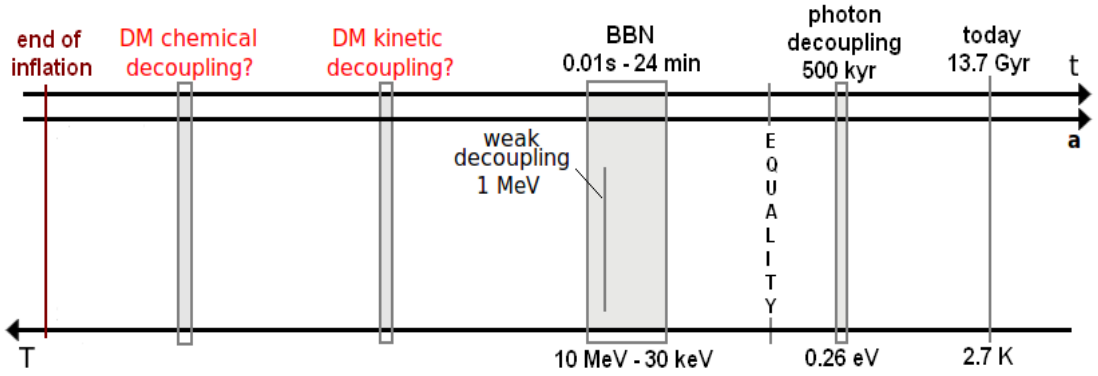

Figure 1.1: A schematic timeline of the most important events in the early Universe.

and $n_p \simeq n_e$, equation (1.23) leads to the *Saha equation*:

$$\frac{1-X_e}{X_e^2} = \frac{g_H}{g_e g_p}\frac{2^{5/2}\zeta(3)}{\pi^{1/2}}\,\eta\left(\frac{k_B T}{m_e c^2}\right)^{3/2}\exp\left(\frac{E_b}{k_B T}\right) \quad . \tag{1.24}$$

It is easy to verify that, for reasonable choices of the cosmological parameters (more precisely, of $\Omega_b^0 h^2$, that fixes η), X_e reduces to negligible amounts for $z \lesssim z_{rec} \simeq 1300$, $k_B T \lesssim k_B T_{rec} \simeq 0.3$ eV [10]. This is the so-called **recombination**, when most of the previously free protons and electrons are bound to hydrogen atoms. Gradually the Universe becomes neutral (not only globally but also locally) and more transparent to photons. Notice that $k_B T_{rec} \simeq 0.3$ eV is significantly smaller than the binding energy $E_b = 13.6$ eV. This happens because in our Universe η^{-1}, the number of photons per baryon, is very large. Therefore the high-energy tail of the photon distribution is enough to ionise the Universe even at $k_B T < E_b$.

Equations (1.23) and (1.24) implicitly assume equilibrium. In fact, the Thomson scattering $e\gamma \to e\gamma$ is still occurring at T_{rec}, which means that the cosmos is not yet totally transparent to photons. The interaction rate per photon is given by $\Gamma_e = n_e \sigma_T c = X_e \eta n_\gamma \sigma_T c$ (where $\sigma_T = \frac{8\pi}{3} r_e^2$ is the Thomson cross-section and r_e the classical electron radius), while the expansion rate of the Universe is now driven by matter $H \propto \rho_m^{1/2} \propto (1+z)^{3/2} \propto T^{3/2}$. The freeze-out temperature turns out to be $k_B T_{dec} \sim 0.26$ eV ($z_{dec} \sim 1100$). This represents the **last scattering surface** of the CMB photons since they will suffer virtually no collisions until the present epoch. Finally, with a small number density of free electrons, also the reaction $pe^- \to H\gamma$ decouples leaving today a *relic ionisation fraction* much larger than the equilibrium value.

To summarise the history of the Universe since its very initial, hot phase until today, Figure 1.1 sketches a rough timeline. It is convenient to stress that as of today Big Bang Nucleosynthesis stands as the *deepest* (i.e. highest temperature) *probe* of our Universe. Before MeV temperatures we can only make educated guesses about the succession of events. One of such events might have been the decoupling of cold or hot relics. Because that is an important piece of the Dark Matter puzzle, the next Section is devoted to analyse it at a fair level of detail.

1.2.3 Hot and cold relics

The specifics of the freeze-out process are addressed in light of the *Boltzmann equation*. For the FLRW cosmology presented in the previous Sections and a particle χ with Maxwell-Boltzmann statistics (valid for symmetric, non-degenerate species with $\mu_\chi/k_BT \ll 1$), the Boltzmann formalism leads to the evolution equation [10]:

$$\dot{n}_\chi + 3Hn_\chi = -\langle\sigma_{ann}v\rangle\left(n_\chi^2 - n_{\chi,eq}^2\right) \quad , \tag{1.25}$$

where $\langle\sigma_{ann}v\rangle$ is the thermally averaged total $\chi\bar{\chi}$ annihilation cross-section times relative velocity, the subscript "eq" refers to the equilibrium distribution and the antiparticles $\bar{\chi}$ are assumed identical to χ. The physical meaning of the different terms in equation (1.25) is very transparent. Firstly, in the absence of interactions, the right hand side vanishes giving $d(n_\chi a^3)/dt = 0$: the χ fluid simply dilutes due to the expansion of the Universe. If additionally the total entropy in a comoving volume is conserved, then $n_\chi/s =$ const. Secondly, the term $-\langle\sigma_{ann}v\rangle n_\chi^2$ accounts for the disappearance of χ particles in annihilations $\chi\bar{\chi} \to f$ (f being any allowed final state), while the piece $+\langle\sigma_{ann}v\rangle n_{\chi,eq}^2$ represents the creation of particles in inverse annihilations. Notice that we have chosen $\mu_\chi = 0$ and therefore $n_\chi = n_{\bar{\chi}}$ and $n_{\chi,eq} = n_{\bar{\chi},eq}$. Now, defining $Y_\chi \equiv k_B n_\chi/s$ and using the conservation of entropy $sa^3 =$ const, equation (1.25) yields

$$\frac{dY_\chi}{dt} = -\langle\sigma_{ann}v\rangle s\left(Y_\chi^2 - Y_{\chi,eq}^2\right)$$

which can be recast as

$$\frac{x}{Y_{\chi,eq}}\frac{dY_\chi}{dx} = -\frac{\Gamma_{ann}}{H}\left(1 + \frac{1}{3}\frac{d\ln g_{*s}}{d\ln T}\right)\left(\frac{Y_\chi^2}{Y_{\chi,eq}^2} - 1\right) \tag{1.26}$$

with $x = m_\chi c^2/(k_BT)$, $\Gamma_{ann} = \langle\sigma_{ann}v\rangle n_{\chi,eq} = \langle\sigma_{ann}v\rangle s Y_{\chi,eq}/k_B$ and

$$\dot{T} = -H\left(1/T + \frac{1}{3}\frac{d\ln g_{*s}}{dT}\right)^{-1}$$

which follows from $sa^3 =$ const, check equation (1.21). The expression (1.26) justifies the decoupling thumb rule stated in the last Section: if $\Gamma_{ann} \gg H$, any deviation from $Y_\chi \simeq Y_{\chi,eq}$ is readily damped; instead, if $\Gamma_{ann} \ll H$, Y_χ may freely deviate from the equilibrium distribution. In the following, approximate solutions of equation (1.26) are derived for hot and cold relics. For simplicity we shall assume $g_{*s} =$ const around freeze-out, but full expressions are straightforward to obtain (see e.g. [16]).

Hot relics are species that freeze-out from radiation when relativistic. Hence the freeze-out occurs at $x = x_f \ll 1$. In this regime (cf. equations (1.13) and (1.21)),

$$Y_{\chi,eq}(x) = \frac{45\zeta(3)\xi_n}{2\pi^4}\frac{g}{g_{*s}(x)} \simeq \text{const}$$

whereas $\Gamma_{ann} \propto T^3 \propto x^{-3}$. In the last scaling the temperature dependence of $\langle\sigma_{ann}v\rangle$ was neglected; although relevant for cold relics, this approximation has no qualitative effect in the following argument as long as $\langle\sigma_{ann}v\rangle \propto T^n$ with $n \geq 0$. We are interested in a decoupling during radiation domination so that $H \propto \rho_r^{1/2} \propto T^2 \propto x^{-2}$ (again, the

temperature dependence of g_{*s} is neglected). Let $\Gamma_{ann}/(Hx) \equiv c_1 x^{-2}$ and $\tilde{Y} = Y_\chi / Y_{\chi,eq}$. Then, equation (1.26) may be written as

$$\frac{d\tilde{Y}}{dx} = -c_1 x^{-2}(\tilde{Y}^2 - 1)$$

whose solution is $\tilde{Y}(x) = \frac{1-\exp(2c_1/x+2c_2)}{1+\exp(2c_1/x+2c_2)}$ with c_2 an integration constant. Requiring $\tilde{Y}(x_i \lesssim x_f = c_1) \simeq 1$, it is easy to check that $\tilde{Y} \simeq 1$ around the freeze-out. Afterwards, annihilations cease and the comoving abundance Y_χ remains constant. Consequently, the current abundance is

$$Y_\chi^0 \simeq Y_{\chi,eq}(x_f) = \frac{45\zeta(3)\xi_n}{2\pi^4}\frac{g}{g_{*s}(x_f)} \quad ,$$

or in terms of the density parameter $\Omega_\chi^0 = m_\chi c^2 n_\chi^0/\rho_c^0 = m_\chi c^2 Y_\chi^0 s_0/(k_B \rho_c^0)$. A well-known hot relic is the **neutrino**. As we have seen, neutrinos decouple at $T_f \sim 0.8$ MeV when $g_{*s}(x_f) = 2 + \frac{7}{8} \times 6 + 2 \times 2$ (photons, three neutrinos, three antineutrinos, electrons and positrons). Using $g = g_{\nu\bar{\nu}} = 2$ we find that

$$\Omega_{\nu\bar{\nu}} h^2 \simeq \sum_\nu m_\nu c^2/(90 \text{ eV}) \quad , \tag{1.27}$$

where the sum runs over neutrino families.

For **cold relics** the thermal decoupling happens at $x_f > 1$. In this case the comoving equilibrium abundance is Boltzmann suppressed,

$$Y_{\chi,eq}(x) = \frac{45g}{2^{5/2}\pi^{7/2} g_{*s}(x)} x^{3/2} \exp(-x) \quad .$$

We can thus safely assume $Y_\chi / Y_{\chi,eq} \gg 1$ and recast equation (1.26) in the form

$$\frac{1}{Y_\chi^2}\frac{dY_\chi}{dx} = -\frac{\langle\sigma_{ann} v\rangle s}{k_B H x} \quad . \tag{1.28}$$

Letting $\langle\sigma_{ann} v\rangle = \langle\sigma_{ann} v\rangle_0 x^{-n}$ $(n \geq 0)$ and

$$\frac{\langle\sigma_{ann} v\rangle s}{k_B H x} = \frac{2\pi^2}{45}\left(\frac{90}{8\pi^3}\right)^{1/2} \frac{g_{*s}(x) m_\chi c}{g_*^{1/2}(x)\hbar^2} M_P \langle\sigma_{ann} v\rangle_0 \, x^{-n-2} \equiv b_1(x)\, x^{-n-2} \quad ,$$

the solution of the latter equation is

$$\frac{1}{Y_\chi^0} = \frac{1}{Y_\chi(x_f)} + \int_{x_f}^\infty b_1(x)\, x^{-n-2}\, dx \sim \frac{b_1(x_f) x_f^{-n-1}}{n+1} \quad , \tag{1.29}$$

where in the last step we have used the fact that the present-day abundance is significantly smaller than that at freeze-out, i.e. $1/Y_\chi(x_f) \ll 1/Y_\chi^0$. Alternative treatments of the decoupling of cold relics may be found in [10, 17, 18]. Now, the value of x_f is determined by defining the freeze-out criterium $Y_\chi(x_f) = \xi Y_{\chi,eq}(x_f)$ with $\xi \gtrsim 1$ and plugging it in

equation (1.26). Such procedure yields an iterative formula $x_f^{(i+1)} = f(x^{(i)})$ where

$$f(x) = \ln\left[\sqrt{\frac{45}{8}}\frac{1}{2\pi^3}\frac{\xi^2-1}{\xi}\,\langle\sigma_{ann}v\rangle(x)\,\frac{x^{1/2}}{x-3/2}\frac{m_\chi M_P c}{\hbar^2}\frac{g}{g_*^{1/2}(x)}\right] \quad .$$

Usual values for x_f are $\sim 25-30$ if $m_\chi \sim \mathcal{O}(100)$ GeV. Using equation (1.29), $\Omega_\chi^0 = m_\chi c^2 \frac{(n+1)x_f^{n+1}}{b_1(x_f)}\frac{s_0}{k_B\rho_c^0}$, which can be rewritten as

$$\begin{aligned}\Omega_\chi^0 h^2 &= \frac{10^{-27}\ \mathrm{cm}^3/\mathrm{s}}{\langle\sigma_{ann}v\rangle_0}(n+1)x_f^{n+1}\frac{g_*^{1/2}(x_f)}{g_{*s}(x_f)} \\ &\overset{n=0}{\sim} \frac{3\times 10^{-27}\ \mathrm{cm}^3/\mathrm{s}}{\langle\sigma_{ann}v\rangle_0}\left(\frac{x_f}{30}\right)\left(\frac{g_*(x_f)}{100}\right)^{1/2}\left(\frac{100}{g_{*s}(x_f)}\right) \quad . \end{aligned} \tag{1.30}$$

Let us notice that equation (1.30) embodies what is usually dubbed the *"WIMP miracle"*, i.e. **WIMPs** with $m_\chi \sim \mathcal{O}(100)$ GeV and weak scale cross-sections

$$\sigma_{ann} \sim \frac{\alpha_{weak}^2}{m_W^2} \sim \frac{(G_F m_W^2/(\sqrt{2}\times 4\pi))^2}{m_W^2} \sim \mathcal{O}(1)\ \mathrm{pb} \quad ,$$

motivated by completely independent reasons on the particle physics arena, present $\langle\sigma_{ann}v\rangle \sim 3\times 10^{-26}\ \mathrm{cm}^3/\mathrm{s}$ and $\Omega_\chi^0 h^2 \sim \mathcal{O}(0.1)$ providing very good Dark Matter candidates. This is, of course, only an order of magnitude argument.

It is straightforward to generalise equations (1.29) and (1.30) for cross-sections $\langle\sigma_{ann}v\rangle = \sum_i \eta_i x^{-i}$. In particular the usual non-relativistic expression is $\langle\sigma_{ann}v\rangle \simeq A + \tilde{B}\langle v^2\rangle \equiv A + B/x$, where $\langle v^2\rangle \propto k_B T/m_\chi = c^2/x$. There are, however, exceptions to such behaviour. Perhaps the most noticeable example is the case of *coannihilations*: if there exists a particle χ' with $m_{\chi'} \gtrsim m_\chi$ and decaying to χ (that is assumed stable), then annihilations $\chi\chi'$ in the early Universe play an important role in the calculation of Ω_χ^0. In this situation equation (1.25) is replaced by

$$\dot{n} + 3Hn = -\langle\sigma_{ann}v\rangle\left(n_\chi^2 - n_{\chi,eq}^2\right) - \langle\sigma_{\chi\chi'}v\rangle\left(n_\chi n_{\chi'} - n_{\chi,eq}n_{\chi',eq}\right) \quad , \tag{1.31}$$

where $n = n_\chi + n_{\chi'}$ and, since χ' particles eventually decay to χ, at late times $n_\chi = n$. The generalisation for several states χ' is straightforward and useful formulae may be found in [19]. The qualitative effect of coannihilations is to increase the effective annihilation cross-section and thus reduce the relic abundance Ω_χ^0.

Throughout this Section we have assumed a vanishing chemical potential $\mu_\chi = 0$. Needless to say, the relic abundance of *asymmetric particles* is treated in a slightly different manner since their equilibrium density in the regime $k_B T \ll m_\chi c^2$ is $(n_\chi + n_{\bar{\chi}}) \propto \cosh(\mu_\chi/(k_B T))$.

1.2.4 Beyond the standard lore

The hot big bang model constitutes today the standard cosmological picture and enjoys great observational success. Besides an expanding Universe, it accommodates the existence of the CMB and provides good understanding of the observed abundance of light elements created during BBN at MeV temperatures. Nevertheless, two of the pillars of

standard cosmology, *isotropy* and *homogeneity*, must not hold at small scales or one would not have the rich stellar, galactic and extragalactic structure observed today. Even disregarding the latter, there are three main issues regarding the initial conditions that the hot big bang model does not solve:

- The *flatness problem* arises from the fact that an almost flat Universe today was even more so in the past. Indeed, from equation (1.8) with $k \neq 0$ it is easy to check that $|\Omega_{tot} - 1| \propto (aH)^{-2} \propto (1+z)^{-2}$ for radiation domination and $|\Omega_{tot} - 1| \propto (1+z)^{-1}$ for matter domination. Hence, either the initial conditions of the Universe force $k = 0$ ($\Omega_{tot} = 1$), or $k \neq 0$ and Ω_{tot} is fine-tuned to a value incredibly close to unity.

- The *horizon problem* stems from the observation of a high degree of isotropy across the sky, for instance in the CMB. It is reasonable to consider that such homogeneous patches must have been in causal contact in the early Universe. However, the angle in the sky subtended by the horizon at recombination $d_H(t_{rec})$ is

$$\Delta\theta \sim d_H(t_{rec})/R(T_{rec}) \sim 2^\circ \quad ,$$

  where we have assumed a flat Universe with $\Omega_\Lambda \sim 0.7$, $\Omega_m \sim 0.25$, $\Omega_r \sim 5 \times 10^{-5}$, $z_{rec} \sim 1300$ and $R(t) = a(t) \int_t^\infty \frac{cdt'}{a(t')} = \frac{c}{1+z} \int_0^z dz'\, H^{-1}(z')$. Therefore, at the time of emission, the Cosmic Microwave Background was not in causal contact and its homogeneity scale was already larger than the horizon. Since in a matter-dominated (radiation-dominated) Universe $a \propto t^{2/3}$ ($a \propto t^{1/2}$) while in both cases $d_H(t) \propto t$, in standard cosmology the CMB homogeneity scale was always outside the horizon (i.e. not in causal contact) for $t < t_{rec}$.

- The *relic problem* – usually known as the monopole problem – consists in explaining why the present energy density of the Universe is not dominated by massive relics. In fact, grand unified theories predict the existence of very heavy particles including monopoles. Because the annihilation cross-section is often a decreasing function of mass, this sort of particles should have decoupled very early in the cosmological timeline and have a present-day abundance large enough to overclose the Universe. Such reasoning holds as long as there is no entropy production as in the case of the hot big bang model.

The **theory of inflation** provides very neat and plausible solutions to the above-mentioned problems by motivating a highly flat, homogeneous and radiation-dominated Universe independently of the initial conditions. To this aim, inflationary models introduce a period of extreme accelerated expansion, that may be produced by a *scalar field* ϕ in an appropriate potential $V(\phi)$. For a homogeneous scalar field, the energy density and pressure are respectively $\rho_\phi = \dot{\phi}^2/2 + V(\phi)$ and $p_\phi = \dot{\phi}^2/2 - V(\phi)$, so if $\dot{\phi}^2/2 \ll V(\phi)$ (slow roll), then $p_\phi = -\rho_\phi$ and ϕ behaves as a cosmological constant. In this regime $H^2 \propto \rho_\phi = \text{const}$, $a \propto \exp(Ht)$, and the flatness problem is alleviated since a total energy density close to critical is easily explained: $(\Omega_{tot} - 1) \propto (aH)^{-2} \propto \exp(-2Ht)$. Also, the horizon problem disappears because an exponential growth of the scale factor provides a mechanism to put the entire present Hubble volume in causal contact during the inflationary period. This epoch, however, cannot continue indefinitely as the Universe is exponentially cooling – a phase of *reheating* is needed in order for the standard radiation domination to kick in. In the case of a scalar field driving inflation, reheating corresponds

to the oscillations of ϕ around the potential minimum that cause it to decay into lighter degrees of freedom which eventually thermalise. Such a huge release of energy, that brings the Universe to the reheating temperature $T_{RH} \lesssim 10^{14}$ GeV, dilutes any supermassive relics, thus providing a reasonable solution to the monopole problem. Moreover, quantum fluctuations of the scalar field are blown up by the period of exponential expansion and give a framework to study primordial density perturbations in the CMB sky.

Now, although inflation provides a good way out for standard cosmology, there is no direct evidence supporting such scenario. In fact the deepest available probe of the early Universe is Big Bang Nucleosynthesis that confirms the hot big bang model. At MeV temperatures, therefore, the Universe was radiation-dominated. What happened before is a matter of speculation: one can extrapolate the standard radiation domination, or assume that the Universe energy density was controlled by a new kind of species. There are several examples of **non-standard cosmological scenarios**:

- *Low reheating temperature scenarios* [20, 21, 22, 23]. The reheating temperature (either from inflation or a later period) can in principle be very low – effectively, BBN only forces $T_{RH} \gtrsim$ MeV. During this reheating epoch, the coherent oscillations of a scalar field ϕ around the potential minimum may be treated as a decay of a massive species, thus $H \propto \rho_\phi^{1/2} \propto a^{-3/2}$, but the release of entropy makes the temperature T decay more slowly with a, namely $T \propto a^{-3/8}$ which yields $H \propto T^4$.

- *Kination* [24, 25, 26, 27]. It is possible that there was period when the Universe was dominated by a scalar field ϕ in "kination" phase, i.e. $\dot{\phi}^2/2 \gg V(\phi)$. In this case, $p_\phi \sim \rho_\phi \sim \dot{\phi}^2/2$ and ϕ behaves like a species with equation of state $w_\phi = 1$ so that $\rho_\phi \propto a^{-6}$. Since there is no entropy creation in these scenarios, $a \propto T^{-1}$ and the expansion rate scales as $H \propto \rho_\phi^{1/2} \propto T^3$.

- *Scalar-tensor theories* [28]. These theories feature a scalar field in the gravity sector that has a metric coupling to matter. It is possible to construct models that basically coincide with General Relativity after BBN but predict very different expansion rates of the Universe at higher temperatures.

It is interesting to point out that, if such periods of non-standard expansion take place around the WIMP freeze-out process, they change radically the calculation presented in Section 1.2.3 where radiation domination was assumed. In particular, most (but not all) of the non-standard cosmological models predict a Hubble parameter growing faster with increasing temperature than $H \propto \rho_r^{1/2} \propto T^2$. This will anticipate the freeze-out time and – unless there is a strong entropy release after decoupling – will produce a larger relic abundance. In other words, in scenarios of non-standard expansion, cold relics such as WIMPs satisfy the condition $\Omega_\chi^0 h^2 \sim 0.1$ for cross-sections $\langle \sigma_{ann} v \rangle$ in excess of the usual value 3×10^{-26} cm^3/s. We shall return to this topic in Section 5.8.

1.3 Evidence for Dark Matter

As of today the most favoured cosmological setup within the hot big bang paradigm is the so-called **ΛCDM (Λ-Cold Dark Matter) model**, specified below, that requires a present-day energy density of the Universe dominated by dark energy and Dark Matter. Both components find no possible explanation within the Standard Model of particle

physics or General Relativity, thus pointing towards the existence of new physics yet to discover. Spanning the scale of galaxies, galaxy clusters and cosmology, the evidence for Dark Matter is particularly strong and convincing so that nowadays we are rather confident that most of the matter in our Universe is of a non-luminous kind. In this Section we briefly review several independent observations supporting the existence of **cold, non-baryonic Dark Matter**. Excellent reviews on this topic are available in the literature, e.g. [17, 29, 30, 31].

1.3.1 Big Bang Nucleosynthesis

We start with Big Bang Nucleosynthesis which is not, strictly speaking, direct evidence for Dark Matter. However, it constrains rather accurately the cosmological abundance of baryonic matter, thus providing a hint on the nature of Dark Matter as we shall see.

BBN is the mechanism that accounts for the production of light elements from the hot primordial plasma. Consider a nucleus i of atomic number Z_i and mass number A_i at a temperature of tens of MeV. At those temperatures the nucleus is non-relativistic and in chemical equilibrium with neutrons and protons so that $\mu_i = Z_i\mu_p + (A_i - Z_i)\mu_n$. Its number density n_i can then be written as [10]

$$n_i = g_i \hbar^{3(A_i-1)} A_i^{3/2} \left(\frac{2\pi}{m_p k_B T}\right)^{3(A_i-1)/2} 2^{-A_i} \exp\left(\frac{B_i}{k_B T}\right) n_n^{A-Z} n_p^Z \quad , \tag{1.32}$$

where $m_n \sim m_p$, $m_i \sim A_i m_p$, $g_p = g_n = 2$, $B_i = (Z_i m_p + (A_i - Z_i)m_n - m_i)c^2$, and equation (1.16) was used. Defining $n_N = n_n + n_p + \sum_i A_i n_i$, one can express (1.32) as an abundance

$$X_i \equiv A_i n_i / n_N \propto X_n^{A-Z} X_p^Z \eta^{A-1}$$

assuming $n_b - n_{\bar{b}} \simeq n_N$, and by consistency $\sum_i X_i = 1$. Neutrons and protons are also in chemical equilibrium with the radiation plasma through reactions as $n \leftrightarrow pe^-\bar{\nu}$. Assuming $|\mu_e|, |\mu_\nu| \ll k_B T$, their number densities are simply related by

$$\frac{n}{p} \equiv \frac{n_n}{n_p} = \exp\left(-\frac{(m_n - m_p)c^2}{k_B T}\right) \quad . \tag{1.33}$$

Naïvely one would expect that the light elements start to form at $k_B T \sim B_i \sim$ few MeV, but as in recombination the high number of photons per baryon $\eta^{-1} \gg 1$ delays this process to much lower temperatures ($\lesssim 0.3$ MeV). Usually, BBN is analysed in three separate steps:

- Firstly, at $k_B T \gtrsim 10$ MeV ($t \lesssim 0.01$ s) all components are in *chemical equilibrium* which results in $n/p \sim 1$ and $X_n \simeq X_p \simeq 1/2$. Initially the abundance of light elements is negligible.

- Afterwards, during the period $k_B T \simeq 10$ MeV $- 80$ keV ($t = 0.01 - 200$ s), the *decoupling of weak interactions* takes place at $k_B T \simeq 0.8$ MeV and a ratio $n/p \simeq 1/6$ freezes out.

- Finally, for $k_B T \simeq 80$ keV $- 30$ keV ($t = 200$ s $- 24$ min) sporadic *weak interactions* and *neutron decays* (with a half-life of 11 min) deplete the neutron-to-proton ratio to about 1/7 [10]. The temperature is now small enough that photons do not

dissociate nuclei immediately after creation, and nuclear reactions such as $pn \rightarrow D\gamma$, $DD \rightarrow {}^3\mathrm{He}\, n$, etc proceed safely. Virtually, all neutrons end up confined in ^{4}He nuclei, $n_4 \simeq n_n/2$. Therefore, the present abundance of ^{4}He should be $X_4 = \frac{4n_4}{n_N} \sim \frac{2\, n/p}{1+n/p} \simeq 0.25$ (where $n/p \sim 1/7$), which yields a surprisingly good match to observations. Slightly heavier elements like ^{7}Li and ^{7}Be are also created even though in small quantities. Due to the absence of stable elements with $A = 5, 8$ and the large Coulomb repulsion between the positively charged nuclei, BBN stops abruptly and no other nuclei are synthesised.

The abundance of ^{4}He is often qualified as a good *"chronometer"* [32] given that it is particularly sensitive to the timing of the n/p freeze-out. It is consequently a good probe of the expansion rate H at MeV temperatures. On the other hand, D and ^{3}He are essentially the fuel of the nuclear reactions occuring in the early Universe. Since these reactions proceed at a rate $\Gamma_{nuc} \propto n_N \propto \eta$, higher values of η correspond to lower abundances D/H and $^3\mathrm{He}/H$. Such behaviour makes deuterium and helium-3 useful *"baryometers"*, i.e. probes of the baryon cosmological abundance $\Omega_b^0 h^2 \sim 3.7 \times 10^7 \eta$.

It is usually a difficult task to infer from observations the primordial abundances of light elements, especially ^{7}Li that is easily destroyed in the interior of stars. Nevertheless, the fact that observations are naturally explained by the (standard) BBN with one parameter only (η, or $\Omega_b^0 h^2$) is a great success for the Standard Model of cosmology. In fact, this success confirms a radiation-dominated Universe whose relativistic degrees of freedom are given by photons and three families of neutrinos and antineutrinos at MeV temperatures[5]. All in all, observations offer the rather stringent bound $4.7 < \eta \times 10^{10} < 6.5$, or $1.7 \times 10^{-2} < \Omega_b^0 h^2 < 2.4 \times 10^{-2}$, which is in stark agreement with the values inferred from CMB anisotropy analyses. The derived baryonic abundance – pertaining both dark and luminous baryons – is clearly smaller than the total matter abundance Ω_m^0 inferred from a number of probes (see next subsections). Hence, BBN supports the case for the existence of **non-baryonic Dark Matter**.

1.3.2 Cosmic Microwave Background

The black body spectrum and large-scale isotropy of the Cosmic Microwave Background is perhaps the strongest evidence for the hot big bang model. As explained earlier in this Chapter, the CMB photons decouple from electrons and protons at $z_{dec} \sim 1100$ and redshift ever since presenting today an impressively accurate black body spectrum with $T_0 = 2.73$ K. The lack of significant spectral distortions (apart from the Sunyaev-Zel'dovich effect described below) is a reflection of the small baryon-to-photon ratio η. However, the tight photon-baryon coupling before decoupling must have produced imprints at a certain scale. The CMB is isotropic down to the 10^{-3} level; below that, temperature fluctuations exist and are usually expanded in spherical harmonics, $\frac{\Delta T}{T}(\theta, \phi) = \sum_{l,m} a_{lm} Y_{lm}(\theta, \phi)$ (for a review see [11]). The most evident deviation from isotropy is the *dipole anisotropy* ($l = 1$) with $\Delta T/T \sim 10^{-3}$ which is interpreted as the result of our motion with respect to the CMB rest frame. Subtracting off the dipole component, one finds *small-scale fluctuations* at the level of 10^{-5} which is about the right amplitude to seed structure formation and explain the present Universe [11]. A prominent feature in the CMB angular power spectrum is the *first acoustic peak* at $l \sim 200$ resulting from the baryon-photon coupling. The

[5]The observations are well accommodated by standard BBN with 3 neutrino families, but a slightly different number is not entirely excluded – see e.g. [32].

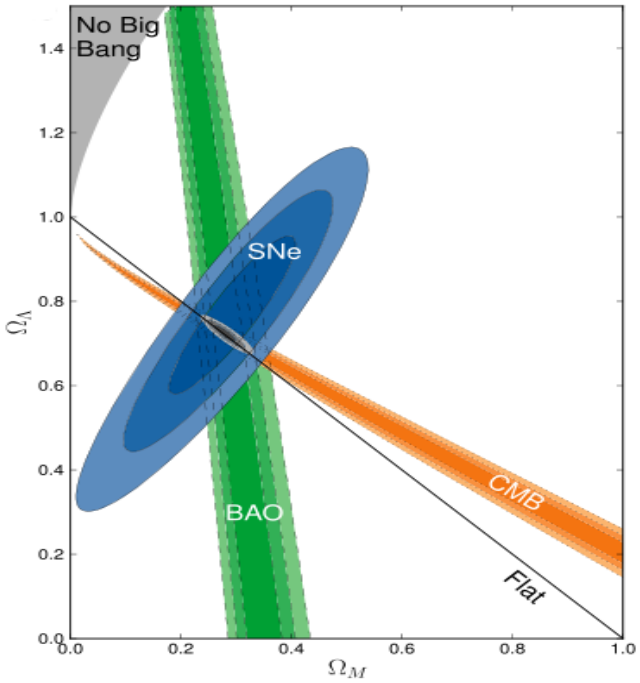

Figure 1.2: The parameter space compatible with CMB, supernova and Baryonic Acoustic Oscillations (BAO) data. Image from [33].

precise measurement of this peak – essentially made possible by WMAP – has important consequences for cosmology. In fact, its location (i.e. l) is an effective probe of the total energy content Ω^0_{tot} and it turns out that $\Omega^0_{tot} \sim 1$, which is naturally explained by inflationary models. On the other hand, the amplitude of the first peak is sensitive to the baryon abundance Ω^0_b (and h). It is remarkable that the values $\Omega^0_b h^2$ deduced from CMB measurements are in good agreement with BBN bounds.

The CMB anisotropies, by themselves, do not provide accurate measurements of Ω^0_m or Ω^0_Λ, but are mostly sensitive to $\sim \Omega^0_{tot} \simeq \Omega^0_m + \Omega^0_\Lambda$. However, as we shall see, supernova cosmology and large scale structure are sensitive to other directions in the $(\Omega^0_m, \Omega^0_\Lambda)$ parameter space and break the degeneracy – see Figure 1.2.

1.3.3 Supernova cosmology

In the late 1990's our perception of the Universe was radically changed by observations of supernovae (SN) type Ia. This kind of supernova results from the explosion of a white dwarf presenting an SiII (singly ionised silicon) line and no hydrogen. The light curve of such events is fairly standard, within a factor 3 [34], which make them good candidates for standard candles. After decades of trying to understand the underlying explosion mechanism and studying light curves (see [34] for a review on the topic), supernovae type Ia could finally be used as standard sources and allowed accurate distance measurements. Using ground-based supernovae surveys, and later follow-up observations from the Hubble Space Telescope, it was possible to detect several SNIa both nearby and at high redshifts $z \sim 1-2$. The corresponding Hubble diagram of luminosity distance d_L vs. redshift z was then used to extract the deceleration parameter q_0 (cf. equation 1.2) since $H_0 d_L \simeq z - (1-q_0)z^2/2$. It was found that $q_0 < 0$, i.e. the Universe is accelerating. Notice that these data constrain $q_0 \simeq -\Omega^0_\Lambda + \Omega^0_m/2$ (see Section 1.2.1), which in the plane $(\Omega^0_m, \Omega^0_\Lambda)$ is

almost orthogonal to Ω^0_{tot} fixed by CMB measurements, see Figure 1.2. The independent data sets seem to point consistently to a single cosmological configuration, the so-called **ΛCDM model** [15]:

$$\Omega^0_m h^2 = 0.135\,, \quad \Omega^0_b h^2 = 0.023\,, \quad \Omega^0_\Lambda = 0.73\,, \quad h = 0.70 \quad ,$$

where we have quoted the latest results from WMAP (7 years) with Baryonic Acoustic Oscillations (BAO) data and H_0 determination. Along this manuscript we shall work within the ΛCDM paradigm. Note that the Planck satellite – already taking data – should be able to improve upon WMAP measurements and shrink further the allowed cosmological parameter space.

Let us finally point out that SNIa observations are not direct evidence for Dark Matter but constitute an important piece of information in establishing the ΛCDM – that features $\Omega^0_m \sim 0.3$ – as the favoured cosmological model.

1.3.4 Structure formation

The observed Universe is manifestly inhomogeneous at small scales; therefore the assumption of homogeneity repeatedly used along this Chapter must break down below a given scale. Indeed, the densities attained in galaxies or galaxy clusters for example are several orders of magnitude above the cosmological average $\rho^0_{tot} = \Omega^0_{tot}\rho^0_c \sim 10^{-29}$ g/cm^3. During a given period in the past, tiny primordial perturbations must have been amplified and eventually undergone gravitational collapse leading to the structure that we see today. Many textbooks exist that introduce the foundations of structure formation theory, see e.g. [10, 35]; here we just recall a few basic results.

The *density contrast* $\delta = \frac{\rho-\bar\rho}{\bar\rho}$ of a given sub-horizon scale perturbation grows as the scale factor a during matter domination and oscillates in radiation-dominated epochs. Hence the matter-radiation equality at $1 + z_{eq} \sim 5 \times 10^3$ signals the onset of structure formation: only after the Universe becomes matter-dominated can perturbations grow appreciably. This is however not true for baryons since they are strongly coupled to the radiation bath until decoupling at $1 + z_{dec} \sim 1100$. Before decoupling subhorizon baryonic inhomogeneities are prevented from collapse by the large radiation pressure, and instead they oscillate as acoustic waves whose detailed pattern depends on the photon-baryon plasma sound speed. These waves leave an imprint in the CMB angular power spectrum and, as we shall see below, in the matter power spectrum. After CMB decoupling, baryonic density perturbations can finally grow freely and steadily. This outline leads to a strong argument for Dark Matter: if all matter in the Universe were baryonic, then matter perturbations could only grow for $1 + z \lesssim 1100$ which is clearly insufficient to explain today's structure from the CMB anisotropy amplitudes [36]. In contrast, if (weakly interacting) Dark Matter is the dominant mass component of the Universe, dark inhomogeneities grow since equality at $1+z_{eq} \simeq 5\times10^3$ and, after decoupling, baryons fall into the overdensities already formed by Dark Matter and together they grow afterwards.

Let $P_i(k) \propto k^n$ denote the Fourier transform of the correlation function $\xi(\vec{x}_1, \vec{x}_2, t) = \langle\delta(\vec{x}_1, t)\delta(\vec{x}_2, t)\rangle$ at a time just after inflation – the so-called **primordial power spectrum**. The case $n = 1$ corresponds to the *Harrison-Zel'dovich spectrum*. $P_i(k)$ describes the initial distribution of perturbations of different comoving wavenumbers $k = \frac{a}{a_0}k_{phys}$ (or wavelength $\lambda = \frac{2\pi}{k} = \frac{a_0}{a}\lambda_{phys}$). Now, the evolution of a given perturbation of comoving scale k depends upon the time of Hubble radius crossing, i.e. when k becomes larger

than $k_H \equiv \frac{aH}{a_0 c}$. In particular, for $k < k_{eq} \equiv \frac{a_{eq} H_{eq}}{a_0 c}$ the processed power spectrum today is $P(k) \propto k^n$, while for $k > k_{eq}$ it reads $P(k) \propto k^{n-4}$.

This would be the end of the story if the different components of the early Universe were perfect, non-interacting fluids, which is not the case. For instance, the epoch of decoupling (or, more exactly, recombination) features a sudden rise in the photon mean free path due to Thomson scattering with electrons. For scales below this mean free path, photons easily diffuse from overdense to underdense patches eliminating any initial density perturbation. This is the so-called **Silk** or **collisional damping**. Dark Matter candidates that are weakly interacting also couple to radiation in the early Universe giving rise to damping in dark inhomogeneities. The scale of the latter damping is fixed by the kinetic decoupling of Dark Matter occurring at T_{kd}, when the exchange of momentum between Dark Matter and the radiation fluid freezes-out [18, 37]. Notice that for many WIMPs this occurs after the chemical decoupling or freeze-out time. A further mechanism to damp dark perturbations is **free-streaming**: after kinetic decoupling or non-thermal production Dark Matter particles travel (almost) freely through the Universe until today. Inhomogeneities on scales smaller than such distance are severely eliminated. The *free-stream length* is simply

$$\lambda_{fs} = a_0 \int_{t_1}^{t_0} v \frac{dt}{a} = a_0 \int_{a_1}^{a_0} \frac{v(a)}{a^2 H(a)} \, da \tag{1.34}$$

where the scale factor a_1 indicates the production time for non-thermal Dark Matter, or the kinetic decoupling for thermal Dark Matter. How the velocity v evolves with a depends on the mass of Dark Matter and its initial momentum but it may be expressed in an unified fashion as

$$\frac{v}{c}(a) = \frac{p(a)c}{E(a)} = \left(1 + \frac{m_\chi^2 c^2 a^2}{p_1^2 a_1^2}\right)^{-1/2} \quad ,$$

where we have used the fact that momentum redshifts in an expanding Universe, $p(a) = p_1 a_1 / a$. For $p_1/(m_\chi c) \gg 1$ this expression returns $v/c \simeq 1$ and for $p_1/(m_\chi c) \ll 1$ one recovers the well-known behaviour $v \simeq v_1 a_1 / a$. For non-thermal candidates p_1 depends entirely on the production mechanism, while for thermal Dark Matter the typical momentum at kinetic decoupling is $p_1 c \sim k_B T_{kd}$ in the relativistic case ($k_B T_{kd} \gtrsim m_\chi c^2$) and $p_1 \sim \sqrt{m_\chi k_B T_{kd}}$ in the non-relativistic case ($k_B T_{kd} \lesssim m_\chi c^2$). Depending on m_χ and T_{kd}, the scale λ_{fs} may vary for several orders of magnitude [37]. However, generically speaking, **hot** Dark Matter particles such as standard neutrinos, featuring $v/c \sim 1$, yield $\lambda_{fs} \sim \mathcal{O}(100)$ Mpc or larger, while **cold** dark relics like WIMPs or axions present $v \propto a^{-1}$ and $\lambda_{fs} \ll$ Mpc. Inbetween the two extremes one has **warm** Dark Matter with intermediate, galaxy-sized free-streaming scales.

The damping mechanisms discussed in the last paragraph lead to exponential-like cutoffs in the processed power spectrum at small scales (large k) [18]. The smallest damping wavenumber is the one that defines the *effective cutoff* k_{cut}. Since the power per logarithmic k decade is proportional to $k^3 P(k)$, inhomogeneities of scale just below k_{cut} (or above $\lambda_{cut} = 2\pi/k_{cut}$) are the first to go non-linear ($\delta \simeq 1$) and collapse. This has very important implications: hot Dark Matter scenarios predict that very large structures are the first to form and their fragmentation leads to smaller objects as galaxies (*top-down*); cold Dark Matter models predict instead that small structures collapse first and

eventually gather to form larger objects (*bottom-up*). The determination of the power spectrum $P(k)$ – especially at small scales – is crucial to discriminate between the two alternatives. Thanks to the remarkable progress in precision cosmology over the last few years, the matter power spectrum has now been probed from 10^4 Mpc scales down to the Mpc scale. Several measurements, namely CMB anisotropies and the galaxy power spectrum, show no evidence of a small-scale cutoff [38]; the robust bound $\lambda_{cut} \lesssim 1$ Mpc therefore holds for the main component(s) of Dark Matter. Hot Dark Matter particles are disfavoured and in particular for standard neutrinos the upper bound $\Omega^0_\nu/\Omega^0_{cdm} < 7\%$ holds [39]. All in all, structure formation strongly supports the existence of large quantities of **cold Dark Matter**.

Another interesting probe is the imprint left by the photon-baryon sound waves (described above) in the matter power spectrum. These *Baryonic Acoustic Oscillations* (BAO) were detected in 2005 by measuring the galaxy correlation function in the Sloan Digital Sky Survey (SDSS) [40] – a peak at $100h^{-1}$ Mpc is clearly present and it turns out that this is a very efficient probe of Ω^0_m as shown in Figure 1.2.

1.3.5 Galaxy clusters

Galaxy clusters consist of more or less significant sets of gravitationally bound galaxies, and they are great laboratories to probe the presence of Dark Matter. The evidence for Dark Matter in these objects is at least threefold, coming from dynamical arguments, X-ray observations and gravitational lensing. *Dynamical data* from the Coma cluster were first analysed in 1933 by Fritz Zwicky who applied the virial theorem to derive a mass-to-light ratio in Coma of ~ 400 (in solar units) based upon the velocity and position of several cluster galaxies. Such a mass-to-light ratio is hardly reached by baryons in the cluster, and therefore Zwicky proposed – for the first time – the presence of large amounts of Dark Matter in the Coma cluster.

Later, *X-ray observations* revealed that the cluster environment is filled with hot ionised gas emitting through bremsstrahlung. The temperature profile of such gas indicates that it cannot be powered by the gravitational potential of luminous matter only. Taking the cluster to be spherically symmetric, the hydrostatic equilibrium reads $\frac{dp}{dr} = -\rho\frac{GM(<r)}{r^2}$, ρ being the mass density of the gas and p its pressure. If the gas is ideal with mean molecular weight μm_u (where $m_u \simeq 0.931$ GeV/c^2 is the atomic mass unit), then the total mass of the galaxy cluster enclosed in a sphere of radius r around its centre is expressed as

$$M(<r) = -\frac{rk_BT(r)}{\mu m_u G}\left(\frac{d\ln T}{d\ln r} + \frac{d\ln\rho}{d\ln r}\right) \quad .$$

Plugging in a roughly flat temperature profile $T(r) \sim 10$ keV and a density $\rho \propto r^{-2}$ [17], the mass enclosed at large radii is

$$M(<r) = \frac{2rk_BT}{\mu m_u G} \sim 9\times 10^{14}\ \mathrm{M}_\odot \left(\frac{r}{\mathrm{Mpc}}\right) \quad ,$$

with $\mu \sim 0.5$ for fully ionised hydrogen gas. This mass scale implies large mass-to-light ratios and a strong evidence for the abundant presence of Dark Matter in clusters of galaxies. X-ray halos are actually also observed in elliptical galaxies where the same reasoning applies. The hot ionised gas in galaxy clusters produces another interesting

signature: in the direction of a cluster, the CMB photons are upscattered through inverse Compton scattering off energetic electrons in the gas leading to distortions in the CMB spectrum. This is the so-called *Sunyaev-Zel'dovich effect* and can be used to constrain the baryonic component of a galaxy cluster and disentangle luminous components and Dark Matter.

Finally, *gravitational lensing* provides further support to the idea that clusters harbour huge amounts of Dark Matter. Einstein's General Relativity predicts that the presence of matter – luminous or not – deforms the space-time metric and thus bends the geodesic trajectories of photons. The more massive the object, the more significant the bending, or lensing, of light. If a background source – say, a quasar – happens to pass behind a galaxy cluster, the source light is lensed leading to multiple images or deformed arcs. In this way, precise photometric images of clusters have been used to probe their total mass and further strengthen the need for Dark Matter. Of course, other objects can serve as lenses (including galaxies and stars), and indeed gravitational lensing is a very promising tool to map the Dark Matter in our surroundings that would otherwise go undetected.

A spectacular test of the Dark Matter hypothesis was the multi-wavelength observation of a merger of two galaxy clusters, the **bullet cluster** [41]. X-ray observations were used to trace the hot gas while gravitational lensing probed the total gravitational potential. In the merger, individual galaxies act as collisionless particles and the hot gas of the two initial objects self-interacts strongly. However, the total mass distribution – reconstructed from the lensing data – appears to have survived the collision intact, with no interaction. This constitutes a strong argument for the presence of huge amounts of Dark Matter and requires essentially non-self-interacting Dark Matter particles. The upper bound on the self-interaction cross-section is of order 2 barn (m_χ/GeV) [42][6], where m_χ is the mass of the DM particle.

1.3.6 Galaxies

There is extensive evidence for Dark Matter on galactic and sub-galactic scales. Examples include the existence of X-ray halos in elliptical galaxies or the motion of stars in the solar neighbourhood, which point to mass-to-light ratios much larger than those of luminous matter. An excellent review on these issues may be found in Chapter 10 of Ref. [43]; here we shall only touch the most striking piece of evidence: rotation curves of individual galaxies (including our own).

The **rotation curve** $v_c(r)$ of a galaxy is the radial profile of the circular velocity of stars and gas – an example is displayed in Figure 1.3. For external galaxies, it may be determined by observing the optical lines of HII (ionised hydrogen) gas and the 21-cm line of HI (neutral atomic hydrogen). The Newtonian laws imply

$$v_c^2(r) = GM(< r)/r \quad .$$

Therefore, if light traced total mass in spiral galaxies, one would expect a "Keplerian" fall $v_c \propto r^{-1/2}$ at radii larger than the extension of the optical disk. However, in the 1970s several spiral galaxies were shown to have essentially flat (in some cases even increasing) rotation curves at several tens of kpc, well beyond the bulk distribution of light. This strongly suggests the presence of large amounts of Dark Matter – usually hypothesised in

[6]For reference, 1 barn = 10^{-28} m^2.

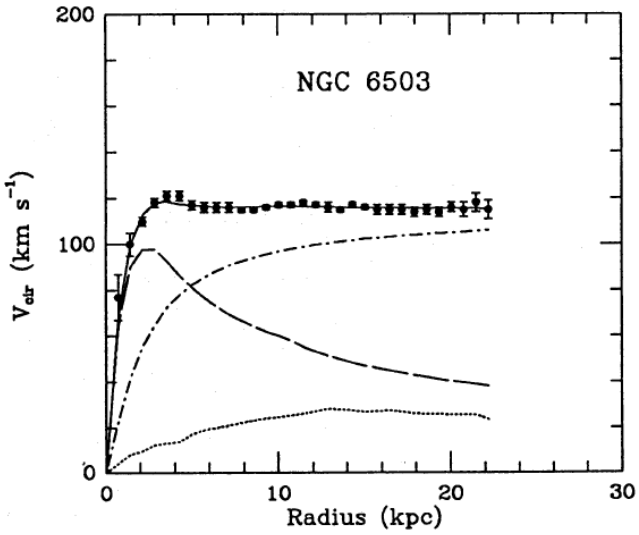

Figure 1.3: The measured rotation curve of NGC 6503, along with the best-fit model including dark halo (dot-dashed), stellar disk (dashed) and gas (dotted) components. Image from [44].

the form of a dark halo – in galaxies, since the gas and disk components do not suffice to explain such rotation curves. Now, a flat rotation curve $v_c \sim$ const requires a mass distribution $M(< r) \propto r$, or (assuming spherical symmetry) a density

$$\rho(r) = \frac{1}{4\pi r^2} \frac{dM(< r)}{dr} \propto r^{-2} \quad .$$

In other words, at large radii the measured rotation curves seem to point to a dark halo with the density profile of an isothermal sphere [43]. Such behaviour towards the centre of the galaxy cannot, of course, hold at very small radii, otherwise the inner features of observed rotation curves would be difficult to explain. Actually, as we shall see in Chapter 2, the Dark Matter halo in the very centre of a galaxy is currently a hot topic, and it is not yet clear from neither observations nor numerical simulations if the inner profile is cuspy (roughly $\rho \propto r^{-1}$) or cored. Another interesting point about rotation curves is that, quite generally, no Keplerian fall-off is detected even at the largest radii which means that we have no direct upper bound on the total mass of spiral galaxies.

The rotation curve of the Milky Way is slightly more difficult to measure given our peculiar position in the Galaxy. In any case, terminal velocities probe the innermost rotation, and the velocity dispersion of specific tracer populations can be used to determine the curve at larger radii (see detailed discussion in Section 2.2). The resulting constraints on the Dark Matter distribution are much looser than in the case of external galaxies. Nevertheless, a roughly flat outer rotation curve seems to be present and therefore there is strong indication of an extended Dark Matter halo embedding the galactic disk and probably contributing most of the total mass of the Milky Way.

1.4 Dark Matter candidates

The last Section outlined convincing evidence for cold, non-baryonic Dark Matter. This evidence holds for single-component Dark Matter, or for the dominant species in the case of multiple components. Over the years many candidates contributing to the dark

budget of the Universe have been put forward (for reviews see [45, 29, 30, 17, 46, 47]); here we present a very brief (and thus incomplete) overview. Dark Matter candidates may be placed in different categories according to their production mechanism (*thermal*, *non-thermal*), inhomogeneity damping scale (*cold*, *warm*, *hot*) and nature (*baryonic*, *non-baryonic*).

Let us start with **dark baryons**. It is almost certain that part of the baryonic matter of the Universe has not been detected yet simply because it is too faint. For instance, the mass-to-light ratio in the solar neighbourhood corresponds to a baryon abundance below BBN lower limit. Viable candidates to account for the missing baryons include faint stars and remnants (brown dwarfs, white dwarfs, neutron stars, black holes), intergalactic neutral or ionised gas, and massive black holes [43]. In particular, sub-solar, low-luminosity *MAssive Compact Halo Objects*, dubbed MACHOS, constitute a plausible explanation of the microlensing events towards the galactic bulge [48] and the Large Magellanic Cloud, even though they are excluded as a dominant mass component of the galactic halo. In any case, as pointed out earlier in the manuscript, BBN sets a strict upper limit on $\Omega_b^0 h^2$ that is clearly smaller than the cosmological matter abundance – non-baryonic candidates are needed. Throughout the rest of the thesis whenever we refer to "Dark Matter" we really mean "non-baryonic Dark Matter".

Within known particles, the only viable Dark Matter candidates are in principle **neutrinos** that were thermally produced in large quantities during the early phases of the Universe. If neutrinos were massless, their present energy density would be negligible (like for photons). However, the observation of oscillations between neutrino flavours has provided solid grounds for non-zero neutrino masses. Solar and atmospheric neutrino anomalies yield squared mass differences of 7×10^{-5} eV^2 and 3×10^{-3} eV^2, respectively, which means that the heaviest neutrino eigenstate has at least $m_\nu c^2 \simeq 0.05$ eV. Thus, one may apply equation (1.27) to derive sizeable abundances if $\sum_\nu m_\nu c^2 \sim \mathcal{O}$(a few) eV. The contribution of neutrinos to Ω_{tot}^0 is inevitable, but its size is unknown. Let us now pass to the problems in using neutrinos to account for a large fraction of $\Omega_m^0 h^2 \sim 0.135$. Firstly, direct ν mass measurements through β decay experiments give an upper limit $m_\nu c^2 \lesssim 2$ eV [11, 49], which already rules out neutrinos as main dark components. Moreover, after 7 years of data taking, the CMB anisotropy spectrum exquisitely determined by WMAP alone yields $\sum_\nu m_\nu c^2 < 1.3$ eV (95% CL for $k = 1$, $w_\Lambda = -1$) [15], which combined with BAO data and the H_0 measurement is pushed to $\sum_\nu m_\nu c^2 < 0.58$ eV (95% CL for $k = 1$, $w_\Lambda = -1$). Another problem with neutrinos lies in the fact that they are hot candidates being at odds with structure formation. The SDSS galaxy power spectrum [40] constrains the neutrino abundance from above and, in combination with CMB and H_0 measurements, gives $\sum_\nu m_\nu c^2 < 0.44$ eV (95% CL for $w_\Lambda = -1$) [15], i.e. $\sum_\nu \Omega_\nu^0 h^2 \lesssim 0.005$. It is interesting to note that the cosmological limits on neutrino masses are approaching the largest mass difference given by atmospheric oscillations, $|\Delta m| c^2 \simeq 0.05$ eV. Finally, being fermions, neutrinos obey the Pauli exclusion principle and, being light, their number density must be very high to account for large Dark Matter abundances. Therefore one can derive a lower limit on the neutrino mass. For instance, if a considerable part of the Dark Matter in dwarf galaxies was made of neutrinos, then $m_\nu c^2 \gtrsim 120$ eV [50, 29], which is clearly incompatible with the upper limits stated above.

The list of cold, non-baryonic candidates is huge and still growing. Arguably, the most well-motivated arise from extensions of the Standard Model of particle physics, introduced to solve problems uncorrelated to Dark Matter. Since the 1980s this has been

a very active field, and we shall focus in the following on three broad classes of candidates: axions, WIMPs and superheavy Dark Matter. For a general test on the viability of several Dark Matter candidates, see [51].

Axions arise from the most convincing solution to the *strong CP problem* in particle physics. The strong CP problem consists in the need to suppress non-perturbative CP-violating terms in the QCD Lagrangian due to the absence of an electric dipole moment for the neutron. In order to explain such fine-tuned cancellation, Peccei and Quinn introduced a spontaneously broken $U(1)$ global symmetry whose Goldstone boson is the axion. Due to QCD effects, the axion is not massless: $m_a \propto 1/f_a$, where f_a is the energy scale at which the Peccei-Quinn symmetry breaks. Depending on f_a, axions may have important signatures both in cosmology and particle physics; currently, stellar cooling arguments, SN1987A data and laboratory measurements exclude scales outside the range $10^9 \lesssim f_a/\mathrm{GeV} \lesssim 10^{12}$ [30], or $6.2 \gtrsim m_a/\mathrm{meV} \gtrsim 6.2 \times 10^{-3}$. Although extremely light, axions are actually cold because they are supposed to have been produced non-thermally and injected in the primeval plasma with low velocities. It is also possible to have thermal production of axions in the early Universe (see e.g. [10]) but in that case interesting relic abundances are only attained for $m_a \sim \mathcal{O}(10)$ eV, which is ruled out by other observations. In a nutshell, it is possible to find a perfectly acceptable window where axions are good Dark Matter candidates. However, their very weak interactions make it difficult to detect them – a caveat to this statement would be the detection of axion conversion into two photons in the presence of a strong magnetic field.

Also very well-motivated on particle physics grounds, **WIMPs** are by far the most studied class of Dark Matter candidates. Being produced thermally in the early Universe and freezing-out at $T_f < m_\chi$, WIMPs yield rather naturally the correct relic abundance and are consistent with structure formation bounds, passing all the tests with flying colours. These massive particles – usually with $m_\chi \sim \mathcal{O}(100)$ GeV – cannot be arbitrarily heavy, though: the *unitarity bound* limits from above the annihilation cross-section $\langle \sigma_{ann} v \rangle$ of a particle of mass m_χ; combined with the requirement $\Omega^0_\chi < \Omega^0_m$, the unitarity bound rules out WIMPs of mass in excess of tens of TeV [17]. Several particle physics extensions of the Standard Model provide WIMPs. One of the most compelling is *Supersymmetry* (SUSY), where the hierarchy problem discussed in Section 1.1 is circumvented by adding to each SM particle a supersymmetric partner with identical quantum numbers but a spin different by 1/2. For instance, each SM fermion f (quark or lepton) has a bosonic spin-0 superpartner $\tilde{f}$ called *sfermion*; each SM gauge boson γ, Z^0, $W^\pm$, g has a fermionic spin-1/2 superpartner called *gaugino* $\tilde{\gamma}$, $\tilde{Z}^0$, $\tilde{W}^\pm$, $\tilde{g}$. In the Higgs sector two doublets are needed to give mass to all particles unlike in the SM, corresponding to five physical states each having a fermionic spin-1/2 superpartner called *higgsino*. With such a field content, in SUSY the radiative corrections to the Higgs mass due to an energy scale $\Lambda \sim M_{GUT}c^2 \sim 10^{16}$ GeV cancel out since bosonic and fermionic loops have opposite signs. Furthermore, if R-parity $R = (-1)^{3B+L+2s}$ (that yields $R = +1$ for SM particles and $R = -1$ for supersymmetric particles) is conserved exactly, then interactions between SM particles can only yield an even number of supersymmetric particles. Analogously, a supersymmetric particle can only decay to an odd number of supersymmetric particles, which automatically makes the Lightest Supersymmetric Particle (LSP) stable. In case the LSP is also neutral it provides an excellent Dark Matter candidate. The most studied example is by far the **neutralino**, which is a Majorana fermion resulting from the superposition of the neutral wino $\tilde{W}_3$, the bino $\tilde{B}$ (or equivalently the superpartners of the

photon and Z-boson, $\tilde{\gamma}$ and $\tilde{Z}$) and the neutral higgsinos $\tilde{H}_1$ and $\tilde{H}_2$. The neutralino is the LSP in a large portion of the supersymmetric parameter space and it presents attractive characteristics such as an annihilation cross-section in the right ball park to yield the appropriate matter relic abundance and sizeable nucleus-WIMP scattering cross-sections so that it can be tested with underground experiments (see Section 1.5 and Chapter 3). Other SUSY Dark Matter candidates are **sneutrinos**, **gravitinos** and **axinos**. It is fair to state at this point that even the most compact SUSY frameworks are not very predictive and to obtain the observed relic abundance for the LSP is a matter of (fine-)tuning the several free parameters of the theory. *Universal Extra Dimensions* (UED) also provide excellent candidates in the form of **Kaluza-Klein excitations** of ordinary particles. One general and very appealing feature of WIMPs is that they produce interesting direct, indirect and collider signatures that may be falsified in the coming years at least for most theoretical models. Along this thesis we shall mainly focus on generic WIMP candidates and explore their phenomenological properties. While it is by no means granted that such kind of particles constitute the major component of matter in our Universe, it is certainly worthwhile exploring this line of research.

Finally, it is also possible that the Dark Matter content of the Universe is composed of **superheavy particles**, such as the so-called Wimpzillas. In fact, the $\mathcal{O}(10)$ TeV upper limit on m_χ discussed in the last paragraph may be evaded by simply hypothesising a particle that was never in thermal equilibrium with the primordial plasma. In this case the particle can be extremely heavy and the present-day abundance depends on the details of its (non-thermal) production. These models – that usually feature masses $\sim 10^{10}$ GeV – were popular in trying to explain ultra high energy cosmic-ray events above the *Greisen-Zatsepin-Kuzmin (GZK) cutoff* by the decay or annihilation of superheavy particles. However, that would imply a large fraction of photons at very high energies which is in tension with the latest results from the Pierre Auger Observatory (PAO) [52].

1.5 Detection strategies

An important property of WIMPs is that their couplings to Standard Model fields are small yet non-negligible, lying in the exact ballpark to be relevant for cosmology and astroparticle physics. It was shown in Section 1.2.3 how WIMPs easily account for the abundance of Dark Matter in the Universe. Besides that, however, these types of particles may lead to a multitude of exciting signatures usually arranged into three broad categories:

- **Direct detection**. If WIMPs constitute part of the Dark Matter component in our Galaxy, then there is in principle a flux of WIMPs crossing the Earth that can trigger nuclear recoils in low background environments. Although it is challenging to reduce background – usually detectors are placed underground and shielded –, this strategy is perhaps one of the cleanest to reveal the presence of WIMPs. Several past, present and planned experiments make direct detection an exciting topic as of today.

- **Indirect detection**. The self-annihilation or decay of WIMPs produces secondary Standard Model particles that can be detected themselves or via their interaction with the surrounding medium. Classic examples are $\gamma-$ray lines at the WIMP mass [53], antiprotons [54] or synchrotron emission from secondary electrons and positrons [55]. With such a wide range of messengers, this technique benefits from numerous

experimental data sets although no dedicated instrument has ever been built. A drawback of indirect searches is the poor discrimination power against astrophysical sources of secondary particles. Another way to search for Dark Matter is through its interaction with the surrounding medium; an example is the potential role of Dark Matter in stars [56, 57].

- **Accelerator/collider searches**. Many extensions of the Standard Model of particle physics introduce new physics at the TeV scale and feature viable WIMP Dark Matter candidates. These particles can therefore be produced and detected (via missing energy) in high-energy collider experiments. Even upon discovery, an issue to settle would be the stability of the particle on cosmological scales. This stresses the importance of pursuing a multi-disciplinary approach to Dark Matter searches. The leading present colliders are the Tevatron at Fermilab and the LHC at CERN.

During the last decades, tremendous effort has been put to detect any of the above-mentioned WIMP signatures. Nevertheless, and despite a few claims, it is fair to say that no uncontroversial DM-induced signal has been observed yet. The work presented in this thesis touches the first two categories above. Chapters 3 and 5 will outline direct and indirect signals in detail along with the relevant data sets.

Astroparticle physics is currently a very dynamic field of research with several experiments running or planned and with ever growing data quality and quantity. In this data-driven context, it is challenging but fundamental to keep up with all the different observations, ranging from high-energy cosmic-ray nuclei to radio waves, collected by all sorts of instruments, ranging from underground detectors to satellite telescopes. This is the only path to achieve a self-consistent view of the field and identify promising future lines of research. For an up-to-date discussion on WIMP detection see Ref. [58].

Chapter 2

Dark Matter distribution

In the previous Chapter we presented the evidence for Dark Matter, from sub-galactic to cosmological scales. The precise distribution of Dark Matter is however poorly known as of today, despite the tremendous progress achieved in the last years thanks to numerical simulations of gravitationally bound systems on the one hand, and observational data on the other hand. After briefly describing the onset of Dark Matter halos in Section 2.1, the DM distribution within the Milky Way (MW) is detailed in Section 2.2 with special emphasis on the uncertainties regarding the local density, profile and velocity distribution, which will be extensively analysed in the following Chapters. Some targets of interest for DM searches besides our Galaxy are then addressed in Section 2.3. The final Section of this Chapter is devoted to the systematic uncertainty in the determination of the local Dark Matter density, which constitutes one of the original contributions of this thesis [1].

2.1 The first halos

In the cosmological limit of large scales and high redshifts, the matter density scales as $\rho_m \propto (1+z)^3$, as seen in Section 1.2.1. This behaviour holds until the non-linear regime of structure formation sets in – roughly characterised by a density contrast $\delta \sim 1$. For a comoving scale R, the redshift z_{nl} at which the evolution becomes non-linear is defined by the condition of unit mass variance σ^2:

$$\sigma^2(R, z_{nl}) \equiv \int_0^\infty \frac{dk}{k} W^2(kR)\, k^3 P(k, z_{nl}) = 1 \quad , \tag{2.1}$$

where $P(k,z)$ is the processed linear power spectrum at redshift z (see definitions in subsection 1.3.4) and W is the Fourier-space window function (per unit volume) usually corresponding to a spherical top hat function [10],

$$W(t) = 3\left(\frac{\sin t}{t^3} - \frac{\cos t}{t^2}\right) \quad .$$

Very crudely, $W(kR)$ in equation (2.1) selects scales $k \lesssim 1/R$.

Now, as briefly described in 1.3.4, the matter power spectrum P has a cutoff at small scales (large k) $R_{cut} \sim 1/k_{cut}$. The cutoff scale is determined by two competing effects that depend on the specific properties of the Dark Matter particle: *free-streaming* (cf. equation (1.34)) and *collisional damping*. Of these processes, the one producing the largest scale

(smallest k) damping defines the effective cutoff of the power spectrum. For typical primordial power spectra and typical WIMP Dark Matter candidates, representative values for the small-scale cutoff range from 10^{-12} $M_\odot$ to 10^{-3} $M_\odot$ [59, 18, 37]. Because there is essentially no power on scales $k > k_{cut}$ and $P(k, z)$ is a decreasing function of z, the redshift $z_{nl}(R)$ obtained through equation (2.1) decreases with increasing R and exhibits a plateau $z_{nl} = 40 - 80$ for $R < R_{min} \sim 1/k_{cut}$ (see details in [18]). Put another way, the existence of a small-scale cutoff in the matter power spectrum fixes the size of the first perturbations to decouple from expansion and collapse, i.e. the very **first (dark) halos**.

Once in the non-linear regime, a perturbation of comoving size R_{cut} and mass $M_{cut} \propto R_{cut}^3$ evolves in a non-trivial way. A simplified, but useful, model to follow the evolution from z_{nl} until today is the *spherical collapse model* (see [35] for a full treatment), in which the perturbation reaches turn-around with a physical radius $r_m = 1.05 R_{cut}/(1 + z_{nl})$ and afterwards it collapses and virialises so that its present-day radius reads $r_0 \simeq r_m/2$. In this process, the density of the perturbation is enhanced, $\rho_0/\rho_c^0 \simeq 7(1 + z_{nl})^3$, while the mass M_{cut} is conserved. Therefore, if these halos survive until today, one should take into account that part of the DM in galaxies, galaxy clusters, etc is concentrated in virialised, small substructures with masses down to $10^{-12} - 10^{-3}$ $M_\odot$.

2.2 The Milky Way

2.2.1 Modelling and observations

To achieve an accurate modelling of our Galaxy is a crucial step in order to extract the underlying Dark Matter distribution. The Milky Way is a complex, gravitationally bound system of stars, gas, dust and Dark Matter, where the Sun sits at a galactocentric distance $R_0 \simeq 8.0 - 8.5$ kpc. The very centre of the Galaxy is believed to host a **supermassive black hole** with $(2-4)\times 10^6$ $M_\odot$ [60, 61] capable of explaining the orbits of Galactic Centre (GC) stars. The inner few kpc are dominated by the **bulge**, a roughly axisymmetric nucleus of stars with mass density $\rho_{bulge}(R, z)$, complemented by a triaxial **bar** region $\rho_{bar}(x, y, z)$ whose major axis lies in the galactic plane – see [62] for a parameterisation. Perhaps the most striking feature of our Galaxy is a luminous **disk** with spiral arms of gas, dust and stars extending out to $\mathcal{O}(10)$ kpc. The *stellar thin disk* is usually parameterised by a mass density [63]

$$\rho_{disk}(R, z) = \frac{\Sigma_{disk}}{2 z_{disk}} \exp\left(-\frac{R}{R_{disk}}\right) \mathrm{sech}^2\left(\frac{z}{z_{disk}}\right) \quad ,$$

where R_{disk} and $z_{disk} \sim \mathcal{O}(0.1)$ kpc are characteristic lengths and Σ_{disk} is the disk surface density. Moreover, in the disk there are also significant amounts of molecular hydrogen (H_2), atomic hydrogen (HI) and ionised hydrogen (HII) – for the respective radial distributions see e.g. [64]. All the just-mentioned galactic mass components are believed to be embedded in an extended **Dark Matter halo** whose size is probably in the order of hundreds of kpc. The specific shape and profile of the halo are discussed in the next subsection.

A central quantity in the MW mass modelling is the radial profile of the circular

velocity or **rotation curve** $v_c(r)$, already introduced in 1.3.6,

$$\frac{v_c^2(r)}{r} = \sum_i \frac{d\phi_i}{dr} = \frac{G}{r^2}\sum_i M_i(<r) \quad , \tag{2.2}$$

where the sum runs over the several mass components, namely bulge, bar, disk and halo. Note that for a spherical halo, one can write

$$M_{DM}(<r) = \int_0^r dr'\, 4\pi r'^2 \rho(r') \quad ,$$

or equivalently

$$\rho(\bar{r}) = \frac{1}{4\pi\bar{r}^2}\left.\frac{dM_{DM}}{dr}\right|_{\bar{r}} \quad ,$$

and equation (2.2) yields a density at $r = R_0$

$$\bar{\rho}_0 \equiv \rho(R_0) = \frac{1}{4\pi R_0^2}\left(\frac{1}{G}\left.\frac{d(v_c^2 r)}{dr}\right|_{R_0} - \sum_{i\neq DM}\left.\frac{dM_i}{dr}\right|_{R_0}\right) \quad , \tag{2.3}$$

in which the main contribution to the sum at R_0 is given by the disk component. If the halo is spherical, the **local DM density** ρ_0 (i.e. the density in the solar neighbourhood) coincides with $\bar{\rho}_0$. If the halo is non-spherical, then the above expression gives the *spherically averaged* local DM density.

Due to our peculiar position within the Galaxy it is a difficult task to constrain tightly the several parameters describing a MW mass model. Fortunately, however, there are several dynamical observables that can be used. Let us firstly focus on the measurement of the rotation curve. The circular velocity $v_c(r)$ inside the Solar circle $r < R_0$ can be probed by determining the *terminal velocities* of gas lying in the galactic plane. The terminal velocity v_T is simply the maximum measured velocity along a given line-of-sight of galactic longitude l. Taking strictly circular gas orbits, it is easy to extract an estimate of the circular velocity at $r = R_0 \sin l$ (see [65])

$$v_c(R_0 \sin l) = v_T(l) + v_c(R_0)\sin l \quad .$$

This inference is usually complicated by non-negligible velocity dispersions. For the outer rotation curve at $r > R_0$, it is common to use measurements of *velocity dispersion of specific tracer star populations*. According to the radial component of Jeans equation, the radial velocity dispersion σ_r in a population of stars with density profile ν obeys [43]

$$\frac{d(\nu\sigma_r^2)}{dr} + \frac{2\beta\nu\sigma_r^2}{r} = -\nu\sum_i \frac{d\phi_i}{dr} = -\nu\frac{v_c^2(r)}{r} \quad , \tag{2.4}$$

where in the last step equation (2.2) was used and $\beta = 1-(\sigma_\theta^2+\sigma_\phi^2)/(2\sigma_r^2)$ is the anisotropy parameter. Knowing how the star profile ν scales with r, it is possible to solve (2.4) for σ_r as a function of $v_c(r)$. In this way, and assuming that the measured line-of-sight dispersion $\sigma_{l.o.s.}$ is roughly equal to σ_r, one can constrain the rotation curve $v_c(r)$ at large r. An example of this procedure can be found in Ref. [63]. The local value of the rotation curve $v_c^0 \equiv v_c(R_0)$ is perhaps a more sensitive issue, partly because R_0 is not accurately known.

reference	estimate
Caldwell & Ostriker '81 [72]	$\rho_0 = 0.23 \pm \times 2$ GeV/cm^3
Gates, Gyuk & Turner '95 [74]	$\rho_0 = 0.30^{+0.12}_{-0.11}$ GeV/cm^3
Bergström, Ullio & Buckley '98 [53]	$\rho_0 \simeq 0.2 - 0.8$ GeV/cm^3
Moore et al '01 [75]	$\rho_0 \simeq 0.18 - 0.30$ GeV/cm^3
Belli et al '02 [76]	$\rho_0 \simeq 0.18 - 0.71$ GeV/cm^3 (isoth.)
Catena & Ullio '09 [63]	$\rho_0 = 0.39 \pm 0.03$ GeV/cm^3
Weber & de Boer '09 [77]	$\rho_0 \simeq 0.2 - 0.4$ GeV/cm^3
Salucci et al '10 [73]	$\rho_0 = 0.43 \pm 0.21$ GeV/cm^3
Lisanti et al '10 [78]	$\rho_0 \simeq 0.3 - 0.7$ GeV/cm^3

Table 2.1: A compilation of different estimates for the Dark Matter density in the solar neighbourhood. The reported values for Ref. [76] correspond to the cored isothermal profile only.

It is useful to express v_c^0 in terms of the *Oort's constants* A and B [43],

$$A - B = \frac{v_c^0}{R_0} \quad , \quad -A - B = \left.\frac{dv_c}{dr}\right|_{R_0} \quad ,$$

that can be constrained by studying the kinematics of different star types or of the GC radio source Sgr A*. Given the significant dispersion in the existing $A - B$ and R_0 measurements, it seems fair to say that $v_c^0 = R_0(A-B)$ is not known at present to better than a few tens of %. In Section 3.3 we shall use a broad range $v_c^0 = 230 \pm 30$ km/s, encompassing most present determinations.

Other observables are complementary to $v_c(r)$ and can be used to constrain the different mass components of our Galaxy. For instance, kinematic data from *Milky Way satellites* probe the total mass enclosed inside $50 - 100$ kpc [66, 67]. Also the motion of nearby stars has been used to measure the *local mean surface density* within $|z| < 1.1$ kpc [68] and the *local visible surface density* [69]. Finally, *microlensing data* have important consequences for the distribution of baryonic mass. In fact, the optical depth $\sim 10^{-6}$ associated with the microlensing events towards the bulge induces a lower limit of $\sim 4 \times 10^{10}$ $M_\odot$ for the baryonic mass inside the Solar circle [70] (see [71] for updated microlensing optical depths).

2.2.2 Mass density and velocity distribution

Let us start the discussion by the local DM density, ρ_0 (its spherical averaged $\bar{\rho}_0$ is given by equation (2.3)). This quantity can be effectively constrained by the several dynamical observables described above. Over the years several authors have extracted ρ_0 (or $\bar{\rho}_0$) by using different observables and different mass models for the Milky Way – see Table 2.1. The values lie in the rather wide interval $0.2 - 0.8$ GeV/cm^3 with uncertainties (mostly statistical) ranging from a factor 2 [72] to 7% [63]. This problematic will be analysed in detail in Section 2.4, so only a couple of points need to be addressed here. Firstly, it is worth noticing that over the decades a "standard" value 0.3 GeV/cm^3 has been systematically used, although this is not certainly a precisely determined quantity and the corresponding uncertainty is large. Secondly, equation (2.3) makes clear that, if the baryonic components are well-known (or irrelevant) at $r = R_0$, then the uncertainty on $\bar{\rho}_0$ is essentially a reflection of the uncertainties on v_c^0 and $dv_c/dr|_{R_0}$ (or, equivalently, $A \pm B$) – this is the idea behind the determination presented in [73].

The outer rotation curve of our Galaxy, measured through the methods described in the previous subsection, is rather uncertain but compatible with a flat behaviour extending

way beyond the luminous disk. This motivates a scaling $M \propto r$ (cf. equation (2.2)), or $\rho \propto r^{-2}$, which is the density profile of a singular isothermal sphere. Let us take a moment to describe the *isothermal sphere model*. Consider an ideal gas of pressure $p = \frac{\rho}{m} k_B T$ (m being the individual mass of the gas particles) at a constant temperature T. Then, under spherical symmetry the hydrostatic equilibrium condition $\frac{dp}{dr} = -\rho \frac{GM(<r)}{r^2}$ implies

$$\frac{k_B T}{m} \frac{d \ln \rho}{d \ln r} = -\frac{GM(<r)}{r} = -v_c^2(r) \quad , \tag{2.5}$$

or upon derivation

$$\frac{k_B T}{m} \frac{d}{dr} \left(r \frac{d \ln \rho}{d \ln r} \right) = -4\pi G r^2 \rho \quad , \tag{2.6}$$

which admits the solution

$$\rho(r) = \frac{k_B T}{m} \frac{1}{2\pi G r^2} \quad . \tag{2.7}$$

This profile, often dubbed singular isothermal profile, is valid for large radii; for small r, $\rho(r)$ is cored roughly following $\rho \propto (r_c^2 + r^2)^{3/2}$, where r_c is the core radius [43]. It is remarkable that equation (2.6) is precisely the Poisson equation for a system with a Maxwell-Boltzmann velocity distribution $f(v) \propto \exp\left(-\frac{v^2}{2\sigma_{1d}^2}\right)$ and $\sigma_{1d}^2 = \frac{k_B T}{m}$ [43]. Notice that σ_{1d} represents the one-dimensional velocity dispersion for this distribution, $\langle v_x^2 \rangle = \langle v_y^2 \rangle = \langle v_z^2 \rangle = \sigma_{1d}^2$, while the three-dimensional dispersion is $\langle v^2 \rangle = \langle v_x^2 \rangle + \langle v_y^2 \rangle + \langle v_z^2 \rangle = 3\sigma_{1d}^2$. Furthermore, plugging the scaling $\rho \propto r^{-2}$ in equation (2.5) one finds

$$v_c^2 = 2\frac{k_B T}{m} = 2\sigma_{1d}^2 = \text{const} \quad . \tag{2.8}$$

Actually, the same result follows from the Jeans equation (2.4) with $\beta = 0$, $\sigma_{1d} = \text{const}$ and a profile $\nu \propto r^{-2}$. Consequently, in the outer part of our Galaxy $r \gtrsim R_0$, where $v_c \sim \text{const}$, it is natural that the Dark Matter profile goes as $\rho \propto r^{-2}$ and the velocity distribution of Dark Matter particles follows

$$f_1(w) \propto \begin{cases} \exp\left(-\frac{w^2}{v_c^2}\right) & \text{for } w \leq v_{esc} \\ 0 & \text{for } w > v_{esc} \end{cases} \tag{2.9}$$

where v_{esc} is the local galactic escape velocity and we have used equation (2.8).

In order to go beyond this simplified picture, one needs to simulate gravitationally bound systems like our Galaxy. Such is the aim of **$N-$body numerical simulations** that follow the evolution of sets of particles[1] under mutual gravitational interaction. In several cases, astrophysical mechanisms need to be treated as well, including for instance supernova feedback, black hole accretion or gas dynamics. Modern simulations make use of impressive computational resources and, despite the remarkable progress over the past years, there is still a lot of work to do before fully understanding the formation of galaxies and other structures in our Universe – for an up-to-date review see Chapter 2 of Ref. [31]. Here we shall focus on the findings of galaxy-sized collisionless (i.e. Dark Matter only) numerical simulations, while the role of baryons is addressed in subsection 2.2.3.

One of the most staggering results of $N-$body simulations run in the ΛCDM cosmo-

[1] In this context, particles are extended cells encompassing a given mass of Dark Matter, stars or gas.

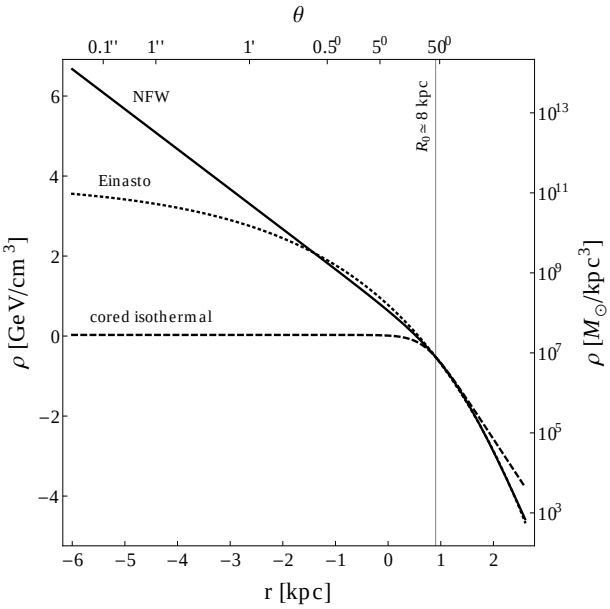

Figure 2.1: The Dark Matter mass density profile in a Milky Way sized object. Shown are the NFW profile with $r_s^{NFW} = 20$ kpc (solid line), the Einasto profile with $r_s^{Ein} = 20$ kpc, $\alpha_{Ein} = 0.17$ (dotted line) and the cored isothermal profile with $r_s^{iso} = 5$ kpc (dashed line). All profiles have been normalised to $\rho(R_0 = 8\text{ kpc}) = 0.3$ GeV/cm^3. Also shown is the angle $\theta = \text{arctg}(r/R_0)$ subentended by a distance r perpendicular to the direction of the Galactic Centre.

logical framework is that cold Dark Matter halos are self-similar presenting an *universal* spherically averaged density profile

$$\rho(r) = \frac{\rho_s}{(r/r_s)^{\gamma}\left(1 + (r/r_s)^{\alpha}\right)^{(\beta-\gamma)/\alpha}} \quad , \tag{2.10}$$

where r_s is the scale radius (which is well-defined for each halo), ρ_s is the scale density (in general $\rho_s \neq \rho(r_s)$) and the power-law indices α, β, γ are fit parameters. Notice that simulated DM-only halos are far from spherical, exhibiting instead triaxial, prolate shapes (see Section 2.4). Surprisingly, the parameterisation (2.10) with $\alpha = 1$, $\beta = 3$, $\gamma = 1$, usually called **Navarro-Frenk-White (NFW) profile**, describes rather accurately halos of masses ranging from $\sim 10^{-6}$ M$_\odot$ [79] to $\sim 10^{15}$ M$_\odot$ [80, 81]. The density profile in equation (2.10) is a running power-law with index $-\gamma$ for small radii $r \ll r_s$ and $-\beta$ for large radii $r \gg r_s$. In the case of the NFW profile this means that $\rho \propto r^{-3}$ (i.e. $M(< r)$ =const) in the outskirts of the halo, $\rho \propto r^{-2}$ at intermediate radii so that a flat rotation curve is generated and $\rho \propto r^{-1}$ towards the inner region. Other parameterisations producing quality fits to the outputs of $N-$body simulations are the **Einasto profile**

$$\rho(r) = \rho_s \exp\left[-\frac{2}{\alpha}\left(\left(\frac{r}{r_s}\right)^{\alpha} - 1\right)\right] \quad , \tag{2.11}$$

where $\alpha \simeq 0.17$ is a fit parameter, and the **cored isothermal profile** (less favoured but useful in assessing the prospects for DM detection) that is described by equation (2.10) with $\alpha = \beta = 2$, $\gamma = 0$. The behaviour of the NFW, Einasto and cored isothermal profiles is very different towards the inner part of the halo as depicted in Figure 2.1, where for illustrative purposes we have fixed $R_0 = 8$ kpc, $\rho_0 = 0.3$ GeV/cm^3, $r_s^{iso} = 5$ kpc, $r_s^{NFW} = r_s^{Ein} = 20$ kpc and $\alpha_{Ein} = 0.17$.

In the above-described parameterisations r_s and ρ_s fix the profile for each case. However, in the context of $N-$body simulations it is more convenient to use another pair of parameters, namely the *halo concentration* c and *mass* M. Along the manuscript we shall adopt $c \equiv c_{200} \equiv r_{200}/r_s$ and $M \equiv M_{200} = \frac{4\pi}{3} r_{200}^3 \times 200\rho_m^0$. The radius r_{200} is defined as the radius that contains a mean density equal to $200\rho_m^0 = 200\Omega_m^0\rho_c^0$. Given M_{200} one easily finds r_{200} and, using the latter and c_{200}, r_s is fixed. Lastly, ρ_s is set by the condition

$$M_{200} = \int_0^{r_{200}} dr\, 4\pi r^2 \rho(r) \quad ,$$

which implies

$$\rho_s = \frac{M_{200}}{\int_0^{r_{200}} dr\, 4\pi r^2 \frac{\rho(r)}{\rho_s}} = \begin{cases} \frac{200 c_{200}^3 \rho_m^0}{3(\ln(c_{200}+1) - c_{200}/(c_{200}+1))} & \text{for NFW} \\ \frac{25\times 8^{1+1/\alpha} \mathrm{e}^{2/\alpha} c_{200}^3 (-1)^{3/\alpha} \alpha^{1-3/\alpha} \rho_m^0}{3\left(\Gamma(3/\alpha) - \Gamma(3/\alpha, -2c_{200}^\alpha/\alpha)\right)} & \text{for Einasto} \\ \frac{200 c_{200}^3 \rho_m^0}{3(c_{200} - \mathrm{arctg}(c_{200}))} & \text{for cored isothermal} \end{cases} ,$$

where $\Gamma(x)$ and $\Gamma(x,y)$ are the standard and incomplete Gamma functions, respectively. Note that for each profile parameterisation there is an unambiguous relation between r_s and the radius at which the circular velocity $v_c(r) \propto \sqrt{M(<r)/r}$ peaks.

The resolution of present-day collisionless simulations is still not enough to confirm if the r^{-1} (or even steeper) cusp behaviour holds way into the central kpc of galaxy-sized objects. Also, this region is dominated by baryons and their influence upon the Dark Matter profile is still not clear. For example, the adiabatic contraction of baryons or the Dark Matter accretion onto the supermassive black hole at the centre of the Galaxy can steepen an eventual cusp, even though other effects such as the scattering off stars and annihilations can reduce significantly the profile within the inner parsec [82]. In particular, if Dark Matter particles self-annihilate with cross-section $\langle\sigma_{ann} v\rangle$, the depletion rate is $\langle\sigma_{ann} v\rangle \frac{\rho}{m_\chi}$ and after an interval Δt the *maximum possible mass density* reads simply

$$\begin{aligned} \rho_{max} &= \frac{m_\chi}{\langle\sigma_{ann} v\rangle \Delta t} \\ &\simeq 2 \times 10^{18}\ \mathrm{M_\odot kpc^{-3}} \left(\frac{m_\chi}{100\ \mathrm{GeV/cm^3}}\right) \left(\frac{4\times 10^{-26}\ \mathrm{cm^3/s}}{\langle\sigma_{ann} v\rangle}\right) \left(\frac{1\ \mathrm{Gyr}}{\Delta t}\right) \quad . \end{aligned} \tag{2.12}$$

This density ultimately defines a core in the very centre ($r \ll$ pc) of our Galaxy. In any case, if $\rho \propto r^{-\gamma}$ with $\gamma \gtrsim 1$ is extrapolated down to pc scales, huge DM-induced signals are expected from the Galactic Centre as discussed in Chapter 5.

As for the **velocity distribution**, $N-$body simulations find that at radii similar to $R_0 \sim 8$ kpc a Maxwell-Boltzmann distribution of the form (2.9) describes well the numerical results, but slightly overestimates the number of high-velocity particles [31, 83, 84, 78]. A better parameterisation is obtained by smoothly joining the two branches of (2.9), i.e.

$$f_2(w) \propto \begin{cases} \left(\exp\left(\frac{v_{esc}^2 - w^2}{k v_c^2}\right) - 1\right)^k & \text{for } w \le v_{esc} \\ 0 & \text{for } w > v_{esc} \end{cases} , \tag{2.13}$$

in which k is a shape parameter. This parameterisation – that will be extensively explored in Chapter 3 – can induce sizeable differences in direct detection rates with respect to the Maxwell-Boltzmann case [78].

Furthermore, $N-$body simulations convincingly demonstrate that the ΛCDM cosmology gives rise to a rich ensemble of **substructure** inside Dark Matter halos. These substructures include not only gravitationally bound spatial overdensities, the so-called *subhalos*, but also *streams*, i.e. sets of unbound particles presenting low spatial density and small velocity dispersion (thus significant phase space density, see [31]). The mass abundance of subhalos found in the simulations follow a power-law $M^{-\alpha}$ with $\alpha = 1.9-2.0$ at least down to $10^{-6}M_h$, where M_h is the host halo mass. This behaviour implies that $\mathcal{O}(10)\%$ of the system mass is enclosed in virialised substructures of mass $M > 10^{-6}M_h$; if the power-law $M^{-\alpha}$ is extrapolated down to the minimal masses discussed in Section 2.1 $M_{cut} = 10^{-12} - 10^{-3}$ $\mathrm{M}_\odot$, then up to half of the total mass of the system is in subhalos [85]. On the other hand, the spatial distribution of subhalos is affected by tidal forces that induce mass loss but increase the concentration parameter. It turns out that the subhalos inside a host halo trace approximately $r\rho(r)$ [31]. All the predictions of $N-$body simulations regarding substructure are, however, not universal in the sense that the subhalo population suffers from non-negligible halo-to-halo scatter.

2.2.3 The role of baryons

It has long been noticed [86] that the dissipational baryonic contraction in galactic halos drags the Dark Matter distribution inwards steepening its density profile. This is the so-called baryonic infall or **adiabatic contraction**. Consider an initial spherical distribution of baryons and Dark Matter, $M_i(< r_i)$, of which a fraction $1 - f_b = 1 - \Omega_b^0/\Omega_m^0$ will end up today distributed as $M_{DM}(< r) = (1 - f_b)M_i(< r_i)$. The final distribution of baryons $M_b(< r)$ is known and in the Milky Way case for instance is dominated by the stellar disk. Taking the particle orbits to be circular and the angular momentum $L = mrv_c \propto \sqrt{rM(< r)}$ to be conserved, one finds [86]

$$r_i M_i(< r_i) = r\left(M_b(< r) + M_{DM}(< r)\right) \quad , \tag{2.14}$$

that can be solved iteratively for r

$$r^{(n+1)} = \frac{r_i M_i(< r_i)}{M_b(< r^{(n)}) + (1 - f_b)M_i(< r_i)} \rightarrow r \quad .$$

In this way it is possible to construct the final Dark Matter mass distribution $M_{DM}(< r)$ and, upon derivation, the corresponding density profile. It turns out that the adiabatic contraction mechanism transforms an initial $\rho \propto r^{-1}$ cusp into $\rho \propto r^{-1.5}$ [82]. Refined models improving the standard adiabatic contraction in equation (2.14) have also been developed [87, 88].

Another relevant effect of baryons on Dark Matter halos is the change of shape. Dark Matter only simulations predict **prolate** halos, i.e. halos elongated along their major axis. The inclusion of baryons at the centre of galaxies modifies significantly the orbits of Dark Matter particles up to large radii, as demonstrated by several numerical simulations [88, 83, 89, 90, 91]. In particular, baryons seem to wash out the original prolateness of Dark Matter halos and induce a more **oblate** shape, i.e. a flattening along the minor axis

of the distribution. The final distribution, although close to axisymmetric, is still triaxial. Section 2.4 presents our new results [1] on this topic in light of very recent simulations of a Milky Way like galaxy, with particular emphasis on the consequences for the local Dark Matter density. Moreover, this issue should be further studied in the context of Dark Matter indirect searches since commonly a spherical density profile is assumed.

Finally, it is worth noticing that the accretion of Milky Way satellites onto the galactic disk creates a disk-like distribution of Dark Matter [92]. This so-called *dark disk* can feature a very significant local density and changes drastically an eventual direct detection signal [93].

2.3 Other targets

There are several regions of the Universe other than the Milky Way that constitute good targets for Dark Matter searches. Here we shall briefly address dwarf galaxies, galaxy clusters and cosmological halos. *Dwarf galaxies* are faint small objects usually orbiting a larger galaxy. Due to their dim luminosity, only nearby dwarf galaxies have been detected and many were found in the past five years or so thanks to data from the Sloan Digital Sky Survey – see [31] for an overview. Measurements of the line-of-sight dispersion of stars in most dwarfs imply huge total masses and thus large mass-to-light ratios. Indeed, these objects are among the highest M/L regions in our Universe and constitute excellent laboratories to probe Dark Matter. Additionally, since baryons are not abundant, the Dark Matter profile can be tested more accurately using collisionless simulations, unlike in the case of our Galaxy for instance. Unfortunately, however, the available spectroscopic data are not enough to definitely confirm or rule out cusp profiles in the inner part of dwarf galaxies. As far as indirect Dark Matter detection is concerned, dwarfs are promising targets given that the expected background emission at high energies is very low allowing good signal-to-background ratios.

Galaxy clusters are also interesting targets for Dark Matter searches since they are believed to harbour huge amounts of Dark Matter, as argued in 1.3.5. Plus, in light of the results of numerical simulations in the ΛCDM framework, a vast population of substructure should be present in galaxy clusters and likely dominates an eventual annihilation signal (see e.g. [94]). Nevertheless, contrary to dwarf galaxies, baryons play an important role in galaxy clusters. In particular, the hot intracluster gas and cosmic-ray acceleration are known or expected to emit radiation across the electromagnetic spectrum, from radio to $\gamma-$rays. Such emission constitutes a serious background for Dark Matter searches and make difficult any claim of discovery.

Lastly, because $\rho_m \propto (1+z)^3$, the abundance of Dark Matter at high redshifts is large. Hence, within any given line-of-sight there are numerous DM halos and subhalos as one goes to larger and larger redshifts. The density profile of these structures is parameterised in the same was as described in the previous Section. The distribution of *cosmological Dark Matter* along the line-of-sight can produce a contribution to the diffuse isotropic $\gamma-$ray flux as pursued in [95, 96].

2.4 Paper I: Systematic uncertainties in the determination of the local Dark Matter density[2]

A precise determination of the local Dark Matter density and an accurate control over the corresponding uncertainties are of paramount importance for Dark Matter searches. Using very recent high-resolution numerical simulations of a Milky Way like object, we study the systematic uncertainties that affect the determination of the local Dark Matter density based on dynamical measurements in the Galaxy. In particular, extracting from the simulation with baryons the orientation of the galactic stellar disk with respect to the DM distribution, we study the DM density for an observer located at $\sim$8 kpc from the Galactic Center *on the stellar disk*, ρ_0. This quantity is found to be always larger than the average density in a spherical shell of same radius $\bar{\rho}_0$, which is the quantity inferred from dynamical measurements in the Galaxy, and to vary in the range $\rho_0/\bar{\rho}_0 = 1.01-1.41$. This suggests that the actual Dark Matter density in the solar neighbourhood is on average 21% larger than the value inferred from most dynamical measurements, and that the associated systematic errors are larger than the statistical errors recently discussed in the literature.

2.4.1 Overview

A wide array of experimental strategies have been devised in order to identify the nature of Dark Matter [29, 30, 17, 31]. A key parameter in many of these searches is the local density of DM, namely the density of DM particles in the solar neighbourhood, ρ_0. For instance, the rate of events in direct detection experiments, that seek to measure the recoil energy in scattering events of DM particles off nuclei in the detector, is obviously proportional to the flux of DM particles through the detector, which in turn is directly proportional to the local DM density. Similarly, the neutrino flux from DM annihilation in the Sun is proportional to the capture rate of DM particles, in turn proportional to the flux of DM particles through the Sun, and therefore to ρ_0. As for indirect searches, the predicted flux of secondary particles, produced by the annihilation of DM particles, is proportional to ρ_0^2. A careful determination of this quantity is therefore of paramount importance in order to extract the properties of DM particles, especially when trying to perform a combined analysis of direct detection and LHC data [97].

Interestingly, as also pointed out in Ref. [73], ρ_0 is often assumed to be equal to 0.3 GeV cm^{-3}, with an error of *a factor of 2* . However, this value is often given without a reference, and when a reference is given, it can be traced back to papers which are a few decades old, e.g. [72, 74]. A number of papers have appeared recently on this subject, where the authors attack the problem of the determination of ρ_0 in light of recent observational results [73, 63, 98]. In Ref. [63] (see also [98]), for instance, the authors considered a large set of observational constraints of the Milky Way, e.g. the local stellar surface density, the local circular velocity and Dark Matter halo mass estimates from the velocity dispersion of halo stars. By adopting a Bayesian approach to mass modelling of the Milky Way components, a local Dark Matter density of 0.385 ± 0.027 GeV/cm^3 (assuming an Einasto profile) was found. The quoted 1σ errors are smaller than in previous studies due to the large set of input constraints, as well as the tight range that exists on a few of them (e.g. the

[2]This Section is based on the article [1], done in collaboration with Oscar Agertz, Gianfranco Bertone, Ben Moore and Romain Teyssier.

combination of Oort's constants $A-B$). This value was found to be quite insensitive to the assumed spherical DM density profile. As we shall demonstrate, the non-sphericity of the dark halo and its reaction to galaxy formation introduces larger systematic uncertainties. An alternative technique has been proposed in Ref. [73], where a constraint on ρ_0 is obtained based on local observables and with presumably no dependence on the mass model of our Galaxy.

Here we estimate the systematic uncertainty on ρ_0, with specific emphasis on the impact of departures from spherical symmetry. This has been studied in Ref. [99] using pure Dark Matter numerical simulations. We focus instead on a high-resolution simulation of a Milky Way like galaxy [100] − which reproduces the correct properties of our Galaxy − and consider its realizations with and without baryons. In particular, extracting from the simulation with baryons the orientation of the galactic stellar disk with respect to the DM distribution, we study the DM density for an observer located at ∼8 kpc from the Galactic Center *on the stellar disk*, and show that it is *systematically larger* than the average density in a spherical shell of the same radius. The latter is the observable that has usually been inferred from dynamical constraints such as the local circular velocity, terminal velocities and velocity dispersions of tracer star populations. Notice that we are disregarding fine grained structures (such as microhalos and streams) since their effect on DM searches is likely negligible as shown in [101].

2.4.2 Cosmological simulations of galaxy formation

Over the last years there has been tremendous effort in trying to understand the formation of galaxies like our own. Several cosmological simulations of galaxy formation have been designed including ever more realistic baryonic physics. A major difficulty in reproducing a Milky Way like galaxy resides in the fact that the dark halo total mass is uncertain, with plausible values ranging from 5×10^{11} $M_\odot$ to 2×10^{12} $M_\odot$ [102, 103]. If the halo mass lies close to the quoted upper limit, then the fraction of baryons in the Galaxy is well below the cosmological fraction $f_b \equiv \Omega_b^0/\Omega_m^0 \simeq 0.17$ and one needs to invoke strong supernova feedback, for instance, to avoid the so-called missing baryons problem. Also, in this case Dark Matter largely dominates the mass distribution and the influence of baryons upon the Dark Matter profile is likely small. On the other hand, if the halo is less massive, the missing baryons problem is alleviated and the role of baryonic physics is central. This latter case has been studied with the hydro+N−body simulations carried out in [100]. One of the major difficulties in obtaining a Milky Way like galaxy at $z = 0$ is that in simulations one usually ends up with large bulges and small disks, the so-called angular momentum problem. This has been circumvented by the authors of Ref. [100] whose final result is a Milky Way like galaxy with a flat rotation curve, a bulge-to-disk ratio $B/D \sim 0.25$ and a well-developed disk of characteristic length $r_{disk} \sim 4 - 5$ kpc. After selecting a halo of appropriate mass and no major merger after $z = 1$ from a cosmological simulation, the halo was resimulated with Dark Matter, gas and stars. Realistic baryonic effects were implemented (see [100] for full details), including star formation (with a given efficiency ϵ_{ff}), supernova feedback, stellar mass loss and gas dynamics. These simulations feature a mass resolution of 2.5×10^6 $M_\odot$ and a spatial resolution of 340 pc. In the following we shall analyse the Dark Matter distribution of two of those simulations: SR6-n01e1ML (with $\epsilon_{ff} = 1\%$) and SR6-n01e5ML (with $\epsilon_{ff} = 5\%$). The former is a galaxy similar to the Milky Way, while the latter is an example of a more baryon-dominated system. We

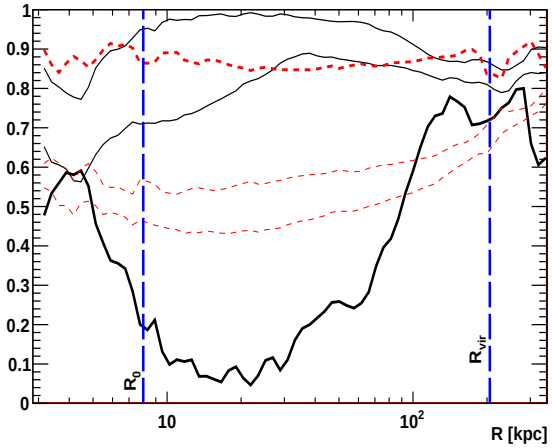

Figure 2.2: The shape parameters b/a, c/a and T for SR6-n01e1ML (solid black lines) and for the corresponding pure Dark Matter realization (dashed red lines), both at $z = 0$. Upper (Lower) thin lines show b/a (c/a), whereas thick curves represent the triaxiality parameter T. Also shown are the Sun galactocentric distance $R_0 \simeq 8$ kpc and the virial radius R_{vir}.

shall also use the DM-only realisation of the same halo.

2.4.3 Systematic uncertainties on the local Dark Matter density

Any departure from spherical symmetry and any modification of the DM enclosed mass due to adiabatic contraction is expected to lead to a systematic error in the determination of the local Dark Matter density at the solar position, as in general it will be different from the average density on a shell of same radius, which is the quantity inferred from most dynamical measurements. In this subsection we study these two effects and quantify the corresponding systematic errors on the determination of ρ_0.

Halo shape

It is well-known (e.g. [88]) that the inclusion of baryons in numerical simulations washes-out the prolateness of Dark Matter halos found in DM-only simulations. In order to measure the shape of the dark halo in the simulations under scrutiny (described in subsection 2.4.2), we follow [104, 91] and compute for a given set of N_p Dark Matter particles the matrix

$$J_{ij} = \frac{\sum_{k=1}^{N_p} m_k x_{i,k} x_{j,k}}{\sum_{k=1}^{N_p} m_k}, \tag{2.15}$$

where $i, j = 1, 2, 3$ index the coordinates in the reference system. The eigenvectors of J_{ij} are the major, intermediate and minor axes $\vec{j}_a$, $\vec{j}_b$ and $\vec{j}_c$, and the eigenvalues $J_a > J_b > J_c$ give the axis ratios through $b/a = \sqrt{J_b/J_a}$ and $c/a = \sqrt{J_c/J_a}$. The major (minor) axis $\vec{j}_a$ ($\vec{j}_c$) corresponds to the axis around which the angular momentum is minimal (maximal). The triaxiality parameter

$$T = \frac{1 - b^2/a^2}{1 - c^2/a^2}$$

distinguishes prolate ($T > 0.5$) from oblate ($T < 0.5$) shapes. For a given R, we start by considering the particles in the sphere of radius R to compute the principle axes, b/a and

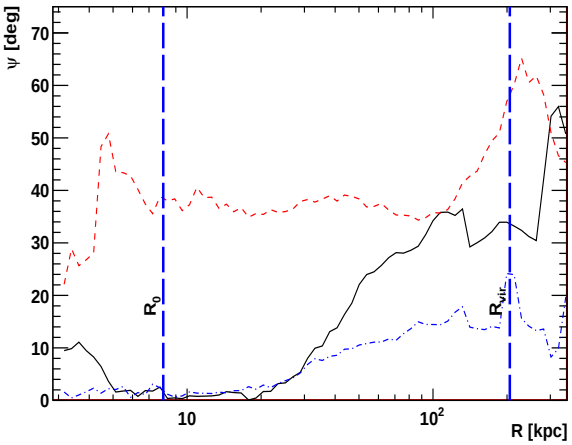

Figure 2.3: The angle between the normal to the stellar disk $\vec{n}_{sd}$ and the minor axis $\vec{j}_c$. The solid black (dot-dashed blue) line corresponds to SR6-n01e1ML (SR6-n01e5ML) at z=0. The dashed red line shows the angle between the minor axis in the pure Dark Matter simulation and the normal to the stellar disk in SR6-n01e1ML. Also shown are the Sun galactocentric distance $R_0 \simeq 8$ kpc and the virial radius R_{vir}.

c/a. We then repeat the procedure selecting particles in the ellipsoid $u^2 + \frac{v^2}{(b/a)^2} + \frac{w^2}{(c/a)^2} < R^2$, where u, v and w are the coordinates along the major, intermediate and minor axes, respectively. The computation is iterated until both b/a and c/a have varied less than 0.5%.

In Figure 2.2 we show b/a, c/a (thin lines) and T (thick lines) computed as described in the previous paragraph. Solid and dashed lines correspond respectively to SR6-n01e1ML and the Dark Matter only realization of the corresponding halo. As expected, in the absence of baryons the dark halo is manifestly prolate i.e. elongated along the major axis $\vec{j}_a$, while the numerical simulation with baryons produces a more oblate shape i.e. flattened along the minor axis $\vec{j}_c$. To check the orientation of the dark halo with respect to the baryonic component we plot in Figure 2.3 the angle ψ between $\vec{j}_c$ and the normal to the stellar disk $\vec{n}_{sd}$. In SR6-n01e1ML the dark and baryonic components are fairly aligned for $R < 20$ kpc. Furthermore, as the dot-dashed blue line indicates, in SR6-n01e5ML both components are even more aligned. Notice that above ∼100 kpc the presence of substructures affects significantly the shape measurement, as clear from Figures 2.2 and 2.3.

Now, we are interested in evaluating how the determination of ρ_0 in studies such as [63] is affected by the DM halo shape, in particular using the latest numerical simulations with baryons. As pointed out in [63], local observables constrain efficiently $\frac{\partial(v_c^2 r)}{\partial r}\Big|_{R_0}$. Such quantity depends on the baryonic content of the Milky Way and on the mass distribution of Dark Matter through the equations

$$M_{DM}(< r) \equiv \int d\varphi \int d\theta \int_0^r dr'\, r'^2 \sin\theta\, \rho(r', \theta, \varphi)$$

$$\frac{1}{G}\left.\frac{\partial(v_c^2 r)}{\partial r}\right|_{R_0} = K_b + \left.\frac{\partial M_{DM}}{\partial r}\right|_{R_0}, \tag{2.16}$$

where K_b encodes the contribution of baryons (at R_0 mainly dominated by the disk

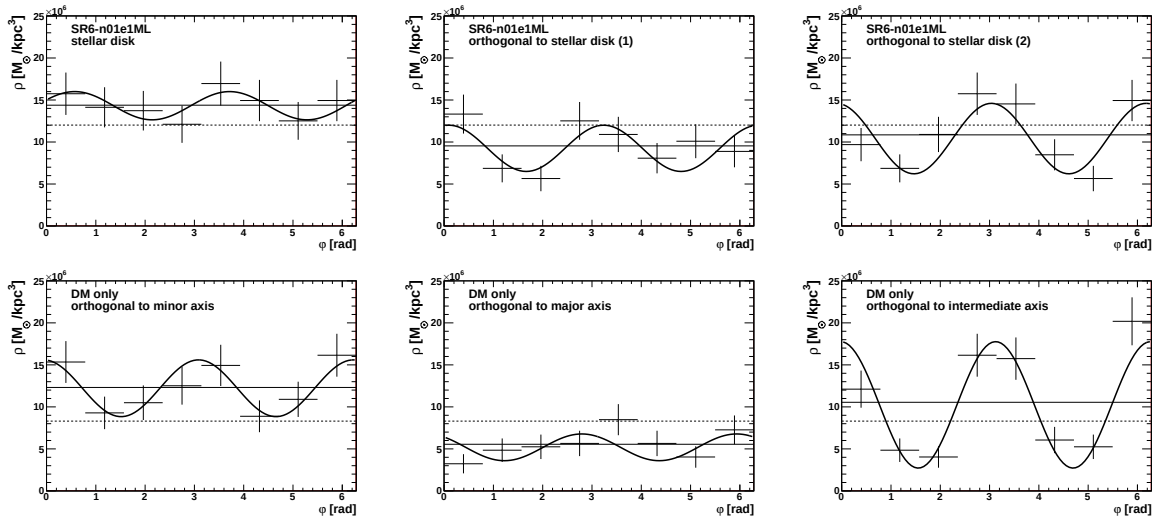

Figure 2.4: The Dark Matter density in the spherical shell $7.5 < R/\mathrm{kpc} < 8.5$ along the stellar disk plane and two perpendicular planes for SR6-n01e1ML (top), and along the planes perpendicular to the principle axes for the pure Dark Matter simulation (bottom). The solid horizontal line represents the mean of the points and the dashed line shows the value of the mean density in the whole shell, dubbed $\bar{\rho}_0$. The sinusoidal curve shown in each plot is the best fit to the points in the form $c_1 + c_2 \sin(2(\varphi + c_3))$.

component). In general,

$$\left.\frac{\partial M_{DM}}{\partial r}\right|_{R_0} = 4\pi R_0^2 \bar{\rho}_0, \tag{2.17}$$

where $\bar{\rho}_0$ is the spherically averaged Dark Matter density at $R_0 \simeq 8$ kpc, as also stressed in equation (2.3). We aim at comparing the mean spherical value $\bar{\rho}_0$ with the local one ρ_0 in the MW-like simulated galaxy SR6-n01e1ML − such comparison yields the systematic uncertainty in the determination of the local Dark Matter density presented in works where spherical halos were assumed. In order to study this effect we select Dark Matter particles that lie inside the spherical shell $7.5 < r/\mathrm{kpc} < 8.5$. Given three orthogonal planes (e.g. the ones defined by the principal axes) we consider the portions of the shell lying at distances from each plane smaller than $\Delta\omega/2 = 0.5$ kpc. This procedure defines three orthogonal ring-like structures each of which we divide in equal parts encompassing an angle $\Delta\varphi = \pi/4$ and thus a volume $V = 2\pi$ kpc^3. For reference in the following,

$$10^7\ \mathrm{M}_\odot/\mathrm{kpc}^3 = 0.38\ \mathrm{GeV/cm}^3 \quad .$$

Figure 2.4 sketches the Dark Matter density distribution in the above-mentioned rings for SR6-n01e1ML and the Dark Matter only simulation. In the former case we have used the stellar disk plane and two perpendicular planes, while in the latter the planes defined by the principle axes (of the set of particles in the shell $7.5 < r/\mathrm{kpc} < 8.5$) were considered. In each plot the angle bins represent portions of the ring encompassing $\pi/4$ rad (as described before) and the vertical error bars are Poissonian. The sinusoidal-like modulations seen for both simulations are naturally expected due to the triaxiality of the halos. As a guiding line, we present in each plot of Figure 2.4 the best fit function $c_1 + c_2 \sin(2(\varphi + c_3))$. Furthermore, one can appreciate large differences between the spherically averaged density $\bar{\rho}_0$ (dashed lines in Figure 2.4) and the density along each ring.

We pick two extreme cases to bracket the systematic uncertainties in the determination

of ρ_0: *(i)* the stellar disk plane in SR6-n01e1ML (Figure 2.4, upper left panel), and *(ii)* the planes perpendicular to the minor and major axes in the Dark Matter only case (Figure 2.4, lower left and lower central panels). Notice that we disregard the plane defined by the intermediate axis in the simulation without baryons because in that plane a stable baryonic disk cannot be formed[3]. In case *(i)*, since the Dark Matter halo is flattened along the stellar disk, the local Dark Matter density is higher than the spherically averaged value:

$$\rho_0/\bar{\rho}_0 = 1.01 - 1.41 \ .$$

In case *(ii)* a broader range is obtained:

$$\rho_0/\bar{\rho}_0 = 0.39 - 1.94 \ ,$$

in rough agreement with [99]. These values translate into systematic shifts on the local densities found e.g. in Ref. [63].

For the sake of completeness a similar analysis was carried out for the simulated galaxy with efficient star formation rate, SR6-n01e5ML. For the equivalent to case *(i)* explained in the last paragraph, we obtain $\rho_0/\bar{\rho}_0 = 1.21 - 1.60$; note nevertheless that this extreme object is not MW-like.

Enclosed mass

Both theoretical arguments and simulations of galaxy-sized objects [86, 87, 88] seem to indicate that baryons induce the contraction of the Dark Matter component towards the central part of the halo. This is also the case for the simulated galaxy SR6-n01e1ML when compared to the corresponding pure Dark Matter realisation. Note that the Dark Matter only simulation needs to be rescaled down by a factor $(\Omega_m^0 - \Omega_b^0)/\Omega_m^0 \simeq 0.8333$ in order to account for the presence of baryons, and that one can only firmly trust the numerical simulation results above about 2 times the resolution scale, i.e. 680 pc. The detailed study of the DM profile and adiabatic contraction models, addressed in Refs. [105, 90, 88, 89] in the framework of different numerical simulations, is of particular importance for indirect Dark Matter searches.

A relevant quantity to analyse when trying to determine the local Dark Matter density is the enclosed dark mass, $M_{DM}(< r)$, since this affects the rotation curve of the Galaxy. Using the spherically averaged density reported in Figure 2.4 (dashed lines), we find that the same enclosed mass $M_{DM}(< 8$ kpc) would result in SR6-n01e1ML and the pure Dark Matter halo if the local DM densities are rescaled such that

$$\frac{\bar{\rho}_0(\text{SR6-n01e1ML})}{\bar{\rho}_0(\text{DM only})} \simeq 0.9 \quad .$$

The lower density in the presence of baryons is simply a reflex of a more concentrated profile. In any case, these estimates do not translate directly into systematic uncertainties in the determination of ρ_0 since precise determinations of local observables − namely the Oort's constants $A \pm B$, the Sun galactocentric distance R_0 and the local visible matter surface density Σ_*, see [63, 73] − constrain efficiently both $\bar{\rho}_0$ (through $\left.\frac{\partial(v_c^2 r)}{\partial r}\right|_{R_0}$) and $M_{DM}(< R_0)$ (through $v(R_0)$). Therefore, we conclude that considering a contracted

[3]We thank J. Diemand for this comment.

Dark Matter profile would not change significantly the determination of the local Dark Matter density from precise dynamical observables, but would eventually prefer smaller concentration parameters (or, equivalently, larger scale radii r_s).

2.4.4 Conclusions

The Dark Matter density in our neighbourhood is the key astrophysical ingredient that fixes the flux of DM particles crossing the Earth and the Sun, thus governing the scattering off nuclei in underground detectors as well as the capture rate in the Sun. Experiments looking for DM-induced nuclei recoils or neutrino fluxes from the Sun are hence crucially dependent on the local Dark Matter density. In the present work we have tried to quantify the systematic uncertainties associated to this parameter, and that affect determinations based on dynamical observables of our Galaxy. Using a very recent successful attempt to simulate a spiral galaxy that resembles the Milky Way, the Dark Matter density at the solar circle was analysed in detail and compared to the pure Dark Matter case.

One major consequence of the inclusion of baryons is a significant flattening of the dark halo in the direction of the normal to the stellar disk, leading to a DM overdensity in the local disk of up to 41% with respect to the spherically averaged value. More specifically, we found that in the MW-like simulated galaxy the local Dark Matter density is higher than the spherically averaged value: $\rho_0/\bar{\rho}_0 = 1.01 - 1.41$. In the DM-only case a broader range is obtained: $\rho_0/\bar{\rho}_0 = 0.39 - 1.94$.

Ideally, one should repeat the analysis in Ref. [63], i.e. a Bayesian approach to mass modeling of the Milky Way components, in presence of a triaxial profile like the one discussed here. However, based on the considerations presented above, a better estimate of the local Dark Matter density can be obtained by raising by 21% the mean value obtained in Ref. [63] for the spherical case, keeping relative statistical errors fixed and adding systematic errors. In the case of an Einasto profile, this procedure suggests

$$\rho_0 = 0.466 \pm 0.033(\text{stat}) \pm 0.077(\text{syst}) \text{ GeV/cm}^3 \ .$$

Notice that the mean 21% enhancement with respect to the spherical local DM density is obtained for a specific simulated galaxy resembling the MW. The actual enhancement in our Galaxy may, of course, be different, but the main points here are that *(i)* the presence of baryons leads quite generally to a DM overdensity about the local disk, and *(ii)* the systematic uncertainties affecting ρ_0 are significant and, in some cases, already larger than the statistical ones.

The baryons are also responsible for a non-negligible contraction of the DM distribution towards the central part of the galaxy. Even though this may be very important in searching for products of DM annihilations – such as positrons or antiprotons from the galactic halo, and γ-rays or neutrinos from the Galactic Centre – we found that it has no significant effect in the determination of the local Dark Matter density using dynamical observables.

An estimate of systematic uncertainties affecting the local Dark Matter density is an important step in assessing realistically our present knowledge on this key parameter. Such knowledge is in turn an input in interpreting direct detection results, combining multiple DM-induced signals, and extracting compatible DM properties. Another relevant ingredient for DM scattering and capture is the velocity distribution $f(v)$ – such topic is out of the scope of this work, but it would be interesting to study it in the set of

simulations analysed here. In case of a positive signal in direct detection experiments, for instance, the identification of the compatible particle physics parameter space and the discrimination between different particle physics frameworks depend crucially upon the state of our knowledge in key astrophysical parameters such as the Dark Matter density in our neighbourhood.

Chapter 3

Direct Dark Matter detection

The weak-scale couplings featured by WIMPs, despite feeble, allow a non-negligible interaction with the surrounding medium, at least in regions of sufficient Dark Matter density. In this Chapter we shall focus on WIMP-nucleus scattering and the phenomenology of direct searches. Several of the ingredients already introduced in Chapter 2 will be used here. After outlining the theoretical framework of direct Dark Matter searches in Section 3.1 and the experimental status in Section 3.2, we proceed to present in Section 3.3 the results of our work [2] on the complementarity of direct detection targets.

3.1 Theoretical framework

3.1.1 WIMP-nucleus scattering

The WIMP-nucleus interaction may be spin-dependent (SD) or spin-independent (SI) according to the existing WIMP couplings to quarks and gluons. In **spin-dependent** interactions, the WIMP "sees" the spin J of a nucleus $N(A,Z)$ by coupling to the quark *axial* current. The corresponding Lagrangian term for a fermion WIMP χ is $\alpha_q(\bar{\chi}\gamma^\mu\gamma_5\chi)(\bar{q}\gamma_\mu\gamma_5 q)$ (for bosons analogous expressions may be found elsewhere [106]) which yields a cross-section:

$$\sigma^{SD}_{\chi-N}(E_R) = \frac{32}{\pi} G_F^2 \mu_N^2 \frac{J+1}{J} \left(a_p\langle S_p^N\rangle + a_n\langle S_n^N\rangle\right)^2 \times F^2_{SD}(A,E_R) \quad \text{(axial)} \quad , \tag{3.1}$$

where $\mu_N = m_N m_\chi/(m_N+m_\chi)$ is the WIMP-nucleus reduced mass, E_R is the nuclear recoil energy after the scattering and $\langle S^N_{p(n)}\rangle$ is the expectation value of the total spin of protons (neutrons) within the nucleus N. For specific values of $\langle S^N_{p(n)}\rangle$ see e.g. [17] and references therein; recall that $\sigma^{SD}_{\chi-N} \sim 0$ for nuclei with even number of protons and neutrons. Now, in the expression above a_p and a_n read

$$a_{p(n)} = \sum_q \frac{\alpha_q \Delta_q^{p(n)}}{\sqrt{2}G_F} \quad ,$$

in which the sum is over the quark types and families and $\Delta_q^{p(n)}$ encode the quark spin content of protons and neutrons. The spin of nucleons is mainly carried by light quarks (u, d, s) so that $\Delta^{p(n)}_{c,b,t} = 0$, and their composition entails $\Delta^n_u = \Delta^p_d$, $\Delta^n_d = \Delta^p_u$, $\Delta^n_s = \Delta^p_s$.

The remaining independent spin content parameters can be determined experimentally with a non-negligible uncertainty (see [107] for a thorough discussion and implications in direct detection):

$$\begin{aligned} \Delta_u^p - \Delta_d^p &= \Delta_d^n - \Delta_u^n = 1.2695 \pm 0.0029 \\ \Delta_u^p + \Delta_d^p - 2\Delta_s^p &= \Delta_d^n + \Delta_u^n - 2\Delta_s^n = 0.585 \pm 0.025 \\ \Delta_s^p &= \Delta_s^n = -0.09 \pm 0.03 \quad . \end{aligned}$$

Notice that, even when considering a well-defined underlying theory that provides a specific WIMP model, the uncertainties above propagate to the calculation of the actual cross-section. These are often called *nuclear uncertainties*, and are especially important for spin-independent interactions, as shown below. Finally, the last term in equation (3.1), F_{SD}, is the **nuclear form factor** that accounts for the non-zero size of the nucleus r_n: indeed, for momentum transfers $q \equiv \sqrt{2m_N E_R} \gtrsim h/r_n$, the nuclear structure becomes relevant and the cross-section must be corrected with respect to the zero-momentum transfer case. For spin-dependent interactions, the following parameterisation is reasonable [108]:

$$F_{SD}(A, E_R) = \begin{cases} \sin(qr_n)/(qr_n) & \text{for } qr_n < 2.55,\ qr_n > 4.5 \\ 0.217 & \text{for } 2.55 \leq qr_n \leq 4.5 \end{cases}$$

with $r_n \simeq 1.0A^{1/3}$ fm and $F_{SD}(A, 0) = 1$. Other parameterisations exist in the literature (see [17, 108]) and in principle depend on the target nucleus. Defining separate WIMP-proton and WIMP-neutron spin-dependent cross-sections

$$\sigma_{\chi-p(n)}^{SD,0} \equiv \frac{32}{\pi} G_F \mu_{p(n)}^2 \frac{J_{p(n)} + 1}{J_{p(n)}} \left(a_{p(n)} \langle S_{p(n)}^N \rangle \right)^2 \quad ,$$

equation (3.1) can be recast as

$$\sigma_{\chi-N}^{SD}(E_R) = \frac{J+1}{3J} \mu_N^2 \left(\frac{\sigma_{\chi-p}^{SD,0}}{\mu_p^2} + \frac{\sigma_{\chi-n}^{SD,0}}{\mu_n^2} + \frac{2\sqrt{\sigma_{\chi-p}^{SD,0} \sigma_{\chi-n}^{SD,0}}}{\mu_p \mu_n} \right) \times F_{SD}^2(A, E_R) \quad .$$

Note the dependence of this type of cross-section on $(J+1)/J$ that renders it dominant for low-mass nuclei with unpaired nucleons.

Spin-independent scattering occurs, roughly speaking, when the WIMP interacts with the nucleus as a whole. Scalar and vector WIMP-quark couplings contribute to this sort of interactions. *Scalar* interactions, arising from Lagrangian terms such as $\beta_q \bar{\chi}\chi\bar{q}q$, correspond to a zero-momentum transfer cross-section given by

$$\bar{\sigma}_{\chi-N}^{SI,0} = \frac{4\mu_N^2}{\pi} \left(Z f_p + (A - Z) f_n \right)^2 \quad \text{(scalar)} \quad , \tag{3.2}$$

where $f_{p(n)}$ represents the WIMP-proton (neutron) coupling:

$$\frac{f_{p(n)}}{m_{p(n)}} = \sum_q \frac{\beta_q}{m_q} f_{T_q}^{p(n)} + \frac{2}{27} f_{TG}^{p(n)} \sum_{\tilde{q}} \frac{\beta_{\tilde{q}}}{m_{\tilde{q}}} \quad ,$$

in which the first (second) sum is over the light quarks $q = u, d, s$ (heavy quarks $\tilde{q} = c, b, t$),

and $f_{\times}^{p(n)}$ parameterise the different quark contributions to the mass of nucleons. In particular, $f_{TG}^{p(n)}$ obeys the relationship $f_{TG}^{p(n)} = 1 - \sum_q f_{T_q}^{p(n)}$. The remaining factors $f_{T_q}^{p(n)}$ may be expressed in terms of the π-nucleon sigma term $\Sigma_{\pi n} \simeq 64 \pm 8$ MeV, the ratio of masses $m_u/m_d \simeq 0.553 \pm 0.043$ and $m_s/m_d = 18.9 \pm 0.8$, and the quantity $B_d^p/B_u^p \equiv f_{T_d}^p m_u/(f_{T_u}^p m_d)$ (see full details in [107]). Such error bands – especially the one associated to $\Sigma_{\pi n}$ – translate into somewhat sizeable uncertainties on the calculation of SI cross-sections which in turn ultimately limit our ability to distinguish between different particle physics models with spin-independent scalar searches. As in the axial case, one can define separate WIMP-proton and WIMP-neutron cross-sections $\bar{\sigma}_{\chi-p(n)}^{SI,0} \equiv \frac{4\mu_{p(n)}^2}{\pi} f_{p(n)}^2$ and rewrite equation (3.2) as

$$\bar{\sigma}_{\chi-N}^{SI,0} = \mu_N^2 \left(\frac{Z^2}{\mu_p^2} \bar{\sigma}_{\chi-p}^{SI,0} + \frac{(A-Z)^2}{\mu_n^2} \bar{\sigma}_{\chi-n}^{SI,0} + \frac{2Z(A-Z)}{\mu_p \mu_n} \sqrt{\bar{\sigma}_{\chi-p}^{SI,0} \bar{\sigma}_{\chi-n}^{SI,0}} \right) \quad \text{(scalar)} \quad . \tag{3.3}$$

Notice that, assuming $\bar{\sigma}_{\chi-n}^{SI,0} \sim \bar{\sigma}_{\chi-p}^{SI,0}$ (i.e. $f_p \sim f_n$),

$$\bar{\sigma}_{\chi-N}^{SI,0} \sim \frac{\mu_N^2}{\mu_p^2} A^2 \bar{\sigma}_{\chi-p}^{SI,0} \sim 2.5 \times 10^7 \bar{\sigma}_{\chi-p}^{SI,0} \quad ,$$

where in the last step we have taken $m_\chi \sim 100$ GeV and $A \sim 100$. As for *vector* interactions, the corresponding Lagrangian terms are of the form $\eta_q (\bar{\chi} \gamma_\mu \chi)(\bar{q} \gamma^\mu q)$ and the cross-section reads

$$\tilde{\sigma}_{\chi-N}^{SI,0} = \frac{\mu_N^2}{64\pi} \left(Z(2\eta_u + \eta_d) + (A-Z)(\eta_u + 2\eta_d) \right)^2 \quad \text{(vector)} \quad . \tag{3.4}$$

It is worth stressing that Majorana WIMPs (such as the neutralino in supersymmetric models) present no vector couplings. The spin-independent cross-section can be globally written as

$$\sigma_{\chi-N}^{SI}(E_R) = \frac{4\mu_N^2}{\pi} \left[\left(Z f_p + (A-Z) f_n \right)^2 + \frac{1}{256} \left(Z(2\eta_u + \eta_d) + (A-Z)(\eta_u + 2\eta_d) \right)^2 \right] \times F_{SI}^2(A, E_R) \quad , \tag{3.5}$$

where the spin-independent nuclear form factor is given by [108]

$$F_{SI}(A, E_R) = 3 \frac{\sin(qr_n) - (qr_n)\cos(qr_n)}{(qr_n)^3} \exp\left(-\frac{(qs)^2}{2} \right)$$

with $q = \sqrt{2 m_N E_R}$, $s \simeq 0.9$ fm, $r_n^2 = c^2 + \frac{7}{3}\pi^2 a^2 - 5s^2$, $c/\text{fm} = 1.23 A^{1/3} - 0.6$ and $a = 0.52$ fm. As evident from (3.3) and (3.4), the magnitude of the spin-independent cross-section scales approximately as A^2 and thus it is dominant for high-mass nuclei: the transition between SD and SI dominance occurs at $A \sim 30$ [109, 110].

Regarding the kinematics of the WIMP-nucleus scattering, it is simple to derive the recoil energy of the target nucleus. Although inelastic scattering is possible and presents interesting phenomenological features, we shall consider *elastic collisions*. Using energy-momentum conservation and the centre-of-mass energy invariant $s = (E_{tot}, \vec{p}_{tot})^2$, one

finds in the centre of momentum (CM) reference a final momentum

$$p'^2_{N,CM} = p'^2_{\chi,CM} = p'^2_{CM} = \frac{m_N^2 p_\chi^2}{m_N^2 + m_\chi^2 + 2E_\chi m_N} \quad .$$

For non-relativistic incoming WIMPs ($p_\chi \sim m_\chi v$) and target nuclei almost at rest ($E_R \sim p'^2_N/(2m_N)$), the boost back to the lab frame yields $p'^2_N = 2\mu_N^2(1-\cos\theta)v^2$, or

$$E_R \simeq \frac{\mu_N^2 v^2(1-\cos\theta)}{m_N} \quad , \tag{3.6}$$

where v is the initial WIMP velocity (in the lab frame) and θ is the scattering angle in the CM frame. Specialising to the case $\cos\theta = -1$, it is immediate to obtain the *minimum WIMP velocity* that produces a nuclear recoil of energy E_R:

$$v_{min}(m_\chi, E_R, A) = \sqrt{\frac{m_N E_R}{2\mu_N^2}} \quad . \tag{3.7}$$

A quantity that will turn out to be very important for direct Dark Matter searches is the differential cross-section $d\sigma_{\chi-N}/dE_R$. Given the range of recoil energies in equation (3.6), $\Delta E_R \sim 2\mu_N^2 v^2/m_N$ and hence $\frac{d\sigma_{\chi-N}}{dE_R} \sim \frac{m_N}{2\mu_N^2 v^2}\sigma_{\chi-N}$:

$$v^2 \frac{d\sigma_{\chi-N}}{dE_R}(E_R) = \frac{m_N}{2\mu_N^2}\left(\sigma^{SI}_{\chi-N}(E_R) + \sigma^{SD}_{\chi-N}(E_R)\right) \quad . \tag{3.8}$$

3.1.2 Event rate

In the previous Chapters we have argued that our neighbourhood is filled with a virialised set of WIMPs of density $\rho_0 \sim 0.3$ GeV/cm^3 and typical velocity $v \sim 200$ km/s. Therefore, presumably, the Earth is being persistently bombarded with a high flux of these particles

$$\phi_\chi \sim \frac{\rho_0 v}{m_\chi} \sim 6 \times 10^4 \left(\frac{100 \text{ GeV}}{m_\chi}\right) \text{ cm}^{-2}\text{s}^{-1} \quad .$$

Let $f(\vec{w}) \geq 0$ be a generic WIMP velocity distribution in the galactic rest frame, and $d\sigma_{\chi-N}/dE_R$ the total differential WIMP-nucleus cross-section given by equation (3.8). Then, the **scattering rate** (usually expressed in counts/ton/yr/keV) of the incoming flux of Dark Matter particles off nuclei $N(A,Z)$ is simply

$$\frac{dR}{dE_R} = \frac{\rho_0}{m_\chi m_N}\int_{v_{min}}^{\infty} d^3\vec{v}\, v f(\vec{v}+\vec{v}_e)\frac{d\sigma_{\chi-N}}{dE_R}(v, E_R) \quad , \tag{3.9}$$

where $\vec{v}_e$ is the Earth velocity in the galactic rest frame, while $v_{min} \equiv v_{min}(m_\chi, E_R, A)$ is given by equation (3.7) and represents the WIMP velocity threshold to induce nuclear recoils of energy E_R. Note that in the above expression $\vec{v}$ is the velocity of the incoming particle in the detector rest frame. Recalling that $v^2 d\sigma_{\chi-N}/dE_R$ is velocity-independent for the interactions in study (check equation (3.8)), equation (3.9) may be recast in a very

convenient way:

$$\begin{aligned}\frac{dR}{dE_R} &= \frac{\rho_0}{m_\chi m_N} \times \left[v^2 \frac{d\sigma_{\chi-N}}{dE_R} \right] \times \int_{v_{min}}^{\infty} d^3\vec{v}\, \frac{f(\vec{v}+\vec{v}_e)}{v} \\ &\equiv \frac{\rho_0}{2m_\chi \mu_N^2} \times \left[\sigma_{\chi-N}^{SD,0} F_{SD}^2(A, E_R) + \sigma_{\chi-N}^{SI,0} F_{SI}^2(A, E_R) \right] \\ &\quad \times \mathcal{F}\left(v_{min}(m_\chi, E_R, A), \vec{v}_e; f\right) \end{aligned} \tag{3.10}$$

in which we have defined the **mean inverse velocity**

$$\mathcal{F} \equiv \int_{v_{min}}^{\infty} d^3\vec{v}\, \frac{f(\vec{v}+\vec{v}_e)}{v} \quad . \tag{3.11}$$

Expression (3.10) renders very clear the interplay between astrophysical quantities (gathered in $\mathcal{F}$ and ρ_0) and detector-related inputs (encoded in μ_N and the middle factor in the equation). An interesting limit is when only scalar SI couplings are considered in which case equation (3.10) reads

$$\frac{dR}{dE_R} = \frac{\rho_0 \bar{\sigma}_{\chi-p}^{SI,0}}{2m_\chi \mu_p^2} \times A^2 F_{SI}^2(A, E_R) \times \mathcal{F}\left(v_{min}(m_\chi, E_R, A), \vec{v}_e; f\right) \quad , \tag{3.12}$$

where it was assumed that $\bar{\sigma}_{\chi-p}^{SI,0} = \bar{\sigma}_{\chi-n}^{SI,0}$.

To link the recoil spectrum dR/dE_R with experimental results, one usually computes the **total number of recoils** in a given energy bin $[E_1, E_2]$:

$$N_R(E_1, E_2) = \sum_i \int_{E_1}^{E_2} dE\, \epsilon(E) \frac{d\tilde{R}^{(i)}}{dE_R}(E) \quad , \tag{3.13}$$

where the sum is over the nuclei present in the target material, ϵ is the effective exposure (i.e. already convoluted with cut efficiencies and acceptance for nuclei recoils) and

$$\frac{d\tilde{R}^{(i)}}{dE_R} = \int dE' \, \frac{dR^{(i)}}{dE_R}(E') \frac{1}{\sqrt{2\pi}\sigma(E')} \exp\left(-\frac{(E-E')^2}{2\sigma^2(E')} \right) \quad .$$

Let us now focus on the astrophysical part of equation (3.10). Firstly, the Earth velocity with respect to the galactic rest frame is time-dependent and is usually expressed as a sum of three terms:

$$\vec{v}_e \equiv \vec{v}_e(t) = \vec{v}_{lsr} + \vec{v}_{pec} + \vec{v}_{orb}(t) \quad ,$$

where $\vec{v}_{lsr}$ is the *velocity of the local standard of rest*, $\vec{v}_{pec}$ is the *Sun's peculiar velocity* (i.e. with respect to $\vec{v}_{lsr}$) and $\vec{v}_{orb}(t)$ is the motion of the Earth around the Sun (i.e. *the Earth orbit*) [106]:

$$\begin{aligned} \vec{v}_{lsr} &= (0, v_c^0, 0) \\ \vec{v}_{pec} &= (10.0 \pm 0.4, 5.2 \pm 0.6, 7.2 \pm 0.4) \text{ km/s} \\ \vec{v}_{orb}(t) &= v_{orb}(\vec{e}_1 \sin\theta(t) - \vec{e}_2 \cos\theta(t)) \end{aligned}$$

with $v_{orb} = 29.8$ km/s, $\vec{e}_1 = (-0.0670, 0.4927, -0.8676)$, $\vec{e}_2 = (-0.9931, -0.1170, 0.01032)$ and $\theta(t) = 2\pi(1 - 0.218)$. In this context, the x-axis is pointed towards the Galactic Centre, the positive y direction is parallel to the local rotation and the z-axis points to the galactic North. The local circular velocity v_c^0 is not accurately measured as of today and a broad range of values is pinpointed by different measurements: $v_c^0 \simeq 200 - 260$ km/s (see Section 3.3 for a detailed discussion). The fact that $\vec{v}_e$ is time-dependent with an 1 year period opens up the possibility to search for a very particular WIMP signature: the *annual modulation* of the recoil spectrum dR/dE_R. When the Earth orbital velocity $\vec{v}_{orb}(t)$ is maximally aligned with the Sun's motion $\vec{v}_{lsr} + \vec{v}_{pec}$ (which happens in the Summer), $|\vec{v}_e|$ reaches a maximum and the WIMP velocities in the Earth frame are shifted to higher values, i.e. more high-speed and less low-speed particles. The opposite happens in the Winter when $\vec{v}_{orb}$ and $\vec{v}_{lsr} + \vec{v}_{orb}$ are minimally aligned. Consequently, one expects a larger (dimmer) recoil spectrum at high (low) energies in the peak of the Summer. This effect usually amounts to a few %, and the DAMA collaboration has actually claimed a positive detection of an annual modulation in their data. The interpretation in terms of WIMP scattering is, however, rather controversial and in tension with other direct detection results. Another signature related to the dynamics of WIMP-nucleus collisions is the *forward-background asymmetry*: in fact, the WIMP flux is peaked around the direction of $\vec{v}_e$, which means that most recoil events should be similarly aligned (in elastic scattering the nuclear recoil direction does not correspond exactly to the incoming particle one but they are strongly correlated).

As discussed in Chapter 2, the exact shape of the **velocity distribution** $f(\vec{w})$ is not known nor univocally predicted by numerical simulations and hence it constitutes a major uncertainty in direct Dark Matter detection. The one-dimensional velocity dispersions σ_r, σ_θ, σ_φ (r, θ, φ in galactic coordinates) are related to the star profile ν through Jeans equations; the radial component for example obeys equation (2.4). Although anisotropic $f(\vec{w})$ are perfectly feasible, one usually works with isotropic models ($\beta = 0$, $\sigma_r = \sigma_\theta = \sigma_\varphi = \sigma_{1d}$) with constant dispersions $\sigma_{1d} = \text{const}$ and presenting Maxwell-Boltzmann distributions

$$f(\vec{w}) \propto \exp\left(-\frac{|\vec{w}|^2}{2\sigma_{1d}^2}\right) \equiv \exp\left(-\frac{|\vec{w}|^2}{v_0^2}\right) \quad ,$$

$v_0 \equiv \sqrt{2}\sigma_{1d}$ being the most probable velocity modulus. For the standard halo model – that features an isothermal sphere $\rho \propto r^{-2}$ – equation (2.4) yields $\sigma_{1d}^2 = v_c^2/2$, as shown in equation (2.8). Examples of commonly used velocity distributions are

$$f_1(w) = \begin{cases} N_1 \exp\left(-\frac{w^2}{v_0^2}\right) & \text{for } w \leq v_{esc} \\ 0 & \text{for } w > v_{esc} \end{cases} \tag{3.14}$$

or

$$f_2(w) = \begin{cases} N_2 \left(\exp\left(\frac{v_{esc}^2 - w^2}{k v_0^2}\right) - 1\right)^k & \text{for } w \leq v_{esc} \\ 0 & \text{for } w > v_{esc} \end{cases} \quad , \tag{3.15}$$

where v_{esc} is the local galactic escape velocity and k is a shape parameter, as already

discussed in subsection 2.2.2. The normalisation constants N_1 and N_2 are given by

$$\begin{aligned} N_1^{-1} &= \pi^{3/2} v_0^3 \left(\mathrm{erf}\left(\frac{v_{esc}}{v_0}\right) - \frac{2 v_{esc}}{\sqrt{\pi} v_0} \exp\left(-\frac{v_{esc}^2}{v_0^2}\right)\right) \\ N_2^{-1}(k=1) &= \pi^{3/2} v_0^3 \exp\left(\frac{v_{esc}^2}{v_0^2}\right) \left(\mathrm{erf}\left(\frac{v_{esc}}{v_0}\right) - \frac{4}{\sqrt{\pi}} \left(\frac{v_{esc}}{2v_0} + \frac{v_{esc}^3}{3v_0^3}\right) \exp\left(-\frac{v_{esc}^2}{v_0^2}\right)\right) \quad . \end{aligned}$$

The astrophysical factor $\mathcal{F}$ (check equations (3.10) and (3.11)) corresponding to these distributions is straightforward to calculate:

$$\mathcal{F} = \int_{v_{min}}^{\infty} d^3\vec{v} \frac{f(\vec{v}+\vec{v}_e)}{v} = \int_0^{2\pi} d\varphi \int_0^{\pi} d\theta \, \sin\theta \int_{v_{min}}^{\infty} dv \, v f(w)$$

with $w^2 \equiv |\vec{v}_e + \vec{v}| = v^2 + v_e^2 + 2 v v_e \cos\theta$. Given the velocity cut above the escape velocity, the previous expression may be written as

$$\mathcal{F} = \int_0^{2\pi} d\varphi \int_{\Delta\theta} d\theta \, \sin\theta \int_{v_1}^{v_2} dv \, v \tilde{f}(w) \quad ,$$

where $\tilde{f}$ is the branch of f_1 or f_2 for $w \leq v_{esc}$, $\Delta\theta = [0, \theta_1] \cup [\pi - \theta_1, \pi]$, $v_1 = \max(v_{min}, v_-)$, $v_2 = \max(v_{min}, v_+)$ and

$$\begin{aligned} \theta_1 &= \min(1, \arcsin(v_{esc}/v_e)) \\ v_\pm &= -v_e \cos\theta \pm \sqrt{w^2 - v_e^2 \sin^2\theta} \quad . \end{aligned}$$

It is possible to find analytic expressions for the case of f_1 (see [111]):

$$\mathcal{F}_1 = \begin{cases} \frac{N_1 \pi^{3/2} v_0^3}{2 v_e} \left(\mathrm{erf}\left(\frac{v_{min}+v_e}{v_0}\right) - \mathrm{erf}\left(\frac{v_{min}-v_e}{v_0}\right) - \frac{4 v_e}{\sqrt{\pi} v_0} \mathrm{e}^{-\frac{v_{esc}^2}{v_0^2}} \right) & \text{for } v_{esc} > v_e, v_{min} > |v_e - v_{esc}| \\ \frac{N_1 \pi^{3/2} v_0^3}{2 v_e} \left(\mathrm{erf}\left(\frac{v_{esc}}{v_0}\right) - \mathrm{erf}\left(\frac{v_{min}-v_e}{v_0}\right) - \frac{2}{\sqrt{\pi} v_0} (v_e + v_{esc} - v_{min}) \, \mathrm{e}^{-\frac{v_{esc}^2}{v_0^2}} \right) & \text{for } |v_e - v_{esc}| < v_{min} < v_e + v_{esc} \\ 1/v_e & \text{for } v_{esc} < v_e, v_{min} < |v_e - v_{esc}| \\ 0 & \text{for } v_e + v_{esc} < v_{min} \end{cases}$$

and f_2 with $k = 1$ (see [112]):

$$\mathcal{F}_2^{k=1} = \begin{cases} \frac{N_2 \pi^{3/2} v_0^3}{2 v_e} \left(\mathrm{erf}\left(\frac{v_{min}+v_e}{v_0}\right) - \mathrm{erf}\left(\frac{v_{min}-v_e}{v_0}\right) - \frac{4 v_e}{\sqrt{\pi} v_0} \mathrm{e}^{-\frac{v_{esc}^2}{v_0^2}} \left(1 + \frac{v_{esc}^2 - v_e^2/3 - v_{min}^2}{v_0^2}\right) \right) \\ \frac{N_2 \pi^{3/2} v_0^3}{2 v_e} \left(\mathrm{erf}\left(\frac{v_{esc}}{v_0}\right) - \mathrm{erf}\left(\frac{v_{min}-v_e}{v_0}\right) - \frac{2}{\sqrt{\pi} v_0} \left(v_e + v_{esc} - v_{min} - \frac{1}{3}(v_e - 2v_{esc} - v_{min})(\frac{v_{esc}+v_e-v_{min}}{v_0})^2\right) \mathrm{e}^{-\frac{v_{esc}^2}{v_0^2}} \right) \\ 1/v_e \\ 0 \end{cases}$$

for the same branches as for $\mathcal{F}_1$.

Let us return to expression (3.12). The apparent degeneracy along the direction $\rho_0 \bar{\sigma}_{\chi-p}^{SI,0}/m_\chi = \text{const}$ may be broken by using different recoil energies and/or different targets since $\mathcal{F}$ is sensitive to a non-trivial combination of m_χ, E_R and A. This is sketched in Figure 3.1 where it is shown how different targets at different energies are sensitive to

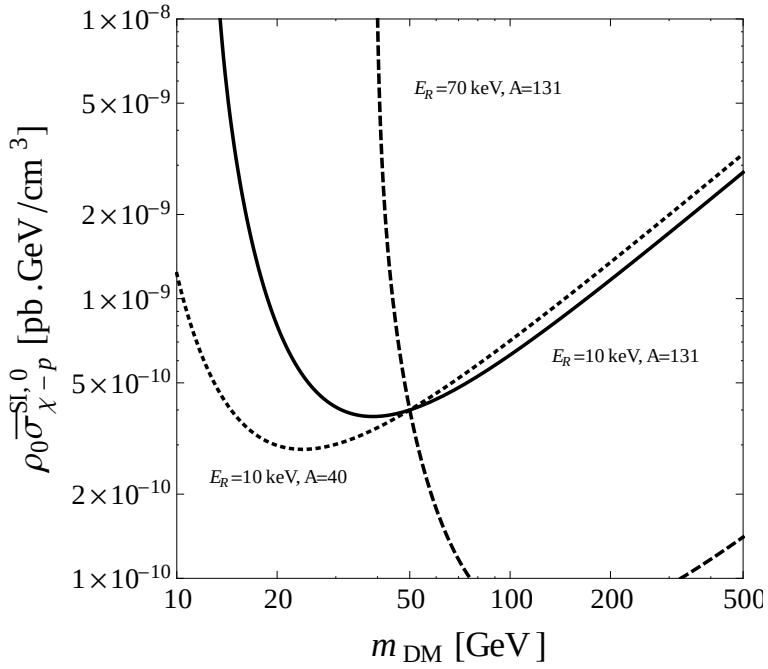

Figure 3.1: The contours of constant dR/dE_R in the $m_\chi - \rho_0\bar{\sigma}^{SI,0}_{\chi-p}$ plane for different values of E_R and A. For this plot it was assumed $m_\chi = 50$ GeV and $\rho_0\bar{\sigma}^{SI,0}_{\chi-p} = 0.4\times10^{-9}$ pb.GeV/cm^3. The complementarity between distinct targets and recoil energy bins is evident and helps determining the true value of $\rho_0\bar{\sigma}^{SI,0}_{\chi-p}$ and m_χ.

distinct directions in the $m_\chi - \rho_0\bar{\sigma}^{SI,0}_{\chi-p}$ plane. The complementarity of numerous targets is therefore crucial in direct detection, and will be studied in detail in Section 3.3. Notice, nevertheless, that for very massive WIMPs $m_\chi \gg m_N \sim \mathcal{O}(100)$ GeV $\gg m_p$, the minimum velocity becomes independent of m_χ, $v_{min} \simeq \sqrt{E_R/(2m_N)}$, and the degeneracy $\rho_0\bar{\sigma}^{SI,0}_{\chi-p}/m_\chi$ cannot be broken. Depending on the target being used, this usually happens for WIMP masses above a few hundred GeV.

3.2 Experimental overview

As seen before, if the ΛCDM paradigm holds, the Earth is being systematically bombarded with a flux of DM particles $\sim \rho_0 v/m_\chi \sim 6\times10^4(100\text{ GeV}/m_\chi)\text{cm}^{-2}\text{s}^{-1}$. In the case of WIMPs – that feature weak-scale cross-sections – such a flux translates into small but in principle detectable rates of WIMP-matter interactions. To observe these rare events is the aim of direct Dark Matter experiments. Needless to say, if Dark Matter is not composed of WIMPs but axions or superheavy particles, the experiments described in this Section are irrelevant.

WIMPs may scatter off atoms through elastic or inelastic processes. In elastic scatterings, the incoming WIMP hits the nucleus of the atom that in turn recoils. Inelastic scatterings, on the other hand, occur when the WIMP excites or ionises the target atom by hitting an orbital electron, or when it excites the nucleus in which case the recoil is followed by the nuclear emission of a photon. For certain sorts of Dark Matter particles, it is also possible to have a WIMP-nucleus inelastic scattering where the WIMP (instead of the nucleus) jumps to an excited state. In the following the focus will be solely on *elastic scattering on nuclei*, that may be spin-independent or spin-dependent as explained

in detail in Section 3.1.

Evidence for WIMP-nucleus elastic scattering requires a particular experimental signature: single nuclear recoils of energy $\sim 1-100$ keV with an exponential energy spectrum and uniformly distributed across the target. As discussed in Section 3.1, different targets should present different recoil spectra. Also, due to the motion of the Earth with respect to the galactic rest frame, the signal is expected to have an annual modulation and a forward-background asymmetry. Of course, several backgrounds exist that can mimic (at least in part) a WIMP signal: γ and $\beta-$rays from radioactive decays, neutrons from the interaction of atmospheric muons on the surrounding environment, and eventually solar neutrinos that scatter off target nuclei. The bottom line of this complicated paradigm is that, in order to observe WIMP scattering, detectors must be massive, shielded, placed deep underground and feature low-energy thresholds (at least $\sim \mathcal{O}(10)$ keV). Furthermore, exquisite background rejection capabilities are required. For instance, recoils happening near the borders of the target volume should be discarded since they are likely due to radioactivity; multiple scattering are probably caused by fast neutrons; etc.

In practice, a nuclear recoil in a target material gives rise to **light (scintillation)**, **charge (ionisation)** and/or **phonons (heat)**. Most current direct detection experiments are sensitive to two of these signals in order to achieve superior background rejection. Indeed, there are instruments using scintillation and ionisation (XENON10/100, ZEPLIN), scintillation and heat (CRESST) or ionisation and heat (CDMS, EDELWEISS). Other collaborations make use of one channel only as in the case of DAMA/LIBRA (scintillation) or CoGeNT (ionisation). Extensive reviews on the experimental efforts to detect Dark Matter directly are found in the literature [109, 110, 31, 113].

As far as spin-independent searches are concerned, two classes of detectors are the most promising ones for the next generation of experiments: cryogenic detectors and noble liquid detectors. **Cryogenic detectors** are essentially calorimeters operated at mK temperatures with target materials such as *germanium* or *silicon*. Important advantages of this technique are very low energy thresholds and good energy resolution. Examples of cryogenic detectors include CDMS, EDELWEISS and CRESST. Instead, **noble liquids** like *neon*, *argon* and *xenon* allow very massive detectors with good position accuracy. XENON100 and ZEPLIN are collaborations applying this strategy where both scintillation and ionisation signals are used. Yet another approach that may prove successful in the future is the use of **superheated liquids**. In this case, any energy deposition above threshold produces "bubbles" in the material that are spotted visually and acoustically. Although this strategy does not allow the extraction of spectral information of the recoils, it has good rejection capabilities against electron recoils and excellent sensitivities to axial, vector and scalar couplings. COUPP, PICASSO and SIMPLE are perhaps the most promising examples of such kind.

As of today no uncontroversial signal has been detected, but stringent upper limits on the WIMP scattering cross-section have been derived. We show in Figure 3.2 the most recent limits on the spin-independent [114] (left frame) and spin-dependent [115] (right frame) cross-sections. Note that these limits are obtained for standard halo parameters. As extensively discussed in the literature over the last few years, there are a few claims of positive signals. The first was produced by the DAMA collaboration. With an impressive total exposure of 1.17 ton-yr (combining DAMA/NaI and DAMA/LIBRA), an annual modulation in the recoil energy range $2-6$ keVee was observed at the 8.9σ confidence level [116]. The interpretation of this signal in terms of WIMP elastic scattering is hin-

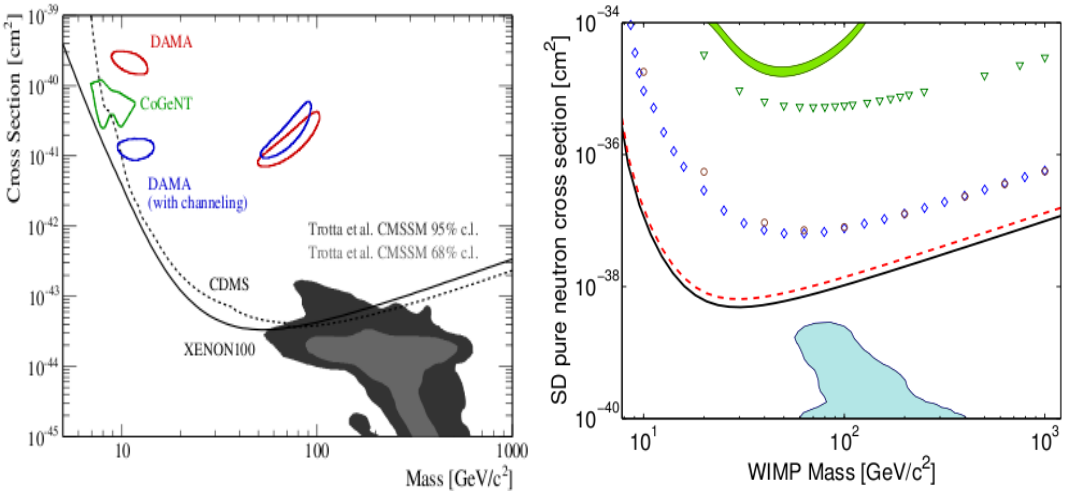

Figure 3.2: The 90% CL upper limits on the WIMP-nucleon scattering cross-section. In the left frame, the limits for the spin-independent cross-section are shown; image from [114]. The right frame presents the upper limits corresponding to spin-dependent neutron couplings; image from [115]. The plot on the right includes results from XENON10 (solid and dashed lines), CDMS (diamonds), ZEPLIN (circles), KIMS (inverted triangles) and DAMA (green area). See Ref. [115] for further details.

dered by the uncertain quenching factors (i.e. the fraction of recoil energy converted into scintillation) in the NaI target. In any case, the DAMA results, if interpreted in terms of DM scattering, are inconsistent (or in tension, to say the least) with other collaborations such as XENON10/100. On the other hand, CoGeNT has observed excess nuclear recoils with an exponential-like spectrum at a few keV [117]. WIMPs compatible with this latter observation are generally light but not fully compatible with DAMA results [118]. Also CRESST reports somewhat anomalous results with excess recoil events. Finally, CDMS has seen, upon unblinding, 2 events in the WIMP signal region with an expected background of 0.8 [119]. All these results have prompted a certain excitement in the field, but care must be taken in interpreting them as WIMP scattering. Clearly, more sensitive experiments are needed to confirm or rule out the WIMP hypothesis.

There are numerous detectors planned or already under construction. In a few years, both cryogenic (Ge) and noble liquid (Xe, Ar) detectors of ton-scale will hopefully shed light on the present disputed results. In particular, the next Section analyses carefully the prospects for DM direct detection in this kind of detectors. Meanwhile, instruments sensitive to the recoil direction are being developed and will be essential to search for a forward-background asymmetry, expected in the case of WIMP scattering.

3.3 Paper II: Complementarity of Dark Matter direct detection targets[1]

We investigate the reconstruction capabilities of Dark Matter mass and spin-independent cross-section from future ton-scale direct detection experiments using germanium, xenon or argon as targets. Adopting realistic values for the exposure, energy threshold and resolution of Dark Matter experiments which will come online within 5 to 10 years, the degree of complementarity between different targets is quantified. We investigate how

[1] This Section is based on the article [2], done in collaboration with Laura Baudis, Gianfranco Bertone, Roberto Ruiz de Austri, Louis E. Strigari and Roberto Trotta.

the uncertainty in the astrophysical parameters controlling the local Dark Matter density and velocity distribution affects the reconstruction. For a 50 GeV WIMP, astrophysical uncertainties degrade the accuracy in the mass reconstruction by up to a factor of ~ 4 for xenon and germanium, compared to the case when astrophysical quantities are fixed. However, combination of argon, germanium and xenon data increases the constraining power by a factor of ~ 2 compared to germanium or xenon alone. We show that future direct detection experiments can achieve self-calibration of some astrophysical parameters, and they will be able to constrain the WIMP mass with only very weak external astrophysical constraints.

3.3.1 Overview

Many experiments are currently searching for Dark Matter in the form of WIMPs, by looking for rare scattering events off nuclei in the detectors, and many others are planned for the next decade [31, 108, 29, 30, 17, 106]. This direct DM detection strategy has brought over the last year several interesting observations and upper limits. The results of the DAMA/LIBRA [116] and, more recently, the CoGeNT [117] collaborations have been tentatively interpreted as due to DM particles. It appears however that these results cannot be fully reconciled with other experimental findings, in particular with the null searches from XENON100 [114, 118, 120] or CDMS [121], and are also in tension with ZEPLIN-III [122]. In this context, the next generation of low-background, underground detectors is eagerly awaited and will hopefully confirm or rule out a DM interpretation.

If convincing evidence is obtained for DM particles with direct detection experiments, the obvious next step will be to attempt a reconstruction of the physical parameters of the DM particle, namely its mass and scattering cross-section (see e.g. Refs. [123, 98]). This is a non-trivial task, hindered by the different uncertainties associated with the computation of WIMP-induced recoil spectra. In particular, galactic model uncertainties – i.e. uncertainties pertaining to the density and velocity distribution of WIMPs in our neighbourhood – play a crucial role. In attempting reconstruction, the simplest assumption to make is a fixed local DM density $\rho_0 = 0.3$ GeV/cm^3 and the "standard halo model", i.e. an isotropic isothermal sphere density profile and a Maxwell-Boltzmann distribution of velocities with a given galactic escape velocity v_{esc} and one-dimensional dispersion $\sigma_{1d}^2 \equiv v_0^2/2 = (v_c^0)^2/2$. However, the galactic model parameters are only estimated to varying degrees of accuracy, so that the true local population of DM likely deviates from the highly idealised standard halo model.

Several attempts have been made to improve on the standard approach [98, 83, 112, 124]. In the case of a detected signal at one experiment, recent analyses have studied how complementary detectors can extract Dark Matter properties, independent of our knowledge of the galactic model [125]. Certain properties of Dark Matter may also be extracted under assumptions about the nature of the nuclear recoil events [126]. Furthermore, eventual multiple signals at different targets have been shown to be useful in constraining both Dark Matter and astrophysical properties [127] and in extracting spin-dependent and spin-independent couplings [128, 129]. Here, using a Bayesian approach, we study how uncertainties on galactic model parameters affect the determination of the DM mass m_χ and spin-independent WIMP-proton scattering cross-section $\sigma_{SI}^p \equiv \bar{\sigma}_{\chi-p}^{SI,0}$. In particular we focus on realistic experimental capabilities for the future generation of ton-scale detectors – to be reached within the next 10 years – with noble liquids (argon,

xenon) and cryogenic (germanium) technologies.

The main focus of this paper is the complementarity between different detection targets. It is well-known (see e.g. [108]) that different targets are sensitive to different directions in the $m_\chi - \sigma^p_{SI}$ plane, which is very useful to achieve improved reconstruction capabilities – or more stringent bounds in the case of null results. This problem has often been addressed without taking proper account of galactic model uncertainties. Using xenon (Xe), argon (Ar) and germanium (Ge) as case-studies, we ascertain to what extent unknowns in galactic model parameters limit target complementarity. A thorough understanding of complementarity will be crucial in the near future since it provides us with a sound handle to compare experiments and, if needed, decide upon the best target to bet on future detectors. Our results also have important consequences for the combination of collider observables and direct detection results (for a recent work see [97]).

Besides degrading the extraction of physical properties like m_χ and σ^p_{SI}, uncertainties in the galactic model will challenge our ability to distinguish between different particle physics frameworks in case of a positive signal. Other relevant unknowns are hadronic uncertainties, related essentially to the content of nucleons [107]. Here, we undertake a model-independent approach without specifying an underlying WIMP theory and using m_χ and σ^p_{SI} as our phenomenological parameters – for this reason we shall not address hadronic uncertainties (hidden in σ^p_{SI}). A comprehensive work complementary to ours and done in the supersymmetric framework has been presented recently [130, 131].

We shall focus on the scalar spin-independent scattering and refer to Section 3.1 for the relevant formulae, in particular equation (3.12). Here, we are not interested in the annual modulation signal nor directional signatures but rather in the average recoil rate – therefore we shall neglect $\vec{v}_{pec}$ and $\vec{v}_{orb}$ and take $\vec{v}_e \simeq \vec{v}_{lsr} = \text{const}$. Three fiducial WIMP models will be used to assess the capabilities of future direct detection experiments: m_χ =25, 50 and 250 GeV, all with $\sigma^p_{SI} = 10^{-9}$ pb. These models are representative of well-motivated candidates such as neutralinos in supersymmetric theories [132].

3.3.2 Upcoming experimental capabilities

Currently, the most stringent constraints on the SI WIMP-nucleon coupling are those obtained by the CDMS [119] and XENON [114] collaborations. While XENON100 should probe the cross-section region down to 5×10^{-45} cm^2 with data already in hand, the XENON1T [133, 134] detector, whose construction is scheduled to start by mid 2011, is expected to reach another order of magnitude in sensitivity improvement. To test the σ^p_{SI} region down to 10^{-47} cm$^2 \equiv 10^{-11}$ pb and below, a new generation of detectors with larger WIMP target masses and ultra-low backgrounds is needed. Since we are interested in the prospects for detection in the next 5 to 10 years, we discuss new projects that can realistically be built on this time scale, adopting the most promising detection techniques, namely noble liquid time projection chambers (TPCs) and cryogenic detectors operated at mK temperatures.

In Europe, two large consortia, DARWIN [135] and EURECA [136], gathering the expertise of several groups working on existing DM experiments are funded for R&D and design studies to push noble liquid and cryogenic experiments to the multi-ton and ton scale, respectively. DARWIN is devoted to noble liquids, having as main goal the construction of a multi-ton liquid Xe (LXe) and/or liquid Ar (LAr) instrument [137], with data taking to start around 2016. The XENON, ArDM and WARP collaborations

target	ϵ [ton×yr]	η_{cut}	A_{NR}	ϵ_{eff} [ton×yr]	E_{thr} [keV]	$\sigma(E)$ [keV]	background events/ϵ_{eff}
Xe	5.0	0.8	0.5	2.00	10	Eq. (3.17)	< 1
Ge	3.0	0.8	0.9	2.16	10	Eq. (3.16)	< 1
Ar	10.0	0.8	0.8	6.40	30	Eq. (3.18)	< 1

Table 3.1: Characteristics of future direct Dark Matter experiments using xenon, germanium and argon as target nuclei. In all cases the level of background in the fiducial mass region is negligible for the corresponding effective exposure. See Section 3.3.2 for further details.

participate actively in the DARWIN project. EURECA is a design study dedicated to cryogenic Dark Matter detectors operated at mK temperatures. The proposed roadmap is to improve upon CRESST [138] and EDELWEISS [139] technologies and build a ton-scale detector by 2018, with a SI sensitivity of about 10^{-46} cm$^2 \equiv 10^{-10}$ pb. The complementarity between DARWIN and EURECA is of utmost importance for Dark Matter direct searches since a solid, uncontroversial discovery requires signals in distinct targets and preferentially distinct technologies.

Given these developments, we will focus on the three most promising targets: Xe and Ar as examples of noble liquid detectors, and Ge as a case-study for the cryogenic technique. In the case of a Ge target, we assume an 1.5 ton detector (1 ton as fiducial target mass), 3 years of operation, an energy threshold for nuclear recoils of $E_{thr,Ge} = 10$ keV and an energy resolution given by

$$\sigma_{Ge}(E) = \sqrt{(0.3)^2 + (0.06)^2 E/\text{keV}} \text{ keV} \quad . \tag{3.16}$$

For a liquid Xe detector, we assume a total mass of 8 tons (5 tons in the fiducial region), 1 year of operation, an energy threshold for nuclear recoils of $E_{thr,Xe} = 10$ keV and an energy resolution of

$$\sigma_{Xe}(E) = 0.6 \text{ keV}\sqrt{E/\text{keV}} \quad . \tag{3.17}$$

Finally, for a liquid Ar detector, we assume a total mass of 20 tons (10 tons in the fiducial region), 1 year of operation, an energy threshold for nuclear recoils of $E_{thr,Ar} = 30$ keV and an energy resolution of

$$\sigma_{Ar}(E) = 0.7 \text{ keV}\sqrt{E/\text{keV}} \quad . \tag{3.18}$$

To calculate realistic exposures, we make the following assumptions: nuclear recoils acceptances A_{NR} of 90%, 80% and 50% for Ge, Ar and Xe, respectively, and an additional, overall cut efficiency η_{cut} of 80% in all cases, which for simplicity we consider to be constant in energy. We hypothesise less than one background event per given effective exposure ϵ_{eff}, which amounts to 2.16 ton×yr in Ge, 6.4 ton×yr in Ar and 2 ton×yr in Xe, after allowing for all cuts. Such an ultra-low background will be achieved by a combination of background rejection using the ratio of charge-to-light in Ar and Xe, and charge-to-phonon in Ge, the timing characteristics of raw signals, the self-shielding properties and extreme radio-purity of detector materials, as well as minimisation of exposure to cosmic rays above ground.

The described characteristics are summarised in Table 3.1. We note that in the following we shall consider recoil energies below 100 keV only; to increase this maximal value may add some information but the effect is likely small given the exponential nature of WIMP-induced recoiling spectra.

Parameter	Prior range	Prior constraint
$\log_{10}(m_\chi/\mathrm{GeV})$	$(0.1, 3.0)$	Uniform prior
$\log_{10}(\sigma^p_{SI}/\mathrm{pb})$	$(-10, -6)$	Uniform prior
$\rho_0/(\mathrm{GeV/cm}^3)$	$(0.001, 0.9)$	Gaussian: 0.4 ± 0.1
$v_0/(\mathrm{km/s})$	$(80, 380)$	Gaussian: 230 ± 30
$v_{esc}/(\mathrm{km/s})$	$(379, 709)$	Gaussian: 544 ± 33
k	$(0.5, 3.5)$	Uniform prior

Table 3.2: Parameters used in our analysis, with their prior range (middle column) and the prior constraint adopted (rightmost column).

3.3.3 Statistical methodology

Our approach is a Bayesian one and we refer to [140] for specific details. The aim of our work is to sample the posterior density function $p(\Theta|d)$ of the parameter set $\Theta \equiv (m_\chi, \sigma^p_{SI}, \rho_0, v_0, v_{esc}, k)$ given the data d on the recoil spectra in different targets. Bayes theorem states that

$$p(\Theta|d) = \frac{\mathcal{L}(\Theta)p(\Theta)}{p(d)} \quad ,$$

where $\mathcal{L}(\Theta)$ is the likelihood function, $p(\Theta)$ is the prior and $p(d)$ is the so-called Bayesian evidence that works simply as a normalisation constant for parameter inference and will be dropped in the following. The priors adopted in our work are given in Table 3.2 – see Section 3.3.4 for details on ρ_0, v_0, v_{esc} and k. Finally, the likelihood function for each of the direct detection experiments is given by a product of independent Poisson likelihoods over the energy bins:

$$\mathcal{L}(\Theta) = \prod_b \frac{N_R^{\hat{N}_b}}{\hat{N}_b!} \exp\left(-N_R\right) \quad , \tag{3.19}$$

where $\hat{N}_b$ is the number of counts in each bin (generated from the true model with no shot noise, as explained below) and $N_R = N_R(E_b^{\min}, E_b^{\max})$ is the number of counts in the b-th bin when the parameters take on the value Θ, and it is given by equation (3.13). Ten bins are used for each experiment, uniformly spaced on a linear scale between the threshold energy and 100 keV. The mock data for each WIMP benchmark are generated according to the experimental capabilities outlined in Section 3.3.2 with no background (cf. Table 3.1) and without any Poisson scatter with respect to the true counts.

The posterior distribution is sampled with the MultiNest code [141, 142, 143] using 2000 live points, an efficiency parameter of 1.0 and a tolerance of 0.8 (see [141, 142] for details).

3.3.4 Velocity distribution and galactic model parameters

We now move onto discussing our modelling of the velocity distribution function and the galactic model parameters that are input for equation (3.12). We model only the smooth component of the velocity distribution – recent results from numerical simulations indicate that the velocity distribution component arising from localised streams and substructures is likely sub-dominant in the calculation of direct Dark Matter detection signals [84, 144].

We model the velocity distribution function as spherical and isotropic, and parameterise it as in equation (3.15). This velocity distribution function was found to be flexible enough to describe the range of Dark Matter halo profiles found in cosmological simulations [78]. Note that, for any value of k, this distribution matches a Maxwellian

distribution for sufficiently small velocities w and if $v_{esc} > v_0$. The high-velocity tail of the distributions found in numerical simulations of pure Dark Matter galactic halos are well modelled by $1.5 < k < 3.5$ [78]. In our analysis we will expand this range to also include models that behave similar to pure Maxwellian distributions near the tail of the distribution, so that in our analysis we vary k in the range

$$k = 0.5 - 3.5 \quad \text{(flat)} \quad . \tag{3.20}$$

We adopt an uniform (i.e., flat) prior within the above range for k.

The range we take for the v_{esc} is motivated by the results of Ref. [145], where a sample of high-velocity stars is used to derive a median likelihood local escape velocity of $\bar{v}_{esc} = 544$ km/s and a 90% confidence level interval 498 km/s $< v_{esc} <$ 608 km/s. Assuming Gaussian errors this translates into an 1σ uncertainty of 33 km/s, and thus

$$v_{esc} = 544 \pm 33 \text{ km/s} \quad (1\sigma) \quad . \tag{3.21}$$

Having specified ranges for v_{esc} and k, it remains to consider a range for v_0 in equation (3.15). As defined in that equation, the quantity v_0 does not directly correspond to the local circular velocity, v_c^0, but rather is primarily set by v_c^0 and the Dark Matter profile. For simplicity and transparency in our analysis, we will consider a similar range for v_0 as for the local circular velocity, so we take $v_0 \equiv \sqrt{2}\sigma_{1d} = v_c^0$ (that holds in the case of the standard halo model, see equation (2.8)). For the local circular velocity, a variety of measurements presents a broad range of central values and uncertainties [102, 146, 147, 148, 149]. To again remain conservative we use an interval bracketing recent determinations:

$$v_0 = v_c^0 = 230 \pm 30 \text{ km/s} \quad (1\sigma) \quad , \tag{3.22}$$

where we take a Gaussian prior with the above mean and standard deviation.

To account for the variation of the local density of Dark Matter in our modelling, we will take a mean value and error given by [63, 1]

$$\rho_0 = 0.4 \pm 0.1 \text{ GeV/cm}^3 \quad (1\sigma) \quad , \tag{3.23}$$

There are several other recent results that determine ρ_0, both consistent [73] and somewhat discrepant [77] with our adopted value. Even in light of these uncertainties, we take equation (3.23) to represent a conservative range for the purposes of our study.

For completeness Table 3.2 summarises the information on the parameters used in our analysis.

3.3.5 Results

Complementarity of targets

We start by assuming the three Dark Matter benchmark models ($m_\chi = 25, 50, 250$ GeV with $\sigma_{SI}^p = 10^{-9}$ pb) and fix the galactic model parameters to their fiducial values, $\rho_0 = 0.4$ GeV/cm^3, $v_0 = 230$ km/s, $v_{esc} = 544$ km/s, $k = 1$. With the experimental capabilities outlined in Section 3.3.2, we generate mock data that in turn are used to reconstruct the posterior for the DM parameters m_χ and σ_{SI}^p. The left frame of Figure 3.3 presents the results for the three benchmarks and for Xe, Ge and Ar separately. The contours in

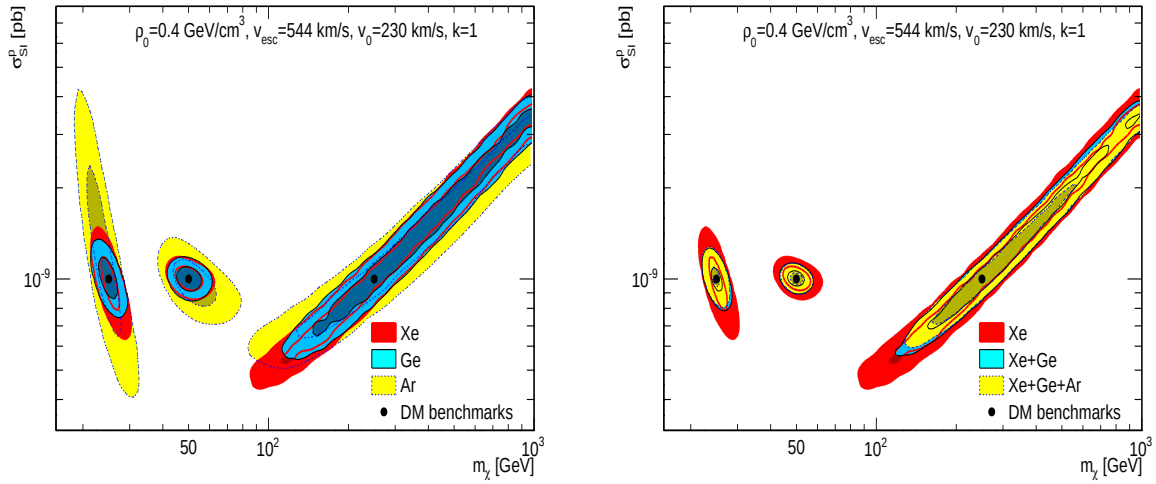

Figure 3.3: The joint 68% and 95% posterior probability contours in the $m_\chi - \sigma^p_{SI}$ plane for the three DM benchmarks ($m_\chi = 25, 50, 250$ GeV) with fixed galactic model, i.e. fixed astrophysical parameters. In the left frame we show the reconstruction capabilities of Xe, Ge and Ar configurations separately, whereas in the right frame the combined data sets Xe+Ge and Xe+Ge+Ar are shown.

	Percent 1σ accuracy	
	$m_\chi = 25$ GeV	$m_\chi = 50$ GeV
Xe	6.5% (14.3%)	8.1% (20.4%)
Ge	5.5% (16.0%)	7.0% (29.6%)
Ar	12.3% (23.4%)	14.7% (86.5%)
Xe+Ge	3.9% (10.9%)	5.2% (15.2%)
Xe+Ge+Ar	3.6% (9.0%)	4.5% (10.7%)

Table 3.3: Marginalised percent 1σ accuracy of the DM mass reconstruction for the benchmarks $m_\chi = 25, 50$ GeV. Figures between brackets refer to scans where the astrophysical parameters were marginalised over (with priors as in Table 3.2), while the other figures refer to scans with the fiducial astrophysical setup.

the Figure delimit regions of joint 68% and 95% posterior probability. Several comments are in order here. First, it is evident that the Ar configuration is less constraining than Xe or Ge ones, which can be traced back to its smaller A and larger E_{thr}. Moreover, it is also apparent that, while Ge is the most effective target for the benchmarks with $m_\chi = 25, 250$ GeV, Xe appears the best for a WIMP with $m_\chi = 50$ GeV (see below for a detailed discussion). Let us stress as well that the 250 GeV WIMP proves very difficult to constrain in terms of mass and cross-section due to the high-mass degeneracy explained in subsection 3.1.2. Taking into account the differences in adopted values and procedures, our results are in qualitative agreement with Ref. [130], where a study on the supersymmetrical framework was performed. However, it is worth noticing that the contours in Ref. [130] do not extend to high masses as ours for the 250 GeV benchmark – this is likely because the volume at high masses in a supersymmetrical parameter space is small.

In the right frame of Figure 3.3 we show the reconstruction capabilities attained if one combines Xe and Ge data, or Xe, Ge and Ar together, *again for when the galactic model parameters are kept fixed.* In this case, for $m_\chi = 25, 50$ GeV, the configuration Xe+Ar+Ge allows the extraction of the correct mass to better than $\mathcal{O}(10)$ GeV accuracy. For reference, the (marginalised) mass accuracy for different mock data sets is listed in Table 3.3. For $m_\chi = 250$ GeV, it is only possible to obtain a lower limit on m_χ.

Figure 3.4 shows the results of a more realistic analysis, that keeps into account the large uncertainties associated with galactic model parameters, as discussed in Section

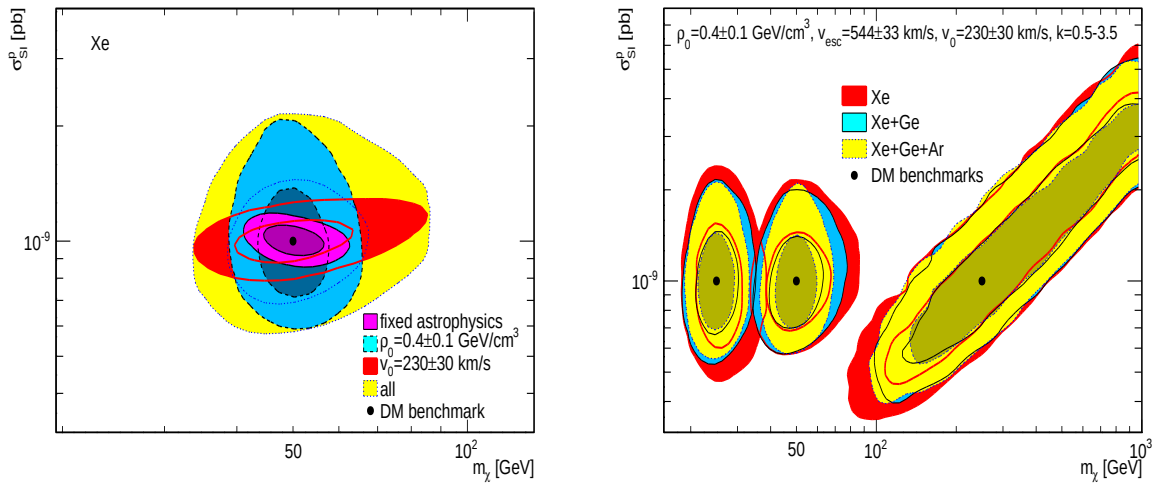

Figure 3.4: The joint 68% and 95% posterior probability contours in the $m_\chi - \sigma^p_{SI}$ plane for the case in which astrophysical uncertainties are taken into account. In the left frame, the effect of marginalising over ρ_0, v_0 and all four (ρ_0, v_0, v_{esc}, k) astrophysical parameters is displayed for a Xe detector and the 50 GeV benchmark WIMP. In the right frame, the combined data sets Xe, Xe+Ge and Xe+Ge+Ar are used for the three DM benchmarks ($m_\chi = 25, 50, 250$ GeV).

3.3.4. The left frame of Figure 3.4 shows the effect of varying only ρ_0 (dashed lines, blue surfaces), only v_0 (solid lines, red surfaces) and all galactic model parameters (dotted lines, yellow surfaces) for Xe and $m_\chi = 50$ GeV. The galactic model uncertainties are dominated by ρ_0 and v_0, and, once marginalised over, they blow up the constraints obtained with fixed galactic model parameters. This amounts to a very significant degradation of mass (cf. Table 3.3) and scattering cross-section reconstruction. Inevitably, the complementarity between different targets is affected – see the right frame of Figure 3.4. Still, for the 50 GeV benchmark, combining Xe, Ge and Ar data improves the mass reconstruction accuracy with respect to the Xe only case, essentially by constraining the high-mass tail.

In order to be more quantitative in assessing the usefulness of different targets and their complementarity, we use as *figure of merit* the inverse area enclosed by the 95% marginalised contour in the $\log_{10}(m_\chi) - \log_{10}(\sigma^p_{SI})$ plane. Figure 3.5 displays this figure of merit for several cases, where we have normalised to the Ar target at $m_\chi = 250$ GeV with fixed galactic model parameters. Analyses with fixed galactic model parameters are represented by empty bars, while the cases where all galactic model parameters are marginalised over with priors as in Table 3.2 are represented by filled bars. Firstly, one can see that all three targets perform better for WIMP masses around 50 GeV than 25 or 250 GeV if the galactic model is fixed. When astrophysical uncertainties are marginalised over, the constraining power of the experiments becomes very similar for benchmark WIMP masses of 25 and 50 GeV. Secondly, Figure 3.5 also confirms what was already apparent from Figure 3.3: Ge is the best target for $m_\chi = 25, 250$ GeV (although by a narrow margin), whereas Xe appears the most effective for a 50 GeV WIMP (again, by a narrow margin). Furthermore, the inclusion of uncertainties drastically reduces the amount of information one can extract from the data: the filled bars are systematically below the empty ones. Now, astrophysical uncertainties affect the complementarity between different targets in a non-trivial way. To understand this point, let us focus on the two rightmost bars for each benchmark in Figure 3.5, corresponding to the data sets Xe+Ge and Xe+Ge+Ar. For instance, in the case of a 250 GeV WIMP, astrophysical uncertain-

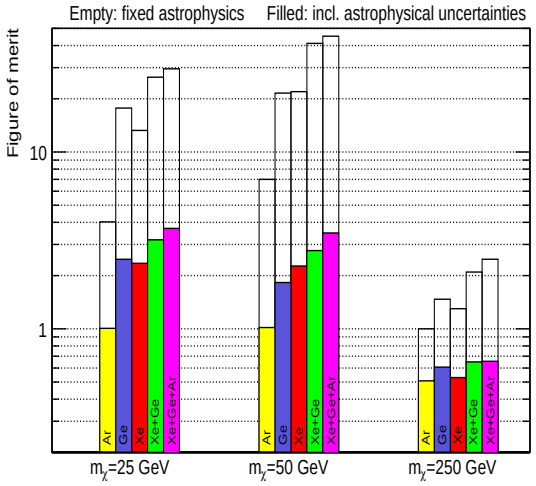

Figure 3.5: Figure of merit quantifying the relative information gain on Dark Matter parameters for different targets and combinations thereof. The values of the figure of merit are normalised to the Ar case at $m_\chi = 250$ GeV with fixed astrophysical parameters. Empty (filled) bars are for fixed astrophysical parameters (including astrophysical uncertainties).

ties seem to reduce target complementarity: adding Ar to Xe+Ge leads to a significant increase in the figure of merit for analyses with fixed astrophysics (empty bars) but has a negligible effect for analyses with varying astrophysical parameters (filled bars). For low mass benchmarks, the effect of combining two (Xe+Ge) or three targets (Xe+Ge+Ar) is to increase the figure of merit by about a factor of 2 compared to Xe alone or Ge alone, almost independently of whether the astrophysical parameters are fixed or marginalised over. However, the overall information gain on the Dark Matter parameters (for light WIMPs) is reduced by a factor ~ 10 if astrophysical uncertainties are taken into account, compared to the case where the galactic model is fixed.

	$m_\chi = 25$ GeV						$m_\chi = 50$ GeV						$m_\chi = 250$ GeV					
	m_χ	σ^p_{SI}	ρ_0	v_0	v_{esc}	k	m_χ	σ^p_{SI}	ρ_0	v_0	v_{esc}	k	m_χ	σ^p_{SI}	ρ_0	v_0	v_{esc}	k
m_χ	–	0.039	-0.006	-0.850	-0.238	-0.002	–	0.098	-0.006	-0.870	-0.079	-0.004	–	0.874	-0.011	-0.615	-0.027	0.022
σ^p_{SI}	–	–	-0.887	-0.237	0.116	0.010	–	–	-0.957	-0.175	0.026	-0.031	–	–	-0.452	-0.525	-0.024	0.015
ρ_0	–	–	–	0.013	-0.005	0.005	–	–	–	0.014	-0.010	0.030	–	–	–	0.002	0.015	0.010
v_0	–	–	–	–	-0.087	-0.004	–	–	–	–	-0.151	0.011	–	–	–	–	-0.049	-0.008
v_{esc}	–	–	–	–	–	0.000	–	–	–	–	–	-0.009	–	–	–	–	–	0.001

Table 3.4: The correlation factors $r(X,Y) = \mathrm{cov}(X,Y)/(\sigma(X)\sigma(Y))$ for the posteriors obtained from the combined data set Xe+Ge+Ar and including the astrophysical uncertainties with priors as in Table 3.2.

Reduction in uncertainties and self-calibration

The uncertainties used thus far and outlined in Section 3.3.4 are a reasonable representation of the current knowledge. For illustration it is also interesting to consider the effect of tighter constraints on galactic model parameters in the reconstruction of WIMP properties. We start by computing the correlation coefficient between the parameters (m_χ, σ^p_{SI}, ρ_0, v_0, v_{esc}, k) when they are constrained by the combined data set Xe+Ge+Ar – see Table 3.4. Clearly, for all benchmark models, σ^p_{SI} and ρ_0 as well as m_χ and v_0 are strongly anti-correlated. The anti-correlation between σ^p_{SI} and ρ_0 is obvious since $dR/dE_R \propto \sigma^p_{SI}\rho_0$. As for the degeneracy between m_χ and v_0, it is easy to verify that, for $v_{min} \ll v_e \sim v_0 \ll v_{esc}$, $\mathcal{F}$ defined in equation (3.11) goes approximately as $1/v_0$ and thus $dR/dE_R \propto 1/(m_\chi v_0)$. Table 3.4 also shows a small (anti-)correlation between σ^p_{SI} and

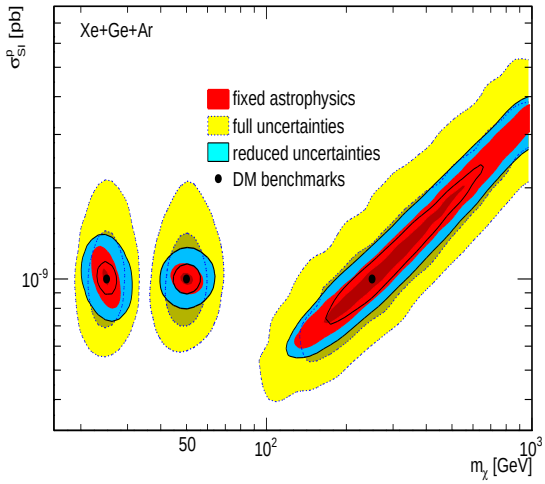

Figure 3.6: The effect of reducing the uncertainty on the astrophysical parameters ρ_0 and v_0. The red surfaces refer to the scan using the fiducial astrophysical setup; the yellow surfaces (and dotted lines) indicate the effect of marginalising over the uncertainties in Table 3.2; the blue surfaces (and solid lines) correspond to the reduced uncertainties $\rho_0 = 0.4 \pm 0.028$ GeV/cm^3, $v_0 = 230 \pm 9.76$ km/s, $v_{esc} = 544 \pm 33$ km/s, $k = 0.5 - 3.5$.

v_0; all other correlations are negligible. Therefore, ρ_0 and v_0 are the dominant sources of uncertainty and their more accurate determination will lead to a significant improvement on the reconstruction of m_χ and σ^p_{SI}. To illustrate this point we follow [63] and apply a 7% (4.2%) uncertainty on ρ_0 (v_0), while maintaining the same central values as before, thus reducing the realistic error bars used above by a factor $\sim 3.0 - 3.5$ for both parameters. The results are shown in Figure 3.6 where we consider the combination Xe+Ge+Ar. A future more constrained astrophysical setup may indeed lead to a better reconstruction of the WIMP mass and scattering cross-section.

To this point we have studied the impact of galactic model uncertainties on the extraction of DM properties from direct detection data. However, once a positive signal is well-established, it may be used to determine some of the galactic parameters directly from direct detection data (see e.g. [127]), without relying on external priors. This would amount to achieving a self-calibration of the astrophysical uncertainties affecting direct detection rates. In order to explore such possibility we re-ran our analysis but dropping the Gaussian priors on ρ_0, v_0 and v_{esc} described in Section 3.3.4. Instead, we used uniform, non-informative priors on ρ_0, v_0, v_{esc} and k in the ranges indicated in the middle column of Table 3.2. We focus on the 50 GeV benchmark and use the data sets Xe, Xe+Ge and Xe+Ge+Ar. With this large freedom on the astrophysical side, it turns out that direct detection data alone leave ρ_0, v_{esc} and k unconstrained within their ranges while σ^p_{SI} is pinpointed within approximately one order of magnitude. Only the DM mass m_χ and the circular velocity v_0 can be constrained by direct detection, as shown in Figure 3.7. This Figure stresses two interesting results. First, if $m_\chi = 50$ GeV (and $\sigma^p_{SI} = 10^{-9}$ pb), the next generation of experiments will be able to determine the WIMP mass within a few tens of GeV (percent 1σ accuracy of 11.8%) even with very loose assumptions on the local DM distribution. Second, the right frame in Figure 3.7 shows that the combination of Xe, Ge and Ar targets is very powerful in constraining v_0 on its own without external priors. In particular, the data set Xe+Ge+Ar (solid blue line) is sufficient to infer at 1σ $v_0 = 238 \pm 22$ km/s (compared to the top-hat prior in the range 80−380 km/s). This

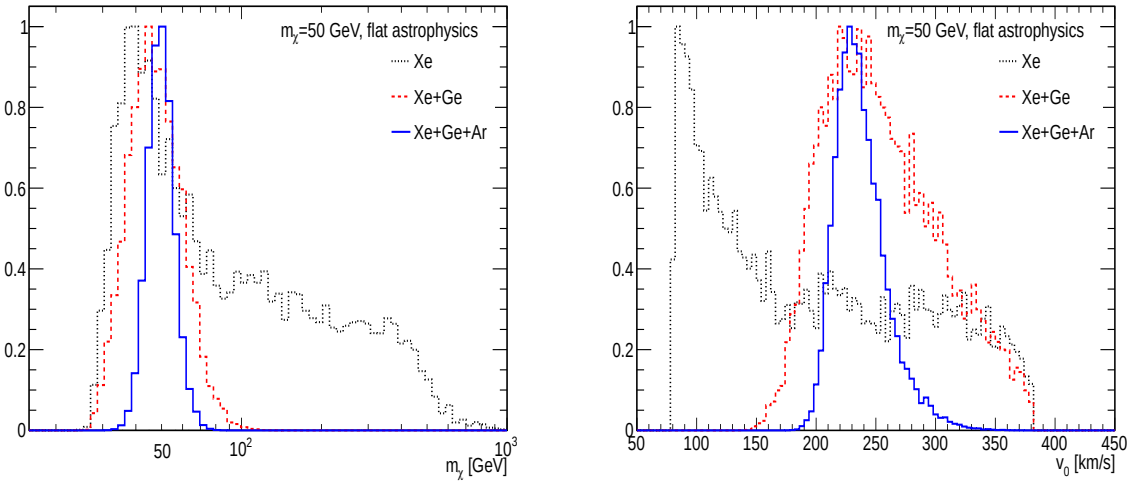

Figure 3.7: The marginalised posterior distribution function for m_χ (left frame) and v_0 (right frame) with the data sets Xe, Xe+Ge and Xe+Ge+Ar for the 50 GeV benchmark. The parameters ρ_0, v_0, v_{esc} and k were varied in the ranges indicated in the middle column of Table 3.2 with an uniform prior and no constraint on astrophysics was applied. The probability distributions are therefore a result of the constraining power of direct detection data only, which have the potential to achieve self-calibration of the circular velocity.

represents already a smaller uncertainty than the present-day constraint that we have taken, $v_0 = 230 \pm 30$ km/s – in case of a positive signal, a combination of direct detection experiments will probe in an effective way the local circular velocity. Repeating the same exercise for the 25 GeV benchmark we find good mass reconstruction but a weaker constraint: $v_0 = 253 \pm 39$ km/s. We stress that the quoted v_0 uncertainties in this paragraph do not take into account possible systematic deviations from the parameterisation in equation (3.15).

3.3.6 Conclusions

We have discussed the reconstruction of the key phenomenological parameters of WIMPs, namely mass and scattering cross-section off nuclei, in case of positive detection with one or more direct DM experiments planned for the next decade. We have in particular studied the complementarity of ton scale experiments with Xe, Ar and Ge targets, adopting experimental configurations that may realistically become available over this time scale.

To quantify the degree of complementarity of different targets we have introduced a figure of merit measuring the inverse of the area enclosed by the 95% marginalised contours in the plane $\log_{10}(m_\chi) - \log_{10}(\sigma^p_{SI})$. There is a high degree of complementarity of different targets: for our benchmark with $m_\chi = 50$ GeV and our fiducial set of galactic model parameters, the relative error on the reconstructed mass goes from 8.1% for an analysis based on a xenon experiment only, to 5.2% for a combined analysis with germanium, to 4.5% adding also argon. Allowing the parameters to vary within the observational uncertainties significantly degrades the reconstruction of the mass, increasing the relative error by up to a factor of $\sim$4 for xenon and germanium, especially due to the uncertainty on ρ_0 and v_0. However, we found that combining data from Ar, Ge and Xe should allow to reconstruct a 50 GeV WIMP mass to 11.8% accuracy even under weaker astrophysical constraints than currently available.

Although the mass reconstruction accuracy may appear modest, any improvement of

this reconstruction is important, in particular in view of the possible measurement of the same quantity at the Large Hadron Collider at CERN. The existence of a particle with a mass compatible, within the respective uncertainties, with that deduced from direct detection experiments would provide a convincing proof that the particles produced in accelerators are stable over cosmological time scales. Although this is not sufficient to claim discovery of DM [97], it would certainly be reassuring.

Despite the strong dependence of direct detection experiments on the galactic model degrades the reconstruction of DM properties, it does open up the possibility to potentially constrain the local distribution of DM, in case of detection with multiple targets. For example in the case of a low mass 50 GeV WIMP, we have shown that the local circular velocity can be determined from direct detection data alone more accurately than it is presently measured using the local distribution of stars and gas clouds. Additionally, directly detecting DM provides the most realistic way of measuring the local DM velocity distribution. This will in principle provide invaluable information on the structure of the Milky Way halo.

Chapter 4

High-energy cosmic rays

Nearly 100 years after the discovery, cosmic rays (CR) are still today a fascinating, hot topic with many loose ends and plenty of fresh data to interpret. Cosmic rays play, in fact, a central role in modern astrophysics, and to understand in detail their origin and propagation until the Earth remains one of the key open questions of our time. Besides being important *per se*, high-energy galactic cosmic rays provide several channels to search for Dark Matter indirectly, namely through antiproton and electron-positron observations. Clearly, a sound knowledge of cosmic-ray physics – still to achieve – is essential in interpreting eventual DM signatures.

Charged cosmic rays are, broadly speaking, all energetic charged particles of extraterrestrial origin arriving at the top of the atmosphere. These include mostly protons, but also antiprotons, electrons, positrons, He nuclei and all sorts of heavier nuclei. Over the years many composition studies and the complementarity between different measurements have taught us a lot about the environment where cosmic rays are accelerated as well as how they travel through the interstellar medium until the Earth. Nevertheless, a fully-consistent picture has not been achieved yet. At low energies – meaning energies below 10^3 TeV/n – the bulk of the cosmic-ray flux is believed to be of galactic origin. Non-relativistic shocks occuring at supernova remnants seem convincing processes to accelerate these particles. At higher energies the cosmic-ray composition is still an open issue and at around 10^{18} eV an extragalactic component is supposed to kick in. The physical mechanism by which such extreme energies are reached is still unclear. In this Chapter we focus solely on galactic cosmic rays at energies $E \lesssim 10^3$ TeV/n, reviewing the mechanisms behind their origin (Section 4.1), the processes mediating propagation throughout the Galaxy (Section 4.2), the theoretical framework usually adopted (Section 4.3) and the experimental status (Section 4.4). Finally, Section 4.5 is dedicated to one of the original contributions of the present thesis: the prospects of the Alpha Magnetic Spectrometer AMS-02 in pinpointing cosmic-ray propagation [3].

4.1 Origin

The existence of high-energy cosmic rays poses by itself tremendous challenges to modern astrophysics. To accelerate particles beyond the TeV scale – and prevent them from losing energy immediately afterwards – is not an easy task even in extreme astrophysical environments such as supernova explosions, supernova remnants or pulsar magnetospheres. Although energetically speaking these sites are powerful enough to explain the bulk of

high-energy cosmic rays, the microphysics of the acceleration mechanism is problematic. A priori charged particles can be efficiently accelerated by external electromagnetic fields. For instance, one can envision huge static electric fields pushing particles to very high energies. However, such situation can hardly occur in astrophysical environments for long enough periods or large enough regions, because the density of free charges is usually high and promptly damps the electric field [64]. Alternatively, quickly varying magnetic fields – as opposed to static ones – induce electric fields capable of steering and accelerating charged particles. In any case, the specific physical mechanism should in principle be a continuous (rather than one-shot) process in order to avoid massive energy losses immediately upon acceleration. Therefore, a crucial point is that the particles are confined long enough at the source so that sizeable energies can be reached. An useful way to pinpoint sources of a given energy is to use the **Hillas criterion**: a particle of charge $Z|e|$ confined to a site of size L and magnetic field B can be accelerated to a maximum energy

$$E_{max} = \alpha Z|e|BLc \simeq 0.3 \times \alpha Z \text{ GeV} \left(\frac{B}{1 \text{ G}}\right)\left(\frac{L}{10 \text{ km}}\right) \quad ,$$

where it was assumed that the particles are relativistic with $v \sim c$, energy losses at the source were neglected and α is a factor of order unity related to the acceleration mechanism. For example, supernova remnants ($L \sim 1$ pc, $B \sim 10^{-4}$ G) feature $E_{max} = 9\alpha Z \times 10^7$ GeV, while pulsar magnetospheres ($L \sim 10$ km, $B \sim 10^{10}$ G) can in principle reach $E_{max} \sim 3\alpha Z \times 10^9$ GeV. Of course, this is only a back-of-the-envelope calculation; the detailed acceleration process needs to be treated carefully.

A first step towards understanding the origin of high-energy cosmic rays was given in 1949 when Enrico Fermi devised the so-called **Fermi acceleration mechanism** (see [64]). Imagine a charged particle of mass m confined to a region with many magnetic field irregularities, dubbed magnetic mirrors in the following. This is a typical environment in several astrophysical sites including clouds in the interstellar medium. The particle will repeatedly scatter off the magnetic mirrors gaining energy in a stochastic manner, as shown below. Consider one such collision where the mirror, of mass $M \gg m$, travels in the positive x-direction with velocity u and the charged particle hits it with a velocity v and pitch angle θ, $\cos\theta \equiv -\vec{u}\cdot\vec{v}/(|\vec{u}|\cdot|\vec{v}|)$. In the laboratory frame, the initial particle energy and momentum are, respectively, $E = \gamma_v mc^2$ and $\vec{p} = -p\cos\theta\,\vec{e}_x - p\sin\theta\,\vec{e}_y$, $p = \gamma_v mv$. Since $M \gg m$, the centre of momentum moves along with the mirror and the particle is reflected conserving energy in that frame, $E_{CM} = E'_{CM}$. Therefore, transforming to the CM frame,

$$\begin{aligned} E_{CM} &= \gamma_u(E - u(-p\cos\theta)) = E'_{CM} \\ p_{x,CM} &= \gamma_u(-p\cos\theta - uE/c^2) = -p'_{x,CM} \\ p_{y,CM} &= -p\sin\theta = p'_{y,CM} \quad , \end{aligned}$$

where the primes refer to quantities after the collision. Transforming the final energy E'_{CM} back to the lab frame results in

$$E_f = \gamma_u\left(E'_{CM} - (-u)p'_{x,CM}\right) = \gamma_u^2 E\left(1 + \frac{2uv\cos\theta}{c^2} + \frac{u^2}{c^2}\right) \quad ,$$

recalling that $p/E = v/c^2$, or

$$\frac{\Delta E}{E} \equiv \frac{E_f - E}{E} = 2\gamma_u^2 \left(\frac{uv\cos\theta}{c^2} + \frac{u^2}{c^2} \right) \sim \frac{2uv\cos\theta}{c^2} + \frac{2u^2}{c^2} \quad , \tag{4.1}$$

where the last step is valid to second order in u/c. The above expression gives the fractional energy gain in one collision, so it must be averaged over the pitch angle θ. The collision probability is simply proportional to the relative velocity $v + u\cos\theta$ (for a complete treatment see [64]), with $0 < \theta < \pi/2$ for head-on collisions and $\pi/2 < \theta < \pi$ for following encounters. As expected, head-on collisions are more likely to happen. Averaging expression (4.1) over the distribution $p(\theta) \propto (v + u\cos\theta)d\Omega = (v + u\cos\theta)\sin\theta\, d\theta$ yields $\langle \frac{\Delta E}{E} \rangle = \frac{8}{3}\frac{u^2}{c^2}$. In words, the efficiency of the acceleration mechanism is quadratic in u/c – this is why it is called *second-order Fermi mechanism*. Several comments are in order here. Firstly, it is important to notice that the fractional energy gain $\langle \frac{\Delta E}{E} \rangle$ is independent of E which means $dE/dt \propto E$. Hence, it is rather natural to produce a power-law source spectrum with Fermi acceleration. To explain a source spectrum $dN/dE \propto E^{-(2-2.5)}$, as requested by observations (after propagation is taken into account), is however another matter. Secondly, in the above reasoning, energy losses – that may play a relevant role in some cases – were disregarded. In particular ionisation losses may well prevent low-energy particles from reaching high-energies. Even if such problem is circumvented, the second-order Fermi mechanism is highly inefficient because *(i)* $\langle \frac{\Delta E}{E} \rangle$ scales as u^2/c^2 and typically $u \ll c$, and *(ii)* the huge number of collisions needed to reach high energies is difficult to attain in many astrophysical sites over reasonable time scales. The pioneer studies of Fermi do not fully explain the origin of high-energy cosmic rays but they set the basics of modern acceleration theory. For instance, equation (4.1) hints that a considerable improvement upon the original Fermi mechanism can be achieved if only head-on collisions occur since then $\langle \frac{\Delta E}{E} \rangle$ would be first-order in u/c. That is the idea behind the *first-order Fermi mechanism* of which non-relativistic strong shock waves stand as the most promising to explain the origin of cosmic rays below $\sim 10^3$ TeV/n – see Refs. [64, 150] for reviews of the different shock types.

Supernova remnants are the ideal environment for particle acceleration with Fermi mechanisms (first or second order). Indeed, the shock front crossing the interstellar medium allows repeated diffusion of particles from upstream to downstream and vice-versa, providing a way to accelerate particles with high efficiency. Actually, Fermi acceleration in supernova explosions circumvents the long-standing problem of adiabatic losses: if particles were accelerated in an one-shot manner during the early phases of the explosion, then adiabatic losses due to the expansion of the spherical front would severely damp the energy gained. Although a lot has been achieved over the decades regarding particle acceleration at supernova remnants, the details of the underlying mechanism and how the particles escape to the interstellar medium are not yet fully understood. Further theoretical developments and more precise multi-wavelength observations will hopefully shed light on this topic over the following years.

Finally, let us notice that, while the origin of cosmic rays below 10^3 TeV/n is not well-understood, the situation for higher energy particles is even more difficult. Following the Hillas criterion, it is fairly easy to find astrophysical objects in principle capable of accelerating particles up to 10^9 GeV or so. However, the specifics of the mechanism are unknown. This topic is very interesting for cosmic-ray physics, but lies outside the scope of this Chapter and shall not be treated here.

4.2 Propagation

Once injected in the galactic medium, charged cosmic rays − unlike photons or neutrinos − undergo several processes capable of steering, degrading energy or determining their extinction along the path towards us − see [151] for a recent review on cosmic-ray propagation. The galactic magnetic fields, for instance, are responsible for deflection and the presence of small magnetic irregularities leads to scattering of charged particles. Therefore, the path of a charged cosmic ray i can be treated as a random walk process with a certain **spatial diffusion coefficient**

$$D_{xx}(\mathbf{x}, R) = \beta D_{0xx} \left(R/R_0\right)^{\alpha} \quad ,$$

where $\beta = v/c = p/E$, $R = pc/(Z_i|e|)$ and R_0 is a reference rigidity. Particles with larger rigidities diffuse more efficiently and escape the Galaxy sooner. An almost inevitable consequence of high-energy particles scattering in the turbulent magnetic field is stochastic acceleration, dubbed **diffusive reacceleration** [152]. Such mechanism gives rise to diffusion in momentum space with diffusion coefficient [153]

$$D_{pp}(\mathbf{x}, R) = \frac{4p^2 v_A^2}{3\alpha(4-\alpha^2)(4-\alpha) D_{xx}(\mathbf{x}, R)} \quad ,$$

where v_A is the Alfvén velocity and represents the typical velocity at which magnetic irregularities propagate in the interstellar medium. Another issue to consider is the possible influence of galactic winds blowing at speed $\vec{V}_c(\mathbf{x})$ which results in the **convection** of particles and **adiabatic energy losses**. Other energy losses, proceeding at a global rate $b_i(\mathbf{x}, p) = -(dE/dt)_{tot}$, occur when the cosmic-ray flux crosses the galactic medium permeated with gas, background photons and magnetic fields. For nuclei, **Coulomb** and **ionisation losses** exist even though they play a minor role in the propagation. On the other hand, GeV electrons and positrons lose significant energy by **inverse Compton** and **synchrotron** radiation; at lower energies also ionisation, Coulomb interactions and **bremsstrahlung** may be relevant. Furthermore, in treating unstable, **radioactive species** one needs to take account of decays occuring with proper mean life τ_i. Lastly, **cosmic-ray spallation** on the interstellar medium − essentially localised in the disk − determines the extinction of the incident particle and creates a secondary flux consisting of gamma-rays from neutral pion decay, electrons, positrons, protons, antiprotons and other nuclei lighter than i. How often spallation occurs and which are the resulting secondaries is fixed by nuclear cross-sections and the distribution of gas (mainly H and He) present in the Milky Way.

4.2.1 Nuclei

Let us start by the energy losses pertaining nuclei. There are essentially two mechanisms at play: ionisation and Coulomb losses. In the process of **ionisation**, the incident high-energy nuclei N, of charge $Z|e|$ and energy $E = \gamma m_N c^2$, interacts with the electrons in the target atoms, resulting in ionisation and heating of the material. The ripped off electrons can afterwards produce further ionisation. Since $m_N \gg m_e$, it is an excellent approximation to assume that the incoming nucleus goes undeviated and maintains its velocity v. Under these assumptions, the energy loss rate of a nucleus $N(A, Z)$ when

crossing a target with electron number density $n_{e,t} = Z_t n_t$ is given by[1] [153, 154]

$$-\left(\frac{dE}{dt}\right)_{ionis} \simeq \frac{Z^2 e^4}{8\pi\epsilon_0^2 m_e v}\, n_{e,t} \left[\ln\left(\frac{2m_e v^2\gamma^2 E_{max}}{\bar{I}_t^2}\right) - 2\frac{v^2}{c^2}\right] \quad , \tag{4.2}$$

where ϵ_0 is the permittivity of free space, $\bar{I}_t$ is the mean ionisation potential averaged over all the states of the electrons in the target atoms (e.g. $\bar{I}_H = 19$ eV, $\bar{I}_{He} = 44$ eV [153]) and E_{max} is the maximum transferred energy,

$$E_{max} = \frac{2m_e m_N^2 v^2\gamma^2}{m_e^2 + m_N^2 + 2\gamma m_e m_N} \overset{m_N \gg \gamma m_e}{\longrightarrow} 2m_e v^2\gamma^2 \quad .$$

Needless to say, in the case of mixed (i.e. non pure) targets, expression (4.2) is summed over the target elements t; a typical example is the interstellar medium (ISM) in our Galaxy mainly composed of H and He. It is worth mentioning two particularities about $(dE/dt)_{ionis}$: *(i)* it scales as $1/m_e$, so that the interaction between incident and target nuclei can be safely neglected, and *(ii)* to first approximation it depends on Z and v only, not on the mass of the incident nucleus m_N.

If the target material is completely ionised, then **Coulomb losses** – due to the interaction of the high-energy incoming nucleus with thermal electrons – are turned on and proceed at a rate [153]

$$-\left(\frac{dE}{dt}\right)_{Coul} \simeq \frac{Z^2 e^4}{8\pi\epsilon_0^2 m_e}\, n_{e,t}\, \ln\left(\frac{m_e^2 m_N \gamma^2 v^4}{\pi r_e \hbar^2 c^2 n_{e,t}(m_N + 2\gamma m_e)}\right) \frac{v^2}{x^3 + v^3} \quad , \tag{4.3}$$

in which $x = \left(\frac{3\pi^{1/2}}{4}\right)^{1/3} \left(\frac{2k_B T}{m_e}\right)^{1/2}$, T is the temperature of the target gas and $r_e = \frac{e^2}{4\pi\epsilon_0 m_e c^2}$ is the classical electron radius. Notice that in the ultra-relativistic limit $v \sim c$, both ionisation and Coulomb losses feature $|dE/dt| \sim \mathcal{O}(\ln\gamma)$ – this behaviour is rather particular and makes these mechanisms important in the low-energy regime as we shall see.

Another important mechanism that drains energy is the process of **adiabatic** expansion, where the work done during the expansion of a gas leads to an energy loss rate (see e.g. [64])

$$-\left(\frac{dE}{dt}\right)_{adiab} = \frac{1}{3}\left(\nabla\cdot v\right) E \quad , \tag{4.4}$$

in the relativistic limit. This term is usually included in the transport equation separately from energy losses (see Section 4.3). Adiabatic losses are especially important for protons and antiprotons, in particular in supernova remnants or whenever convective winds are present.

It is very common to express energy losses in terms of the time scale necessary for the species to lose a significant part of its initial energy:

$$\tau_{tot}(E) \equiv -\frac{T_k}{\sum_j \left(\frac{dE}{dt}\right)_j} \equiv \left(\sum_j \tau_j^{-1}(E)\right)^{-1} \quad , \tag{4.5}$$

[1] For the sake of clarity, SI units are used throughout this and the following subsections.

where $T_k = E - m_N c^2$ is the kinetic energy ($T_k \simeq E$ for relativistic particles). As expected, at a given energy E, the dominant energy loss mechanism is the one with smallest $\tau_j(E)$.

Besides energy losses, the propagation of high-energy nuclei is controlled by **spallation**, i.e. inelastic scattering off target nuclei. Globally, in these interactions the incoming nucleus – the primary – is destroyed giving rise to numerous secondary particles, including (but not limited to) lighter nuclei, neutrons and pions $\pi^{\pm}$, π^0. Subsequently, charged pions $\pi^{\pm}$ decay into neutrinos and muons (that decay into electrons or positrons and neutrinos), while neutral pions π^0 originate pairs of $\gamma-$rays. Soft $\gamma-$ray lines may also be produced by excited daughter nuclei that return to the ground state. In the context of high-energy galactic cosmic rays, spallation is of utmost importance in two different environments: the galactic disk, against which cosmic rays spallate in their way from the source to us; and the atmosphere, where Extensive Air Showers are initiated allowing the measurement of the highest energy cosmic rays, see Section 4.4. Generically speaking, a nucleus of total inelastic cross-section against target i σ_{Ni}^{inel} is destroyed at a rate

$$\Gamma_N \equiv \tau_{sp,N}^{-1} = \sum_i \sigma_{Ni}^{inel} v_{Ni} n_i \quad , \tag{4.6}$$

where the sum runs over the target nuclei, v_{Ni} is the relative velocity (for target nuclei at rest, $v_{Ni} \sim v_N$) and n_i is the number density of target nuclei i. Again, when considering spallation against the interstellar medium, i =H,He. As described above, in the same reaction where the primary, incoming nucleus is destroyed, one or more lighter nuclei N' are produced with source term

$$Q_{sp,N'} = \sum_N \sum_i \sigma_{Ni \to N'X'} \, v_{Ni} \, n_i \, n_N \quad , \tag{4.7}$$

n_N being the number density of parent nuclei N and $\sigma_{Ni \to N'X'}$ the partial inelastic cross-section to produce N' nuclei from cosmic ray $-$ target spallation. Typical spallation events in galactic cosmic rays include ^{12}C $\to^9$ Be,^{10}Be or ^{12}C $\to^{10}$ B,^{11}B, that are crucial in studying the ratios B/C and ^{10}Be/^{9}Be. It is also worth noticing that the cross-sections σ_{Ni}^{inel} and $\sigma_{Ni \to N'X'}$ have an energy dependence that is not extremelly well-known experimentally, even though a great deal has been achieved over the decades (see e.g. [154]).

Finally, one has to take into account that several nuclei are **radioactive** with given proper mean life $\tau_N \equiv \tau_{1/2,N} / \ln 2$. The corresponding decay time in the laboratory frame is simply $\tau_{d,N} = \gamma \tau_N$. Species with $\tau_{d,N}$ of the order of the diffusion time scale $\sim L^2/D_{xx}$ are especially useful in probing CR propagation parameters, as explained in the next Sections. These species include ^{10}Be ($\tau_{1/2} \sim 1.4 \times 10^6$ yr), ^{26}Al ($\tau_{1/2} \sim 7.2 \times 10^5$ yr) and ^{36}Cl ($\tau_{1/2} \sim 3.0 \times 10^5$ yr).

4.2.2 Protons and antiprotons

Protons and antiprotons are treated basically in the same manner as CR nuclei specialising the formulae presented in the previous subsection to $Z = 1$. Because these channels are particularly important for Dark Matter indirect searches and to constrain CR injection/propagation models, some further details are given here. Firstly, the total inelastic

p−H interaction cross-section is given by [155, 156, 157, 158]

$$\sigma_{pH}^{inel} = 32.2 \text{ mb} \times \begin{cases} 0 & \text{for } T_p < 0.3 \\ \frac{1+0.0273\ln\left(\frac{E_p}{200\text{ GeV}}\right)}{1+0.00262T_p^{-(17.9+13.8\ln T_p+4.41\ln^2 T_p)}} & \text{for } 0.3 \leq T_p < 3 \\ 1+0.0273\ln\left(\frac{E_p}{200\text{ GeV}}\right) & \text{for } 3 \leq T_p < 200 \\ 1+0.0273\ln\left(\frac{E_p}{200\text{ GeV}}\right)+0.01\ln^2\left(\frac{E_p}{200\text{ GeV}}\right) & \text{for } T_p \geq 200 \end{cases} , \quad (4.8)$$

while the total inelastic $\bar{\text{p}}$−H cross-section reads [159, 155, 156, 157, 158]

$$\sigma_{\bar{p}H}^{inel} = 24.7 \text{ mb } \left(1+0.584T_{\bar{p}}^{-0.115}+0.856T_{\bar{p}}^{-0.566}\right) \quad (T_{\bar{p}} > 0.05) \quad , \quad (4.9)$$

with $\sigma_{\bar{p}H}^{inel} = \sigma_{\bar{p}H}^{ann} + \sigma_{\bar{p}H}^{non-ann}$ and the inelastic annihilation cross-section is [159, 155, 156, 157, 158, 160]

$$\sigma_{\bar{p}H}^{ann} = \begin{cases} 661 \text{ mb } \left(1+0.0115T_{\bar{p}}^{-0.774}-0.948T_{\bar{p}}^{0.0151}\right) & \text{for } T_{\bar{p}} < 15.5 \\ 36 \text{ mb } T_{\bar{p}}^{-0.5} & \text{for } T_{\bar{p}} > 15.5 \end{cases} \quad , \quad (4.10)$$

where T_p and $T_{\bar{p}}$ are the kinetic energies of protons and antiprotons in GeV units and E_p is the total proton energy. The destruction rate of antiprotons against the interstellar medium is usually written as

$$\Gamma_{\bar{p}} = \sigma_{\bar{p}H}^{inel}\, v_{\bar{p}} \left(n_H + 4^{2/3} n_{He}\right) \quad ,$$

and analogously for protons, where the factor $4^{2/3}$ accounts for the higher geometrical cross-section of He with respect to H nuclei, $n_H \simeq 1$ cm^{-3} is the hydrogen number density in the galactic disk and $n_{He} \simeq 0.07 n_H$.

Besides the source term discussed in Section 4.1 and the secondary fluxes generated by heavier nuclei interactions, there is another contribution to the flux of antiprotons, the so-called *tertiary* $\bar{p}$ [161]. These are the antiprotons that undergo non-annihilating inelastic interaction with the target gas being scattered to lower energies. For multi-GeV energies, the tertiary contribution to the total antiproton flux is negligible.

An usual assumption in modelling high-energy proton and antiproton fluxes is to ignore energy losses (ionisation or Coulomb). Such assumption is well justified: indeed, Figure 4.1 shows that the time scale of interactions in the galactic gas $1/\Gamma_{\bar{p}(p)}$ is much smaller than the energy loss time scale, for both high-energy protons and antiprotons. Only in the low energy regime are losses relevant.

4.2.3 Electrons and positrons

Electrons and positrons are produced as secondaries in the spallation of CR species against the interstellar medium. Among the most important reactions are the interactions between cosmic-ray protons and He nuclei with H and He in the ISM. The outcome of these inelastic scattering processes include abundant fluxes of charged pions $\pi^{\pm}$ and other mesons, that eventually decay into muons $\mu^{\pm}$. Finally, the muons decay injecting electrons and positrons into the interstellar medium. Other less important sources of secondary elec-

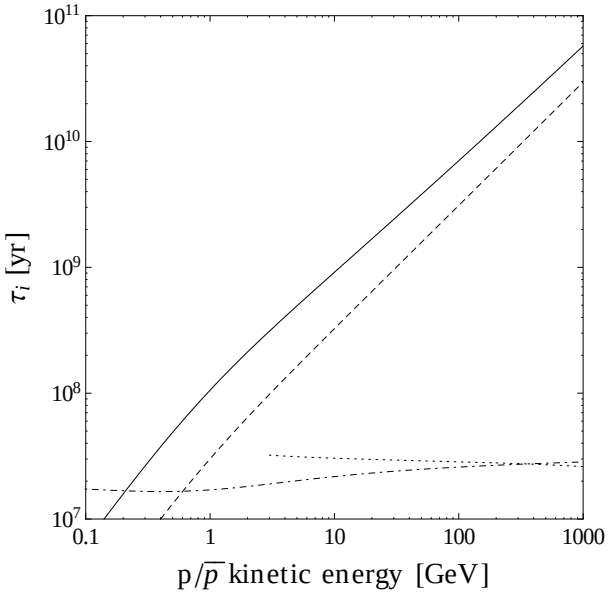

Figure 4.1: The time scale for spallation of protons (dotted line) and antiprotons (dot-dashed line) on the galactic gas as compared to the time scales for energy losses by ionisation (solid line) and Coulomb (dashed line). For the spallation time scales equation (4.10) and the high-energy branches of equation (4.8) were used. It was assumed that the galactic gas is composed of H and He with densities $n_H = 1$ cm^3 and $n_{He} = 0.07$ cm^3. The ionisation potential used are $\bar{I}_H = 19$ eV and $\bar{I}_{He} = 44$ eV [153]. For illustration purposes the Coulomb losses were calculated with the same densities as stated above and $T = 300$ K.

trons and positrons are the decay of radioactive species (e.g. ^{26}Al) as well as the creation of $e^{\pm}$ pairs by photon-photon collisions or photon conversion in the field of a nucleus. An up-to-date, thorough evaluation of the galactic secondary yield of positrons can be found in Ref. [162]. As in the case of antiprotons, positrons constitute an important probe for DM annihilations or decays.

Now, due to their small mass, electrons and positrons – in particular when ultra-relativistic – are affected by significant energy losses. As in the case of nuclei, electrons and positrons suffer from **ionisation losses** when crossing a target gas. These amount to [154]

$$-\left(\frac{dE}{dt}\right)_{ionis} = \frac{e^4}{8\pi\epsilon_0^2 m_e v}\, n_{e,t} \times \left[\ln\left(\frac{E^2\beta^2(\gamma-1)}{2\bar{I}_t^2}\right) - \left(\frac{2}{\gamma}-\frac{1}{\gamma^2}\right)\ln 2 + \frac{1}{\gamma^2} + \frac{1}{8}\left(1-\frac{1}{\gamma}\right)^2\right] , \quad (4.11)$$

where $E = \gamma m_e c^2$ is the energy of the incident electron or positron and $\beta = v/c$ its velocity. Notice that the last three terms inside the squared brackets reduce to $1/8$ in the ultra-relativistic limit $\gamma \to \infty$. In that limit, both electrons and protons travel at $v \sim c$ and the expressions (4.2) and (4.11) roughly coincide.

In a fully ionised target, the **Coulomb losses** are given by [153]

$$-\left(\frac{dE}{dt}\right)_{Coul} = \frac{e^4}{8\pi\epsilon_0^2 m_e v}\, n_{e,t} \left[\ln\left(\frac{E m_e c^2}{4\pi r_e \hbar^2 c^2 n_{e,t}}\right) - \frac{3}{4}\right] \quad . \quad (4.12)$$

Additionally, being charged particles, electrons and positrons lose energy whenever

accelerated or decelerated emitting electromagnetic radiation. The corresponding **radiative losses** of a particle of charge q and Lorentz factor γ in the lab frame is generically expressed as [154]:

$$-\left(\frac{dE}{dt}\right)_{rad} = \frac{q^2\gamma^4}{6\pi\epsilon_0 c^3}\left[a^2 + \gamma^2\left(\frac{\vec{v}\cdot\vec{a}}{c}\right)^2\right] \tag{4.13}$$

with $\vec{a}$ the particle acceleration vector and $\vec{v}$ its velocity. The emitted radiation has some remarkable characteristics, namely *(i)* it is polarised, and *(ii)* its power follows a $\sin^2\theta$ distribution, θ being the angle with respect to the acceleration vector. There are three radiative processes of importance for electrons and positrons: bremsstrahlung, inverse Compton scattering (ICS) and synchrotron. In the following we shall analyse the energy losses associated to these variants as well as the photon yields produced by ICS and synchrotron emission.

Bremsstrahlung occurs when electrons or positrons are deviated in the electric field of ions, nuclei, protons or atomic electrons. In the case of an ionised target gas, bremsstrahlung losses (due to nuclei and electrons) amount to approximately [153]

$$-\left(\frac{dE}{dt}\right)_{brem} = 4r_e^2\alpha_{em}cEZ_t(Z_t+1)\,n_t\left(\ln(2\gamma) - \frac{1}{3}\right) \quad , \tag{4.14}$$

where Z_t is the atomic number of the target and n_t its number density. Useful formulae for bremsstrahlung losses on neutral gas can be found in [153]. The bremsstrahlung photon emission is an important probe of different astrophysical sites; for relevant parameterisations of the corresponding spectra in different limits see Refs. [64, 94].

Another important phenomenon is **Compton scattering**, i.e. the interaction between electrons (or positrons) and photons. The electron-photon scattering is a radiative process in which the electron feels the electric field of the incoming electromagnetic wave (of angular frequency $\omega = 2\pi c/\lambda$) and oscillates radiating away photons of frequency ω'. In the interaction electron and photon can be treated as point-like particles and the conservation of the s-invariant in the lab frame gives

$$\hbar w\ (E_e - p_e\cos\theta) = \hbar w'\ (E_e' - p_e'\cos\theta') \quad ,$$

where primes denote variables after the collision, θ is the angle between $\vec{p}_e$ and $\vec{p}_\gamma = \frac{E_\gamma}{c}\vec{e}_\gamma$ and θ' is the angle between $\vec{p}_e\,'$ and $\vec{p}_\gamma\,'$. Using energy and momentum conservation separately, it is easy to express E_e' and $p_e'\cos\theta'$ in terms of the other variables of the problem and obtain

$$\frac{\omega'}{\omega} = \frac{1 - \frac{v_e}{c}\cos\theta}{1 - \frac{v_e}{c}\cos(\theta+\alpha) + \frac{\hbar w}{E_e}(1-\cos\alpha)} \quad , \tag{4.15}$$

α being the angle between $\vec{p}_\gamma$ and $\vec{p}_\gamma\,'$. In the traditional Compton limit, the electrons are stationary ($v_e \sim 0$) and receive energy from the incident photons resulting in a longer wavelength of the scattered radiation: $\frac{\lambda'}{\lambda} = \frac{\omega}{\omega'} = 1 + \frac{\hbar w}{E_e}(1-\cos\alpha) > 1$. Now consider the opposite limit when electrons are relativistic and $\hbar w \ll E_e = \gamma m_e c^2$. This regime – usually called **inverse Compton scattering** – is extremely important in astrophysics and provides the means to upscatter low-frequency photons to extreme energies. The

maximum photon energy increase happens for head-on collisions ($\cos\theta = -1$, $\cos(\alpha+\theta) = +1$) with $v_e \sim c$:

$$\frac{\omega'_{max}}{\omega} \sim \frac{1+v_e/c}{1-v_e/c} = \gamma^2(1+v_e/c)^2 \sim 4\gamma^2 \quad .$$

From the viewpoint of high-energy electrons (or positrons), inverse Compton scattering is a very efficient energy loss mechanism. Considering a radiation density distribution $n(E_\gamma \equiv \hbar w) \equiv d^2N/dVdE_\gamma$, the loss rate is given by [163, 153, 154, 94]

$$-\left(\frac{dE}{dt}\right)_{ICS} = \int dE_\gamma \int dE'_\gamma \, (E'_\gamma - E_\gamma)\, n(E_\gamma)\, \frac{\sigma_{KN} c}{E_\gamma} \quad , \tag{4.16}$$

where σ_{KN} is the Klein-Nishina cross-section

$$\sigma_{KN} = \frac{3\sigma_T}{4\gamma^2}\left[2q\ln q + q + 1 - 2q^2 + \frac{(\Gamma q)^2(1-q)}{2(1+\Gamma q)}\right]$$

with $\sigma_T = \frac{8\pi}{3} r_e^2 = \frac{e^4}{6\pi\epsilon_0^2 m_e^2 c^4}$ and

$$q(E_\gamma, E'_\gamma) = \frac{E'_\gamma}{\Gamma(\gamma m_e c^2 - E'_\gamma)} \qquad\qquad \Gamma(E_\gamma) = \frac{4E_\gamma \gamma}{m_e c^2} \quad .$$

The integral over E'_γ in equation (4.16) can be easily transformed into an integral in q [163]:

$$-\left(\frac{dE}{dt}\right)_{ICS} = 3\sigma_T c \int dE_\gamma \, E_\gamma \, n(E_\gamma) \int_{\frac{1}{4\gamma^2}}^{1} dq \, \frac{(4\gamma^2 - \Gamma)q - 1}{(1+\Gamma q)^3}\left[2q\ln q + q + 1 - 2q^2 + \frac{(\Gamma q)^2(1-q)}{2(1+\Gamma q)}\right] \quad , \tag{4.17}$$

where the integral in q can be solved analytically (see e.g. [153]). In the Thomson limit, $\gamma E_\gamma \ll m_e c^2$ (or $\Gamma \ll 1$), $q \sim \frac{E'_\gamma}{4\gamma^2 E_\gamma}$ and the above expression reduces to

$$-\left(\frac{dE}{dt}\right)_{ICS} = \frac{4}{3}\sigma_T c \gamma^2 u_{rad} \tag{4.18}$$

in which $u_{rad} \equiv \int dE_\gamma \, E_\gamma n(E_\gamma)$ is the energy density of the radiation field. Notice the dependence $|(dE/dt)_{ICS}| \propto E^2$, that makes ICS especially important for high-energy electrons and positrons. In several astrophysical environments there are numerous photon fields (CMB, starlight, etc) so that the total energy losses by ICS are

$$\left(\frac{dE}{dt}\right)_{ICS,tot} = \sum_{rad}\left(\frac{dE}{dt}\right)_{ICS,rad} \quad .$$

Along this thesis we shall be also interested in the ICS radiated photons since they constitute an excellent astrophysical probe. Let us begin with the Thomson case where the rate of electron-photon scatterings is $\Gamma_T = \sigma_T c n_\gamma \simeq \sigma_T c \frac{u_{rad}}{E_\gamma}$ and therefore the mean

energy of the scattered photon is

$$\langle E'_\gamma \rangle \sim \frac{|(dE/dt)_{ICS}|}{\Gamma_T} = \frac{4}{3}\gamma^2 E_\gamma \quad .$$

Consequently, if γ is large enough, very low-frequency photons can be upscattered to very high energies. For instance, 100 GeV electrons or positrons can upscatter CMB photons with $E_\gamma \sim 2 \times 10^{-4}$ eV to $E'_\gamma \sim 8$ MeV. In full generality, the spectra of the emitted radiation (in units of photons/s) per electron of energy E is [163, 94]

$$\begin{aligned} P_{ICS}(E'_\gamma, E) &= \int dE_\gamma \, (E'_\gamma - E_\gamma) \, n(E_\gamma) \, \frac{\sigma_{KN} c}{E_\gamma} \\ &= \frac{3\sigma_T c}{4\gamma^2} E'_\gamma \int_{\frac{1}{4\gamma^2}}^{1} dq \, \frac{n(E_\gamma(q))}{q} \times \\ &\left(1 - \frac{m_e c^2}{4q\gamma(\gamma m c^2 - E'_\gamma)}\right) \left[2q \ln q + q + 1 - 2q^2 + \frac{(\Gamma q)^2 (1-q)}{2(1+\Gamma q)}\right] . \end{aligned} \quad (4.19)$$

Finally, the mechanism of **synchrotron emission** plays a crucial role in the life of electrons and positrons. When a relativistic charged particle is gyrating in a magnetic field $\vec{B}$, it emits radiation, dubbed synchrotron radiation, essentially aligned with the particle velocity $\vec{v}$ – for a full treatment see [64]. As in the case of ICS, the energy loss rate pertaining electrons and positrons follows from equation (4.13) and reads [64]

$$-\left(\frac{dE}{dt}\right)_{syn} = 2\sigma_T c \frac{B^2}{2\mu_0} \beta^2 \gamma^2 \sin^2 \alpha \quad , \quad (4.20)$$

in which α is the pitch angle (i.e. the angle between $\vec{B}$ and $\vec{v}$). Consider an isotropic distribution of electrons (or positrons), and therefore of α; then the mean value of $\sin^2 \alpha$ is simply

$$\langle \sin \alpha \rangle = \frac{\int_0^\pi d\alpha \, \sin \alpha \, \sin^2 \alpha}{\int_0^\pi d\alpha \, \sin \alpha} = 2/3 \quad ,$$

and the average energy loss rate amounts to

$$-\langle \left(\frac{dE}{dt}\right)_{syn} \rangle = \frac{4}{3} \, \sigma_T c \, u_{mag} \, \beta^2 \gamma^2 = \frac{e^4 B^2 \beta^2 \gamma^2}{9\pi \epsilon_0^2 \mu_0 m_e^2 c^3} \quad , \quad (4.21)$$

where we have defined the magnetic energy density $u_{mag} = \frac{B^2}{2\mu_0}$. This expression is very similar to the Thomson limit of the inverse Compton scattering (4.18): indeed, in a region of identical radiation and magnetic energy densities $u_{rad} = u_{mag}$, relativistic electrons or positrons suffer from identical synchrotron and ICS losses. The explanation for such behaviour is easily traced back to equation (4.13) – roughly speaking, the energy loss depends on the acceleration of the charged particle and not on the mechanism that generates it. Also important is the fact that $|(dE/dt)_{syn}| \propto E^2$, exactly as in the Thomson limit for ICS. Consequently, these two processes will be the most important ones when studying very high-energy electrons and positrons. For completeness we show in Figure 4.2 a comparison of all the time scales τ_i (cf. equation (4.5)) for the mechanisms presented

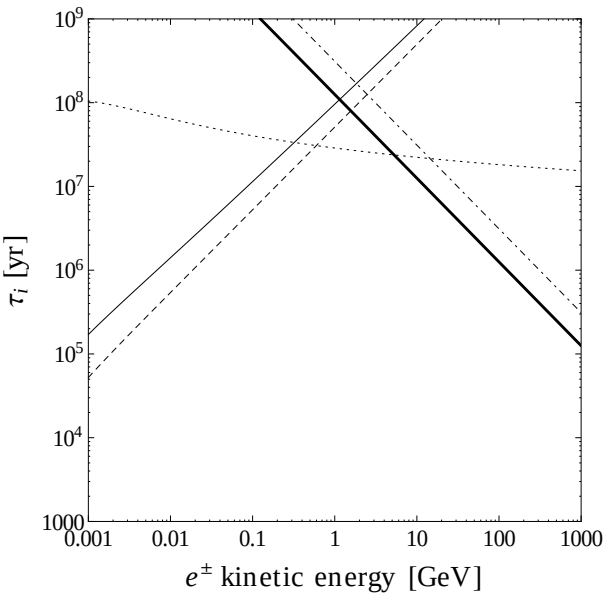

Figure 4.2: The energy loss time scales for electrons and positrons: ionisation (thin solid line), Coulomb (dashed line), bremsstrahlung (dotted line), inverse Compton Scattering in the Thomson limit (dot-dashed line) and synchrotron (thick solid line). For this plot a target hydrogen density of 1 cm^3 was assumed, and $\bar{I}_H = 13.6$ eV [153]. The ICS losses were computed with a radiation energy density $u_{rad} = 1$ eV/cm^3, while synchrotron losses refer to a magnetic field $B = 1$ nT.

in this subsection. As can be seen, ionisation and Coulomb losses dominate at low energies while ICS and synchrotron are the most effective above the GeV scale. In some cases, the total rate of energy density released by a given distribution of electrons (or positrons) $n_e \equiv \frac{d^2N_e}{dVdE}$,

$$\frac{d^2E}{dVdt} = \int dE\, n_e \sum_i \left|\frac{dE}{dt}\right|_i \quad ,$$

is an interesting quantity to compute and can provide important clues about the heating of different media (e.g. the intracluster gas in galaxy clusters, see [94]).

The spectrum of the radiated synchrotron photons is an useful probe of astrophysical sources. The frequency of the emitted electromagnetic waves is closely related to the gyrofrequency of the electron or positron $\nu_g = \frac{eB}{2\pi m_e}$ (in the non-relativistic limit) and its energy $E = \gamma m_e c^2$. The bulk of the synchrotron photons is emitted around the so-called *critical frequency*

$$\nu_c = \frac{3}{2}\gamma^2\nu_g = \frac{3eBE^2}{4\pi m_e^3 c^4} \simeq 4.2 \text{ MHz} \left(\frac{E}{m_e c^2}\right)^2 \left(\frac{B}{1 \text{ G}}\right) \quad . \tag{4.22}$$

The exact shape of the spectrum per electron is given by [64]

$$\left(\frac{dW}{d\nu}\right)_{syn} = \frac{\sqrt{3}e^3 B \sin\alpha}{4\pi\epsilon_0 c m_e} F\left(\frac{\nu}{\nu_c}\right) \tag{4.23}$$

in units of W/Hz≡J and where

$$F(x) = x\int_x^\infty dx'\, K_{5/3}(x') \qquad\qquad \int_0^\infty dx\, F(x) = \frac{8\pi}{9\sqrt{3}} \quad , \tag{4.24}$$

where K_n is the modified Bessel function of the second kind and order n. The function F – and hence the radiation spectrum – is peaked around its maximum at $\nu_{max} \simeq 0.29\nu_c$. A crude, but useful, approximation is to assume all radiated power is concentrated at ν_{max}. In this case $F(x)$ may be approximated by a Dirac delta,

$$F(x) \simeq \frac{8\pi}{9\sqrt{3}}\delta(x - 0.29)$$

in which the normalisation constant preserves the integral of F (cf. equation (4.24)). It will turn out to be useful to express the previous δ function in terms of the electron or positron energy E. First, let us find the energy of the $e^{\pm}$ that contribute the most to a given frequency ν; solving $\nu/\nu_c - 0.29$ gives

$$E_p = \left(\frac{4\pi m_e^3 c^4}{3eB}\frac{\nu}{0.29}\right)^{1/2} \quad . \tag{4.25}$$

Now, using the δ function property $\delta(f(x)) = \sum_i \delta(x - x_i)/|f'(x_i)|$ (in which the sum runs over the simple zeros of f),

$$\delta(\nu/\nu_c - 0.29) = \delta(E - E_p)\left(2\nu\frac{4\pi m_e^3 c^4}{3eBE_p^3}\right)^{-1} = \delta(E - E_p)\frac{E_p}{2 \times 0.29} \quad . \tag{4.26}$$

Finally, in certain situations it is important to take into account two unavoidable effects associated to synchrotron radiation: the *self-absorption* of synchrotron photons by the electrons and positrons (see [64]), and the *self-synchrotron Compton*, i.e. the ICS of synchrotron photons by the same population of electrons and positrons that radiate them away.

4.3 Theoretical framework

The transport equation that models all the processes described in the previous Section for a specific cosmic-ray species i is [151, 64]

$$\begin{aligned}\frac{\partial n_i}{\partial t} =& Q_{tot,i}(\mathbf{x}, p, t) + \vec{\nabla} \cdot \left(D_{xx}(\mathbf{x}, R)\vec{\nabla} n_i - \vec{V}_c(\mathbf{x}) n_i\right) \\ &+ \frac{\partial}{\partial p} p^2 D_{pp}(\mathbf{x}, R)\frac{\partial}{\partial p}\frac{n_i}{p^2} - \frac{n_i}{\tau_{d,i}} - \frac{n_i}{\tau_{sp,i}} \\ &+ \frac{\partial}{\partial p}\left(b_i(\mathbf{x}, p) n_i + \frac{p}{3}\vec{\nabla} \cdot \vec{V}_c(\mathbf{x})\, n_i\right) \quad ,\end{aligned} \tag{4.27}$$

where $n_i = n_i(\mathbf{x}, p, t) \equiv \frac{d^2N}{dVdp}$ is the number density of particles i per unit momentum (or unit energy in the relativistic limit) and $b_i = -\sum_i \left(\frac{dE}{dt}\right)_i$. Notice that the source term $Q_{tot,i}$ includes the primary injection spectrum (usually from acceleration at supernova remnants) as well as the products of decay and spallation of heavier cosmic-ray species. Formally, $Q_{tot,i}$ may also include "exotic" primary contributions produced for instance by Dark Matter annihilations or particle acceleration in the surroundings of pulsars. Such components are disregarded here, but studied in detail in Chapter 5.

The standard approach to solve (4.27) for n_i is to assume the *steady state condition*

$\partial n_i/\partial t = 0$ (or solve the full equation until an approximate steady state is reached) and adopt a cylindrical diffusive halo with radius $r_{max} \simeq 20$ kpc and half-thickness L inside which the diffusion coefficient $D_{xx}(\mathbf{x}, R_i)$ follows a given parameterisation. The half-thickness L is much larger than the half-thickness of the galactic disk $h \sim 0.1$ kpc and n_i is forced to vanish at the cylinder boundaries since the particles escape to the intergalactic medium. To proceed one may either apply **(semi-)analytical methods** (e.g. [164, 165, 166]) or recur to **numerical codes** (e.g. GALPROP [167, 153] or DRAGON [168, 169]). Even though analytical methods are invaluable in many cases, once we want to model the Galaxy in a realistic fashion taking account of different features, the numerical approach seems the only possible. In Section 4.5 we make use of GALPROP code v50.1p [167] that solves (4.27) by assuming a homogeneous power-law coefficient $D_{xx}(R) = D_{0xx}(R/R_0)^\alpha$ in a cylindrical diffusive halo as stated above – it is also possible to implement a double power-law for D_{xx} and in 3D mode to define a halo with limited ranges in x, y and z. Then, the densities n_i, from the heaviest nucleus ^{64}Ni down to protons and electrons, are computed until a steady state is reached. The flux of particles i at the Sun position $\mathbf{x}_\odot = (r_\odot, z_\odot) = (8.5, 0)$ kpc follows immediately through

$$\Phi_i(\mathbf{x}_\odot, T) \equiv \frac{d^4N}{dSd\Omega dtdT} = \frac{cA}{4\pi} n_i(\mathbf{x}_\odot, p) \quad ,$$

where $T = (\sqrt{(RZ_i|e|)^2 + m_i^2c^4} - m_ic^2)/A$ is the kinetic energy per nucleon and $dT = dE/A = \beta dp/A$. GALPROP implements a realistic interstellar hydrogen distribution and interstellar radiation field based on state-of-the-art surveys, and an updated nuclear reaction network is also used. The primary sources of cosmic rays are assumed to have an unique isotope composition and single or double power-law injection spectrum. Moreover, the distribution of sources can be specified but is usually taken to be such that the EGRET gamma-ray data are well reproduced. Convection can be switched on and it is assumed that galactic winds blow along the vertical direction, outwards the disk and with linear profiles

$$\vec{V}_c(\mathbf{x}) = sgn(z)(V_{c,0} + |z|dV_c/dz)\vec{e}_z \quad .$$

Diffusive reacceleration with a given Alfvén velocity v_A may as well be included. Finally, the local interstellar flux Φ_i gets modulated by the **solar wind** before arriving at the top of the atmosphere. In the *force field approximation* [170],

$$\bar{\Phi}_i(\bar{T}) = \frac{(\bar{T}A + m_ic^2)^2 - m_i^2c^4}{(TA + m_ic^2)^2 - m_i^2c^4} \Phi_i(\mathbf{x}_\odot, T) \quad ,$$

where $T = \bar{T} + Z_i|e|\phi_F/A$ and ϕ_F models solar activity. Further details of the GALPROP package are described in [167, 153]. A difference of GALPROP w.r.t. other codes like DRAGON [168, 169] is the assumption of a space-independent diffusion coefficient inside the diffusive halo.

Now, cosmic-ray data provide a few crucial hints on propagation through the Milky Way. For example, the highly isotropic distribution of arrival directions below 10^3 TeV/n implies that cosmic rays do not simply free-stream out of the Galaxy. Instead, they should be confined in a given volume during a certain period of time and such behaviour is naturally explained by diffusion in the interstellar medium. The diffusive term $\vec{\nabla} \cdot (D_{xx}\vec{\nabla}n_i)$ in equation (4.27) can indeed be replaced by a term $-n_i/\tau_{esc}$ expressing the

escape of cosmic rays after a typical time τ_{esc}: recalling that in one-dimensional diffusion the length covered in Δt is $l \sim 2\sqrt{D_{xx}\Delta t}$, we can write $\tau_{esc} \sim \frac{L^2}{4D_{xx}} \propto R^{-\alpha}$, which is much larger than the free-streaming time L/c.

Cosmic-ray composition studies are of extreme relevance as well. First of all, the contrast of abundances of elements found in the Solar System and in low-energy cosmic rays indicates similar compositions but a clear overabundance of Li, Be, B and sub-Fe elements in the latter. If the sources have the same composition as the Solar System (or the local galactic medium), then this observation is evidence for spallation of primary cosmic rays, namely C, N, O and Fe nuclei. Since $\tau_{sp,i} \gg L/c$, we find again arguments in favour of the confinement of galactic cosmic rays and supporting the idea of diffusion by scattering in magnetic irregularities. Furthermore, the energy dependence of the cosmic-ray composition is essential in order to constrain models of propagation. Of particular importance are secondary-to-primary ratios and unstable ratios.

Secondary-to-primary ratios include B/C, Cr/Fe, sub-Fe/Fe (i.e. (Sc+Ti+V)/Fe) and $\bar{p}/p$. B/C is frequently used because it is the best measured in a wide range of energies and involves well-known cross-sections. The mean values of such ratios, combined with nuclear cross-sections and the transport equation, yield an estimate of the *path length crossed* by primaries. The rule of thumb is a few g/cm^2 [64]. In most cases the behaviour with energy of secondary-to-primary measurements shows a peak at kinetic energies around GeV/n and a steady decrease towards higher energies. Since nuclear cross-sections do not feature such a decrease with energy, the most energetic primaries must escape the Galaxy sooner leaving them less time to spallate. This is understandable in light of the process of diffusion. Considering that reacceleration and convection do not play a major role at high energies and that energy losses for nuclei are negligible, the steady state distribution of a stable secondary s obeys (cf. equation (4.27)) $n_s/\tau_{esc} = Q_{sp,s}$, where $\tau_{esc} \sim \frac{L^2}{4D_{xx}}$ and spallation of s was neglected. The source term is due to spallation of a primary species p onto the interstellar gas with mean density in the diffusive halo $\langle n_{gas} \rangle \sim \frac{N_{gas}}{\pi r_{max}^2 L}$:

$$Q_{sp,s} \sim \sigma_{p\to s} c \langle n_{gas} \rangle n_p \quad ,$$

being $\sigma_{p\to s}$ the partial cross-section for production of s from spallations of p. Thus,

$$n_s/n_p \sim \tau_{esc}\, \sigma_{p\to s} c \langle n_{gas} \rangle \propto \frac{L R^{-\alpha}}{D_{0xx}} \quad . \tag{4.28}$$

The energy-dependent measurement of stable secondary-to-primary ratios constrains the diffusion index α and is degenerate in L/D_{0xx}. Notice that too large values of α would induce significant anisotropy at high energies since escape times scale as $R^{-\alpha}$. As for the peak observed at low energies, models with reacceleration, unlike those with convection, seem to accommodate it properly [153].

Unstable nuclei are as well very good probes of cosmic-ray propagation. The degree of their presence among the particles arriving at the top of the atmosphere indicates the time elapsed since production. Therefore, unstable nuclei are said to be cosmic-ray clocks. Particularly useful are radioactive isotopes with proper mean lifes in excess of $\sim 10^5$ yr such as ^{10}Be, ^{26}Al or ^{36}Cl. Let us focus on the unstable ratio ^{10}Be/^{9}Be since ^{10}Be is the lightest and best measured radioactive isotope presenting a β-decay into ^{10}B with mean life $\tau_{^{10}\mathrm{Be}} \sim 10^6$ yr. Now, both the unstable ^{10}Be and the stable ^{9}Be are supposed to be produced by spallation of carbon and oxygen [64]. If the distance between the spallation

site and us is much less than $c\gamma\tau_{^{10}\mathrm{Be}}$, then ^{10}Be/^{9}Be should roughly reflect the ratio of cross-sections for production of the isotopes. Deviations from such value quantify the distance travelled by these secondary nuclei. Rewriting equation (4.27) for ^{10}Be and ^{9}Be without reacceleration, convection, energy losses nor spallations, one gets the steady state ratio

$$^{10}\mathrm{Be}/^{9}\mathrm{Be} = \left(1 + \frac{\tau_{esc}}{\tau_{d,^{10}\mathrm{Be}}}\right)^{-1} \frac{Q_{sp,^{10}\mathrm{Be}}}{Q_{sp,^{9}\mathrm{Be}}} \quad ,$$

where $\tau_{esc} \propto L^2 R^{-\alpha}/D_{0xx}$ has been taken the same for both isotopes. ^{10}Be/^{9}Be data give information about the escape time τ_{esc} but do not constrain α because only a small number of energy bins is available (and at energies where solar modulation is unavoidable). Also, the constraints are degenerate in L^2/D_{0xx}. Notice that only a few fairly precise data points on the ratio ^{10}Be/^{9}Be would be invaluable to understand cosmic-ray propagation in our Galaxy. For a review on recent cosmic-ray nuclei data and covering acceleration and propagation, see [150].

4.4 Experimental overview

Perhaps the most staggering feature of cosmic rays is the energy spectrum, which is basically a power-law of spectral index -2.7 spanning over 30 orders of magnitude in flux. There are four important deviations from this smooth power-law behaviour:

- at very low energies ($E \lesssim$ GeV) where the *solar wind* modulates the spectrum;
- the *knee* at 10^3 TeV that is believed to signal the transition from proton cosmic rays to heavier nuclei;
- the *ankle* at 10^6 TeV which is possibly due to the transition from galactic to extra-galactic particles; and
- the *Greisen-Zatsepin-Kuzmin (GZK) cutoff* at $\sim 10^{19.6}$ eV observed independently by HiRes [171] and the Pierre Auger Observatory (PAO) [172], that accounts for the photo-desintegration of ultra high-energy protons on CMB photons over cosmological distances.

Apart from these mild, but certainly interesting, deviations from a power-law $E^{-2.7}$, it is clear that low-energy cosmic rays are much more abundant than high-energy ones. This characteristic motivates the use of distinct detection methods for high and low energies. Low-energy particles ($E \lesssim$10 TeV) are *directly detected* high in the atmosphere or above it with relatively small instruments since fluxes are copious. Usually, the particles are bent under an applied magnetic field, shower and deposit energy in a calorimeter, so that charge and energy are estimated accurately. These detectors include both space instruments such as PAMELA or AMS-01, and balloon-borne experiments as BESS, ATIC, HEAT or CAPRICE. PAMELA, for instance, is a multi-purpose detector designed to measure electrons, positrons, protons, antiprotons as well as light nuclei, all in the sub-TeV range. The instrument – launched in June 2006 and still taking data – consists of a magnetic spectrometer, a calorimeter and a time-of-flight system (among other components) that provide precise measurements of energy and charge of incoming cosmic rays. As we

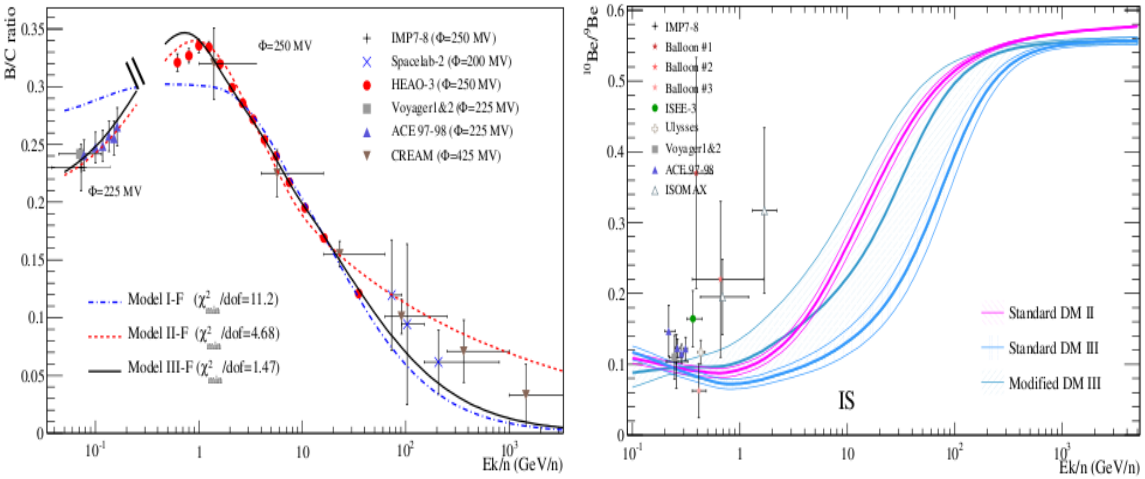

Figure 4.3: A compilation of the most recent data on the B/C (left frame) and ^{10}Be/^{9}Be (right frame) ratios. From Ref. [173].

shall see in Section 5.5, PAMELA has produced the most accurate determinations of the positron fraction and antiproton-to-proton ratio to date.

High-energy cosmic rays, instead, are far too rare to be detected by the small-area devices one is able to deploy in space or at the top of the atmosphere. A fortunate coincidence is that the atmosphere serves as a *huge calorimeter* for energetic particles, thus solving the problem of statistics. When a charged cosmic ray enters the atmosphere, it interacts with an air molecule originating mostly high-energy nucleons and pions. Nucleons will hit other molecules or nuclei giving rise to a hadronic shower component, while neutral pions decay promptly (with proper mean life $\tau_{\pi^0} \sim 10^{-16}$ s) into a pair of photons that trigger in turn an electromagnetic cascade. On the other hand, charged pions – presenting proper mean life $\tau_{\pi^\pm} \sim 10^{-8}$ s – may either interact with air nuclei feeding the hadronic component, or decay into muons and neutrinos. Finally, depending on the energy and altitude, muons arrive at the Earth surface or decay generating electrons (or positrons) and more neutrinos. This complex set of interactions is collectively called an Extensive Air Shower (EAS) and provides the means for high-energy cosmic ray detection. If the primary particle is an electron or a positron, the cascade proceeds as described in Section 5.5 for $\gamma-$rays. At the ground level, the EAS can be detected through the secondaries themselves or the light emitted along shower development. Besides the *Čerenkov emission* (see Section 5.5), *fluorescence light* is produced when charged secondaries excite nitrogen molecules – unlike Čerenkov, however, fluorescence emission is isotropic. All this information can be used and combined to reconstruct the initial properties of the primary (direction, energy) and, relying on numerical simulations of EAS, discriminate between different compositions, i.e. atomic number Z. Examples of experiments applying this sort of technique are MILAGRO and, at ultra-high energies, the Pierre Auger Observatory.

The focus here will be on high-energy cosmic rays, of energies $E \simeq$ GeV $-$ 10TeV, exactly where the two detection methods above-described are useful and where a cross-calibration of energies is in principle possible. As pointed out before, high-energy cosmic rays are mostly protons, but nuclei up to iron (and beyond) have been detected. The relative elemental abundances as well as energy spectra are invaluable tools to understand the origin and propagation of galactic cosmic rays – for excellent reviews on the topic see e.g. [151, 150]. In particular, stable secondary-to-primary ratios tell us about

the effective column density crossed by cosmic rays. The best measured of such ratios is B/C, shown in the left frame of Figure 4.3; another important ratio is the sub-Fe/Fe (i.e. (Si+Ti+V)/Fe). Moreover, radioactive species such as ^{10}Be, ^{14}C, ^{26}Al or ^{36}Cl, that present half-lives relevant for cosmic-ray propagation, give information on the time elapsed since production. The best measured unstable ratio is ^{10}Be/^{9}Be (see right frame of Figure 4.3), even though the data is deemed by huge uncertainties (both statistical and systematic). Section 4.5 deals with the prospects for measuring B/C and ^{10}Be/^{9}Be in the future and the corresponding consequences for cosmic-ray physics. Although cosmic-ray nuclei are not produced by DM annihilations or decays, this topic assumes particular importance in reducing the uncertainties associated to propagation throughout the Galaxy that affect the DM-induced fluxes of electrons/positrons and antiprotons. It is worth pointing out that recent experimental data from ATIC [174] and CREAM [175] show a hardening of the proton and helium spectra at a few TeV/n. This has important implications in the standard paradigm of cosmic rays [176, 177, 178] and is a topic to follow with particular attention in the following years. The Alpha Magnetic Spectrometer AMS-02 [179] will hopefully settle this and other open questions. AMS-02 is a large-acceptance spectrometer, to be installed at the International Space Station in 2011, designed to measure with unprecedent statistics cosmic-ray nuclei as heavy as iron ($Z \leq 26$) up to TeV/n energies. Good rejection capabilities will also enable precise determinations of the fluxes of electrons, positrons and antiprotons. Featuring a permanent magnet (instead of the initially projected superconducting magnet), AMS-02 will likely operate for more than the initially expected 3 years[2].

4.5 Paper III: Pinpointing cosmic ray propagation with the AMS-02 experiment[3]

The Alpha Magnetic Spectrometer AMS-02, which is scheduled to be deployed onboard the International Space Station in 2011, will be capable of measuring the composition and spectra of GeV-TeV cosmic rays with unprecedented precision. In this paper, we study how the projected measurements from AMS-02 of stable secondary-to-primary and unstable ratios (such as boron-to-carbon and beryllium-10-to-beryllium-9) can constrain the models used to describe the propagation of cosmic rays throughout the Milky Way. We find that within the context of fairly simple propagation models, all of the model parameters can be determined with high precision from the projected AMS-02 data. Such measurements are less constraining in more complex scenarios, however, which allow for departures from a power-law form for the diffusion coefficient, for example, or for inhomogeneity or stochasticity in the distribution and chemical abundances of cosmic ray sources.

4.5.1 Overview

Stable secondary-to-primary and unstable-to-stable secondary ratios are neatly complementary and have been used to constrain the properties of different propagation setups, e.g. [153]. Two recent studies in which limits on propagation parameters were derived

[2]The prospects for the performance of AMS-02 are studied in detail in the next Section and in Section 5.7.

[3]This Section is based on the article [3], done in collaboration with Dan Hooper and Melanie Simet.

using several data sets are [169] and [180]. In particular, [180] used GALPROP to draw 1, 2 and 3σ contour plots on the parameters D_{0xx}, L and α. There are some degeneracies between the parameters so that the present data do not point to a single propagation scheme. In the present work we focus on the expected performances of the Alpha Magnetic Spectrometer 02 AMS-02 [179] to be launched soon, in particular on the ratios B/C and ^{10}Be/^{9}Be, and investigate the impact that its data may have on our knowledge about galactic cosmic-ray propagation. Also using GALPROP numerical code, we address the question of whether AMS-02 will give us enough information to single out an unique propagation model and whether we will be able to distinguish between models with different assumptions (including power-law diffusion coefficients, reacceleration, convection and source distribution and abundance). Besides being a subject of extreme relevance itself for astrophysics, propagation plays a crucial role in interpreting cosmic-ray "anomalies" such as the rise in the positron fraction [162]. Furthermore, its detailed understanding will reduce the so-called astrophysical uncertainties on the calculation of cosmic-ray fluxes induced by non-standard primary sources like Dark Matter annihilations [181] or decay [182] or particle acceleration in the surroundings of pulsars [183].

4.5.2 Prospects for AMS-02[4]

The second and final version of the Alpha Magnetic Spectrometer AMS-02 [179, 184] is a large acceptance cosmic ray detector scheduled to be placed onboard the International Space Station in 2011. Over its mission duration of at least three years, it will measure with unprecedented statistics and precision the spectrum of cosmic rays over an energy range of approximately 100 MeV to 1 TeV [185, 186]. The AMS-02 instrument will be able to detect and identify nuclei as heavy as iron ($Z \lesssim 26$) with rigidity up to 4 TV [184], and separate isotopes of light elements (namely, H, He and Be) over a kinetic energy range of 0.5−10 GeV/n [187, 188, 189]. High precision measurements of the ratios B/C and sub-Fe/Fe (D/p, ^{3}He/^{4}He and ^{10}Be/^{9}Be) up to energies of ∼1 TeV/n (∼10 GeV/n) are anticipated. Due to a high level of proton rejection, positron and antiproton spectra will also be measured with unprecedented precision [190, 188].

The principal goals of the AMS-02 experiment [184, 191] include searches for primordial anti-matter among cosmic ray nuclei and signatures of Dark Matter annihilations or decays. Additionally, however, AMS-02 will contribute considerably to our understanding of the origin and propagation of galactic cosmic rays. In fact, being the largest acceptance (~ 0.45 m^{2}sr) space-based magnetic spectrometer, AMS-02 will bypass the atmospheric systematics which affect baloon-borne experiments and simultaneously feature an acceptance more than two orders of magnitude above the ~ 0.002 m^{2}sr of the PAMELA satellite [192]. Besides largely improved statistics, AMS-02 will also provide cosmic ray flux measurements up to $\sim$ TeV/n and separate Be isotopes up to $\sim$ 10 GeV/n while PAMELA can only reach a few hundred GeV/n and separate H and He isotopes. Therefore, a precise B/C ratio over a wide energy range and high energy ^{10}Be/^{9}Be measurements will be obtained. These data are extremely useful in constraining cosmic ray diffusion parameters. Of particular importante will be the ratio ^{10}Be/^{9}Be since as of today there are no data points above 3 GeV/n.

[4]Let us note that this paper was finished prior to the decision of replacing the superconducting magnet of AMS-02 by the permanent one. The consequences of this change in the measurement of CR nuclei still need to be studied.

Focusing on the ratios B/C, ^{10}Be/^{9}Be and $\bar{p}/p$, we can estimate the systematic and statistical errors of AMS-02. To begin, the rigidity resolution of AMS-02 will be $\Delta R/R \sim 1-2\%$ at $\sim$10 GV, for both protons and He nuclei, and around 20% at $\sim$0.5 TV ($\sim$1.0 TV) for protons (He) [193, 188, 194]. Assuming similar capabilities for heavier nuclei as well, we take a conservative value $\Delta R/R = 20\%$, which in the case of relativistic particles translates directly into a kinetic energy resolution $\Delta T/T \simeq 20\%$. Such resolution allows logarithmic bins of width $\log_{10} \frac{T+\Delta T/2}{T-\Delta T/2} \simeq 0.087$, or $11-12$ bins per decade. In the following we assume 10 bins per decade of kinetic energy regardless of the cosmic ray species.

In order to compute the statistical errors associated with the ratio N_i/N_j, we need the number of i and j particles detected,

$$N_i = \epsilon_i \, acc_i \, \Phi_i \, \Delta T \Delta t_i \quad ,$$

and likewise for j, ϵ_i being the efficiency, acc_i the geometrical acceptance of the instrument, and Δt_i the operating time. Then,

$$\frac{\Delta(N_i/N_j)_{stat}}{N_i/N_j} = \frac{1}{\sqrt{N_i}} + \frac{1}{\sqrt{N_j}} \quad .$$

The geometrical acceptance is a function of the particle type; we adopt $acc_B = acc_C = acc_{Be} = 0.45$ m^{2}sr [195, 184], $acc_p = 0.3$ m^{2}sr [189], and $acc_{\bar{p}} = 0.160(0.033)$ m^{2}sr for $\bar{p}$ momenta $1-16$ ($16-300$) GeV [196, 185, 195]. Following Ref. [194], we fix $\epsilon_B = \epsilon_C = 95\%$ and all other efficiencies to 100%. Lastly, we consider one year of operation.

As for systematics, we estimate the errors associated with the mismeasurement of the atomic number of cosmic ray nuclei. Using the full capabilities of the AMS-02 silicon tracker, the author of Ref. [194] used Monte Carlo simulations to estimate the level of misidentifications, finding fewer than one percent for $2 \leq Z \leq 11$. Conservatively, we take

$$\frac{(\Delta N_B)_{syst}}{N_B} = \frac{(\Delta N_C)_{syst}}{N_C} = 1\% \quad .$$

The ^{10}Be/^{9}Be measurement, on the other hand, is more delicate since it relies not only on charge, but also mass separation. From Ref. [197], we take a mean mass resolution for Be of $\Delta m/m \sim 2.5\%$. Requiring a separation of consecutive isotopes within 0.5 atomic mass units, this mass resolution results in misidentification of ^{9}Be as ^{10}Be and vice-versa less often than $f \sim 2.275\%$. Hence we use a systematic error for $N_{^{10}Be}$ given by

$$\frac{(\Delta N_{^{10}Be})_{syst}}{N_{^{10}Be}} = \left| -f + f \, \frac{N_{^{9}Be}}{N_{^{10}Be}} \right| \quad ,$$

and analogously for $N_{^{9}Be}$. Clearly, the systematics become unacceptable when either $f \, N_{^{9}Be}/N_{^{10}Be}$ or $f \, N_{^{10}Be}/N_{^{9}Be}$ approaches unity. Finally, for the antiproton-to-proton ratio, the dominant fraction of the systematic error comes from the $\bar{p}$ measurement. In order to confidently identify antiprotons, the large background of protons and electrons must be rejected with high efficiency. In the multi-GeV energy range, at which $p/\bar{p} \sim 10^4$ ($e^-/\bar{p} \sim 10^2$) [198, 196], the rejection power expected for AMS-02 is $p : \bar{p} \sim 10^5 - 10^6$ ($e^- : \bar{p} \sim 10^3 - 10^4$) [196, 195], leading to a systematic error of order $\frac{10^4}{10^5 - 10^6} = 1 - 10\%$

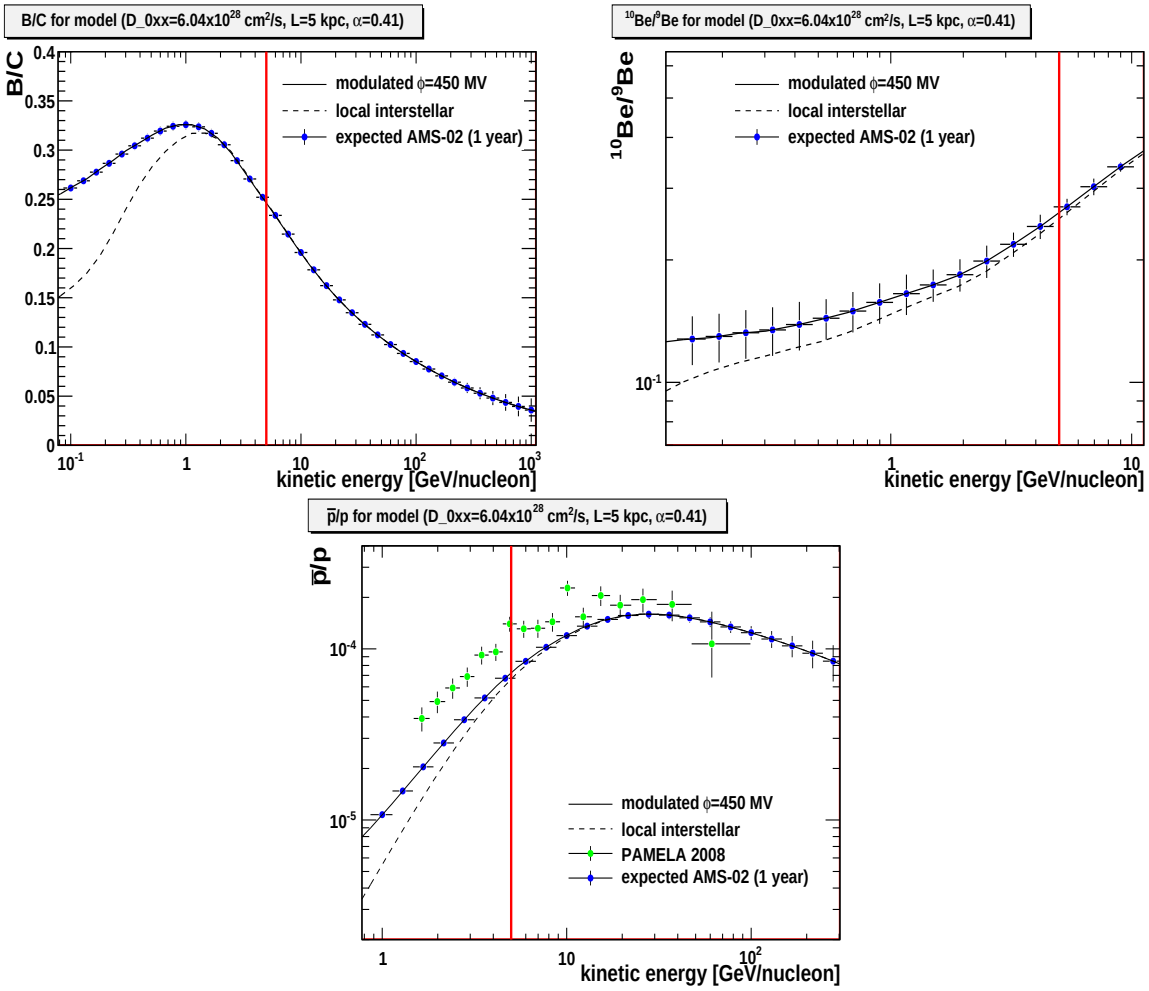

Figure 4.4: Projections for ability of the AMS-02 experiment to measure selected stable secondary-to-primary and unstable cosmic ray ratios: B/C, ^{10}Be/^{9}Be and $\bar{p}/p$. As a benchmark, we have considered the best-fit model of Ref. [180]. Systematic and statistical uncertainties are included in the AMS-02 error bars, and 1 year of data taking is assumed. The thick vertical line indicates the energy cut, $T > 5$ GeV/n, imposed to reduce the impact of solar modulation on our results. In the lower frame, the PAMELA measurement of the antiproton-to-proton ratio [198] is also shown.

$(\frac{10^2}{10^3-10^4} = 1 - 10\%)$. Consequently, we take

$$\frac{(\Delta N_{\bar{p}})_{syst}}{N_{\bar{p}}} = 5\% \quad .$$

We add all of the systematic errors discussed in this paragraph in quadrature to the statistical uncertainties.

At this point we can forecast the AMS-02 measurements of various cosmic ray spectra. As a benchmark model, we adopt the best-fit propagation parameters found in Ref. [180]: $D_{0xx} = 6.04 \times 10^{28}\mathrm{cm}^2/\mathrm{s}$ (at a reference rigidity of $R_0 = 4$ GV), $L = 5$ kpc, $\alpha = 0.41$, $v_A = 36$ km/s, and no significant convection. The remaining specifications are as in galdef_50p_599278 file [167], including a distribution of cosmic ray sources optimized to meet EGRET gamma ray data, and a double power-law injection spectrum – with indices $\gamma_1 = 1.82$ and $\gamma_2 = 2.36$ below and above $\tilde{R}_0 = 9$ GV – to reproduce low-energy cosmic ray data. The ratios B/C, ^{10}Be/^{9}Be and $\bar{p}/p$ corresponding to this model (hereafter the *true model*) and calculated with GALPROP v50.1p are plotted in Figure 4.4 along

with the projected error bars of the AMS-02 instrument (including both systematic and statistical uncertainties). For detailed simulations of the capabilities of AMS-02, we refer the reader to Ref. [187, 197] and references therein.

As shown in the lower frame of Figure 4.4, the antiproton-to-proton ratio for the true model is somewhat lower than the values measured by the PAMELA collaboration [198], especially at low energies. Solar modulation, however, may have a significant impact on this ratio at such energies. As the impact of solar modulation varies with respect to the time period observed, the PAMELA antiproton measurement is not necessarily expected to mimic that to be measured by AMS-02. To reduce the dependence on this effect, we apply an energy cut $T > 5$ GeV/n throughout our analysis. In our calculations, we have modulated the cosmic ray spectra with $\phi_F = 450$ MV. Common values of the modulation parameter ϕ_F range from a few hundred MV up to over a GV (e.g. [199]); however, 450 MV is a reasonable value for data taken around a solar minimum which presumably will be the case of AMS-02 first year[5]. In any case, we stress that our results do not depend much on the solar modulation parameter since only energies above 5 GeV/n are considered. In the remainder of the work, unless otherwise stated, we shall use the modulated data set presented in Figure 4.4 to perform our analysis.

4.5.3 Constraining propagation models

In this subsection, we attempt to estimate how well the projected AMS-02 measurements described in the previous subsection will be able to constrain the propagation model parameter space. For the moment, we fix the Alfvén speed to $v_A = 36$ km/s, neglect the effects of convection ($V_{c,0} = dV_c/dz = 0$), and proceed in a fashion similar to Ref. [180] to run GALPROP 245 times, in a 7x7x5 grid of the parameters (D_{0xx}, L, α) over the following ranges: $D_{0xx} = 4.54 - 8.03 \times 10^{28}$ cm^2/s, $L = 3.5 - 6.5$ kpc and $\alpha = 0.39 - 0.43$. Linearly-(Logarithmically-)spaced gridpoints were implemented for L, α (D_{0xx}). An infill of 3 points between consecutive gridpoints (corresponding to a reduction of the spacing by a factor 4) was performed and the relevant cosmic ray ratios for each additional propagation model were obtained through 3-dimensional interpolation of the GALPROP runs. The extended grid includes 25x25x17=10,625 different parameter sets. For each set, we calculate the χ^2 using the projected B/C and ^{10}Be/^{9}Be AMS-02 measurements.

Using the above described parameter scan and the projected B/C and ^{10}Be/^{9}Be presented in Figure 4.4, we show in Figure 4.5 the resulting 1, 2 and 3σ regions in the L vs. D_{0xx} plane where we have marginalized over α. From this figure, one can immediately identify the complementarity between stable secondary-to-primary and unstable ratio measurements. Whereas stable secondary-to-primary ratios provide an approximate measure of the quantity L/D_{0xx}, unstable ratios help to determine L^2/D_{0xx} (for a fixed value of α). The combination of B/C and ^{10}Be/^{9}Be precise measurements can thus provide a determination of both L and D_{0xx}. Although the projected $\bar{p}/p$ data, shown in the lower frame of Figure 4.4, introduce some additional information into the analysis, it provides a constraint region with a similar shape but broader than that provided by the B/C data. For this reason, we do not include $\bar{p}/p$ in our chi-squares.

Figure 4.6 shows, for the same scan of propagation parameters as used in Figure 4.5, the 1, 2 and 3σ contours from the combination of B/C and ^{10}Be/^{9}Be projected measurements presented in Figure 4.4. In each frame we have marginalized over the

[5]This paper was finished before the successive delays in AMS-02 mission.

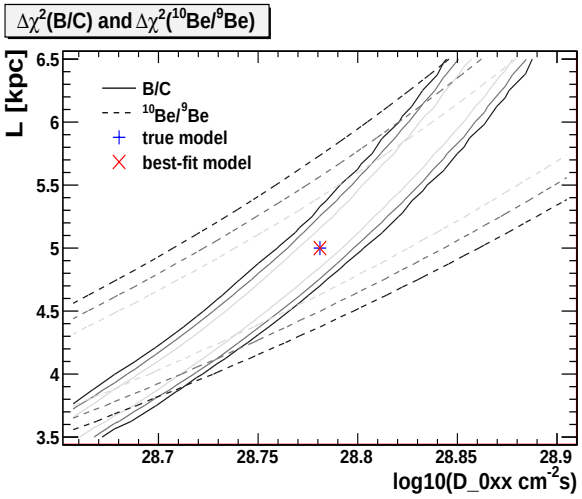

Figure 4.5: Constraints on cosmic ray propagation parameters from the projected AMS-02 B/C and ^{10}Be/^{9}Be measurements presented in Figure 4.4. The solid lines delimit 1, 2, and 3 σ regions using the B/C data set, whereas dashed lines refer to ^{10}Be/^{9}Be. Here, the propagation parameters were varied in the ranges $D_{0xx} = 4.54-8.03\times10^{28}$ cm^2/s, $L = 3.5-6.5$ kpc and $\alpha = 0.39-0.43$. We have assumed $v_A = 36$ km/s, $V_{c,0} = dV_c/dz = 0$, and have marginalized over α.

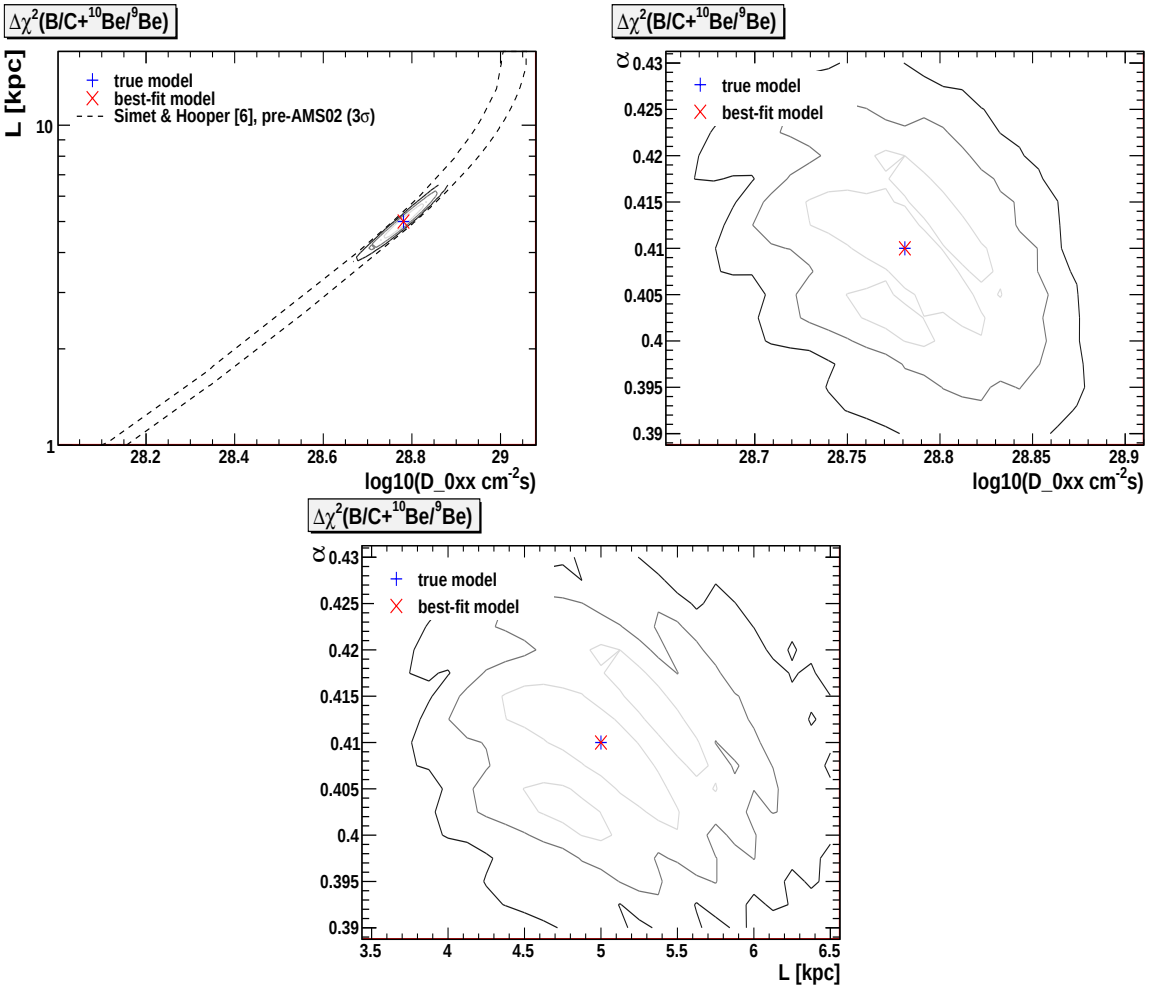

Figure 4.6: Regions consistent (within 1, 2 and 3σ) with projected B/C and ^{10}Be/^{9}Be AMS-02 data from Figure 4.4 in the L vs. D_{0xx}, α vs. D_{0xx}, and α vs. L planes. Here, the propagation parameters were varied in the ranges $D_{0xx} = 4.54 - 8.03 \times 10^{28}$ cm^2/s, $L = 3.5 - 6.5$ kpc and $\alpha = 0.39 - 0.43$. We have assumed $v_A = 36$ km/s, $V_{c,0} = dV_c/dz = 0$, and have marginalized in each frame over the parameter not shown. In the top left frame we show in dashed the 3σ contour from Ref. [180].

$B/C + {}^{10}\mathrm{Be}/{}^{9}\mathrm{Be}$ best-fit model ($N_{dof} = 21$)			
v_A	dV_c/dz	$(D_{0xx}\,[10^{28}\mathrm{cm}^2\mathrm{s}]\,,\, L\,[\mathrm{kpc}]\,,\, \alpha)$	χ^2/N_{dof}
36	0	(6.04, 5.000, 0.4100)	0
15	0	(6.04, 8.000, 0.4850)	1.36
0	0	(6.04, 8.997, 0.5000)	2.17
0	10	(3.89, 5.623, 0.5000)	12.78

Table 4.1: Best-fit models and reduced chi-squares for the combined B/C+^{10}Be/^{9}Be projected AMS-02 data set, for various combinations of reacceleration and convection parameters. In each case, the data set used is that presented in Figure 4.4. Propagation parameters were varied in the ranges $D_{0xx} = 0.57 - 19.5 \times 10^{28}$ cm^2/s, $L = 1.22 - 20.48$ kpc and $\alpha = 0.32 - 0.50$. v_A and dV_c/dz are given in units of km/s and km/s/kpc, respectively, and $V_{c,0} = 0$. The presence of significant convection will be highly observable to AMS-02. To a lesser extent, the value of the Alfvén velocity will also be testable.

parameter not shown. As this figure demonstrates, the projected AMS-02 measurements of B/C and ^{10}Be/^{9}Be are sufficient (within the context of the simple models presently being considered) to determine the underlying propagation parameters with an accuracy of $\Delta D_{0xx} \sim 1.4 \times 10^{28}$ cm^2/s, $\Delta L \sim 1.0$ kpc, and $\Delta\alpha \sim 0.02$ (at 1σ). This precision is much greater than that obtained with present (pre-AMS-02) data; see Refs. [180, 169]. In particular the degeneracy between D_{0xx} and L is broken as can be seen in the upper frame of Figure 4.6 where we have overplotted in dashed the 3σ contour from Ref. [180].

Thus far, we have not considered any effects of convection and/or variations in the Alfvén velocity from our default value of $v_A = 36$ km/s. As the quantity and quality of cosmic ray data improves, however, it will become increasingly possible to test these assumptions, and determine the related parameters. In order to study this possibility, we have repeated the procedure described in the previous paragraphs using the following values for the Alfvén velocity and the convection velocity: $(v_A[\mathrm{km/s}], dV_c/dz[\mathrm{km/s/kpc}]) = \{(36, 0), (15, 0), (0, 0), (0, 10)\}$, while leaving $V_{c,0} = 0$. We have focused here on Alfvén velocities smaller than the reference value 36 km/s since some studies (e.g. Ref. [169]) find that lower values of v_A are preferred. For each combination of v_A and dV_c/dz, we ran 343 GALPROP jobs in a 7x7x7 grid with ranges $D_{0xx} = 0.57 - 19.5 \times 10^{28}$ cm^2/s, $L = 1.22 - 20.48$ kpc and $\alpha = 0.32 - 0.50$. Linearly-(Logarithmically-)spaced gridpoints were implemented for α (D_{0xx}, L). An infill of 3 points between consecutive gridpoints was applied resulting in 25x25x25=15,625 different models. Using the projected B/C and ^{10}Be/^{9}Be data sets shown in Figure 4.4, we found the best-fit models given in Table 4.1. As greater departures from our default assumptions are considered, the fits to the projected data become considerably worse. In particular, even modest ($\sim$10 km/s/kpc) amounts of convection lead to very poor fits to the projected data. Large variations in v_A also lead to observable effects, thus enabling AMS-02 to be sensitive to the details of diffusive reacceleration.

It is well-known that propagation setups with lower Alfvén velocities yield lower B/C at energies 1$-$100 GeV/n [153, 169], and that this can be compensated by an increase of L/D_{0xx}. But, since reacceleration has negligible influence at high energies, the increase in L/D_{0xx} must be accompanied by a larger value of α so that B/C is sufficiently suppressed in the high energy range. On the other hand, lower values of v_A enhance ^{10}Be/^{9}Be at multi-GeV energies which is also compensated by an increase of L/D_{0xx}. This behaviour is illustrated in Figure 4.7 where we sketch the 3σ contours from the ^{10}Be/^{9}Be projected data shown in Figure 4.4 for different values of v_A. Here, we have used the parameter scan described in the previous paragraph, and marginalized over α.

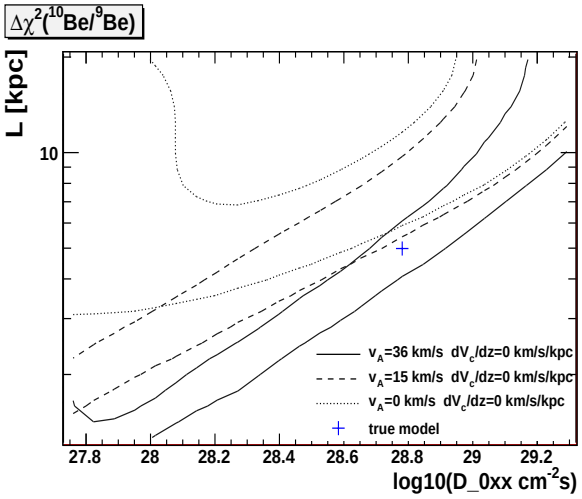

Figure 4.7: The effect of changes in the Alfvén velocity, v_A, in the ^{10}Be/^{9}Be 3σ region projected onto the L vs. D_{0xx} plane. Solid, dashed and dotted lines correspond to $v_A = 36, 15, 0$ km/s, respectively. Propagation parameters were varied in the ranges $D_{0xx} = 0.57 - 19.5 \times 10^{28}$ cm^2/s, $L = 1.22 - 20.48$ kpc and $\alpha = 0.32 - 0.50$, and the data set used is that presented in Figure 4.4. Here, we have neglected convection, and marginalized over α. A preference for larger L and lower D_{0xx} is evident as v_A decreases.

4.5.4 Breaking the assumptions

In order to make the questions addressed in this study tractable, we have thus far relied on a number of simplifying assumptions. In particular, we have assumed homogeneity of the diffusion coefficient D_{xx} over the volume of the diffusion zone, considered cylindrical symmetry for the system, and adopted a smooth distribution of cosmic ray sources with universal injected chemical composition and spectra. While such assumptions are reasonable and have been useful up to this point in time, they will eventually have to be discarded or revised as they break down under the increasing precision of future cosmic ray data. In this subsection, we study a few of the possible ways in which data from AMS-02 could potentially require us to revise the assumptions commonly made in modelling galactic cosmic ray production and propagation.

We first consider fluctuations in the recent cosmic ray injection rate. Cosmic ray sources are indeed believed to be of stochastic nature both in space and time − therefore, one does not expect the rate at which cosmic rays are introduced into the Milky Way to be homogeneous or constant over time. Galactic supernova remnants (SNR), in particular, are created at a typical rate of ~ 0.03 per year, and stay active for $\sim 10^4 - 10^5$ yr [200]. Depending on whether such an event has taken place recently and nearby, the observed cosmic ray spectrum will vary accordingly. The GALPROP code gives the possibility to model such stochastic fluctuations [167, 201, 202] by solving the transport equation in a three-dimensional spatial grid (unlike thus far used in this work) and defining two further parameters: the average time t_{SNR} between consecutive SNR events occuring in a kpc^3 volume around us, and the time interval t_{CR} during which the SNR keeps injecting cosmic rays. We adopt $t_{SNR} = 10^4$ yr − corresponding to ~ 0.03 SNR events per year for a standard distribution of sources −, $t_{CR} = 10^4$ yr and run GALPROP with all other parameters as in the true model of subsection 4.5.2. In the upper plots of Figure 4.8 we show with thin lines the resulting B/C and ^{10}Be/^{9}Be for different positions in the local galactic disk. For comparison, the central thick lines denote the ratios obtained at $r = 8.5$ kpc in the true propagation model with no stochastic SNR events (but ran

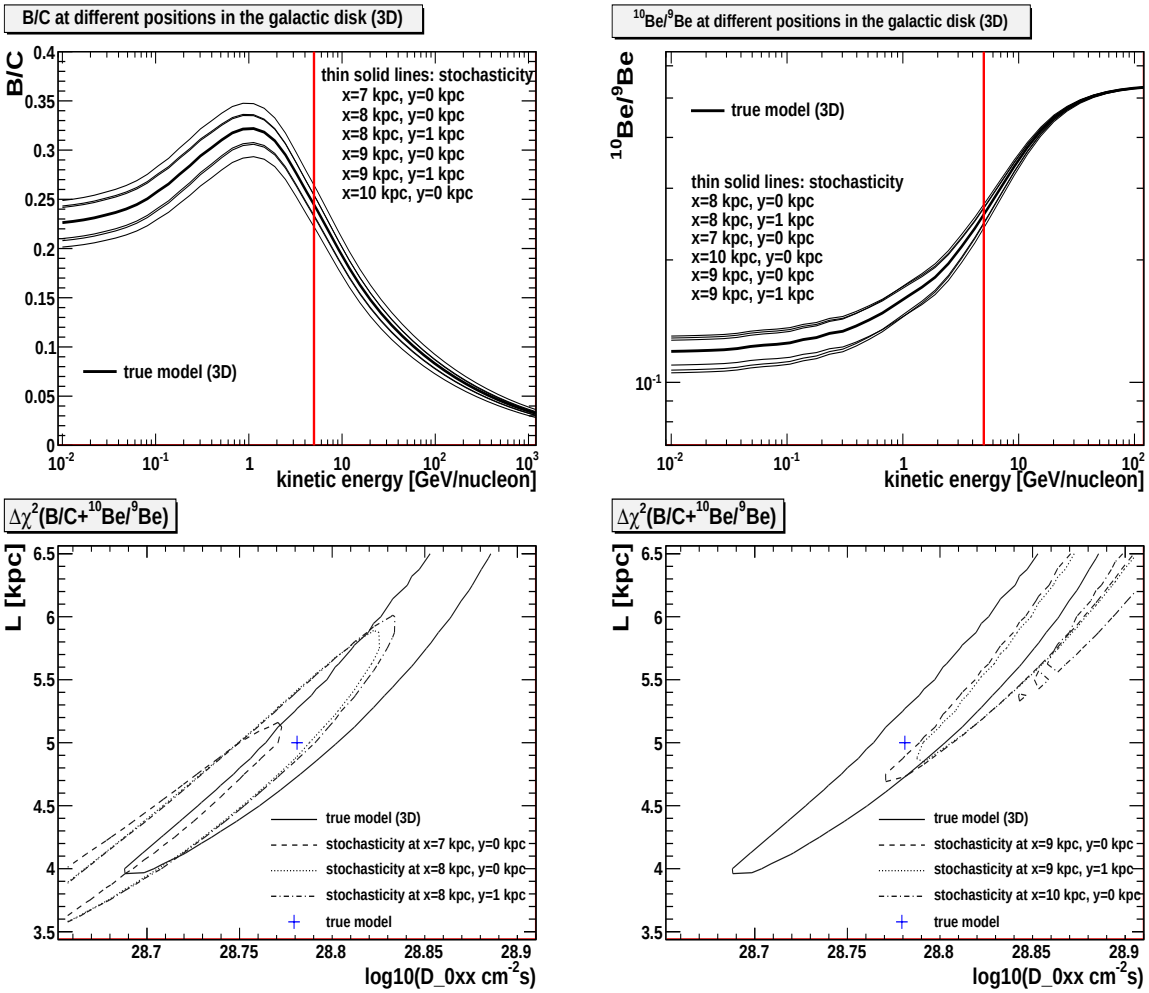

Figure 4.8: The impact of the stochastic nature of sources in the injection of cosmic rays on the B/C and ^{10}Be/^{9}Be ratios (top frames), and on the inferred propagation parameters (bottom frames). In the top frames we show the ratios in different positions in the local galactic disk – the legend is ordered according to the values of the thin lines at low kinetic energies. In the bottom frames we have marginalized over α and the legend indicates the propagation model used to simulate AMS-02 data; in all cases $v_A = 36$ km/s, $V_{c,0} = dV_c/dz = 0$, and the propagation parameters were varied in the ranges $D_{0xx} = 4.54 - 8.03 \times 10^{28}$ cm^2/s, $L = 3.5 - 6.5$ kpc and $\alpha = 0.39 - 0.43$. We have assumed a rate of 0.03 galactic supernova per year and show 3σ contours in the lower frames. Stochastic variations limit our ability to deduce the underlying cosmic ray propagation model from stable secondary-to-primary and unstable ratio measurements. See the text for more details.

with three spatial dimensions). Using the thin lines in the upper frames of Figure 4.8 to project AMS-02 data, we show in the lower plots how such variations impact the (3σ) propagation parameter space inferred. Here, $v_A = 36$ km/s, $V_{c,0} = dV_c/dz = 0$, the propagation parameters were varied in the ranges $D_{0xx} = 4.54 - 8.03 \times 10^{28}$ cm^2/s, $L = 3.5 - 6.5$ kpc and $\alpha = 0.39 - 0.43$, and we have marginalized over α in the lower frames of Figure 4.8. Additionally, we provide in Table 4.2 the best-fit configurations and reduced chi-squares. At some level, stochasticity of cosmic ray sources ultimately limits our ability to deduce the underlying propagation model from stable secondary-to-primary and unstable ratio measurements.

Another example we have considered was the possibility that the diffusion coefficient does not follow a simple power-law, as assumed in the preceding subsections. A simple extension of the power-law form is a broken power-law, with indices α_1 and α_2 below and above a reference rigidity, R_0. To explore this possibility, we adopt a model identical to our previous benchmark model (see subsection 4.5.2), but with diffusion coefficient

$B/C + {}^{10}\mathrm{Be}/{}^{9}\mathrm{Be}$ best-fit model ($N_{dof} = 21$)			
broken assumption	specification	$(D_{0xx}\ [10^{28}\mathrm{cm}^2\mathrm{s}]\ ,\ L\,[\mathrm{kpc}]\ ,\ \alpha)$	χ^2/N_{dof}
true model (3D) (*)		(6.04, 5.000, 0.4175)	0.03 [0.06]
Stochasticity (*)	$x = 7$ kpc, $y = 0$ kpc	(4.76, 4.000, 0.4000)	0.03 [1.49]
	$x = 8$ kpc, $y = 0$ kpc	(5.24, 4.375, 0.4125)	0.02 [0.58]
	$x = 8$ kpc, $y = 1$ kpc	(5.24, 4.375, 0.4125)	8×10^{-3} [0.24]
	$x = 9$ kpc, $y = 0$ kpc	(7.48, 6.375, 0.4275)	0.05 [0.36]
	$x = 9$ kpc, $y = 1$ kpc	(7.66, 6.500, 0.4250)	0.06 [0.55]
	$x = 10$ kpc, $y = 0$ kpc	(8.03, 6.500, 0.4300)	0.41 [2.85]
Diffusion Coefficient	$\alpha_1 = 0.39, \alpha_2 = 0.43, R_0 = 4$ GV	(6.18, 5.250, 0.4300)	0.07 [0.12]
	$\alpha_1 = 0.39, \alpha_2 = 0.43, R_0 = 10$ GV	(5.76, 5.000, 0.4300)	0.03 [0.19]
	$\alpha_1 = 0.39, \alpha_2 = 0.43, R_0 = 10^2$ GV	(6.04, 5.125, 0.4000)	0.13 [0.75]
	$\alpha_1 = 0.39, \alpha_2 = 0.43, R_0 = 10^3$ GV	(6.04, 5.000, 0.3900)	8×10^{-4} [5×10^{-4}]
	$\alpha_1 = 1/3, \alpha_2 = 1/2, R_0 = 4$ GV(+)	(5.21, 4.446, 0.5000)	0.75 [1.18]
	$\alpha_1 = 1/3, \alpha_2 = 1/2, R_0 = 10$ GV(+)	(5.21, 5.000, 0.4775)	0.63 [4.75]
	$\alpha_1 = 1/3, \alpha_2 = 1/2, R_0 = 10^2$ GV(+)	(6.04, 5.623, 0.3725)	2.45 [16.1]
	$\alpha_1 = 1/3, \alpha_2 = 1/2, R_0 = 10^3$ GV(+)	(6.04, 5.000, 0.3275)	0.12 [0.07]
Source Abundances	${}^{12}\mathrm{C} \times 1.2$	(6.80, 5.500, 0.4200)	0.02 [0.26]
	${}^{12}\mathrm{C} \times 0.8$	(5.11, 4.375, 0.3975)	0.04 [0.75]
	$({}^{12}\mathrm{C}, {}^{14}\mathrm{N}, {}^{16}\mathrm{O}) \times 2$	(6.18, 4.875, 0.4125)	0.03 [0.27]
Source Distribution	SNR distribution	(5.76, 4.625, 0.4000)	0.04 [0.05]
	pulsar distribution	(5.36, 4.750, 0.3925)	0.12 [0.39]
	reference + nearby source (*)	(6.33, 5.250, 0.4200)	0.03 [0.10]

Table 4.2: Best-fit models and reduced chi-squares for the combined B/C+^{10}Be/^{9}Be data set, assuming different variations to the underlying true model. For each model, an AMS-02 data set was projected according to the corresponding broken assumption. The presented best-fit models were found for $v_A = 36$ km/s and $V_{c,0} = dV_c/dz = 0$. For configurations marked with (+) the propagation parameters were varied in the ranges $D_{0xx} = 0.57 - 19.5 \times 10^{28}$ cm^2/s, $L = 1.22 - 20.48$ kpc and $\alpha = 0.32 - 0.50$; for the remaining cases the ranges of the parameter scan were $D_{0xx} = 4.54 - 8.03 \times 10^{28}$ cm^2/s, $L = 3.5 - 6.5$ kpc and $\alpha = 0.39 - 0.43$. Configurations marked with (*) have been run in GALPROP with three spatial dimensions; for comparison we also present the best-fit model in the case of generating AMS-02 data with the 3-dimensional true model. In the last column the chi-squares in squared brackets were obtained using AMS-02 projected proton flux in addition to the ratios B/C and ^{10}Be/^{9}Be ($N_{dof} = 42$).

power-law indices of $\alpha_1 = 0.39$ and $\alpha_2 = 0.43$ below and above the reference rigidity, $R_0 = \{4, 10, 10^2, 10^3\}$ GV, while fixing $D_{xx}(4\ \mathrm{GV}) = 6.04 \times 10^{28}\mathrm{cm}^2/s$. Next, we once again use GALPROP to compute cosmic ray fluxes and ratios in these models and make projections for the observations of AMS-02. Table 4.2 shows the results found when we fit these projected data using propagation models without a broken power-law diffusion coefficient. In particular, we use the parameter scan with $v_A = 36$ km/s, $V_{c,0} = dV_c/dz = 0$, and ranges $D_{0xx} = 4.54 - 8.03 \times 10^{28}$ cm^2/s, $L = 3.5 - 6.5$ kpc and $\alpha = 0.39 - 0.43$. Disappointingly, good fits are found in each case, thus revealing that small variations in α are unlikely to be discernable from AMS-02 data. In order to verify whether more extreme variations in α are testable, we consider a broken power law for D_{0xx} with indices $\alpha_1 = 1/3$ and $\alpha_2 = 1/2$, and $R_0 = \{4, 10, 10^2, 10^3\}$ GV, again fixing $D_{xx}(4\ \mathrm{GV}) = 6.04 \times 10^{28}\mathrm{cm}^2/s$. The index 1/3 (1/2) corresponds to a Kolmogorov (Kraichman) power spectrum of magnetic inhomogeneities. Proceeding in the same fashion as before but using the scan of propagation parameters with ranges $D_{0xx} = 0.57 - 19.5 \times 10^{28}$ cm^2/s, $L = 1.22 - 20.48$ kpc and $\alpha = 0.32 - 0.50$, we obtain the best-fit configurations reported in Table 4.2. Acceptable fits (and wrong best-fit parameters) result in all cases except for $R_0 = 10^2$ GV. Therefore, if α changes suddenly from 1/3 to 1/2 well inside AMS-02 high energy range − notice that 10^2 GV corresponds to a proton (^{10}B) kinetic energy per nucleon of 99.1 (49.1) GeV/n −, the upcoming data on stable secondary-to-primary and unstable ratios should be sufficient to detect the presence of such a drastic break.

In a similar way, we can test the sensitivity provided by the projected AMS-02 data to the source composition and distribution. A reasonable possibility is that nearby cosmic ray sources produce various species of cosmic rays in relative quantities which differ from

best-fit model				
	$B/C + {}^{10}\mathrm{Be}/{}^{9}\mathrm{Be}\,(N_{dof}=21)$		$B/C + {}^{10}\mathrm{Be}/{}^{9}\mathrm{Be} + p\,(N_{dof}=42)$	
γ_2	$(D_{0xx}\,[10^{28}\mathrm{cm}^2\mathrm{s}]\,,\,L\,[\mathrm{kpc}]\,,\,\alpha)$	χ^2/N_{dof}	$(D_{0xx}\,[10^{28}\mathrm{cm}^2\mathrm{s}]\,,\,L\,[\mathrm{kpc}]\,,\,\alpha)$	χ^2/N_{dof}
2.26	(6.04, 5.000, 0.4100)	0.13	(7.00, 5.000, 0.3500)	2.55
2.31	(6.04, 5.000, 0.4100)	0.03	(7.00, 5.623, 0.3875)	0.66
2.34	(6.04, 5.000, 0.4100)	5×10^{-3}	(7.00, 5.623, 0.3875)	0.50
2.38	(6.04, 5.000, 0.4100)	5×10^{-3}	(6.04, 5.000, 0.4100)	0.56
2.41	(6.04, 5.000, 0.4100)	0.03	(6.04, 5.623, 0.4475)	1.63
2.46	(6.04, 5.000, 0.4100)	0.14	(6.04, 5.623, 0.4550)	4.61

Table 4.3: Best-fit models and reduced chi-squares for the combined B/C+^{10}Be/^{9}Be and B/C+^{10}Be/^{9}Be+p data sets, assuming different high energy injection indices γ_2. For each model, the AMS-02 data were projected according to the corresponding γ_2. The presented best-fit models were found for $v_A = 36$ km/s, $V_{c,0} = dV_c/dz = 0$, $\gamma_1 = 1.82$, $\gamma_2 = 2.36$ and $\tilde{R}_0 = 9$ GV. The propagation parameters were varied in the ranges $D_{0xx} = 0.57 - 19.5 \times 10^{28}$ cm^2/s, $L = 1.22 - 20.48$ kpc and $\alpha = 0.32 - 0.50$.

the average over the Milky Way (and differ from the default GALPROP assumptions). Unfortunately, Table 4.2 shows that we have very little sensitivity to a $\pm 20\%$ change in the source abundance of carbon nor even to a factor 2 in the source abundances of C, N and O. In all cases, very good fits to AMS-02 projected B/C and ^{10}Be/^{9}Be are obtained, although the apparent best-fit parameters are not necessarily the parameters of the true model, opening the possibility that we may infer a very well-fit, but incorrect, cosmic ray propagation model from AMS-02 data. We illustrate such effect for the case of a 20% enhanced source abundance of C: Figure 4.9 shows the 1, 2 and 3σ contours using $v_A = 36$ km/s, $V_{c,0} = dV_c/dz = 0$, and propagation parameters in the ranges $D_{0xx} = 4.54 - 8.03 \times 10^{28}$ cm^2/s, $L = 3.5 - 6.5$ kpc and $\alpha = 0.39 - 0.43$. In each frame we have marginalized over the parameter not shown.

Moreover, we have studied the impact of varying the distribution of cosmic ray sources. The usual parameterization optimized to reproduce EGRET gamma-ray data follows $Q_{inj} \propto (r/r_\odot)^\eta \exp(-\xi \frac{r-r_\odot}{r_\odot} - \frac{|z|}{0.2\ \mathrm{kpc}})$ with $\eta = 0.5$, $\xi = 1.0$ and a cut-off radius $r_{max} = 20$ kpc [153]. Following Ref. [167], we consider alternative scenarios, namely a supernova remnant-like distribution (with $\eta = 1.69$, $\xi = 3.33$), and a pulsar-like distribution (with $Q_{inj} \propto \cosh(r_\odot/r_c) \exp(-\frac{|z|}{0.2\ \mathrm{kpc}})/\cosh(r/r_c)$, $r_c = 3.5$ kpc). As indicated in Table 4.2, high quality fits are found in both cases; and again the best-fit models do not coincide with the parameters of the true model. The same holds in the case of the usual parameterization with $\eta = 0.5$, $\xi = 1.0$ and $r_{max} = 20$ kpc plus a nearby source that we put at $(x, y, z) = (8.66, 0, 0)$ kpc (Geminga approximate position). We are, therefore, forced to conclude that AMS-02 data will likely be insensitive to different assumptions pertaining to the source composition and distribution, and that the values of the propagation parameters may even be potentially misinferred as a result.

Now, it is interesting to check if any of the best-fit configurations listed in Table 4.2 induce cosmic ray fluxes that conflict with the corresponding true model. For such, besides B/C and ^{10}Be/^{9}Be, we also project the one-year AMS-02 proton flux, in the range 5 GeV $-$ 1 TeV and with 3% of assumed systematics. In the last column of Table 4.2 we show in squared brackets the reduced chi-squares of the combined data set including B/C, ^{10}Be/^{9}Be and the proton flux for the best-fit models previously found using B/C and ^{10}Be/^{9}Be only. In some cases $-$ notably when assuming a break from 1/3 to 1/2 in the diffusion coefficient index $-$ the proton flux helps discriminating wrong non-minimal assumptions. In the remaining situations, however, the misinference of propagation parameters discussed in the previous paragraphs still persists.

Finally, we turn our attention to the source spectral index. Up to this point the

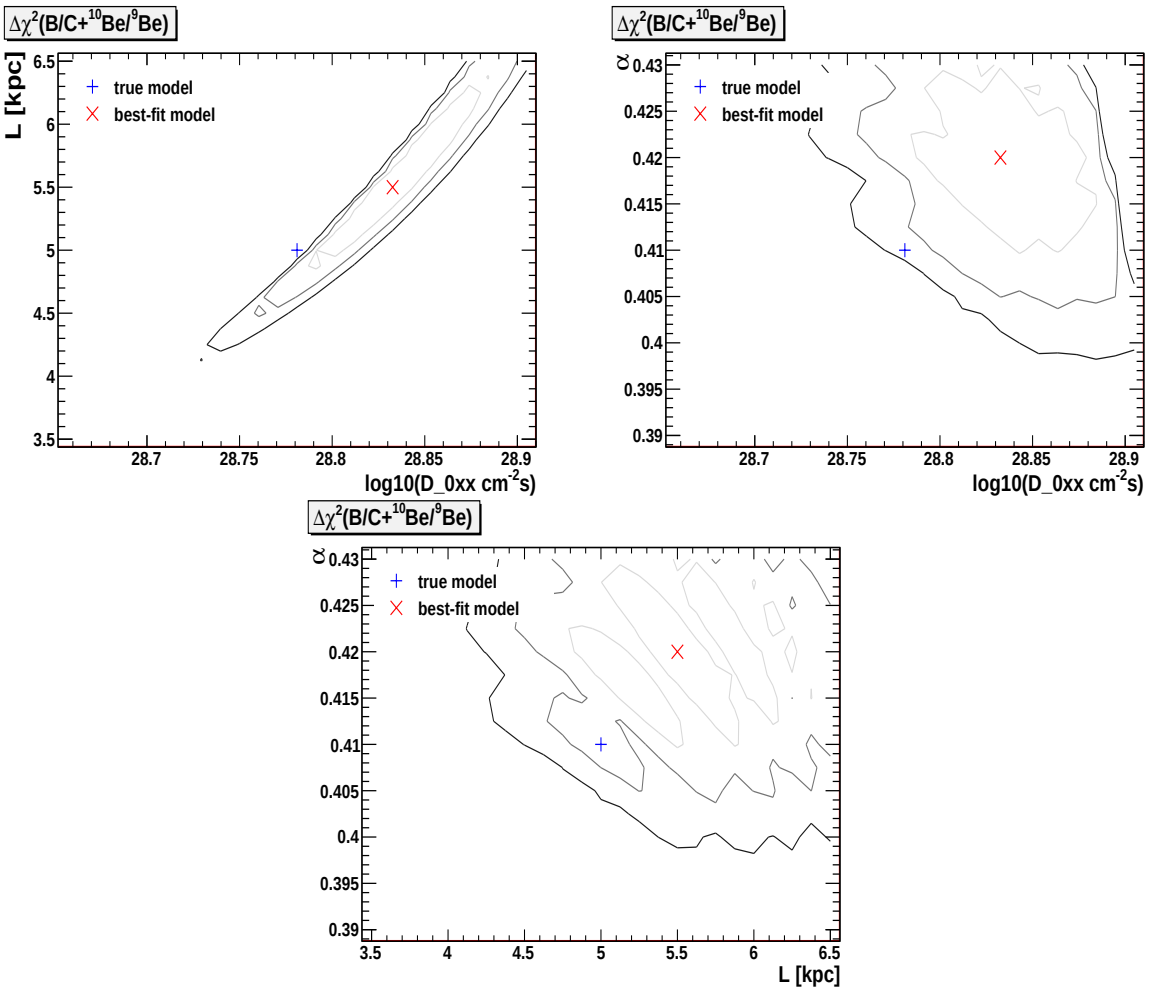

Figure 4.9: Regions consistent (within 1, 2 and 3σ) with projected B/C and ^{10}Be/^{9}Be AMS-02 data in the L vs. D_{0xx}, α vs. D_{0xx}, and α vs. L planes. Here, the AMS-02 data were projected assuming a true model with a source abundance of ^{12}C 20% higher than in the default model of Ref. [180]. Propagation parameters were varied in the ranges $D_{0xx} = 4.54 - 8.03 \times 10^{28}$ cm^2/s, $L = 3.5 - 6.5$ kpc and $\alpha = 0.39 - 0.43$. We have assumed $v_A = 36$ km/s, $V_{c,0} = dV_c/dz = 0$, and have marginalized in each frame over the parameter not shown. Notice that, although a good fit was found to the data in this case, the apparent best-fit parameters are significantly different from the values of the true model.

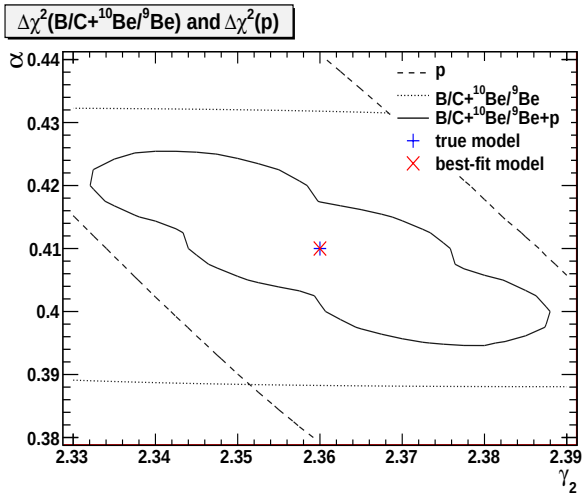

Figure 4.10: Inferred parameter regions (within 3σ) in the plane α vs. γ_2. The dashed (dotted) [solid] lines refer to the case where the AMS-02 projected data set consisted of the proton flux (B/C and ^{10}Be/^{9}Be) [proton flux, B/C and ^{10}Be/^{9}Be]. Here, the propagation parameters were varied in the ranges $D_{0xx} = 4.54 - 8.03 \times 10^{28}$ cm^2/s, $\gamma_2 = 2.33 - 2.39$ and $\alpha = 0.38 - 0.44$. We have assumed $v_A = 36$ km/s, $V_{c,0} = dV_c/dz = 0$, and have marginalized over D_{0xx}. The complementarity between the ratios B/C and ^{10}Be/^{9}Be and the proton flux is evident.

injection spectrum at the sources was assumed to be a double power law in rigidity with indices $\gamma_1 = 1.82$ and $\gamma_2 = 2.36$, and a break $\tilde{R}_0 = 9$ GV as mentioned in subsection 4.5.2. We now release this assumption by taking several values for γ_2 − the low energy rigidity index γ_1 and the break $\tilde{R}_0$ are kept fixed since we are focussing on high energy data only. Proceeding as earlier, we generate the projected AMS-02 data for each true model and then find the best-fit configuration using only B/C and ^{10}Be/^{9}Be or including also the proton flux − the results are reported in Table 4.3, where we have used the parameter scan with ranges $D_{0xx} = 0.57 - 19.5 \times 10^{28}$ cm^2/s, $L = 1.22 - 20.48$ kpc and $\alpha = 0.32 - 0.50$. As can be inferred from this Table, the B/C and ^{10}Be/^{9}Be data set is not sensitive to a variation of γ_2 in the range 2.26−2.46. Such conclusion was expected because cosmic ray ratios are largely independent of the source term. In order to break such degenaracy a cosmic ray flux measurement − e.g. of protons − must be used. The proton flux at high energies is supposed to go as $E^{-(\alpha+\gamma_2)}$ and consequently it helps discriminating wrong values for the injection index γ_2. In fact, as shown in Table 4.3, the analysis with a combined data set including B/C, ^{10}Be/^{9}Be and the proton flux produces relatively large reduced chi-squares of the best-fit configurations. This indicates that γ_2 is deviating from the assumed value of 2.36. Notice as well that, when one uses the projected proton data, the best-fit values for α are smaller for smaller injection indices γ_2, and vice-versa − this is because the proton flux is sensitive to the combination $\alpha + \gamma_2$. To proceed further and quantify how sensitive AMS-02 will be to the cosmic ray injection spectrum, we scan the parameter space $(D_{0xx}, \gamma_2, \alpha)$ and fix $v_A = 36$ km/s, $V_{c,0} = dV_c/dz = 0$, and $L = 5$ kpc (notice that D_{0xx} and L are approximately degenerate). We ran GALPROP 343 times, in a 7x7x7 grid of the parameters $(D_{0xx}, \gamma_2, \alpha)$ over the ranges $D_{0xx} = 4.54 - 8.03 \times 10^{28}$ cm^2/s, $\gamma_2 = 2.33 - 2.39$ and $\alpha = 0.38 - 0.44$. Linearly-(Logarithmically-)spaced gridpoints were implemented for γ_2, α (D_{0xx}). An infill of 3 points between consecutive gridpoints was applied resulting in 25x25x25=15,625 different models. Figure 4.10 shows the 3σ regions in the α vs. γ_2 plane (marginalized over D_{0xx}) from the projected AMS-02 measurements of the *(i)* proton flux (dashed lines), *(ii)* B/C and ^{10}Be/^{9}Be (dotted lines), and *(iii)* B/C, ^{10}Be/^{9}Be and proton flux (solid lines). Such

as anticipated earlier, the ratios B/C and ^{10}Be/^{9}Be are efficient probes of the diffusion index but insensitive to γ_2, while the proton flux constrains essentially the quantity $\alpha+\gamma_2$. Hence, within minimal propagation models, AMS-02 has the potential to pinpoint both the diffusion index α and the high energy source spectral index γ_2 with good accuracy. Note that this result stems exactly from the combination of the B/C and ^{10}Be/^{9}Be ratios and the proton flux. While a reasonably precise high energy proton flux has been measured by past and present instruments (e.g. PAMELA [203]) − allowing corrispondingly precise estimates of $\alpha + \gamma_2$ −, only AMS-02 (or future detectors) will be able to break down the degeneracy between α and γ_2 with high energy quality cosmic ray ratios.

4.5.5 Conclusions

In this paper, we have considered the ability of the upcoming AMS-02 experiment to measure stable secondary-to-primary and unstable ratios (such as boron-to-carbon and beryllium-10-to-beryllium-9), and studied to what extent this information could be used to constrain the model describing cosmic ray propagation in the Milky Way. Within the context of relatively simple propagation models, we find that the parameters can be very tightly constrained by the projected AMS-02 data; considerably more so than is possible with currently existing data [180, 169].

The ability of AMS-02 to constrain the cosmic ray propagation model can be considerably reduced, however, if more complex models with larger numbers of free parameters are considered. Only a rough determination can be made of the Alfvén velocity (which dictates diffusive reacceleration) in most cases, for example. On the other hand, if even a relatively small degree of convection (at the level of $\sim$10 km/s/kpc) is present, this is expected to be discernable from the AMS-02 data. Other aspects of cosmic ray propagation (including, for example, the detailed energy dependence of the diffusion coefficient, or variations in the source distribution or injected chemical composition) are unlikely to be significantly constrained by upcoming data on stable secondary-to-primary and unstable ratios. In some cases, we have found that the parameters of the underlying diffusion model could be misinferred due to inaccurate assumptions implicit in the model. Local variations in recent supernova activity could also lead to somewhat skewed determinations of propagation parameters. The source spectral index, in constrast, is likely to be well constrained within minimal models if proton flux measurements are used in addition to the ratios B/C and ^{10}Be/^{9}Be. With the latter case we have therefore exemplified how in some situations cosmic ray observables other than ratios are powerful tools in discriminating non-minimal assumptions.

In summary, the introduction of data from AMS-02 will make it possible to significantly expand our understanding of how cosmic rays propagate through the interstellar medium of the Milky Way. As we have demonstrated, the characteristics of simple propagation models will be tightly constrained by this data set. Moving beyond such simple scenarios, some of the underlying model assumptions will also become testable with such data, allowing us to better refine our cosmic ray predictions.

Chapter 5

Indirect Dark Matter detection

Indirect Dark Matter detection is based on the search for annihilation (or decay) products, presumably photons, electrons, positrons, protons, antiprotons, neutrinos and antineutrinos. These particles, or their interaction with the surrounding medium, can be searched for in different astrophysical targets and used to probe the presence of annihilating (or decaying) Dark Matter candidates. Although conceptually simple, this task turns out to be complicated by the underlying particle physics and astrophysical uncertainties, as already discussed in detail in Chapters 2 and 4. After reviewing the theoretical framework of indirect searches in Section 5.1, we focus on photons and neutrinos (Section 5.2), electrons/positrons (Section 5.3) and antiprotons (Section 5.4). The experimental status is given in Section 5.5. The last three Sections of the present Chapter are reserved to present the original constributions of the thesis regarding indirect detection, namely multi-messenger constraints on the annihilating Dark Matter interpretation of the positron fraction [4] (Section 5.6), the ability for AMS-02 to discriminate the source of high-energy electrons and positrons [5] (Section 5.7) and finally the constraints on pre-BBN non-standard cosmologies arising from astrophysical bounds on Dark Matter annihilation cross-sections [6] (Section 5.8).

A multitude of other indirect experimental signatures have been proposed and searched for over the years, including for instance high-energy neutrinos from DM annihilations or decays in the Sun, Earth, Galactic Centre, galaxy clusters or dwarf galaxies; cosmic antideuterons from DM annihilations or decays in the galactic halo; and the impact of DM on stars and in the early Universe. The reader is referred to broad-purpose reviews such as [17, 31] for the indirect detection strategies not treated in this Chapter. Another useful reference is the DarkSUSY code and respective documentation [19, 204] that cover extensively DM indirect signatures.

5.1 Theoretical framework

5.1.1 Annihilation yields

As described in detail in subsection 1.2.3, in the standard WIMP scenario, the mechanism of freeze-out is controlled by the annihilation of DM particles. This same process of annihilation may be responsible today for the injection of high-energy particles in various regions of the observable Universe – the main difference with respect to freeze-out being the relative velocity v of the annihilating DM particles. For instance, in galaxies like our

own typical velocities are $v_{gal}/c \sim 10^{-3}$ as opposed to $v_f/c \sim p_f/m_\chi \simeq \sqrt{2m_\chi k_B T}/m_\chi = \sqrt{2/x_f} \sim 1/3$ attained at chemical decoupling. In any case, for several annihilation channels, $\langle\sigma_{ann}v\rangle$ is roughly constant and thus annihilations today are not suppressed. Now, from equation (1.25) the rate of depletion of DM particles is $\langle\sigma_{ann}v\rangle n_\chi$; hence the **annihilation rate** reads

$$\Gamma_{ann} = \frac{1}{2}\langle\sigma_{ann}v\rangle n_\chi \quad , \tag{5.1}$$

where the factor 1/2 accounts for the fact that two χ disappear per annihilation event. This is valid for Majorana particles that are identical to their own antiparticles (i.e. $\chi \equiv \bar{\chi}$). For species with non-identical antiparticles (as the case of Dirac fields), equation (1.25) is replaced by

$$n_\chi + 3Hn_\chi = -\langle\sigma_{ann}v\rangle \left(n_\chi n_{\bar{\chi}} - n_{\chi,eq}n_{\bar{\chi},eq}\right) \quad ,$$

and analogously for $n_{\bar{\chi}}$. Defining $n \equiv n_\chi + n_{\bar{\chi}}$ and considering symmetric species ($n_\chi = n_{\bar{\chi}}$),

$$\dot{n} + 3Hn = -\langle\sigma_{ann}v\rangle\frac{1}{2}\left(n^2 - n_{eq}^2\right) \quad ,$$

which yields

$$\Gamma_{ann} = \frac{1}{4}\langle\sigma_{ann}v\rangle n$$

in constrast to equation (5.1).

The next step is to identify the **annihilation final states**, i.e. the injected particles. This depends on the DM candidate under consideration and the underlying theory. Supersymmetric neutralinos, for example, often annihilate into *gauge bosons* (W^+W^-, Z^0Z^0), *gluons*, *Higgses* (H^+H^-, $W^\pm H^\mp$) or *quarks* ($u\bar{u}$, $d\bar{d}$, $s\bar{s}$, $c\bar{c}$, $b\bar{b}$, $t\bar{t}$) as long as those states are kinematically allowed. For detailed branching ratios and worked-out cross-sections see Refs. [45, 17, 205]. Other annihilating channels include *lepton pairs* (e^+e^-, $\mu^+\mu^-$, $\tau^+\tau^-$), featured by Kaluza-Klein models, *photons* ($\gamma\gamma$, $Z^0\gamma$) and *neutrinos* ($\nu\bar{\nu}$). Apart from e^+e^-, $\gamma\gamma$ and $\nu\bar{\nu}$ that are injected monochromatically, in all other cases the final state particles decay, fragment or hadronise shortly after the annihilation producing secondary particles. Gauge bosons and Higgses decay into leptons and quarks; then, quarks, as well as gluons, hadronise generating bunches of particles. The hadronisation process gives rise to abundant fluxes of photons, particularly through the creation and subsequent decay of neutral pions π^0 and other mesons. This photon yield, complemented with the radiative photons emitted by the charged particles in the cascade, constitutes a **continuous spectrum** extended up to the DM mass. Annihilations into gauge bosons, Higgses and quarks also result in electrons and positrons, particles that are at the bottom of the decay chains, and protons and antiprotons, eventually formed from the combinations of hadrons in the cascade. These chains are extremely complex and need to be modelled with Monte Carlo codes such as PYTHIA [206, 207, 208].

The $\mu^+\mu^-$ and $\tau^+\tau^-$ channels undergo electromagnetic showering and generate broad, continuous spectra of electrons, positrons and photons, again extended up to m_χ. On top of all the processes above-described, whenever the final state consists of a pair of charged particles, an extra photon contribution needs to be taken into account: **internal bremsstrahlung** (IB) [209]. This sort of bremsstrahlung results in the emission of a final state photon without requiring magnetic fields. There are two distinct IB components:

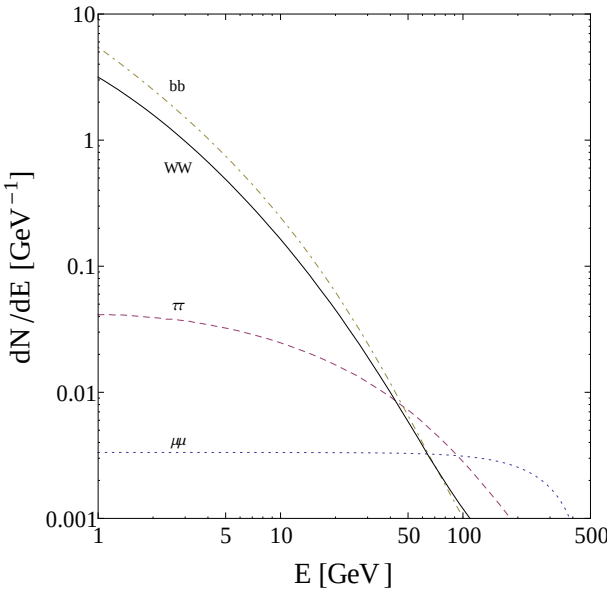

Figure 5.1: The positron spectrum per annihilation dN_{e^+}/dE for several annihilation channels and $m_\chi = 500$ GeV.

final state radiation (FSR), when the photon is radiated by one of the outgoing charged particles, and *virtual internal bremsstrahlung* (VIB), when a virtual particle in the annihilation process is responsible for the emission. While FSR is rather model-independent and amount to an almost-universal parameterisation, VIB is model-dependent and can also be important in some particular cases, see [209, 210]. The total IB spectrum behaves as $dN_\gamma/dE \propto E^{-1}$ which makes it usually dominates over the continuous spectrum at energies near m_χ.

All in all, DM annihilations give rise to sizeable yields of electrons/positrons, photons, protons/antiprotons and neutrinos/antineutrinos. For illustration, Figure 5.1 shows the positron yield dN_{e^+}/dE (the same holds for electrons) for different annihilation channels and $m_\chi = 500$ GeV. It is worth noticing that in certain cases radiative corrections to these spectra need to be considered – see [211, 212].

By convoluting the number of annihilations per unit time and unit volume $\Gamma_{ann} n_\chi$ with the annihilation spectra dN_i/dE, one obtains the **total source term**

$$\frac{d^2 n_i}{dtdE}(E,\vec{x}) = \xi_\chi \langle \sigma_{ann} v \rangle \frac{dN_i}{dE}(E) \times \left(\frac{\rho(\vec{x})}{m_\chi} \right)^2 \equiv Q_{ann,i}(E,\vec{x}) \quad , \tag{5.2}$$

where $\xi_\chi = 1/2$ (1/4) for Majorana (Dirac) particles and $n_\chi = \rho/m_\chi$ is the Dark Matter number density. Notice that the particle physics dependence, $\xi_\chi \langle \sigma_{ann} v \rangle dN_i/dE$, is a function of energy and may be factored out from the astrophysical factor, $(\rho/m_\chi)^2$, that is target-dependent. This important phenomenological feature will be emphasised in the following Sections.

How the source term in equation (5.2) turns into a local measurable flux depends on the nature of the particle i and on the medium at the annihilation site. Before specialising to each case, some comments are in order here. Firstly, note that $Q_{ann,i} \propto \rho^2$, which means that regions of high DM density yield particularly enhanced signals. Also, for the same reason, the overall flux from a given object sensitively depends on the existence of localised

high concentrations of Dark Matter – such as the virialised substructures discussed in Chapter 2 – and not only on the mean density. This would not be the case of $Q_{ann,i} \propto \rho$, as happens for decaying Dark Matter candidates. In (very) optimistic conditions, the different scalings with DM density could even be used to distinguish between the two scenarios [213]. Although decaying DM is not the main focus of this thesis, it is fair to say that there are several candidates well-motivated on particle physics grounds and presenting decay times of order $\tau \sim 10^{26}$ s [214, 215]. The decay spectra are distinct – but qualitatively similar – to the annihilation ones shown in Figure 5.1, and we shall focus on the latter for the rest of the manuscript.

5.1.2 Sommerfeld enhancement

We have considered throughout the previous subsection an annihilation cross-section essentially independent of v, $\langle \sigma_{ann} v \rangle = \text{const}$. However, in some cases $\langle \sigma_{ann} v \rangle$ can be very enhanced especially at small velocities and that brings new phenomenological features. This is the case of the so-called *Sommerfeld enhancement* [216, 217, 218], which is a non-perturbative, non-relativistic quantum mechanical effect in the interaction between two particles. In a few words, imagine an attractive potential $V(\vec{x})$ centred in the origin and an incoming particle with velocity v. The probability that the particle falls into the origin – i.e. interacts – is larger if v is smaller, and thus the cross-section is enhanced in the low-velocity regime. The wavefunction $\psi(\vec{x})$ obeys the Schrödinger equation:

$$-\frac{\hbar^2}{2m_\chi}\nabla^2\psi + V(\vec{x})\psi = \left(\frac{1}{2}m_\chi v^2\right)\psi \quad , \tag{5.3}$$

where we are considering the interaction between two DM particles of mass m_χ, one of which put at the origin. Assuming a central potential $V = V(r)$ and writing the r-dependence of the wavefunction as $\psi(r) = \eta(r)/r$

$$-\frac{\hbar^2}{2m_\chi}\frac{d^2\eta}{dr^2} + V(r)\eta = \frac{1}{2}m_\chi v^2 \eta \quad .$$

Setting a Yukawa potential $V(r) = -\alpha \exp(-m_\phi r)/(2r)$ (corresponding to the exchange of a scalar of mass m_ϕ) and $r' = \alpha m_\chi r$,

$$\hbar^2\frac{d^2\eta}{dr'^2} + \left(\frac{1}{r'}\exp\left(-\frac{m_\phi r'}{\alpha m_\chi}\right) + \frac{v^2}{\alpha^2}\right)\eta = 0 \quad . \tag{5.4}$$

The Sommerfeld enhancement, i.e. the increase in cross-section with respect to the case with no potential, is given by $S = |\eta(\infty)/\eta(0)|^2$, where $\eta(r)$ is the solution of (5.4) with the condition $\eta'(\infty) = i m_\chi v\, \eta(\infty)$ (see Ref. [219] for further details). In general, equation (5.4) needs to be solved numerically given m_ϕ, α, m_χ and v; it is nevertheless instructive to consider the Coulomb limit of a massless scalar ϕ, $V(r) = -\alpha/(2r)$, in which case the analytical solution exists and yields ($\hbar = 1$) [219]

$$S = \left|\frac{\pi\alpha}{v}\left(1 - \exp\left(-\frac{\pi\alpha}{v}\right)\right)^{-1}\right| \quad . \tag{5.5}$$

At sufficiently low velocities this expression gives a divergent $1/v$ enhancement, while $S \to 1$ for high velocities as expected. The divergent behaviour saturates if the scalar is massive and $v < v_{sat} \equiv cm_\phi/m_\chi$. Also, for certain fine-tuned combinations of $(v, m_\phi, m_\chi, \alpha)$ resonances are turned on and produce huge enhancements. Finally, let us notice that repulsive potentials (with $\alpha < 0$) produce easily suppressions of the cross-section, $S < 1$, as testified by equation (5.5).

The Sommerfeld enhancement has important consequences for the phenomenology of Dark Matter indirect searches. Indeed, taking for illustration an enhancement $S \propto 1/v$, one concludes that the annihilation source term (5.2) is largest not for the highly concentrated places, but for the regions with highest ρ^2/v. This renders DM objects presenting small velocity dispersions (such as virialised substructures and dwarf galaxies) and early Universe effects – recall that $\frac{v}{c} \sim 0.3\left(\frac{k_B T}{5\text{ GeV}}\right)$ – as privileged targets. The Sommerfeld enhancement has the neat property that, although annihilation fluxes are enhanced in many DM targets, the freeze-out epoch is left untouched since $S \sim \mathcal{O}(1)$ when $v/c \sim \mathcal{O}(0.3)$. In the recent literature, particularly after the PAMELA results on the positron fraction, Sommerfeld-enhanced cross-sections have been thoroughly scrutinised as detailed in Section 5.6.

5.1.3 Collisionless simulations: Via Lactea II and Aquarius

Over the last few years, N-body simulations have improved considerably, and recently two groups have published the results of high-resolution simulations, **Via Lactea II** (VL2) [220] and **Aquarius** (Aq) [85]. In the former, both smooth and clumpy components are well fitted by Navarro-Frenk-White profiles and the abundance of subhalos follows the rather steep behaviour M^{-2}, while in the latter the density profiles seem to be Einasto-like and a shallower subhalo abundance $\propto M^{-1.9}$ is found. Let us stress that the simulations use different cosmological parameters and the differences found are in the best fits, not necessarily in the actual findings. A common feature is the presence of many resolved subhalos and a characteristic dependence of their concentration on the position inside the halo. In the following we detail our implementation of the findings of Via Lactea 2 and Aquarius (see [4]).

The *smooth density profile* is well modelled, in the VL2 and Aquarius scenarios, by:

$$\rho_{sm}^{VL2}(r) = \frac{\rho_s}{\frac{r}{r_s}\left(1+\frac{r}{r_s}\right)^2} \quad ,$$

$$\rho_{sm}^{Aq}(r) = \rho_s \exp\left[-\frac{2}{\alpha}\left(\left(\frac{r}{r_s}\right)^\alpha - 1\right)\right], \;\; \alpha = 0.17 \quad ,$$

where r is the distance to the Galactic Centre. The local density is $\rho_0 \equiv \rho_{sm}(R_0 = 8\text{ kpc})$. Following equation (2.12), the NFW profile of Via Lactea II is considered to saturate below a radius r_{sat} such that $\rho_{sm}(r_{sat}) \equiv \rho_{max} = 2 \times 10^{18}\ \mathrm{M_\odot kpc^{-3}}$.

The density profiles inside clumps are NFW in Via Lactea II and Einasto with $\alpha = 0.17$ in Aquarius. The corresponding *concentration parameters* are well fitted by a double

power law in mass [4]

$$c_{200}(M,r) = \left(\frac{r}{R_{200}}\right)^{-\alpha_R} \left(C1\left(\frac{M}{\mathrm{M}_\odot}\right)^{-\alpha_{C1}} + C2\left(\frac{M}{\mathrm{M}_\odot}\right)^{-\alpha_{C2}}\right) \quad ,$$

where M is the mass of the clump and r again the galactocentric distance. In this way, the clump inner density profile $\rho_{cl}(M,r,r')$ is unambiguously defined once the clump mass M and the distance to the Galactic Centre r are specified. A quantity that turns out to be relevant for DM-induced positrons and antiprotons is the so-called *annihilation volume*,

$$\xi(M,r) = \int_0^{r_{200}} dr'\, 4\pi r'^2 (\rho_{cl}(M,r,r')/\rho_0)^2 \quad . \tag{5.6}$$

Another important input from N-body simulations is the *spatial and mass distribution of clumps* [4]:

$$\mathrm{VL2}: \quad \frac{d^2N_{sh}}{dMdV}(M,r) = \frac{A_{sh}(M/\mathrm{M}_\odot)^{-2}}{\left(1+\frac{r}{R_a}\right)^2},$$

$$\mathrm{Aq}: \quad \frac{d^2N_{sh}}{dMdV}(M,r) = A_{sh}(M/\mathrm{M}_\odot)^{-1.9} \times \exp\left[-\frac{2}{\alpha}\left(\left(\frac{r}{R_a}\right)^\alpha - 1\right)\right],\ \alpha = 0.678$$

in units of $\mathrm{M}_\odot^{-1}\mathrm{kpc}^{-3}$.

We fixed the normalisation A_{sh} according to the findings of numerical simulations. In the VL2 case, we impose that 10% of the galaxy mass M_{200} is virialised in structures with mass in the range $[10^{-5}M_{200}, 10^{-2}M_{200}]$. In the case of Aquarius, we require that 13.2% of M_{200} is concentrated in halos with mass between $1.8\times10^{-8}M_{200}$ (corresponding to the mass resolution in the Aquarius simulation) and $10^{-2}M_{200}$.

It is convenient to recast the above distribution in the form

$$\frac{d^2N_{sh}}{dMdV}(M,r) = N_{cl}\frac{dP_M}{dM}(M)\frac{dP_V}{dV}(r) \quad ,$$

where

$$\int_{M_{min}}^{M_{max}} dM\, \frac{dP_M}{dM} = 1 = \int_0^{R_{vir}} dr\, 4\pi r^2 \frac{dP_V}{dV} \quad .$$

This implies the definition of a subhalo mass range: while M_{max} is usually fixed at $\sim 10^{-2}M_{200} \sim 10^{10}$ $\mathrm{M}_\odot$, M_{min} depends on the nature of Dark Matter, as discussed in Section 2.1. We choose to fix $M_{min} = 10^{-6}$ $\mathrm{M}_\odot$ which is a typical value for WIMPs [18]. As will be shown in Section 5.6 the positron and antiproton clumpy fluxes scale with the total number of clumps times the mean annihilation volume per clump $N_{cl}\langle\xi\rangle_M$, where

$$\langle\xi\rangle_M = \int_{M_{min}}^{M_{max}} dM\, \frac{dP_M}{dM}(M)\xi(M,R_0) \quad . \tag{5.7}$$

Other relevant quantities are the total mass in clumps $M_{cl}^{tot} = N_{cl}\int_{M_{min}}^{M_{max}} dM\, M\frac{dP_M}{dM}$, the local clump fraction $f_\odot = \frac{M_{cl}^{tot}}{\rho_0}\frac{dP_V}{dV}(R_0)$ and the total clump fraction $f_{cl}^{tot} = \frac{M_{cl}^{tot}}{M_{200}}$. Table 5.1 displays these and other parameters for both Via Lactea II and Aquarius setups.

	Via Lactea II	Aquarius	
virial radius	r_{200} [kpc]	402	433
virial mass	M_{200} [$M_\odot$]	$1.93 \cdot 10^{12}$	$2.50 \cdot 10^{12}$
scale radius	r_s [kpc]	21	20
scale mass density	ρ_s [$10^6 M_\odot kpc^{-3}$]	3.7	2.4
local DM density	ρ_0 [GeV cm^{-3}]	0.19	0.48
subhalo concentration parameterisation	α_R	0.286	0.237
	C1	119.75	232.15
	C2	-85.16	-181.74
	α_{C1}	0.012	0.0146
	α_{C2}	0.026	0.008
clump distribution normalisation	A_{sh} [$M_\odot^{-1} kpc^{-3}$]	1.7×10^4	25.86
clump distribution scale radius	R_a[kpc]	21	199
total number of clumps	N_{cl}	$2.79 \cdot 10^{16}$	$1.17 \cdot 10^{15}$
local clump number density	$\frac{dP_V}{dV}(R_0)$ [kpc^{-3}]	$3.20 \cdot 10^{-7}$	$8.47 \cdot 10^{-8}$
mean annihilation volume per clump	$\langle\xi\rangle_M$ [kpc^3]	$3.45 \cdot 10^{-10}$	$7.19 \cdot 10^{-10}$
total clumpy mass	$M_{cl}^{tot}(< R_{vir})$ [$M_\odot$]	$1.05 \cdot 10^{12}$	$4.33 \cdot 10^{11}$
total clump fraction	$f_{cl}^{tot}(< R_{vir})$	0.54	0.18
local clump fraction	$f_\odot$	$6.3 \cdot 10^{-2}$	$2.7 \cdot 10^{-3}$

Table 5.1: Parameters fixing the characteristics of the Dark Matter distribution as deduced from Via Lactea II and Aquarius results. Notice that we are setting $M_{min} = 10^{-6}$ $M_\odot$ to compute N_{cl}, $\langle\xi\rangle_M$, M_{cl}^{tot}, $f_\odot$ and f_{cl}^{tot} . Our implementation of the VL2 and Aquarius setups was first presented in [4], where the smooth normalisation at R_0, ρ_0, was incorrectly obtained by rescaling the smooth+clumpy density in the simulations by the total smooth mass fraction $1 - f_{cl}^{tot}$, instead of taking into account that at ~ 8 kpc most of the total (Dark Matter) density is contributed by the smooth component. The correct values in the local DM density row read approximately 0.41 GeV/cm^3 for VL2 and 0.58 GeV/cm^3 for Aquarius. Notice that this error also propagates to the quantity $f_\odot$. Section 5.6, that presents the results obtained in [4], uses the (incorrect) values in this table, while Sections 5.7 and 5.8 use the correct values just quoted.

5.2 Photons and neutrinos

There are only a few cases where high-energy photons and neutrinos do not propagate freely without attenuation (apart from neutrino oscillations) throughout the galactic and extragalactic medium. For instance, if created inside dense environments like the interior of the Sun or neutron stars, even neutrinos lose energy and in some cases cannot escape the source site. Another example is the attenuation of photons of certain energies when propagating over cosmological distances. In the following we shall disregard such exceptions and work on the *free propagation regime*. In this regime, the connection between injection and local spectra is trivial, and a direct study of the sources is possible.

As discussed above, Dark Matter annihilation can generate sizeable on-the-spot yields of photons and neutrinos. This is the so-called **prompt** contribution that in the case of photons includes the γ *lines*, the *broad continuous spectrum* as well as *internal bremsstrahlung* whenever applicable. There are at least two further contributions to the DM-induced photon flux: **inverse Compton scattering** and **synchrotron emission**[1]. In fact, it is almost unavoidable that DM annihilations produce high-energy $e^\pm$ which radiate synchrotron in the presence of a magnetic field and upscatter any existing radiation distribution. An important difference between ICS or synchrotron and prompt photons is that the latter are emitted just below the DM mass, while the former usually present much lower energies. Also, whereas prompt emission traces the spatial distribution of DM at the source, the morphology of ICS and synchrotron spectra is closely related to the distance travelled by electrons and positrons before radiating.

The local flux of prompt neutrinos and prompt, ICS and synchrotron photons in the

[1]In full generality also bremsstrahlung emission and self-synchrotron Compton should be taken into account.

free propagation regime may be written in an unified fashion:

$$\phi(E) = \frac{1}{4\pi} \int_{\Delta\Omega} d\Omega \int_{\text{l.o.s.}} ds\ \mathcal{G}(E, \vec{x}) \quad , \tag{5.8}$$

where $\Delta\Omega$ is the observed solid angle, l.o.s. represents the line-of-sight and

$$\mathcal{G}(E, \vec{x}) = \begin{cases} Q_{ann,i}(E, \vec{x}) & \text{for prompt } i = \gamma, \nu \\ \frac{1}{E} \int_{m_e c^2}^{m_\chi c^2} dE' \, \frac{dn_{e^\pm}}{dE}(E') \, P_{ICS}(E, E') & \text{for ICS} \\ \int_{m_e c^2}^{m_\chi c^2} dE' \, \frac{dn_{e^\pm}}{dE}(E') \, \left(\frac{dW}{d\nu}\right)_{syn}(\nu, E') & \text{for synchrotron} \end{cases} \quad , \tag{}$$

in which $E = h\nu$ for synchrotron, $dn_{e^\pm}/dE = dn_{e^-}/dE + dn_{e^+}/dE = 2dn_{e^-}/dE$ is the distribution of DM-induced electrons and positrons, and $Q_{ann,i}$, P_{ICS} and $(dW/d\nu)_{syn}$ are given by equations (5.2), (4.19) and (4.23), respectively. In this setup, the flux ϕ has units of $\text{GeV}^{-1}\text{m}^{-2}\text{s}^{-1}$ for the prompt and ICS contributions, while for synchrotron it is measured in Jy$\equiv$ $\text{Wm}^{-2}\text{Hz}^{-1}$. Since $\Delta\Omega = \Delta S/d^2$ (d being the distance to the source), in the case of high-density, far away sources the line-of-sight integral in (5.8) reduces to a volume integral:

$$\int_{\Delta\Omega} d\Omega \int_{\text{l.o.s.}} ds \to \frac{1}{d^2} \int_{V_s} dV \quad ,$$

where V_s is the source volume.

The photon signals just described are extensively used in Sections 5.6 and 5.8. They are very powerful in constraining different Dark Matter models and provide the possibility to perform directional studies, especially in the regions of highest expected DM densities. Let us make two comments at this point. Firstly, it is worth rewriting equation (5.8) for prompt contributions:

$$\phi(E) = \frac{\xi_\chi \langle \sigma_{ann} v \rangle}{4\pi m_\chi^2} \frac{dN_i}{dE}(E) \times \int_{\Delta\Omega} d\Omega \int_{\text{l.o.s.}} ds\ \rho^2(\vec{x}) \quad . \tag{5.9}$$

This expression reveals clearly that, for prompt DM-induced fluxes, the spectral shape is decoupled from the spatial morphology – such does not happen in certain cases, e.g. in the presence of Sommerfeld enhancements where $\langle \sigma_{ann} v \rangle$ is a function of v (and therefore $\vec{x}$). In other words, the first factor in equation (5.9) – usually called **"particle physics factor"** – controls the number density and rate of particles injected per annihilation event, whereas the second factor – the **"astrophysical factor"** – determines the total number of annihilations in a given line-of-sight.

The second comment refers to the distribution $dn_{e^\pm}/dE$ that yields the ICS and synchrotron fluxes. In general, one should solve the transport equation including all the relevant effects (diffusion, reacceleration, etc, see Chapter 4). However, in many cases the energy loss rate is large enough that the *steady state solution* of equation (4.27) for electrons and positrons is simply

$$\begin{aligned} n_{e^\pm}(E, \vec{x}) \equiv \frac{d^2 N_{e^\pm}}{dV dE_{e^\pm}} &= \frac{1}{b(E, \vec{x})} \int_E^\infty dE' \, Q_{ann,e^\pm}(E', \vec{x}) \\ &= \frac{\xi_\chi \langle \sigma_{ann} v \rangle}{m_{\chi^2}} \, \rho^2(\vec{x}) \, \frac{N_{e^\pm}(> E)}{b(E, \vec{x})} \quad , \end{aligned} \tag{5.10}$$

	L [kpc]	D_0 [kpc^2/Myr]	α	V_c [km/s]
M2	1	0.00595	0.55	–
MIN	1	0.0016	0.85	13.5
MED	4	0.0112	0.70	12.0
MAX	15	0.0765	0.46	5.0

Table 5.2: Sets of propagation parameters yielding maximal, mean and minimal anti-matter fluxes [181, 221].

where $b = -\sum_i (dE/dt)_i$ and $N_{e^\pm}(>E) = \int_E^{m_\chi c^2} dE' \frac{dN_{e^\pm}}{dE}(E')$.

5.3 Electrons and positrons

As seen in Chapter 4, positrons[2] produced in the Milky Way undergo different processes that change their direction and energy while crossing the galactic medium. The galactic magnetic fields, for instance, are responsible for deflection and, due to their (poorly known) inhomogeneities, the evolution of a positron can be treated as a random walk with a certain diffusion coefficient D_{e^+}. Other important phenomena are energy losses through inverse Compton scattering off the Cosmic Microwave Background and starlight and synchrotron emission, which proceed at a space-independent rate $b(E_{e^+}) \simeq E_{e^+}^2/(\mathrm{GeV} \cdot \tau_E)$ with $\tau_E \simeq 10^{16}$ s [162, 181]. Neglecting galactic convective winds and diffusive reacceleration, the number density per unit energy $n_{e^+}(t, \mathbf{x}, E_{e^+}) \equiv \frac{d^2 N_{e^+}}{dV dE_{e^+}}$ follows the diffusion equation [162, 181]

$$\frac{\partial n_{e^+}}{\partial t} - D_{e^+}(E_{e^+})\nabla^2 n_{e^+} - \frac{\partial}{\partial E_{e^+}}\left(b(E_{e^+}) n_{e^+}\right) = Q_{e^+}(\mathbf{x}, E_{e^+})\,, \tag{5.11}$$

and we are interested in positrons from annihilations of Dark Matter particles with mass m_χ and density ρ corresponding to the source term (cf. equation (5.2))

$$Q_{e^+}(\mathbf{x}, E_{e^+}) = \frac{1}{2}\left(\frac{\rho(\mathbf{x})}{m_\chi}\right)^2 \sum_k \langle \sigma_{ann} v \rangle_0^k \frac{dN_{e^+}^k}{dE_{e^+}}(E_{e^+})\,, \tag{5.12}$$

where the $1/2$ factor is valid for Majorana self-annihilating fermions and the sum runs over all the relevant annihilation channels.

Following the standard approach we assume steady state conditions (i.e. $\partial n_{e^+}/\partial t = 0$) and adopt a cylindrical diffusion halo with radius $r_{max} = 20$ kpc and a half-thickness L inside which the diffusion coefficient is supposed to be space-independent [162, 181], $D_{e^+}(E_{e^+}) \simeq D_0\,(E_{e^+}/\mathrm{GeV})^\alpha$. The half-thickness L extends much further than the half-thickness of the galactic disk $h \simeq 0.1$ kpc and n_{e^+} vanishes at the cylinder boundaries since the particles escape to the intergalactic medium. The propagation model is defined by the set of parameters (L, D_0, α) which turn out to be loosely constrained by cosmic ray data, namely B/C measurements. Following [181, 221] we use the sets of parameters labelled M2, MIN, MED and MAX in Table 5.2 that are likely to reflect the **propagation uncertainty** on Dark Matter induced anti-matter fluxes. M2 (MIN) is the set that minimises the positron (antiproton) flux. The value of the galactic wind speed will be used in the antiproton analysis while being neglected here.

Once the steady state solution is found, the flux of positrons is given by $\phi_{e^+}(\mathbf{x}, E_{e^+}) =$

[2] At the energies of interest, electrons are treated in the same way as positrons.

$\frac{v_{e^+}}{4\pi} n_{e^+}(\mathbf{x}, E_{e^+})$. We disregard solar modulation, since it is unimportant for multi-GeV positrons. Following [222, 162], the positron flux at Earth due to the **smooth Dark Matter component** of the Milky Way is

$$\phi^0_{e^+,sm}(E) = \frac{v_{e^+}}{4\pi} \frac{1}{b(E)} \frac{1}{2} \left(\frac{\rho_0}{m_\chi}\right)^2 \times \int_E^\infty dE_S \, f^{e^+}_{inj}(E_S) \, I^{e^+}_{sm}\left(\lambda_D(E, E_S)\right), \tag{5.13}$$

where the sun is at $(x_\odot, y_\odot, z_\odot) = (8, 0, 0)$ kpc, $v_{e^+}/c = (1 - m_e^2 c^4/E^2)^{1/2}$ and

$$f^{e^+}_{inj}(E_S) = \sum_k \langle \sigma_{ann} v \rangle^k_0 \frac{dN^k_{e^+}}{dE_{e^+}}(E_S) \quad .$$

$\lambda_D(E, E_S)$ is the positron *diffusion length* from a source energy E_S down to a detection energy $E \leq E_S$ and reads

$$\lambda_D(E, E_S) = \sqrt{\frac{4 D_0 \tau_E}{1-\alpha} \left(\left(\frac{E}{\text{GeV}}\right)^{\alpha-1} - \left(\frac{E_S}{\text{GeV}}\right)^{\alpha-1} \right)}.$$

$I^{e^+}_{sm}(\lambda_D)$ is the *dimensionless halo function* and is given by

$$I^{e^+}_{sm}(\lambda_D) = \int_{DZ} d^3\mathbf{x} \left(\frac{\rho_{sm}(\mathbf{x})}{\rho_0}\right)^2 G^{e^+}_\odot(\mathbf{x}, \lambda_D), \tag{5.14}$$

where DZ stands for the cylindrical diffusive zone and $G^{e^+}_\odot$ is the Green function evaluated at the solar neighbourhood:

$$G^{e^+}_\odot(\mathbf{x}, \lambda_D) = \frac{1}{\pi \lambda_D^2} \exp\left(-\frac{(x - x_\odot)^2 + (y - y_\odot)^2}{\lambda_D^2}\right) \times G^{e^+}_{1D}(z, \lambda_D) \quad ,$$

with $G^{e^+}_{1D}$ given in [222] (and references therein) for the limiting cases $L > \lambda_D$ and $L \leq \lambda_D$.

The contribution from one single clump is very similar to the smooth one replacing ρ_{sm} with ρ_{cl} in equation (5.14). However, we will be interested in the signal from a population of subhalos distributed throughout the Galaxy in a certain range of masses, say $\frac{d^2 N_{sh}}{dM dV} = N_{cl} \frac{dP_M}{dM} \frac{dP_V}{dV}$ as modelled in 5.1.3. Considering every clump a point source and given the local character of the Green function, the mean positron flux from the **clumpy Dark Matter component** in the Galaxy is [222]

$$\langle \phi^0_{e^+,cl} \rangle(E) = \frac{v_{e^+}}{4\pi} \frac{1}{b(E)} \frac{1}{2} \left(\frac{\rho_0}{m_\chi}\right)^2 N_{cl} \langle \xi \rangle_M \times \int_E^\infty dE_S f^{e^+}_{inj}(E_S) \langle G^{e^+}_\odot \rangle_V \left(\lambda_D(E, E_S)\right) \quad , \tag{5.15}$$

where

$$\langle G^{e^+}_\odot \rangle_V(\lambda_D) = \int_{DZ} d^3\mathbf{x} \, G^{e^+}_\odot(\mathbf{x}, \lambda_D) \frac{dP_V}{dV}(\mathbf{x})$$

and the mean annihilation volume per clump $\langle \xi \rangle_M$ was introduced in equation (5.7). Equation (5.15) is valid if the density profile of the clump does not depend on its position within the Milky Way. Therefore, we set $c_{200}(M) \equiv c_{200}(M, R_0)$ which is anyway reasonable for our analysis since multi-GeV positrons detected at the Earth travelled at most a

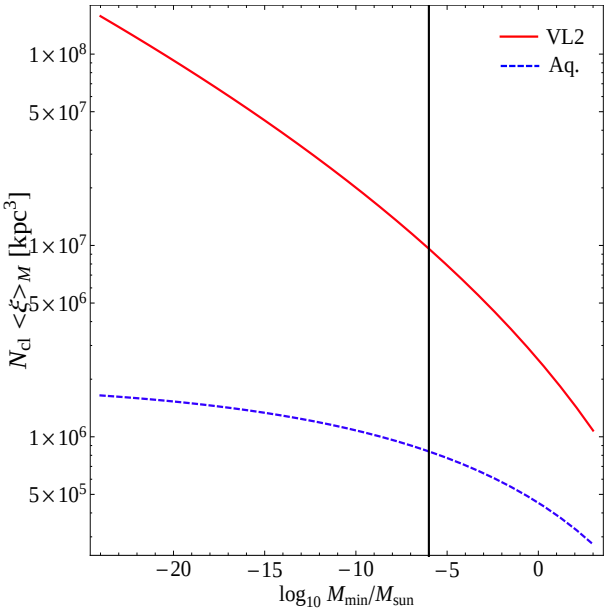

Figure 5.2: The total number of clumps times the mean annihilation volume per clump $N_{cl}\langle\xi\rangle_M$ as a function of M_{min} for Via Lactea II (solid red line) and Aquarius (dashed blue line). The vertical line indicates the value used throughout the thesis (in particular in Chapter 5), $M_{min} = 10^{-6}$ M$_\odot$.

few kpc [162]. To understand how the clumpy fluxes of positrons (and also antiprotons, see next Section) scale with the minimal subhalo mass M_{min}, we display in Figure 5.2 the total number of clumps times the mean annihilation volume per clump $N_{cl}\langle\xi\rangle_M$.

5.4 Antiprotons

As in the previous Section, we follow [222] to model the flux of antiprotons at the Earth. Differently from positrons, antiprotons do not lose much energy by synchrotron or inverse Compton since $m_p \gg m_e$. Instead, they may be swept away by galactic winds, assumed to be constant and perpendicular to the disk: $\vec{V}_c(\mathbf{x}) = sgn(z)V_c\vec{e}_z$. Furthermore, annihilations $p\bar{p}$ are responsible for the disappearance of primary antiprotons. These annihilations take place essentially along the galactic plane where the interstellar medium is concentrated, and therefore the diffusion equation for antiprotons contains a term $-2h\delta_D(z)\Gamma^{ann}_{\bar{p}}n_{\bar{p}}$ with $\Gamma^{ann}_{\bar{p}} = (n_H + 4^{2/3}n_{He})\sigma^{ann}_{\bar{p}H}v_{\bar{p}}$, $n_H \simeq 0.9$ cm^{-3}, $n_{He} \simeq 0.1$ cm^{-3} [223] and $\sigma^{ann}_{\bar{p}H}$ is given by equation (4.10). The diffusion coefficient is $D_{\bar{p}}(T_{\bar{p}}) = D_0\beta_{\bar{p}}\left(\frac{p_{\bar{p}}}{\text{GeV}}\right)^{\alpha}$ with $\beta_{\bar{p}} = \left(1 - \frac{m_p^2}{(T_{\bar{p}}+m_p)^2}\right)^{1/2}$ and $p_{\bar{p}} = (T_{\bar{p}}^2 + 2m_pT_{\bar{p}})^{1/2}$. All in all, the steady-state solution of the antiproton diffusion equation obeys

$$-D_{\bar{p}}(T_{\bar{p}})\nabla^2 n_{\bar{p}} + \frac{\partial}{\partial z}\left(\text{sgn}(z)V_c n_{\bar{p}}\right) = Q_{\bar{p}}(\mathbf{x}, T_{\bar{p}}) - 2h\delta_D(z)\Gamma^{ann}_{\bar{p}}(T_{\bar{p}})n_{\bar{p}} \quad ,$$

with $Q_{\bar{p}}$ of form analogous to (5.12) where $T_{\bar{p}}$ is the antiproton kinetic energy.

Once again, $\phi_{\bar{p}}(\mathbf{x}, T_{\bar{p}}) = \frac{v_{\bar{p}}}{4\pi}n_{\bar{p}}(\mathbf{x}, T_{\bar{p}})$. Because we are interested in high-energy antiprotons we have neglected solar modulation and reacceleration effects. Similarly to the

positron case, one has

$$\phi^0_{\bar{p},sm}(T) = \frac{v_{\bar{p}}}{4\pi}\frac{1}{2}\left(\frac{\rho_0}{m_\chi}\right)^2 f^{\bar{p}}_{inj}(T)\, I^{\bar{p}}_{sm}(T) \quad , \tag{5.16}$$

with

$$I^{\bar{p}}_{sm}(T) = \int_{DZ} d^3\mathbf{x} \left(\frac{\rho_{sm}(\mathbf{x})}{\rho_0}\right)^2 G^{\bar{p}}_{\odot}(\mathbf{x}, T, L, D_0, \delta, V_c) \quad ,$$

and

$$\langle\phi^0_{\bar{p},cl}\rangle(T) = \frac{v_{\bar{p}}}{4\pi}\frac{1}{2}\left(\frac{\rho_0}{m_\chi}\right)^2 N_{cl}\,\langle\xi\rangle_M\, f^{\bar{p}}_{inj}(T)\,\langle G^{\bar{p}}_{\odot}\rangle_V(T) \quad , \tag{5.17}$$

where

$$\langle G^{\bar{p}}_{\odot}\rangle_V(T) = \int_{DZ} d^3\mathbf{x}\, G^{\bar{p}}_{\odot}(\mathbf{x}, T, L, D_0, \delta, V_c)\,\frac{dP_V}{dV}(\mathbf{x}) \quad .$$

The Green function for antiprotons $G^{\bar{p}}_{\odot}$ is given in [222].

5.5 Experimental overview

Dark Matter annihilations or decays are probed through numerous channels or messengers. Photons, in particular, have an enormous potential given that multi-wavelength data are available, including radio, microwave, optical, X−ray and γ−ray observations. Being neutral, photons have the undisputed virtue of pointing back to the sources which allows directional studies. Among the most relevant targets for Dark Matter searches, the Galactic Centre of the Milky Way, galaxy clusters and dwarf galaxies play an important role.

Experimental techniques to detect photons depend, of course, on the wavelength of interest. For instance, X−rays and microwaves cannot cross the whole atmosphere and need to be detected with balloon-borne or satellite-based instruments. In contrast, radio waves, optical light and high-energy γ−rays can be observed with ground telescopes. Because **γ−ray astronomy** is currently a very hot field, we shall focus on it in this Section even though observations at other frequencies can also effectively constrain Dark Matter – examples include radio measurements or the optical depth of the CMB.

The atmosphere of the Earth is opaque to γ−rays (broadly defined as photons with energies $E_\gamma \gtrsim 0.1$ MeV), meaning that these particles interact destructively in the top layers of the atmosphere. Therefore, **direct detection** is only possible from space observatories. For $E_\gamma \gtrsim 30$ MeV, the incoming γ−ray interacts with the detector material generating an electron-positron pair whose energy is deposited in a calorimeter. For details and other techniques see Ref. [154]. These detectors have a small effective area, large field of view and are not sensitive above a few hundred GeV due to statistical limitations. EGRET [224] and Fermi-LAT [225] are perhaps the most prominent examples of such instruments. The Fermi Gamma-ray Space Telescope (FGST) was launched in June 2008 and has been releasing extraordinary results since then. The Large Area Telescope (LAT) is the main instrument onboard the FGST and consists of a set of conversion foils (where the γ−rays convert to $e^\pm$ pairs), a calorimeter, an anticoincident detector (that rejects charged cosmic rays) and a tracker. The LAT has optimal performance above 1 GeV featuring an acceptance of $\sim 1-2$ m^{2}sr, an angular resolution better than 1° and an

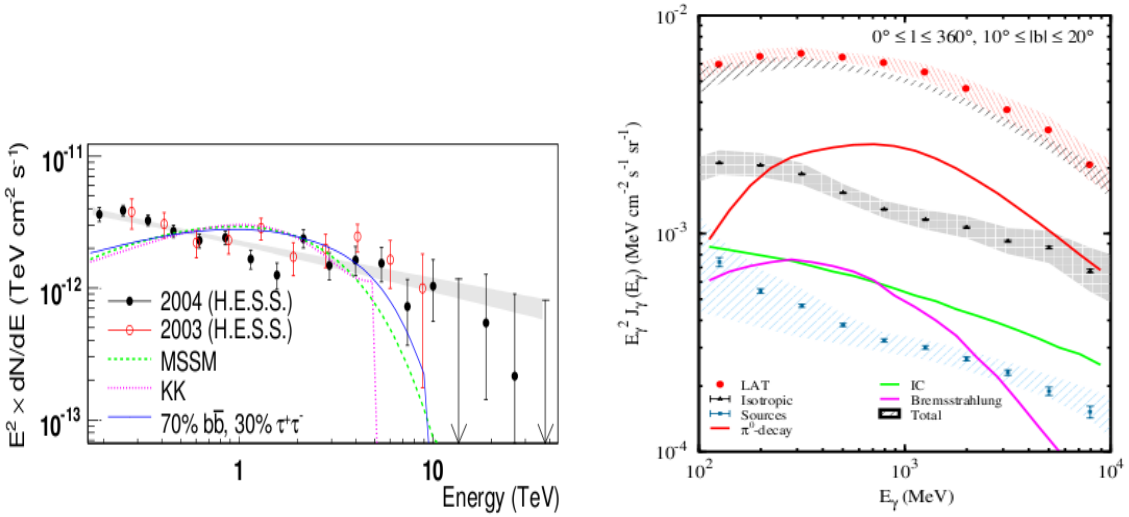

Figure 5.3: The left frame shows the Galactic Centre source spectra as seen by H.E.S.S. (image from [230]), while the right frame shows the diffuse emission at intermediate galactic latitudes $10° < |b| < 20°$ measured by Fermi-LAT (image from [96]).

energy resolution of about 10%.

Although $\gamma-$rays cannot cross freely the atmosphere, their interaction in the field of atmospheric nuclei produces $e^{\pm}$ pairs that radiate photons which in turn produce more $e^{\pm}$ pairs and so on. The result is an electromagnetic cascade roughly aligned with the direction of the primary $\gamma-$ray. It is hence possible to detect high-energy $\gamma-$rays ($E_\gamma \sim \mathcal{O}(10)$ GeV) with ground-based instruments in an **indirect fashion**: one may collect the *secondary particles* of the cascade at the surface level and/or measure the *Čerenkov radiation* emitted by ultra-relativistic charged secondaries throughout the shower development. The latter strategy is applied by the so-called Air Čerenkov Telescopes (ACT). These are optical mirror telescopes specifically designed to detect shower Čerenkov light, that arrives within a few degrees of the shower axis and constitutes a ∼200 m "pool" at the surface level. ACT experiments usually include several telescopes and present a small field of view, thresholds energies of tens of GeV, and huge effective areas ($10^4 - 10^5$ m^2) since the atmosphere is used as a calorimeter. The main challenge here is to distinguish high-energy $\gamma-$ray showers from hadronic ones that are much more frequent and nearly isotropic. The discrimination is possible with the help of numerical simulations that predict different shower morphologies. It is worth stressing that ACTs cannot distinguish electromagnetic showers initiated by electrons or positrons from those initiated by $\gamma-$rays – however, unlike electrons and positrons, photons trace back sources and can in principle be isolated at least in a statistical way. Finally, let us notice that *ground-based telescopes* are complementary to *space-borne instruments* and extend the energy range to well above the TeV. The main ACTs currently in operation are MAGIC [226], VERITAS [227] and H.E.S.S. [228]. The High-Energy Spectroscopic System (H.E.S.S.), for instance, is an array of telescopes situated in Namibia featuring a $\sim 4°$ field of view, angular resolution better than 0.1° and an energy resolution of 15% above 100 GeV. The Cherenkov Telecope Array (CTA) [229], instead, is a projected facility that aims at achieving an improved sensitivity over the energy range 10 GeV to 100 TeV, and is supposed to start operation around 2013.

The Fermi-LAT and H.E.S.S., along with other experiments, have released over the last years a multitude of observations useful to search for indirect Dark Matter signatures:

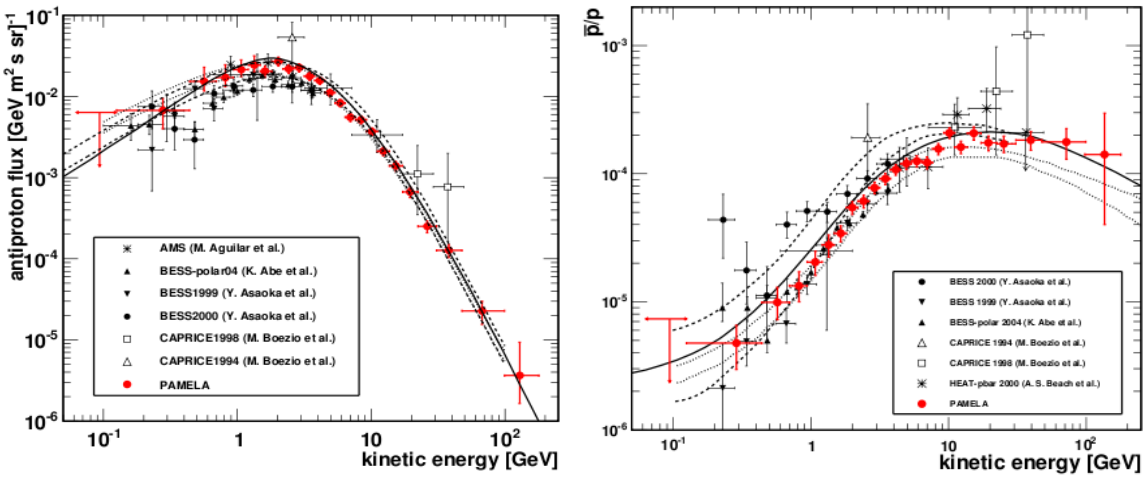

Figure 5.4: The measured antiproton flux (left frame) and antiproton-to-proton ratio (right frame). The most stringent data points (in red) are due to the PAMELA satellite. Images from [237].

the Galactic Centre emission [230] (shown in the left frame of Figure 5.3), the diffuse emission at intermediate latitudes [231] (shown in the right frame of Figure 5.3), the isotropic diffuse signal [96], the search for monochromatic lines [232] as well as upper limits on dwarf galaxies [233, 234] and galaxy clusters [235, 236]. None of these data sets shows a smoking-gun signature for DM annihilations or decays, but instead they are very powerful in constraining DM properties.

As for antiprotons and electrons/positrons, Section 4.4 has already discussed the experimental detection methods; hence here we limit ourselves to present the most important results regarding these messengers. Antiprotons are supposed to be of secondary origin only (i.e. produced in the spallation of primary cosmic rays on the galactic gas), opening a good window to detect an eventual primary signal at high energies. However, as clear from Figure 5.4, current data on the $\bar{p}$ spectrum – especially from the PAMELA satellite [198, 237] – show no spectacular features and are actually consistent with standard production [161]. Turning the argument around, antiprotons pose rather powerful constraints on several DM models, and will be extensively used along this Chapter.

Electrons and positrons constitute perhaps a more complicated channel since these particles suffer from very significant energy losses particularly at high energies (so that any excess should have a local origin), and sources need to be considered as discrete. In the 1990s, HEAT [238] and CAPRICE [239] hinted at a large fraction of positrons in the electronic cosmic-ray component at a few GeV, a claim later reinforced by AMS-01 [240] and confirmed by the spectacular rise in the positron fraction $e^+/(e^+ + e^-)$ measured by PAMELA [241]. Also ATIC [242] saw an excess on the flux of electrons plus positrons $e^+ + e^-$ that is not, however, consistent with the observations of Fermi-LAT [243, 244] and H.E.S.S. [245]. The latter experiments detect a hardening of the e^+e^- spectrum at $\sim \mathcal{O}(100)$ GeV and a tentative cutoff at the multi-TeV scale – see Figure 5.5 for a collection of data. These exciting data have triggered many works putting forward Dark Matter annihilations or decays as a feasible explanation, but any strong statement is very far from being robust. Indeed, even the quantification of an eventual excess of electrons/positrons with respect to "standard" cosmic-ray propagation is matter of intense debate nowadays [162]. A large portion of the rest of the present Chapter is devoted

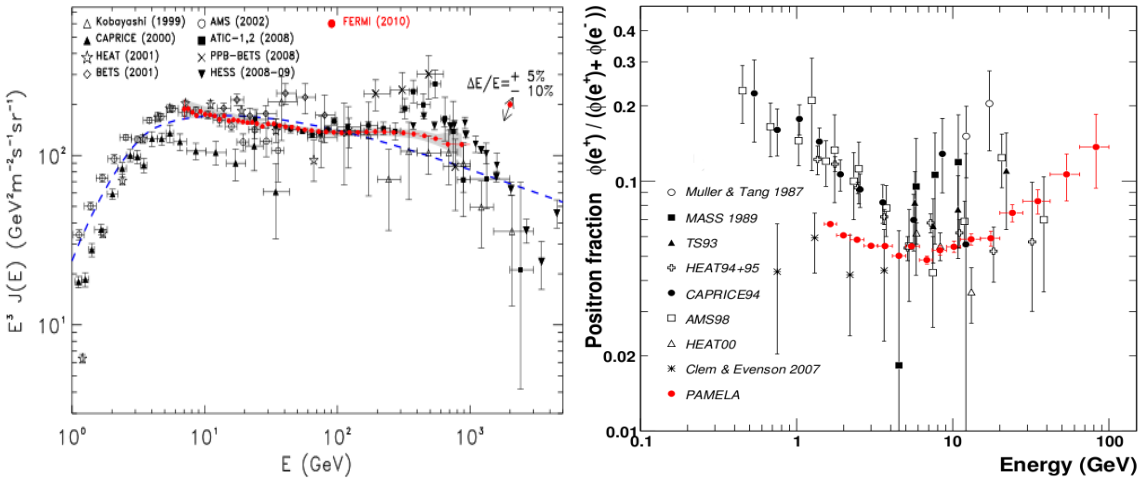

Figure 5.5: The measured electron plus positron flux (left frame, from [244]) and positron fraction (right frame, from [241]).

to scrutinise the data in Figure 5.5 against other data sets. Further $e^{\pm}$ observations, hopefully provided soon by AMS-02, will be useful but probably insufficient to settle this issue as discussed in Section 5.7.

5.6 Paper IV: Multi-messenger constraints on the annihilating Dark Matter interpretation of the positron excess[3]

The rise in the energy spectrum of the positron fraction, observed by the PAMELA satellite above 10 GeV, and other cosmic ray measurements, have been interpreted as a possible signature of Dark Matter annihilation in the Galaxy. However, the large number of free parameters, and the large astrophysical uncertainties, make it difficult to draw conclusive statements about the viability of this scenario. Here, we perform a multi-wavelength, multi-messenger analysis, that combines in a consistent way the constraints arising from different astrophysical observations. We show that if standard assumptions are made for the distribution of Dark Matter and the propagation of cosmic rays, current Dark Matter models cannot explain the observed positron flux without exceeding the observed fluxes of antiprotons or gamma-ray and radio photons. To visualize the multi-messenger constraints, we introduce "star plots", a graphical method that shows in the same plot theoretical predictions and observational constraints for different messengers and wavelengths.

5.6.1 Overview

Dark Matter annihilation or decay can in principle produce significant fluxes of positrons, antiprotons, photons, neutrinos and other secondary particles. Recently, the positron channel has received a lot of attention, since the PAMELA collaboration has released the data relative to the positron fraction [241] that exhibit a spectacular rise, which is in

[3]This Section is based on the article [4], done in collaboration with Lidia Pieri and Gianfranco Bertone.

agreement with earlier results from AMS-01 [240] and HEAT [238, 246, 247], and compatible with the claimed 300−800 GeV excess in the electron plus positron spectrum measured by ATIC-2 balloon flights [242]. Lying in the energy range $\gtrsim 10$ GeV, such an excess has prompted a large number of papers putting forward explanations that include DM annihilations or decays in the Galaxy, and nearby astrophysical objects like pulsars.

Here, we consider the DM annihilation hypothesis and perform a multi-messenger analysis in order to constrain the properties of viable DM candidates. More specifically, we study positrons, antiprotons, γ-rays and synchrotron emission due to the propagation of electrons and positrons in the galactic magnetic field. The multi-messenger approach has already provided useful constraints on DM scenarios. For instance, the non-observation of an excess of cosmic-ray antiprotons up to ~ 100 GeV by the PAMELA satellite [198] indicates that hadronic annihilation channels should be strongly suppressed. This motivates a simple distinction between DM candidates: *leptophilic*, i.e. that annihilate mainly into lepton pairs, and *hadrophilic*, whose annihilation final states are gauge bosons or quark pairs and induce non-negligible fluxes of both positrons and antiprotons. Obviously, the former override $\bar{p}$ bounds, while the latter need to be rather heavy in order to suppress $\bar{p}$ fluxes below ~ 100 GeV, but predict inevitably significant fluxes at higher energies, that should be soon probed. Other interesting messengers for DM searches are high-energy neutrinos. In fact, neutrino observatories such as Super-Kamiokande [248] and IceCube [249] are able to detect upward-going muons produced in the interaction of high-energy neutrinos within the Earth interior. Therefore, once the DM profile is fixed, neutrino observations of the Galactic Centre region effectively constrain the properties of Dark Matter, especially for multi-TeV candidates − see e.g. [250, 251].

Now, if one assumes that DM candidates are thermal relics from the early Universe, the present annihilation cross-section needs to be $\langle \sigma_{ann} v \rangle \sim \mathcal{O}(10^{-26})$ cm^{3}s^{-1} in order to produce the observed relic abundance $\Omega^0_{cdm} h^2 \sim 0.1$. Such a thermal relic with a TeV mass needs a $\sim 10^3$ boost in the annihilation flux to accommodate the PAMELA excess [252], which can hardly be provided by the "clumpiness" of the galactic halo. Non-thermal relics, non-standard cosmologies, or velocity dependent ("Sommerfeld enhanced") annihilation cross-sections have been invoked to circumvent this problem, but the question remains of whether the large cross-sections needed to explain the positron data can be made consistent with other astrophysical observations. We perform here an extensive analysis of the multi-messenger constraints in the framework of the latest high-resolution numerical simulations of a Milky Way like halo. We explore two specific classes of models: leptohilic candidates, inspired in Refs. [219, 253], and hadrophilic candidates, with a specific emphasis on models of Ref. [254]. For all these models we compute the flux of: *(i)* positrons, *(ii)* anti-protons, *(iii)* gamma-rays from the Galactic Centre, *(iv)* gamma-rays from the galactic halo, and *(v)* synchrotron emission due to the propagation of electrons and positrons at the Galactic Centre. We take into account the dependence of the annihilation cross-section on the relative velocity. In particular, we calculate the boost factor due to Sommerfeld enhanced substructures, in the framework of the Via Lactea II [220] and Aquarius [85] simulations, and we discuss the consequences for the gamma-ray flux from DM annihilations. Since the astrophysical input has already been discussed in 5.1.3, we proceed with the particle physics input in the following subsection.

label	Ref.	m_χ/TeV	$m_{\phi,s}$/GeV	$\langle\sigma_{ann}\rangle_0/(10^{-26}\mathrm{cm}^3\mathrm{s}^{-1})$	annihilation channel	$S(v_\odot)$	S_{max}
□ AH700	[219]	0.70	0.10 (ϕ)	3	$\phi\phi; \phi \to e^+e^-$	43	762
• NT1	[253]	1.00	34.0 (s)	3	$sa; s \to 97\%aa, 3\%b\bar{b}; a \to \mu^+\mu^-$	100	100
○ NT2	[253]	1.20	5.60 (s)	3	$sa; s \to 95\%aa, 5\%\tau\bar{\tau}; a \to \mu^+\mu^-$	100	100
⋆ $\mu\mu$	[256]	1.60	–	3	$\mu^+\mu^-$	1100	1100
■ $\tau\tau$	[257]	2.00	–	3	$\tau^+\tau^-$	1000	1000
× MDM3	[254]	2.70	–	~ 1	WW, ZZ	273	273
⊗ MDM5	[254]	9.60	–	~ 1	WW, ZZ	1210	1210

Table 5.3: Properties of DM candidates recently proposed in the literature and presenting Sommerfeld-enhanced cross-sections. The label of each model is preceded by the corresponding symbol to be used in the plots of the next subsections.

5.6.2 Particle physics input

The anomalous positron fraction reported by PAMELA and the electron plus positron excess claimed by ATIC have prompted the interest of the particle physics community, and motivated the quest for DM models leading to enhanced DM fluxes. Among them, strong emphasis has been put on the Sommerfeld enhancement [216, 217, 218], arising from the presence of an attractive potential, that for low relative velocities leads to a peculiar behaviour of the annihilation cross-section $\langle\sigma_{ann}v\rangle \propto 1/v$ down to a given v_{sat}, below which $\langle\sigma_{ann}v\rangle$ saturates. In this scheme, as discussed in 5.1.2, one can have Dark Matter particles that at chemical decoupling presented the appropriate annihilation cross-section of weak strength, $\langle\sigma_{ann}v\rangle_0 \sim \mathcal{O}(10^{-26})$ cm^{3}s^{-1}, and today, in the galactic halo, have a much higher $\langle\sigma_{ann}v\rangle$ since the local velocity dispersion is $\beta_\odot = v_\odot/c \sim 5 \cdot 10^{-4}$. The subscript 0 in $\langle\sigma_{ann}v\rangle_0$ denotes the value of the annihilation cross-section without Sommerfeld corrections. The Sommerfeld effect typically leads to small corrections of the annihilation cross-section at decoupling [255], while boosting significantly local antimatter fluxes. Notice that the relic abundance of a Sommerfeld-enhanced DM particle may be reduced with respect to the standard case by a factor of order unity: indeed, in Ref. [255] the authors have computed the thermal relic abundance of wino-like neutralinos including Sommerfeld corrections and found a reduction of about 50% compared to the standard calculation.

The Sommerfeld enhancement is rather model-dependent and thus we choose a few examples in the literature, shown in Table 5.3. These do not cover all the possibilities but are meant to be representative benchmarks. We consider specific implementations of Arkani-Hamed et al. [219] and Nomura & Thaler [253] models as leptophilic-like candidates. In the former, the Dark Matter particle annihilates into pairs of scalars or vector bosons ϕ which then decay into muons or electrons. We use $m_\phi = 100$ MeV (that means ϕ decays entirely into e^+e^-) and put $\alpha = \lambda^2/(4\pi) = 0.01$. As for Nomura & Thaler models, Dark Matter annihilates into a scalar s and an axion a. We implement the two benchmarks of [253] where s decays mainly into a pair of axions but has small branching ratios to $b\bar{b}$ and $\tau\bar{\tau}$ – see Table 5.3. The axion a is assumed to decay entirely into muons. Placing Nomura & Thaler models on Figure 6 of [219], one sees that the Sommerfeld enhancement is already saturated at $v = v_\odot$ and reads $\sim 100 - 300$. We set $S(v_\odot) = S_{max} = 100$ and note that taking a different value is equivalent to rescale $\langle\sigma_{ann}v\rangle_0$ since we are lying in the saturation regime. Lastly, inspired by the recently published electron plus positron spectrum from Fermi [243] and HESS [245], the authors of Ref. [256] propose an 1.6 TeV particle annihilating into $\mu^+\mu^-$, which fits well Fermi, HESS and PAMELA data given an enhancement of 1100. Even though such enhancement is not necessarily due to Sommerfeld corrections, we consider this candidate setting $S(v_\odot) = S_{max} = 1100$. Similarly,

we also analyse a 2 TeV particle annihilating into $\tau^+\tau^-$ with $S(v_\odot) = S_{max} = 1000$ [257].

For hadrophilic candidates we adopt the case of minimal Dark Matter [254], namely the fermion triplet and quintuplet. All examples displayed in Table 5.3 are Majorana fermions.

Essential ingredients to proceed further are the energy spectra per annihilation dN/dE of positrons, antiprotons and photons produced in Dark Matter annihilations. Arkani-Hamed et al. models feature particles that annihilate in an 1-step cascade into e^+e^-; the relevant formulae for the positron spectrum are given in Appendix A of [258]. The Nomura & Thaler cases considered here annihilate mainly in an 1.5-step cascade into $\mu^+\mu^-$ – which is basically half an 1-step cascade and half a 2-step cascade – and the referred Appendix gives the necessary expressions for dN_{e^+}/dE_{e^+}. The corrections due to the branching ratios into $b\bar{b}$ or $\tau\bar{\tau}$ are introduced following subsection 5.1.1. With the small branching ratios into $\tau\bar{\tau}$ and $b\bar{b}$ presented in Table 5.3, the positron spectra obtained in this way are very similar to the ones obtained in a pure 1.5-step cascade. However, an important difference is a non-zero yield of antiprotons (that will turn out to be small) and possibly significant γ-ray production. Lastly, energy spectra from minimal Dark Matter annihilations are given in reference [254] for $x \gtrsim 10^{-4}$. We implement the e^+ and $\bar{p}$ spectrum of [254] down to $x = 10^{-4}$ and a flat dN/dE is assumed below that.

5.6.3 Positrons and antiprotons

To compute the flux of positrons and antiprotons we use the formalism outlined in Section 5.3 and 5.4. The Sommerfeld enhancement is introduced in the following way. The smooth contribution $\phi^0_{e^+,sm}$ (see equation (5.13)) will be boosted by $S(v_\odot)$ given the local origin of high-energy positrons. As far as clumps are concerned, we assume that the whole population of subhalos presents velocity dispersions below v_{sat} which means the clumpy contribution $\langle\phi^0_{e^+,cl}\rangle$ (see equation (5.15)) will be roughly rescaled by S_{max}. Such simplification is conservative in the sense that we maximise the contribution of substructures – indeed, clumps with masses close to $M_{max} = 10^{10}$ M$_\odot$ may not be in the saturation regime, but that would lead to an enhancement smaller than S_{max}. In this framework and following [222], the total positron flux at Earth for a specific Dark Matter candidate and a certain propagation model is

$$\phi_{e^+}(E) = (1 - f_\odot)^2\, S(v_\odot)\, \phi^0_{e^+,sm}(E) \,+\, S_{max}\, \langle\phi^0_{e^+,cl}\rangle(E) \quad , \tag{5.18}$$

and analogously for the antiprotons with $\phi^0_{e^+,sm}$ replaced by $\phi^0_{\bar{p},sm}$ (check equation (5.16)) and $\langle\phi^0_{e^+,cl}\rangle$ by $\langle\phi^0_{\bar{p},cl}\rangle$ (check equation (5.17)).

As an example we show in Figure 5.6 the quantities $(1-f_\odot)^2 S(v_\odot)\phi^0_{e^+,sm}$ and $S_{max}\langle\phi^0_{e^+,cl}\rangle$ (and analogously for antiprotons) for the MDM3 candidate presented in Table 5.3. Both Via Lactea II and Aquarius parameters are used and the MED propagation set is assumed. On the one hand, the smooth contribution with Aquarius is larger because its local DM density is higher than in Via Lactea II – check Table 5.1. On the other hand, the Via Lactea II simulation predicts (through extrapolation of $d^2N_{sh}/dMdV$ down to $M_{min} = 10^{-6}$ M$_\odot$) more low-mass clumps than Aquarius and thus the corresponding clumpy contribution is more significant. In fact, the ratio between the two clumpy fluxes

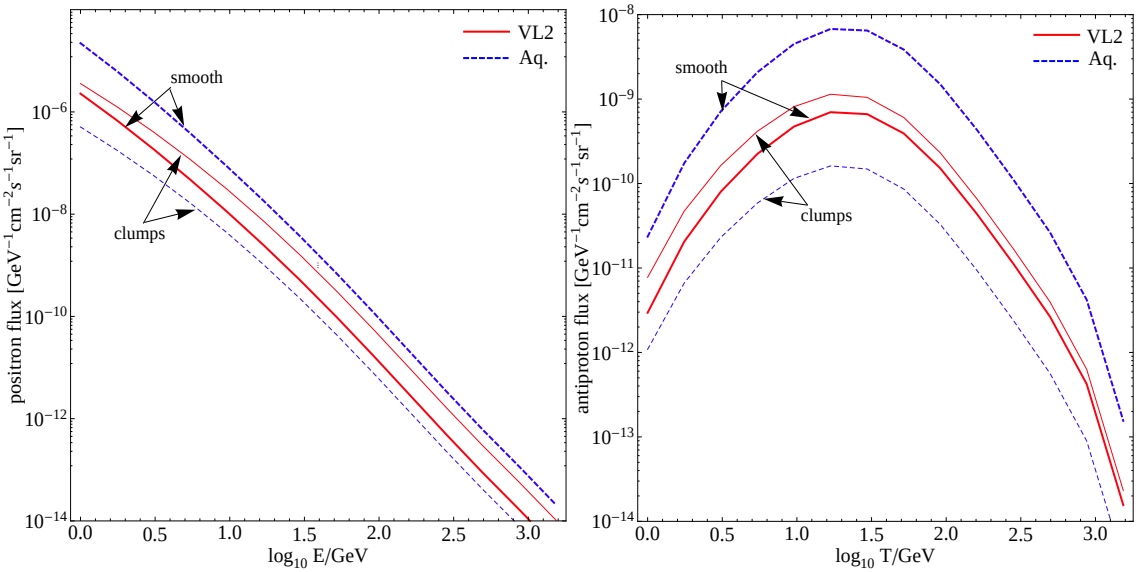

Figure 5.6: The Sommerfeld-enhanced fluxes $(1-f_\odot)^2 S(v_\odot)\phi^0_{sm}$ and $S_{max}\langle\phi^0_{cl}\rangle$ of positrons and antiprotons for the MDM3 candidate. Solid red (dashed blue) lines refer to Via Lactea II (Aquarius) density profiles. The thick (thin) curves represent the smooth (clumpy) contribution. The MED propagation model is adopted and $M_{min} = 10^{-6}$ M$_\odot$.

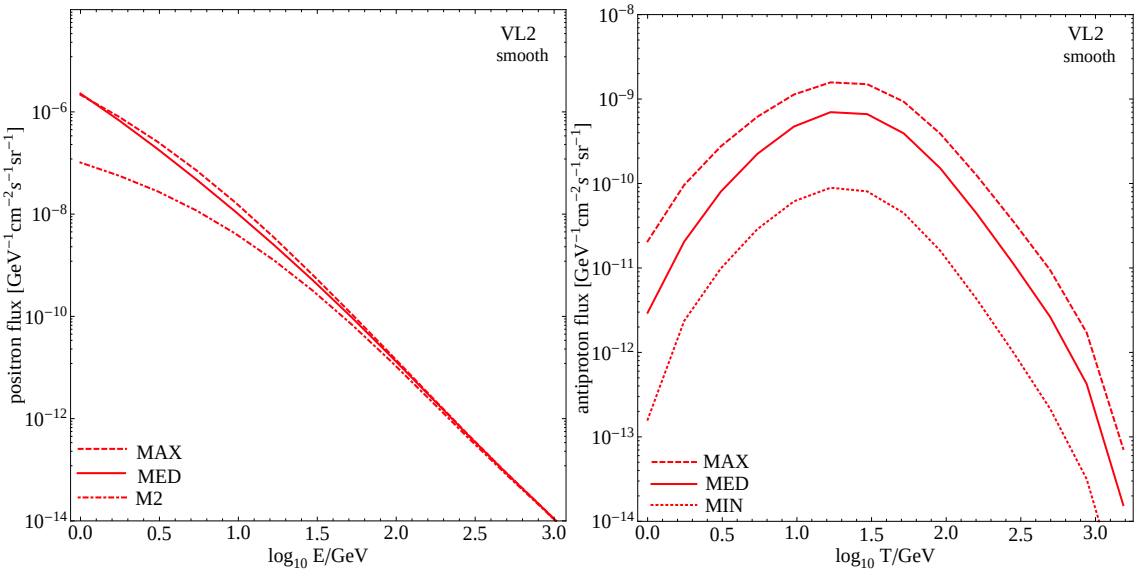

Figure 5.7: The smooth quantity $(1-f_\odot)^2 S(v_\odot)\phi^0_{sm}$ for the MDM3 candidate using the M2 (dot-dashed), MIN (dotted), MED (solid) and MAX (dashed) propagation models. For clarity, the clumpy component is omitted and just the results for Via Lactea II are plotted.

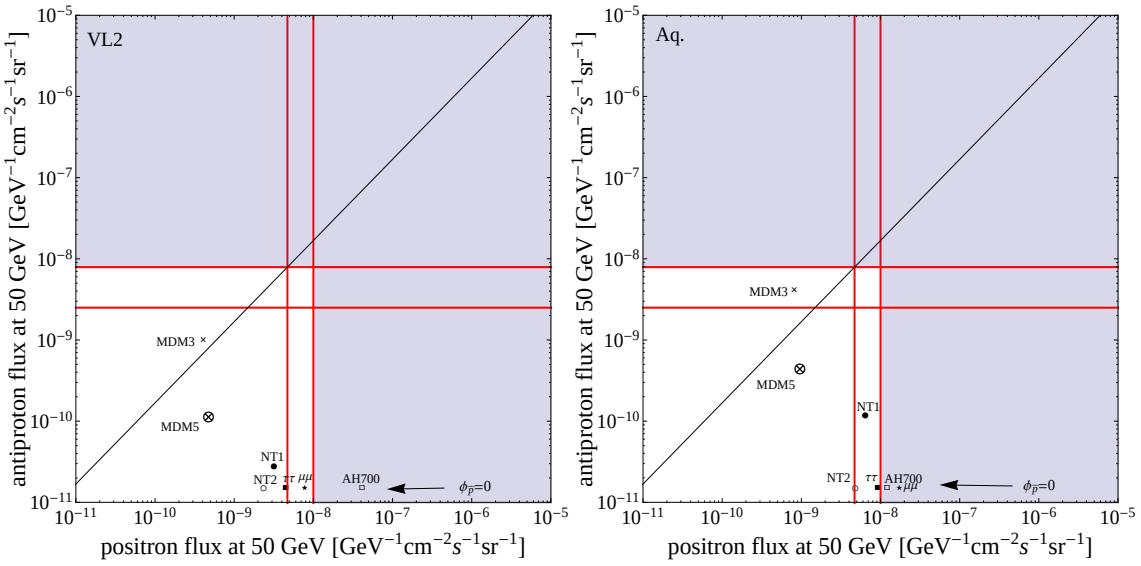

Figure 5.8: Total positron and antiproton fluxes at 50 GeV for the models in Table 5.3 and for both Via Lactea II and Aquarius parameters. The MED propagation is used and $M_{min} = 10^{-6}$ M$_\odot$. The solid lines indicate the fluxes deduced from PAMELA data assuming electron and proton fluxes at 50 GeV – see equations (5.19), (5.20) – and the corresponding excluded regions are shown as shaded. Candidates lying above the diagonal line cannot be rescaled to explain PAMELA positron excess without overproducing antiprotons.

for a fixed DM candidate is simple to understand if one computes the ratio

$$\frac{\left[\rho_0^2\, N_{cl} \langle\xi\rangle_M \frac{dP_V}{dV}(R_0)\right]_{\text{Aquarius}}}{\left[\rho_0^2\, N_{cl} \langle\xi\rangle_M \frac{dP_V}{dV}(R_0)\right]_{\text{Via Lactea II}}} \simeq 0.14 \quad .$$

Note that, as stated in subsection 5.1.3, we are fixing $M_{min} = 10^{-6}$ M$_\odot$; clumpy fluxes scale according to Figure 5.2.

Figure 5.7 shows the effect of varying the propagation parameters for the candidate considered above (MDM3), for the Via Lactea II case without clumps.

For clarity in visualising the e^+ and $\bar{p}$ yields from the candidates in Table 5.3, we choose to plot fluxes at 50 GeV which is well inside the energy range where PAMELA detected the positron excess and collected antiprotons. Moreover, both positrons and antiprotons of such energy are not significantly affected by solar modulation or reacceleration effects. At 50 GeV the PAMELA data indicates [241, 198] $\phi_{e^+}/(\phi_{e^-} + \phi_{e^+}) \sim 0.1$ and $\phi_{\bar{p}}/\phi_p \sim 0.7 - 2.2 \cdot 10^{-4}$ that we translate using Figures 9 and 10 in [162] and equation (1) in [54] into the fluxes:

$$\tilde{\phi}_{e^+}(50\ \text{GeV}) = \begin{cases} 1.0 \cdot 10^{-8} & \text{for hard } e^- \\ 4.7 \cdot 10^{-9} & \text{for soft } e^- \end{cases} \quad , \text{ and} \tag{5.19}$$

$$\tilde{\phi}_{\bar{p}}(50\ \text{GeV}) = \begin{cases} 7.9 \cdot 10^{-9} & \text{for } \phi_{\bar{p}}/\phi_p = 2.2 \cdot 10^{-4} \\ 2.5 \cdot 10^{-9} & \text{for } \phi_{\bar{p}}/\phi_p = 0.7 \cdot 10^{-4} \end{cases} \quad , \tag{5.20}$$

in units of GeV^{-1}cm^{-2}s^{-1}sr^{-1}.

Our aim in the present work is not to perform a fitting procedure or a likelihood analysis to PAMELA (or ATIC) data, but rather to investigate which DM particles are able to produce positron fluxes near the above-stated values. Figure 5.8 shows the total positron and antiproton fluxes at 50 GeV for the models in Table 5.3 assuming the MED propagation configuration and $M_{min} = 10^{-6}$ M$_\odot$. We see immediately that some

models violate the positron and/or antiproton data. However, all candidates may present $\langle\sigma_{ann}v\rangle_0$ a few times more or less than presented in Table 5.3, which accounts for a scaling along diagonals in Figure 5.8 since a change of $\langle\sigma_{ann}v\rangle_0$ modifies equally the positron and the antiproton fluxes. Conservatively, we are interested in knowing which points in Figure 5.8 may be rescaled to touch the left vertical line without being above the upper horizontal line. In other words, we wish to pin down the particles that can meet the PAMELA positron excess without violating antiproton bounds. Candidates lying above the diagonal line in Figure 5.8 cannot. For the DM distribution suggested by Via Lactea II the model labelled MDM3 is disfavoured. The situation for Aquarius is similar, but more constraining. Lastly, leptophilic candidates produce no antiprotons and automatically pass the $\bar{p}$ test; they are plotted in Figure 5.8 for completeness and with an artificial $\phi_{\bar{p}}$. The exception is NT1 model that features a non-zero BR($s \to b\bar{b}$), even though the corresponding antiproton flux is rather low.

As mentioned above, Figure 5.8 refers to the MED propagation parameters. From Figure 5.7 one sees that at 50 GeV the positron flux is not very sensitive to the propagation parameters, while the antiproton flux at 50 GeV may be roughly one order of magnitude above or below the flux computed with MED. Since the antiproton bound will turn out to be the less constraining one, we can safely stick to the MED propagation in presenting our main results.

5.6.4 Gamma-rays

The flux of $\gamma-$rays is calculated according to equation (5.9). When including the Sommerfeld enhancement of the annihilation cross-section, the term $\langle\sigma_{ann}v\rangle$ in equation (5.9) is replaced by the velocity-dependent expression $\langle\sigma_{ann}v\rangle_0 S(\vec{x}, M)$, where M is the halo mass and $\vec{x}$ is the coordinate within it. The enhancement S depends on the halo mass and radial coordinate inside the halo, which takes into account the features of the velocity dispersion curve that has lower values closer to Galactic Centre – see e.g. [259]. Therefore, the line-of-sight integral in equation (5.9) becomes

$$\int_{\Delta\Omega} d\Omega \int_{\text{l.o.s.}} ds\ S(\vec{x}, M)\rho^2(\vec{x}, M) \quad . \tag{5.21}$$

We compute the prompt γ-rays coming from DM annihilation in the smooth halo and the subhalo population of our Galaxy.

The HESS telescope has observed the GC source in 2003 and 2004, measuring an integrated flux above 160 GeV of $\Phi(> 160\text{ GeV}) = 1.89 \times 10^{-11}$ cm^{-2}s^{-1} [230]. In Figure 5.9 we show the result of our computation for the particle physics models of Table 5.3, in the cases where the Milky Way halo is described by either the VL2 or the Aquarius setups. Also shown is a table with the expected flux above 160 GeV at the GC, for direct comparison with the HESS limit. Considering $\langle\sigma_{ann}v\rangle_0 = 3 \times 10^{-26}$ cm^{3}s^{-1}, the $\tau\tau$ candidate is ruled out while the $\mu\mu$ candidate is at odds with HESS measurement for the Aquarius setup.

We model the subhalo population according to subsection 5.1.3 and consider subhalo masses down to $M_{min} = 10^{-6}$ M$_\odot$. The number of photons from annihilations in galactic substructure is shown in Figure 5.10, where the expected flux from the subhalos is compared with the EGRET diffuse emission (galactic + extragalactic) background. Although the EGRET flux has been rescaled down by ∼15% in the light of the new measurement

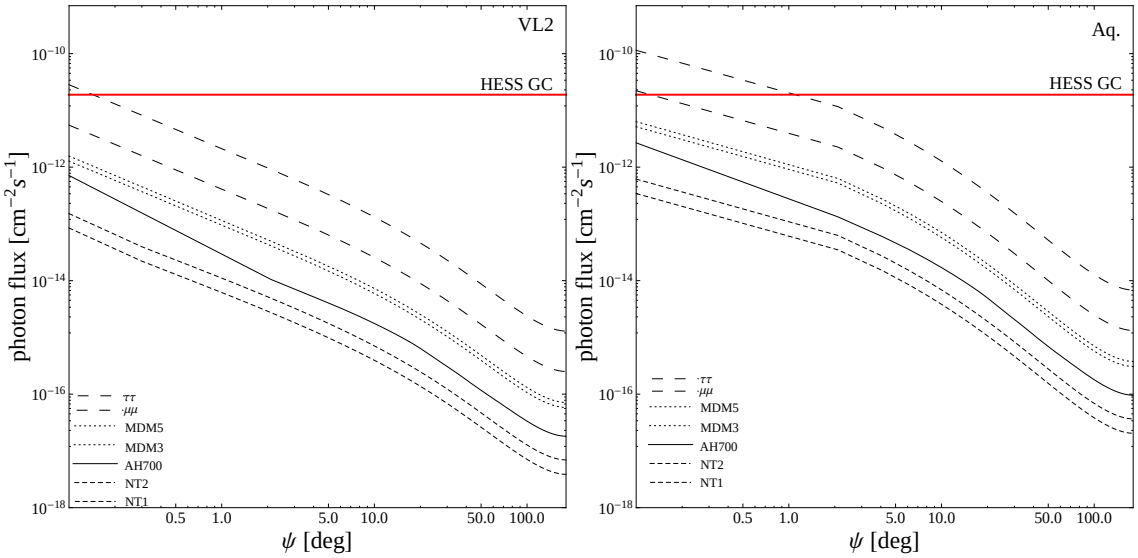

label	$\phi_{MW}(\psi = 0°)$ [cm^{-2}s^{-1}] Via Lactea II	Aquarius
AH700	$1.15 \cdot 10^{-12}$	$3.38 \cdot 10^{-12}$
NT1	$1.33 \cdot 10^{-13}$	$4.16 \cdot 10^{-13}$
NT2	$2.39 \cdot 10^{-13}$	$7.47 \cdot 10^{-13}$
$\mu\mu$	$8.67 \cdot 10^{-12}$	$2.70 \cdot 10^{-11}$
$\tau\tau$	$4.47 \cdot 10^{-11}$	$1.39 \cdot 10^{-10}$
MDM3	$2.01 \cdot 10^{-12}$	$6.25 \cdot 10^{-12}$
MDM5	$2.47 \cdot 10^{-12}$	$7.69 \cdot 10^{-12}$
HESS GC	$1.89 \cdot 10^{-11}$	

Figure 5.9: The γ-ray flux above 160 GeV as a function of the angle ψ with respect to the GC. The legend in the plots is ordered according to the values of the curves at $\psi = 0.1°$. The HESS measurement towards the GC is shown by the horizontal thick line and the table shows the fluxes for $\psi = 0°$.

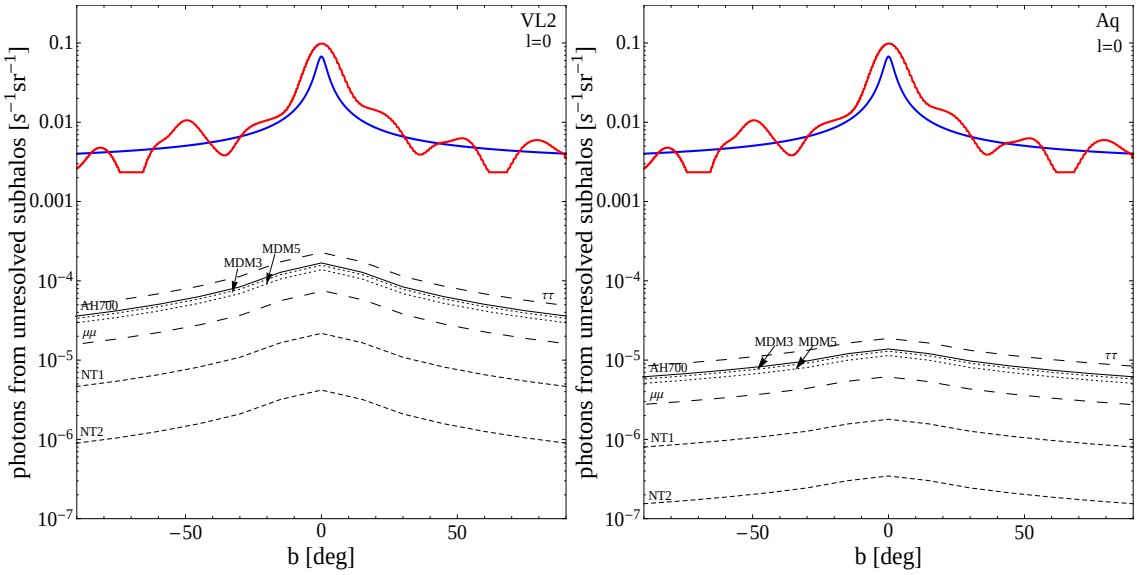

Figure 5.10: Number of photons above 3 GeV from unresolved subhalos at a galactic longitude $l = 0°$ for Via Lactea II and Aquarius parameters. Again, we fix $M_{min} = 10^{-6}$ M$_\odot$. Shown in thick solid are the EGRET map for diffuse background as well as the smooth approximation of reference [53], both scaled to Fermi results.

from the Fermi telescope which does not confirm the GeV bump, the diffuse emission measurements turn out to be less constraining than the GC one.

Note that our bounds refer to prompt γ-rays only. DM annihilations in extragalactic halos and subhalos can also give rise to a γ-ray flux by producing high-energy electrons and positrons that up-scatter CMB photons. This inverse Compton scattering contribution is particularly relevant for leptophilic models and has been computed in [260, 261] where it has been shown that COMPTEL and EGRET extragalactic observations place interesting limits on DM annihilation cross-sections. These constraints are competitive with the ones derived here with prompt γ-rays from the Galactic Centre. Another effect of the presence of inverse Compton photons is the ionisation of the baryonic gas after recombination and thus the decrease of the CMB optical depth – see Refs. [262, 263].

5.6.5 Synchrotron radiation

Synchrotron emission arises from relativistic electrons and positrons propagating in the galactic magnetic field. Since all annihilation channels usually considered produce high-energy electrons and positrons, a DM-induced synchrotron signal is expected from regions of the Galaxy where a substantial magnetic field is active and the Dark Matter density is significant – see e.g. [264, 55, 210]. Let us focus on a region towards the Galactic Centre, small enough so that diffusion does not play an important role and where the galactic magnetic field is strong enough to neglect electron (and positron) energy losses other than synchrotron emission. Assuming further that advection is negligible as in [55, 210], the steady-state distribution of electrons and positrons is given by equation (5.10). Now, using the synchrotron spectrum and definitions introduced in Section 4.2.3, the total synchrotron power emitted by the distribution of DM-induced electrons and

positrons reads

$$\nu \frac{d\tilde{W}_{syn}}{d\nu} = \int_{V_{obs}} dV \int_{m_e}^{m_\chi} dE\, n_{e^\pm}(\mathbf{x}, E)\, \nu \frac{dW_{syn}}{d\nu}(\mathbf{x}, E)$$
$$= \frac{\langle \sigma_{ann} v \rangle}{2m_\chi^2} \int_{V_{obs}} dV\, \rho^2(\mathbf{x})\, E_p(\mathbf{x}, \nu)\, \frac{N_{e^\pm}(> E_p)}{2}\,, \tag{5.22}$$

where in the last step equation (4.26) was used.

It was pointed out in [55] that low-frequency radio constraints do not depend much on the magnetic field profile adopted. Following that work, we choose to implement a constant $B = 7.2$ mG inside the accretion region $r \leq R_{acc} = 0.04$ pc, $B \propto r^{-2}$ for $R_{acc} < r < 84.5 R_{acc}$ and $B = \mu$G for $r \geq 84.5 R_{acc}$.

In order to place constraints on $\langle \sigma_{ann} v \rangle / m_\chi^2$, we consider the three configurations studied in [265]: a cone of half-aperture 4" pointed at the GC and $\nu = 0.408$ GHz (case 1), a region with angles from the GC between 5' and 10' and $\nu = 0.327$ GHz (case 2), and finally a cone of half-aperture 13.5' pointed at the GC and $\nu = 0.327$ GHz (case 3). We use the measured fluxes quoted in [265]. It turns out that, independently of the annihilation channel, case 1 gives the most stringent bounds when using the NFW smooth profile suggested by Via Lactea II simulation. For the Aquarius simulation and its Einasto smooth profile, case 2 is the most constraining one.

In principle, for DM particles with Sommerfeld-enhanced cross-sections, a full calculation of the synchrotron emission should include the enhancement $S(v)$ inside the integral in expression (5.22). Nevertheless, for our present proposes it suffices to put $\langle \sigma_{ann} v \rangle \sim S(v_\odot) \langle \sigma_{ann} v \rangle_0$ since the signal comes mainly from regions where $v \sim v_\odot$ – recall that $v \sim v_\odot$ at $r = R_{acc} = 0.04$ pc. In case 1, for instance, one is looking into a region of size ~ 0.16 pc around the GC. The region defined in case 2 encompasses distances of $\sim 10 - 20$ pc from the GC where $v < v_\odot$ and $S(v) \geq S(v_\odot)$; hence, in this case, considering $\langle \sigma_{ann} v \rangle \sim S(v_\odot) \langle \sigma_{ann} v \rangle_0$ yields actually a lower bound on the radio flux.

The results for the radio flux (case 1 for Via Lactea II and case 2 for Aquarius) are presented in Figure 5.11, plotted against the corresponding positron fluxes at 50 GeV. In the case of Via Lactea II, we can see that most candidates seem to be at odds with radio observations even when a rescaling of $\langle \sigma_{ann} v \rangle_0$ is applied to meet the positron excess. The situation for Aquarius (using case 2) is similar.

5.6.6 Conclusions

Table 5.4 summarizes our main results. There, we present for each model under consideration the maximum $\langle \sigma_{ann} v \rangle_0$ allowed by the antiproton bound, the HESS measurement from the GC and radio observations. For antiprotons we conservatively use the largest value in equation (5.20). The most constraining of the three limits, i.e. the one yielding a minimal $\langle \sigma_{ann} v \rangle_{0,max}$, is displayed in bold. We have disregarded here diffuse γ-rays as well as radio fluxes in the cases 2 and 3 (1 and 3) for Via Lactea II (Aquarius) since they give subdominant contraints. Furthermore, the e^+ column shows the value of $\langle \sigma_{ann} v \rangle_0$ needed to meet the lowest positron flux in equation (5.19); these numbers are underlined only if allowed by the most stringent bound in bold. Notice that we apply this procedure to MDM3 and MDM5 even though minimal Dark Matter is a rather predictive scheme.

Firstly, we immediately see from Table 5.4 that radio observations are rather con-

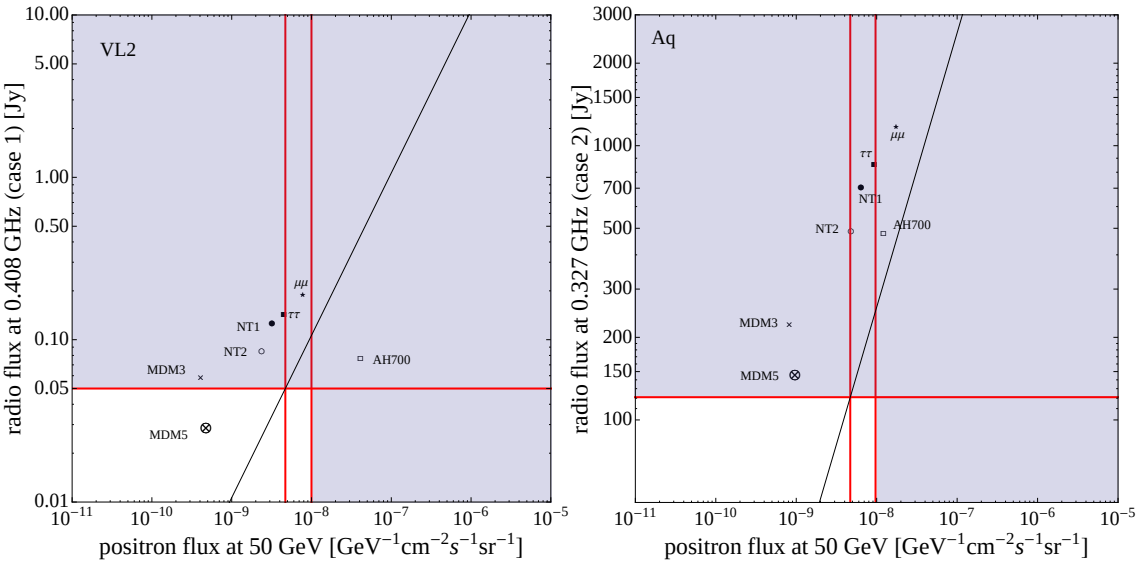

Figure 5.11: The radio flux for case 1 (2) and Via Lactea II (Aquarius) parameters against the positron flux at 50 GeV already presented in Figure 5.8. The MED propagation is used and $M_{min} = 10^{-6}$ M$_\odot$. The horizontal line indicates the measured flux (see [265] for details). Similarly to Figure 5.8, candidates lying above the diagonal line cannot be rescaled to explain PAMELA positron excess without violating radio bounds. Shaded regions are excluded by PAMELA (assuming the electron fluxes discussed in the text) and radio observations.

	$\langle\sigma_{ann}v\rangle_{0,max}/(10^{-26}\text{cm}^3\text{s}^{-1})$							
	Via Lactea II				Aquarius			
label	e^+	$\bar{p}$	γ GC	radio (1)	e^+	$\bar{p}$	γ GC	radio (2)
AH700	<u>0.34</u>	–	49	**2.0**	1.2	–	17	**0.76**
NT1	4.4	840	427	**1.2**	2.2	200	136	**0.51**
NT2	6.0	–	238	**1.8**	2.9	–	76	**0.74**
$\mu\mu$	1.8	–	6.5	**0.80**	0.81	–	2.1	**0.31**
$\tau\tau$	3.1	–	1.3	**1.1**	1.5	–	**0.41**	0.43
MDM3	12	7.9	9.4	**0.86**	5.7	1.9	3.0	**0.54**
MDM5	9.9	69	7.7	**1.7**	4.9	18	2.5	**0.82**

Table 5.4: The maximum allowed $(\sigma_{ann}v)_0$ by the antiproton bound, the γ-ray measurement from the GC and radio observations. The MED propagation is used and $M_{min} = 10^{-6}$ M$_\odot$. The bold values represent the most constraining channel and the e^+ columns display the $\langle\sigma_{ann}v\rangle_0$ needed to meet the positron excess. Underlined values manage to explain the positron excess while being allowed by our multi-messenger scheme of constraints.

straining with respect to antiprotons or γ-rays for models trying to explain the positron excess. In the case of Via Lactea II DM distribution, just one candidate survives the studied bounds: AH700. There is still some tension with the data though. In fact, in order to fit the PAMELA data, this model needs to be rescaled down to $\langle\sigma_{ann}v\rangle_0$ of $\sim 10^{-27}$ cm^{3}s^{-1}, which means either that such particles would overclose the Universe in the standard thermal relic scenario, or that they are prevented to be the dominant Dark Matter component in the Universe. As far as Aquarius is concerned, we identify no model that can evade all the implemented bounds.

In Figure 5.12 we introduce a new method to visualise the multi-messenger constraints. We place each of the channels in a semi-axis and normalise it to the experimental limits. Since we are interested in the viability of the DM explanation of the positron excess, we only show models that are able to reproduce the observed PAMELA flux, and thus cross the "up" axis at 1. Configurations exceeding the boxes on other axes violate observational bounds and are therefore ruled out. Configurations not crossing the boxes are in principle viable, but one has to check then whether the cross-section allows to achieve the appropriate relic abundance, whether the "boost-factors" are reasonable, and whether the

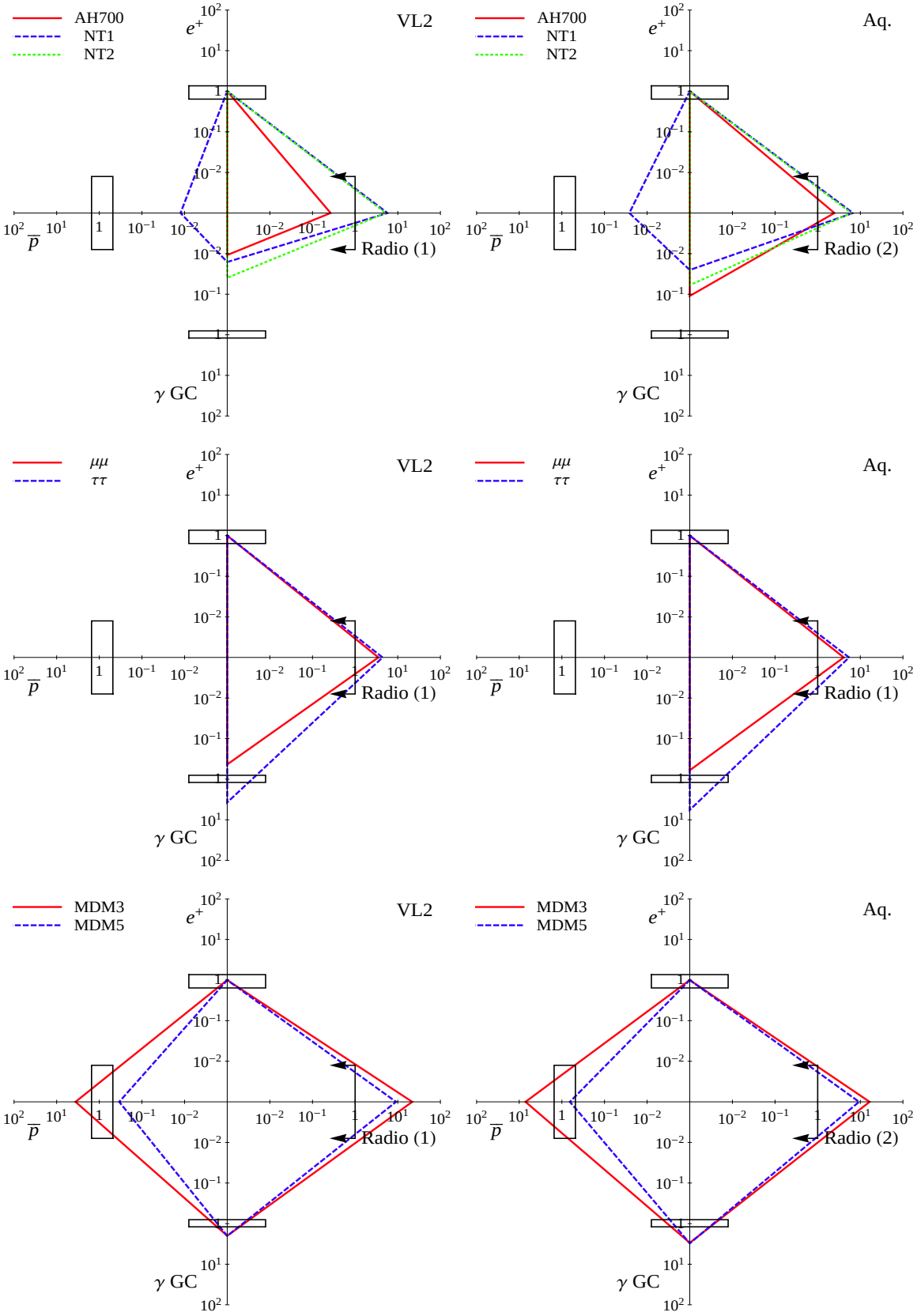

Figure 5.12: Multi-messenger bounds for several DM candidates. The MED propagation is used and $M_{min} = 10^{-6}\,\mathrm{M}_\odot$. The e^+, $\bar{p}$, γ-ray, radio (cases 1 and 2) axes are normalised to $\phi_{e^+}(50\ \mathrm{GeV}) = 7.35 \cdot 10^{-9}\ \mathrm{GeV}^{-1}\mathrm{cm}^{-2}\mathrm{s}^{-1}\mathrm{sr}^{-1}$, $\phi_{\bar{p}}(50\ \mathrm{GeV}) = 5.2 \cdot 10^{-9}\ \mathrm{GeV}^{-1}\mathrm{cm}^{-2}\mathrm{s}^{-1}\mathrm{sr}^{-1}$, $\phi_{MW}(\psi = 0°) = 1.89 \cdot 10^{-11}\mathrm{cm}^{-2}\mathrm{s}^{-1}$, 0.05 Jy and 121 Jy, respectively. The boxes encompass the values in equations (5.19) and (5.20) for positrons and antiprotons, and a 20% uncertainty on top of the HESS measurement for γ-rays. Notice that changing the value of $\langle\sigma_{ann}v\rangle_0$ leads to an overall scaling of the polygon.

model provides a good fit to *all* PAMELA data. We stress that once the model is specified, the shape of the polygon in Figure 5.12 (angles and number of vertices) is fixed, and changing the cross-section corresponds to increasing or decreasing its overall size. Note for instance that leptophilic configurations (first and second rows of Figure 5.12) have a different shape with respect to hadrophilic ones (third row).

To sum up, we have analysed the possibility that the models in Table 5.3, recently suggested in the literature, may explain the PAMELA positron excess without violating bounds in the antiproton, γ-ray and radio channels. It turns out that − even considering both substructure and Sommerfeld enhancement − the candidates that provide a good fit to positron data, inevitably overproduce antiprotons, gamma-rays or radio emission. Our conclusions hold for the DM distributions from Via Lactea II and Aquarius simulations, the MED propagation model and $M_{min} = 10^{-6}$ $M_\odot$. As discussed in subsection 5.6.3, modifying the propagation parameters does not change our main results. This is because the antiproton bound − the most sensitive to propagation − is subdominant. Thus, a different propagation model is not sufficient to reconcile the studied candidates with the observational constraints. A non-standard DM profile, and a non-standard magnetic field profile at the Galactic Centre, can in principle make theoretical models compatible with observations, at the expenses of introducing new ad-hoc hypotheses on these quantities.

5.7 Paper V: Discriminating the source of high-energy positrons with AMS-02[4]

We study the prospects for discriminating between the Dark Matter and pulsar origin of the PAMELA positron excess with the Alpha Magnetic Spectrometer AMS-02. We simulate the response of AMS-02 to positrons (and electrons) originating from DM annihilations, and determine the pulsar parameters (spin-down luminosity, distance and characteristic age) that produce a satisfactory fit to the mock AMS-02 data. It turns out that it is always possible to mimic a DM signal with pulsars. Although the fit in some cases requires values of spin-down luminosity and characteristic age different from those of known pulsars in the ATNF and Fermi-LAT catalogues, these catalogues are known to be incomplete, and therefore the pulsar interpretation can hardly be ruled out. We also show that if the positron excess is due to a single pulsar, it is always possible to find a DM candidate that provides a good fit to the mock AMS-02 data. The discrimination between the two scenarios will thus require a better knowledge of the underlying sources, or complementary data.

5.7.1 Overview

The nature of high-energy cosmic ray electrons and positrons remains an open problem in modern astrophysics and it is currently a matter of intense debate. Data accumulated over the years led to the description of the electronic component in local cosmic rays as a single power-law with spectral index around 3.4 at multi-GeV energies [266], where positrons are much less abundant than electrons. A standard picture has therefore emerged to explain the local flux of cosmic ray electrons and positrons in the context of galactic

[4]This Section is based on the article [5], done in collaboration with Massimiliano Lattanzi and Gianfranco Bertone.

cosmic ray propagation. In this framework, positrons result from the inelastic scattering of cosmic ray protons and nuclei against the interstellar gas in our Galaxy (mainly H and He nuclei), and then diffuse and lose energy before arriving at the Earth. Electrons instead are believed to be primaries, presumably accelerated in supernova remnants [64] and injected into the interstellar medium. In the standard picture, the propagation of this injection spectrum would lead to the bulk of the local cosmic ray electrons.

Several hints, however, have challenged over the years the secondary nature of high-energy cosmic positrons, in particular the results of CAPRICE [239] and HEAT [238, 247] that indicate a rather large positron fraction at multi-GeV energies. In the last few years, a host of observations of high-energy electrons and positrons has become available, including results from ATIC [242], PPB-BETS [267], PAMELA [241, 268], Fermi-LAT [243, 244] and H.E.S.S. [269, 245]. PAMELA, for instance, has measured a steeply rising positron fraction above $\sim$10 GeV and up to $\sim$100 GeV. Fermi-LAT results, on the other hand, show an electron plus positron flux of spectral index $\sim$3.0 above $\sim$20 GeV and with a possible hardening at about 300 GeV, while H.E.S.S. hints at a cutoff of a few TeV. This so-called electron/positron excess is at odds with the standard picture described above. In fact, cosmic ray spallation on the galactic disk fails to produce enough positrons and, more importantly, is incompatible with a positron fraction that rises with increasing energies [162, 270]. As pointed out in [271], one needs one or more nearby and recent sources to accommodate the data. This is because $\sim$100 GeV positrons (and electrons) lose energy efficiently through inverse Compton scattering and synchrotron emission, presenting a cooling time of about $\sim 2 \times 10^6$ yr which translates into kpc-scale diffusion distances. Several possible sources were put forward many years ago and recently revisited in the light of new electron-positron data.

One of the most popular hypotheses is to invoke Dark Matter annihilations [252] or decays [214] in the galactic halo. Such annihilations or decays would produce high-energy electrons and positrons either directly or through the decay of secondary particles. Although exciting, this interpretation requires non-standard Dark Matter properties – such as high annihilation cross-sections [272, 273, 219, 274, 275, 276] – that are in tension with other data, including radio emission and γ-rays [55, 260, 261, 4] as seen in the last Section, or Cosmic Microwave Background measurements [277, 278, 263]. Moreover, the DM interpretation requires annihilation mainly to leptonic channels in order to be consistent with the data on the antiproton flux, that itself is completely consistent with what is expected from secondary production [252, 54]. Another possible origin for the excess is the emission of electrons and positrons from mature pulsars [271, 279, 183, 280, 281]. Indeed, electrons can be accelerated in the magnetosphere of pulsars and, due to the existing magnetic fields, emit curvature radiation which will generate $e^{\pm}$ pairs and subsequently an electromagnetic cascade. The uncertainties inherent to this scenario are significant, but it is very likely that one or more known pulsars contribute non-negligibly to the flux of cosmic ray electrons and positrons [282] – check Ref. [283] for the implications of recent γ-ray observations of supernova remnants and pulsar wind nebulae on the positron fraction (and antiproton-to-proton ratio). A third hypothesis, put forward in Refs. [284, 285], posits that secondary particles are accelerated in the sites where hadronic primary cosmic rays are injected. If secondary particles (including electrons and positrons, but also antiprotons, boron and beryllium) are created in the acceleration site by spallation of primaries on the surrounding medium, then they will be accelerated themselves to high energies. A neat feature of this mechanism is that

it can be easily tested since, besides a rising positron fraction, also rising secondary-to-primary ratios are predicted [286]. Still other possibilities exist to accommodate the electron/positron excess, see e.g. Section I of Ref. [280] for an overview. In the following, we shall consider only the DM and the pulsar interpretations.

The main goal of the present work is to assess whether upcoming measurements of cosmic ray electrons and positrons will be sufficient to discriminate between different origins of the electron/positron excess. It is often claimed (see e.g. [287]) that DM annihilations directly into e^+e^- – that produce a sharp spectral cutoff at the mass of the DM particle – can be distinguished from a single pulsar spectrum with future data. Here, we start by assuming DM annihilations into leptons as the source of the cosmic ray lepton excess, anticipate upcoming measurements and evaluate to what degree one can discard the single pulsar hypothesis in that case. The inverse problem is also explored: assuming that the origin of the excess is a pulsar, and thus that a pulsar-like cut-off is detected, we quantify how well one can reject the DM hypothesis. Several DM masses are considered and, besides direct annihilation into electron-positron pairs, democratic annihilation into leptons (33% e^+e^-, 33% $\mu^+\mu^-$, 33% $\tau^+\tau^-$) is also considered. In order to study the role of known pulsars, we make use of the ATNF catalogue [288] and the γ-ray pulsars discovered by Fermi-LAT [289, 290]. Furthermore, the anisotropy potentially produced by individual pulsars is also discussed as a discriminating tool.

We model the response of the Alpha Magnetic Spectrometer AMS-02 [179], scheduled to be installed in the International Space Station in 2011, including both systematic and statistical uncertainties. Future balloon-borne and ground-based experiments may also prove useful in measuring high-energy electrons and positrons, but we shall not consider them here since the associated systematics are likely larger than for AMS-02 (due to the influence of the atmosphere).

Several experimental results have been used along the work, namely measurements of the electron flux (CAPRICE [239], HEAT [291], AMS-01 [292]), the positron flux (CAPRICE [239], HEAT [291], AMS-01 [292]), the electron plus positron flux (HEAT [291], BETS [293], PPB-BETS [267], ATIC [242], H.E.S.S. [269, 245], Fermi-LAT [243, 244]), and the positron fraction (CAPRICE [239], HEAT [238, 247], AMS-01 [240], PAMELA [268]).

5.7.2 Injection and propagation of high-energy electrons and positrons

High-energy electrons and positrons in the galactic medium are mainly affected by two processes in their way to Earth: energy losses and diffusion. Energy losses in the multi-GeV range are dominated by inverse Compton scattering off Cosmic Microwave Background, optical and infrared photons, and synchrotron emission. In the Thomson limit, these losses amount globally to $b(E) \simeq b_0 E^2$ with $b_0 \sim 1.4 \times 10^{-16}$ GeV^{-1}s^{-1}. Diffusion instead is caused by the galactic magnetic irregularities and it is usually parametrized with a homogeneous power-law diffusion coefficient $D(E) = D_0 (E/\mathrm{GeV})^\alpha$. Under these assumptions and neglecting convection and reacceleration, the number density of electrons and positrons per unit energy $n(\mathbf{x}, E, t)$ is driven by the transport equation[5]

$$\frac{\partial n}{\partial t} = Q(\mathbf{x}, E, t) + D(E)\nabla^2 n + \frac{\partial}{\partial E}\left[b(E) n\right] \quad , \tag{5.23}$$

[5]This is formally the same equation as (5.11), but we repeat it here for clarity in the rest of the Section.

Q being the source term. Usually this equation is solved in steady state conditions ($\partial n/\partial t = 0$) and inside a cylindrical diffusive halo of half-thickness L. The local interstellar flux then follows directly from the solution of equation (5.23) through $\phi(\mathbf{x}_\odot, E) = \frac{v}{4\pi} n(\mathbf{x}_\odot, E)$, where $\mathbf{x}_\odot$ is the position of the solar system in galactic coordinates.

In this subsection we briefly review the strategies adopted to compute the propagated injection spectra of electrons and positrons from each of the sources studied: DM annihilations and pulsar emission. On top of the flux generated by each source, one has of course to take into account the baseline astrophysical flux described in the previous subsection, where positrons are merely a by-product of the spallation of hadronic cosmic rays on the disk and electrons derive mainly from a galactic primary component. We shall refer to these standard yields as "background" since we are interested in the electron/positron excess. In order to be roughly compatible with Fermi-LAT measurements while not explaining the rising positron fraction observed by PAMELA [241, 268], we use "model 1" of Ref. [294] as our background reference setup. This model features a common high-energy injection index of 2.42 for electrons (above 4 GeV) and nuclei (above 9 GV), and the propagation parameters are fixed to the following values: $L = 4$ kpc, $D_0 = 3.6 \times 10^{28}$ cm^2/s and $\alpha = 0.33$. As in [294], we use GALPROP [167, 153] (version 50.1p) to compute the local fluxes of background electrons and positrons within the framework just described, and normalise to Fermi-LAT $e^\pm$ measurements at 100 GeV.

Before arriving at the top of the atmosphere, low-energy charged particles such as electrons and positrons are modulated by the solar wind. Our analysis focuses on energies above 10 GeV so that this effect is minimal. Nevertheless, all fluxes are modulated according to the force field approximation [170] with a potential $\phi_F = 550$ MV.

It is worth stressing that, even though different methods are used to compute the propagated fluxes of each source and background, the propagation parameters are kept fixed to the values mentioned above, and therefore our analysis is performed in a consistent propagation framework. However, as extensively discussed in the literature, the parameters L, D_0 and α are not well-constrained by present cosmic-ray data, and hence the propagation configuration we use is not unique. Adopting other propagation parameters would affect differently the local fluxes of background, Dark Matter and pulsar electrons and positrons, but our results are representative of typical propagation models. Moreover, taking into account the uncertainties in the propagation parameters would add flexibility to fit the data and therefore strengthen our results. In the future it would be interesting to study how the AMS-02 ability to discriminate high-energy electron-positron sources depends on propagation details, perhaps using already the cosmic-ray nuclei measurements that will hopefully be provided by AMS-02 itself (see Section 4.5). Along these lines, another matter that deserves further investigation is the impact of the hardening of the proton and helium fluxes recently reported by CREAM [175] and ATIC [174] at $\sim$ TeV/n energies (see also [176, 177, 178]).

Dark Matter annihilations

If Dark Matter is composed of annihilating WIMPs, the galactic halo should be regarded as a continuous, nearby source of electrons and positrons. WIMPs of mass m_χ and total averaged annihilation cross-section times velocity $\langle \sigma_{ann} v \rangle$ give rise to a constant source term (5.2).

The distribution of Dark Matter in the Milky Way is poorly constrained by observations, but one can learn a great deal with the help of numerical simulations. In particular,

one strong prediction of pure cold Dark Matter simulations is a large galactic population of virialised clumps in addition to a smooth halo component. Here, the DM density $\rho(\mathbf{x})$ is modelled according to the high-resolution Dark Matter only simulation Via Lactea II [220], where the smooth+clumpy distribution is well fitted by a Navarro-Frenk-White profile and the abundance of subhalos of mass M is proportional to M^{-2}. Within this setup, the spherically averaged local smooth DM density is $\rho_0 = 0.41$ GeV/cm^3 [4, 6], and we extrapolate the results of the simulation down to a minimal subhalo mass of 10^{-6} $M_\odot$ which is a fiducial value for WIMPs [18] even though it may vary by several orders of magnitude [37]. Further technical details can be found in 5.1.3.

Now, the transport equation (5.23) with source term (5.2) can be solved semi-analytically. We use the formulae derived in Section 5.3 to compute the local flux of electrons and positrons created by DM annihilations in the smooth and clumpy components. Notice that the so-called substructure boost factor – which quantifies the enhancement in the annihilation flux due to the presence of DM clumps with respect to the smooth only case – is not a constant, but rather an energy- and particle-dependent function [222]. Also, unlike sometimes assumed, it amounts to small rather than large enhancements.

We wish to point out that the distribution of DM particles in our Galaxy is uncertain, for what concerns the radial profile, the substructure population as well as the local DM density. However, such uncertainties are not crucial for our work and do not change our conclusions since different DM distributions or local densities would simply correspond to different normalisations $\langle\sigma_{ann}v\rangle$ and thus would produce essentially the same spectral features (unless the unlikely case of a nearby, massive clump is considered).

Two annihilation channels will be studied in the present paper: *direct annihilation* to e^+e^-, and *democratic annihilation* to charged leptons (i.e. $BR_{e^+e^-} = BR_{\mu^+\mu^-} = BR_{\tau^+\tau^-} = 1/3$). While in the former case the injection spectrum of electrons and positrons is simply a Dirac delta at $E = m_\chi$, the latter model injects $e^\pm$ pairs with a broad range of energies up to m_χ. Indeed, muons decay almost entirely to electrons and taus decay either to electrons, or to muons and hadronic particles that subsequently generate more electrons.

Other annihilation channels such as light quarks or gauge bosons are not considered because they lead to less characteristic features in the electron-positron spectrum and are thus more challenging to discriminate. Moreover, when normalized to the PAMELA positron fraction, models with annihilation to light quarks or gauge bosons usually produce an unacceptably large antiproton flux, at variance with observations [252, 54]. Note that the annihilation modes under study, i.e. direct annihilation to leptons only, are difficult to realise in the context of minimal supersymmetrical models, but are typical of the so-called *leptophilic DM models* [295], where tree-level DM annihilations to states other than leptons are forbidden by an *ad hoc* symmetry (see also [296] for a supersymmetric implementation of leptophilic DM). Models of Kaluza-Klein (KK) DM also preferentially annihilate to charged leptons in a democratic way and, despite the significant branching ratio to hadronic channels, can satisfy the constraints on the antiproton flux [297].

In this framework, for each annihilation model there are thus two free parameters in our analysis: the DM mass m_χ and the annihilation cross-section $\langle\sigma_{ann}v\rangle$ (the latter entering basically as a normalisation factor). We shall use both in a model-independent, phenomenological manner in the remainder of the work.

Pulsars

Pulsars are highly magnetised, rotating neutron stars. Their main observational feature is the emission of pulsed and directional electromagnetic radiation (from radio photons to γ-rays) which suggests that the magnetic and rotation axes are misaligned. Unlike Dark Matter, pulsars are known sources of high-energy electrons and positrons, being thus a natural class of candidates to explain the cosmic ray lepton excess as pursued for example in Refs. [183, 280, 294]. In fact, the magnetosphere of a pulsar can easily host potential gaps in excess of 10^{12} V which accelerate primary electrons to TeV energies or above. These electrons quickly emit synchrotron and/or curvature radiation in the strong magnetic field, or upscatter background (radio, microwave, infrared or X-ray) photons to TeV-scale energies. Such γ-rays in turn are likely to interact with existing low energy photons or the magnetic fields and create high-energy $e^{\pm}$ pairs that subsequently generate an electromagnetic cascade. Further acceleration may also occur in the nebula or remnant surrounding the pulsar. Consequently, along with γ-rays (that have been detected), pulsars are very credible sources of high-energy cosmic ray electrons and positrons.

The rotation frequency of a pulsar $\Omega = 2\pi/P$ decreases with time so that its rotational energy is dissipated at a rate

$$\dot{E} = \frac{d}{dt}\left(\frac{1}{2}I\Omega^2\right) = I\Omega\dot{\Omega} \quad ,$$

where $I = \frac{2}{5}M_\star R_\star^2$ is the moment of inertia of a spherical pulsar with mass $M_\star$ and radius $R_\star$. *Magnetic braking*, that accounts for the energy lost by magnetic dipole emission, is certainly a mechanism contributing to this spin-down behaviour even though there might be others. This process amounts to an energy loss rate [64] $\dot{E}_{mag} = -(8\pi\Omega^4 R_\star^6 B_\star^2)/(3c^3\mu_0)$, where $B_\star$ is the magnetic field at the star surface. In the simple case where magnetic braking dominates the pulsar spin-down luminosity, one can write $\dot{E} \simeq \dot{E}_{mag}$ that leads to

$$\Omega(t) = \Omega_0\left(1 + \frac{t}{\tau_0}\right)^{-1/2} \quad , \tag{5.24}$$

Ω_0 being the initial ($t = 0$) rotational frequency and $\tau_0 = (3I\mu_0 c^3)/(16\pi R_\star^6 B_\star^2 \Omega_0^2)$. Notice that τ_0 is essentially the luminosity decay time since

$$\dot{E} = I\Omega\dot{\Omega} \propto (1 + t/\tau_0)^{-2} \quad .$$

Therefore, very old pulsars ($t \gg \tau_0$) – whose early $e^{\pm}$ emission has already diffused and diluted – are not very likely to contribute to the bulk of the present local flux. Put another way, local high-energy electrons and positrons must have been produced recently as argued in subsection 5.7.1. On the other hand, the electron-positron pairs produced by young pulsars need to diffuse through the pulsar nebula or the surrounding supernova remnant before reaching the ISM, which takes $t_0 \sim 10^4 - 10^5$ yr. The two opposite effects make mature pulsars – of ages around 10^5 yr – the dominant source of a pulsar-induced $e^{\pm}$ galactic flux, and hence we shall focus on this type of pulsars in the present work. Let us notice at this point that the escape of $e^{\pm}$ pairs into the ISM is not fully understood yet – an important step along this direction has been taken in [298].

The characteristic age of a pulsar is obtained by integrating $\dot{E} \simeq \dot{E}_{mag}$ under the assumption that the initial rotational frequency Ω_0 is very large ($\Omega_0 \gg \Omega$). This results

in the well-known expression $t_{ch} = -\Omega/(2\dot{\Omega}) = P/(2\dot{P})$. The actual age of the pulsar, t_{PSR}, may however differ from t_{ch}, the discrepancy being of order $10^4 - 10^5$ yr [280]. We shall disregard such discrepancy and identify t_{PSR} with t_{ch}.

A major ingredient to compute the yield of electron-positron pairs injected by pulsars is the electronic energy output

$$E_{e^\pm}(t_{ch}) = \eta_{e^\pm} \int_0^{t_{ch}} dt\, |\dot{E}| \quad ,$$

$\eta_{e^\pm}$ being the fraction of rotational energy transferred to electrons and positrons (we assume $\eta_{e^+} = \eta_{e^-} = \eta_{e^\pm}/2$). Using equation (5.24) and assuming $t_{ch} \gg \tau_0$ (roughly valid for mature pulsars), one obtains

$$E_{e^\pm}(t_{ch}) \simeq \eta_{e^\pm} \frac{I}{2} \Omega_0^2 \simeq \eta_{e^\pm} |\dot{E}| \frac{t_{ch}^2}{\tau_0} \quad , \tag{5.25}$$

where in the last step we have used the approximate behaviour of equation (5.24) for $t_{ch} \gg \tau_0$, $\Omega(t_{ch}) \simeq \Omega_0 \, (t_{ch}/\tau_0)^{-1/2}$. We have assumed here that the output in electron-positron pairs is proportional to the rotational energy loss. This needs not be the case; for alternative scenarios see e.g. Ref. [280].

As for the $e^\pm$ injection spectrum we use a rather phenomenological approach by considering a power-law with an exponential cutoff at high energies,

$$Q_{e^\pm}(E) = Q^0_{e^\pm} (E/\mathrm{GeV})^{-\Gamma} \exp(-E/E_{cut}) \quad .$$

Since electron-positron pairs and γ-rays are produced by the same physical process, the spectral index Γ is probably correlated to the spectral indices seen in γ-ray observations of pulsars, or other multi-wavelength measurements, which suggest $1 \lesssim \Gamma \lesssim 2$. The cutoff energy E_{cut} instead is usually placed above the TeV. Finally, the normalisation $Q^0_{e^\pm}$ is fixed by the output (5.25) through $E_{e^\pm}(t_{ch}) = \int_{m_e}^\infty dE\, E\, Q_{e^\pm}(E)$.

We now turn to the propagation of the injection spectrum just described. Pulsars may be modelled as bursting, point-like sources of $e^\pm$ pairs [279, 183, 280, 282, 294]. Indeed, the injection region is much smaller than the typical propagation distance covered by high-energy electrons and positrons, and the emission period is much shorter than the travel time to Earth. Thus, the source term reads

$$Q_{e^\pm}(\mathbf{x}, E, t) = Q_{e^\pm}(E) \delta(\mathbf{x} - \mathbf{r}_0) \delta(t - t_0) \quad , \tag{5.26}$$

in which $\mathbf{r}_0$ is the position of the pulsar and we shall consider times $t = t_{ch} \gg t_0$ as natural for mature pulsars. In addition, the problem assumes spherical symmetry if one considers local sources, namely at distances smaller than the half-thickness of the diffusive halo L. The effect of boundaries at $z = \pm L$ has been studied in [280] and shown to be negligible for the energies and pulsar ages of interest if $L > 1 - 2$ kpc. The spherically symmetric analytical solution of equation (5.23) was derived in Ref. [271] for arbitrary energy losses and injection spectrum. Applying that result with the source term (5.26), the local density of electrons and positrons is found to be

$$n_{e^\pm}(d, E, t_{ch}) = \frac{Q_{e^\pm}(E') b(E')}{b(E) \pi^{3/2} r^3_{dif}(E, t_{ch})} e^{-\frac{d^2}{r^2_{dif}(E, t_{ch})}} \, , \tag{5.27}$$

	Γ	E_{cut} [GeV]	$\lvert\dot{E}\rvert$ [erg/s]	t_{ch} [yr]	E_{max} [GeV]	d [kpc]	f
PSR1	1.7	1000	10^{35}	5×10^5	453	0.75	0.9
PSR2	1.3	1000	4×10^{34}	12×10^5	189	0.4	0.9
PSR3	1.7	500	8×10^{34}	3×10^5	755	0.2	0.9

Table 5.5: The pulsar fiducial setups. In all cases $\tau_0 = 10^4$ yr and $\eta_{e^\pm} = 0.4$ as explained in the text. f represents the background rescaling factor (see Section 5.7.4).

where $E'(E, t_{ch}) = E/(1 - E/E_{max}(t_{ch}))$ is the initial energy of a particle detected at energy E assuming $b(E) = b_0 E^2$, $E_{max}(t_{ch}) = 1/(b_0 t_{ch})$ is the maximum energy allowed by losses, d is the distance to the considered pulsar, and

$$\begin{aligned} r^2_{dif}(E,t) &= 4\int_E^{E'} d\tilde{E}\, D(\tilde{E})/b(\tilde{E}) \\ &= \frac{4D(E)tE_{max}(t)}{(1-\alpha)E}\left(1-\left(1-\frac{E}{E_{max}(t)}\right)^{1-\alpha}\right) . \end{aligned}$$

Replacing $Q_{e^\pm}$ and b in equation (5.27),

$$\begin{aligned} n_{e^\pm}(d,E,t_{ch}) =& \frac{Q^0_{e^\pm}(E/\mathrm{GeV})^{-\Gamma}}{\pi^{3/2} r^3_{dif}(E,t_{ch})}\left(1-\frac{E}{E_{max}(t_{ch})}\right)^{\Gamma-2} \\ & \times \exp\left(-\frac{E/E_{cut}}{1-E/E_{max}(t_{ch})} - \frac{d^2}{r^2_{dif}(E,t_{ch})}\right) \end{aligned} \tag{5.28}$$

for $E < E_{max}$, and 0 otherwise. Notice that $n_{e^-} = n_{e^+} = n_{e^\pm}/2$ since we are assuming $\eta_{e^+} = \eta_{e^-} = \eta_{e^\pm}/2$. It is worth pointing out that the spectrum in equation (5.28) features a cutoff at $\min(E_{max}, E_{cut})$. The nature and morphology of the cutoff is different in the two cases, $E_{max} \gtrless E_{cut}$. For instance, for very large cutoff energies E_{cut}, the maximum energy local electrons and positrons can reach is fixed by energy losses and is therefore a function of the pulsar age. To illustrate this point we pick the three fiducial pulsar setups in Table 5.5 that yield the positron fractions shown in Figure 5.13. Notice the different cutoff steepness in the each case – we shall return to this issue later on.

Despite the fact that diffusion erases the initial direction of charged particles, the output of a pulsar still creates a dipole anisotropy on the cosmic ray electron-positron sky. Given a certain direction in the sky, let N_{max} denote the number of detected photons in the hemisphere centred in that direction, and N_{min} the number of photons in the opposite hemisphere. The size of the anisotropy is energy-dependent and given by

$$\delta_{e^\pm} = \frac{N_{max} - N_{min}}{N_{max} + N_{min}} = \frac{3D(E)|\vec{\nabla} n_{e^\pm}(E)|}{c n^{tot}_{e^\pm}} \quad ,$$

$n^{tot}_{e^\pm}$ being the sum of the pulsar signal $n_{e^\pm}$ and the background. Applying equation (5.28) one readily obtains

$$\delta_{e^\pm}(d,E,t_{ch}) = \frac{6D(E)d}{c\, r^2_{dif}(E,t_{ch})} \frac{n_{e^\pm}(d,E,t_{ch})}{n^{tot}_{e^\pm}(d,E,t_{ch})} \quad . \tag{5.29}$$

The expressions for the electron- or positron-only anisotropies are analogous.

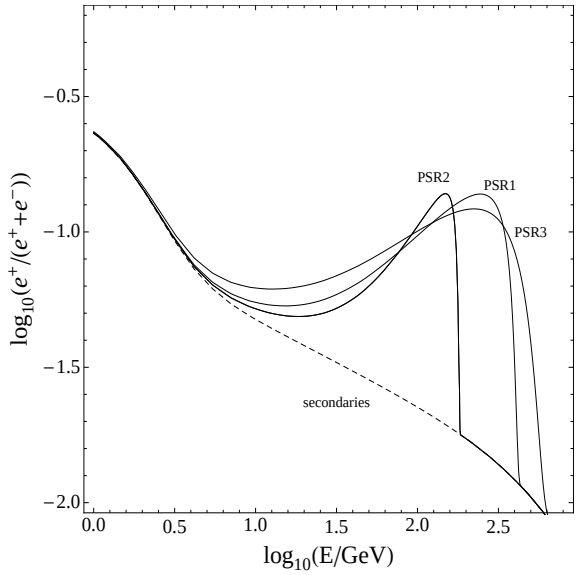

Figure 5.13: The positron fraction produced by the three pulsar fiducial models indicated in Table 5.5. The solid (dashed) line shows the total (background) contribution. In order of increasing cutoff energies, the plotted curves correspond to PSR2, PSR1 and PSR3.

In order to explore the possible features of the electron-positron spectrum generated by mature pulsars we scan the parameter space defined by the spin-down luminosity $|\dot{E}|$, the distance d and the characteristic age t_{ch} in the ranges $|\dot{E}| = 10^{32} - 10^{36}$ erg/s, $d = 0.1 - 5$ kpc and $t_{ch} = 10^4 - 10^7$ yr. Following [280, 282], we adopt $\tau_0 = 10^4$ yr and the rather large $e^{\pm}$ fractional output $\eta_{e^{\pm}} = 0.4$. Notice however that τ_0 and $\eta_{e^{\pm}}$ are both degenerate with $|\dot{E}|$ for mature pulsars − check equation (5.25) − so that our results may be simply rescaled to account for different values of $\eta_{e^{\pm}}$ for instance. For the spectral injection index and the cutoff energy we take the reference values $\Gamma = 1.7$ and $E_{cut} = 1$ TeV, but we also address the effect of varying these parameters in the ranges $1.3 \leq \Gamma \leq 1.9$ and $0.5 \leq E_{cut} \leq 10$ TeV. Once $|\dot{E}|$, d, t_{ch}, $\eta_{e^{\pm}}$, τ_0, Γ and E_{cut} are specified, the local flux of high-energy electrons and positrons produced by a single mature pulsar is unambiguously fixed through equation (5.28).

Throughout the work we shall use the ATNF catalogue [288], that contains the most comprehensive list of pulsars observed in different wavelengths, as well as Fermi-LAT γ-ray pulsars including both the objects listed in the catalogue [289] (for the pulsars in the catalogue without distance estimate we use the γ-ray distance as determined by [282]) and eight recently discovered ones [290]. This will give us insight on the regions in parameter space occupied by known pulsars and their role in explaining the electron/positron excess. Every pulsar catalogue suffers from more or less important uncertainties, in particular related to the distance and characteristic age estimates. Hence, we will show the distance error in Fermi-LAT pulsars and the age uncertainty due to the timing measurements reported in ATNF catalogue.

5.7.3 Modelling AMS-02 experimental capabilities

In order to study the prospects for discriminating the source of the electronic component in cosmic rays, we focus on the expected performances of the Alpha Magnetic Spectrometer (AMS-02) [179]. Being a large-acceptance spectrometer in space, AMS-02 will likely

be invaluable in the measurement of cosmic ray nuclei spectra and ratios. Moreover, good rejection capabilities will enable a precise determination of cosmic ray electrons and positrons in the GeV−TeV range. We start by studying the energy range 1−300 GeV for both electrons and positrons [196], where the energy resolution has been determined using a test beam at CERN [299]:

$$\frac{\Delta E}{E} = \sqrt{(0.106/\sqrt{E/\mathrm{GeV}})^2 + (0.0125)^2} \quad .$$

This corresponds to $\sim 10.7\%$ (1.4%) energy resolution at $E = 1\,(300)$ GeV, and conservatively we assume 15 energy bins per decade. The recent replacement of the superconducting magnet by the permanent one will allow AMS-02 to last more than the initial mission duration of 3 years, even though with a downgraded performance. In this work we take a data-taking period of 18 years. We have, however, verified that, for an 1 year period, the projected AMS-02 data shown in the following are essentially unchanged since the uncertainties are dominated by systematics.

For a given energy bin of central energy E_b and width δE, we estimate the detected number of X particles as

$$N_X = \Delta t\, \delta E\, A_X \int dE'\, \phi_X(E')\, \frac{e^{-\frac{(E'-E_b)^2}{2\sigma^2}}}{\sqrt{2\pi\sigma^2}} \quad , \tag{5.30}$$

where $\sigma = \Delta E(E_b)/2$, Δt is the operating time (taken to be 18 year as stated in the last paragraph), A_X is the geometrical acceptance of the instrument for X particles and ϕ_X is the differential flux. Following [300], we take a mean acceptance for electrons and positrons of $A_{e^-} = A_{e^+} = 0.045$ m^{2}sr, valid in the energy range 1−300 GeV. Notice that the Gaussian smearing in the above formula is of particular importance for spectral features such as cutoffs, while being less relevant for smooth parts of the energy spectrum.

The relative statistical uncertainty inherent to the measurement of the flux ϕ_X in a certain energy bin is simply $1/\sqrt{N_X}$. Systematic errors instead result mainly from the misidentification of other particles as electrons and/or positrons. Protons in particular represent the major background for the measurement of the electronic component. To estimate their number in each energy bin we adopt the proton flux measured by BESS [301] (extrapolated where needed) and use expression (5.30) without Gaussian smearing and with $A_p = 0.3$ m^{2}sr. For electrons, we adopt a rejection power against protons $e^- : p = 3 \times 10^5$ [302, 303]. For positrons, the rejection powers against protons and electrons are respectively $e^+ : p = 3\times10^5$ and $e^+ : e^- = 10^4$ [300]. In a given energy bin, the relative systematic uncertainties are thus $\frac{N_p/N_{e^-}}{e^-:p}$ for the electron flux, and $\frac{N_p/N_{e^+}}{e^+:p} + \frac{N_{e^-}/N_{e^+}}{e^+:e^-}$ for the positron flux. For the rest of this work we shall add in quadrature systematic and statistical uncertainties.

It is not entirely clear to what extent will AMS-02 measure electrons and positrons above a few hundred GeV. In addition to the range 1−300 GeV, we also consider the window 300−800 GeV with the characteristics detailed above. Note that this is an optimistic approach since the AMS-02 performance will be likely worse above a few hundred GeV.

Finally, we analyse the prospects for detecting a dipole anisotropy in the flux of cosmic ray electrons and positrons. A nearby source may in fact produce a non-negligible anisotropy, in particular at high energies. Experimentally, the anisotropy measurement is limited by the presence of the (nearly) isotropic electron-positron background. Sup-

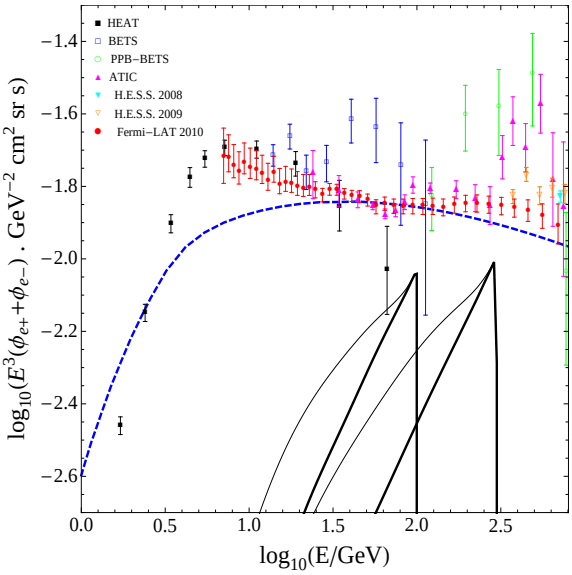

Figure 5.14: The electron plus positron spectrum produced by DM annihilations into e^+e^- (thick solid lines) and democratic leptons (thin solid lines). DM masses are fixed to 100 and 300 GeV, and annihilation cross-sections are chosen arbitrarily for plotting purposes. The dashed line indicates the background used in this work, corresponding to "model 1" of Ref. [294]. The data sets include HEAT [291], BETS [293], PPB-BETS [267], ATIC [242], H.E.S.S. 2008 [269], H.E.S.S. 2009 [245] and Fermi-LAT [244].

pose $N \pm \Delta N$ is the number of background particles (electrons, positrons or both) in a hemisphere along a certain direction. Here, ΔN represents a global uncertainty including systematic and statistical errors. Then, the minimum detectable anisotropy at n sigma is simply $\delta_{0,n\sigma} = n\Delta N/N$. Later on we shall use the 2σ positron and electron plus positron anisotropy reaches of AMS-02 in 18 years, modelled according to the above formula and the details given in the previous paragraphs. We will also apply the 2σ electron plus positron anisotropy reach of Fermi-LAT ($A_{e^\pm} \sim 1$ m^{2}sr) after 5 years and considering statistical errors only, even though this is a rather optimistic limit. A dedicated search for $e^\pm$ anisotropies was already performed by the Fermi-LAT collaboration with 1 year of data [304] producing interesting upper limits on $\delta_{e^\pm}$.

5.7.4 Distinguishing Dark Matter and single pulsar spectra

In this subsection we quantitatively study the impact of future cosmic-ray electron data on distinguishing Dark Matter and single pulsars as the source of the lepton excess. We start by assuming a Dark Matter origin and assess to what extent one can discard the pulsar hypothesis. If Dark Matter particles directly annihilate into electron-positron pairs only or democratically into the three charged leptons, then a rather abrupt cutoff at the DM mass is expected. This is illustrated in Figure 5.14, where the expected $e^\pm$ background (detailed in Section 5.7.2) is also shown. In the following we shall focus on direct annihilations into $e^\pm$ since its extreme spectral feature is in principle more difficult to mimic with pulsars. We consider three phenomenological sets of DM properties − summarised in Table 5.6 − that feature a rise in the positron fraction as seen by PAMELA and a cutoff at 100, 300 and 500 GeV. The normalisation of the baseline $e^\pm$ flux was rescaled by a factor f (with respect to Fermi-LAT data point at 100 GeV) in order to give some room for the extra component. All three models produce electron plus positron fluxes compatible with Fermi-LAT and H.E.S.S. at the 3σ level. We use these three models as our fiducial models.

	m_χ [GeV]	$\langle\sigma_{ann}v\rangle$ [cm^3/s]	f
DM1	100	5.0×10^{-26}	0.97
DM2	300	3.5×10^{-25}	0.87
DM3	500	9.0×10^{-25}	0.83

Table 5.6: The Dark Matter fiducial setups. Besides mass m_χ and annihilation cross-section $\langle\sigma_{ann}v\rangle$, also shown is f, the background rescaling factor. In all cases direct annihilation into e^+e^- is assumed.

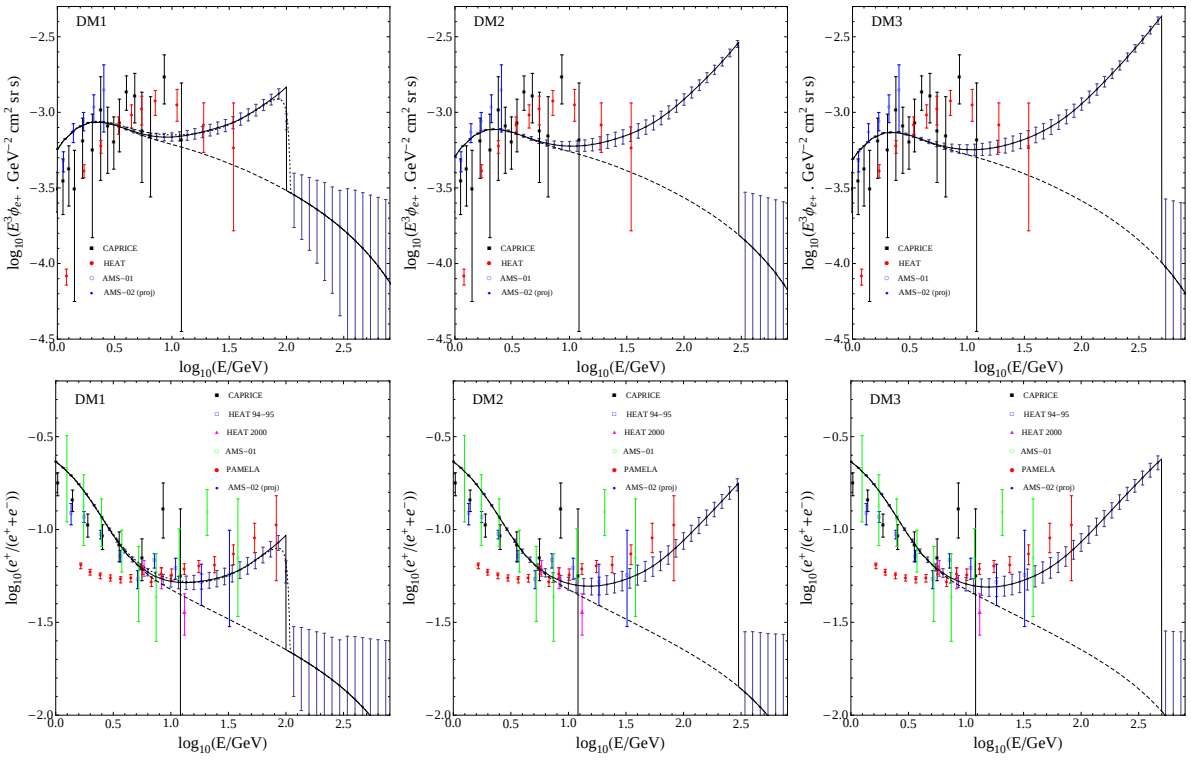

Figure 5.15: Mock AMS-02 data (filled blue circles) and corresponding error bars for the DM fiducial setups in Table 5.6. The solid (dashed) line shows the total (background) contribution. The top row of frames features the positron flux while the bottom one the positron fraction. From left to right, the columns correspond to DM1, DM2 and DM3. In the left column the dotted line shows a pulsar spectrum that fits well the AMS-02 mock data. For the positron flux, the data sets include CAPRICE [239], HEAT [291], AMS-01 [292]. For the positron fraction, the data sets include CAPRICE [239], HEAT 1994-1995 [238], HEAT 2000 [247], AMS-01 [240] and PAMELA [268].

For each DM fiducial model, "mock" AMS-02 measurements of the cosmic ray electronic component are generated according to the capabilities outlined in Section 5.7.3. The resulting positron fraction and positron flux are shown in Figure 5.15. Using these data (we consider only energies above 10 GeV to minimise solar modulation dependence), the pulsar hypothesis is tested by performing a fixed grid scan within the ranges $|\dot{E}| = 10^{32} - 10^{36}$ erg/s, $d = 0.1 - 5$ kpc and $t_{ch} = 10^4 - 10^7$ yr. In this work we are interested in the goodness of fit and not in extracting best-fit parameters and the corresponding uncertainties. Therefore, we compute the χ^2 for each pulsar parameter set and draw the contours outside which parameters are excluded at $1 - \alpha = 99\%$ or 50% confidence level (using as degrees of freedom the number of available energy bins above 10 GeV). The two dimensional contours presented in the following are obtained by selecting the minimum values of χ^2 along the hidden dimension. Figure 5.16 shows the results for DM1, $\Gamma = 1.7$ and $E_{cut} = 1$ TeV, as well as ATNF and Fermi-LAT pulsars. Also indicated are the regions where a single pulsar − plus background − contributes $> 50\%$ to the positron fraction (thick solid red) and positron flux (thick dashed red) at ∼86 GeV, along with the pulsars producing anisotropies visible at 2σ to Fermi-LAT after 5 years (dotted blue). The spectra produced by the best fit pulsar parameter set is shown by the dotted line in the left column of Figure 5.15 – the distinction between DM and pulsars seems virtually impossible with AMS-02 mock data. Several comments are in order here. First, the benchmark DM1 features a cutoff at 100 GeV which is well inside AMS-02 range and hence in this case a precise measurement of the spectral feature is anticipated. This is an optimistic scenario where the compatible regions in the pulsar parameter space are tight, as shown in Figure 5.16. In particular, the contours restrict very effectively the values for the pulsar characteristic age t_{ch} needed to mimic the DM signal. This is because t_{ch} fixes the maximal energy $E_{max} \simeq 1/(b_0 t_{ch})$ that induces a rather sharp cutoff (in this case where $E_{cut} > E_{max}$). The normalisation is instead given by $|\dot{E}|$ and d: more distant pulsars require larger energy inputs to produce the same propagated spectrum. Such a behaviour − illustrated in the top right plot of Figure 5.16 − breaks when $d \ll r_{dif}$ (check equation (5.28)) in which case $|\dot{E}|$ alone fixes the normalisation.

In Figure 5.17 we show how the confidence regions in the plane t_{ch} vs. $|\dot{E}|$ are affected by the choice of the spectral index Γ, the cutoff energy E_{cut} and the DM fiducial model. As it is evident from the left plot of this figure, data featuring cutoffs at higher energy select younger pulsars (since $E_{max} \propto t_{ch}^{-1}$), and are compatible with larger portions of the pulsar parameter space because of the larger experimental uncertainties at high energies. On the other hand, changing the spectral index or the cutoff energy changes less importantly the allowed regions in the pulsar parameter space.

We summarise in Table 5.7 the number of catalogue pulsars producing good fits to the mock data and the ones expected to contribute non-negligibly to the electron/positron anticipated spectrum. Notice that the ATNF and Fermi-LAT catalogues have common objects (though with different derived properties) and so the figures in Table 5.7 report the number of different pulsars found in each case. The bottom line of this calculation is that, from the phenomenological viewpoint, it is possible to mimic a DM-like spectrum with single pulsars, even in the extreme case of direct DM annihilations into electron-positron pairs where a sharp cutoff is present. By construction, the mock data shown in Figure 5.15 are better fit by DM than pulsars, but, statistically speaking, one cannot exclude at a high confidence level the regions inside the contours drawn in Figures 5.16 and 5.17. However, within these regions we find very few or none known catalogue pulsars as

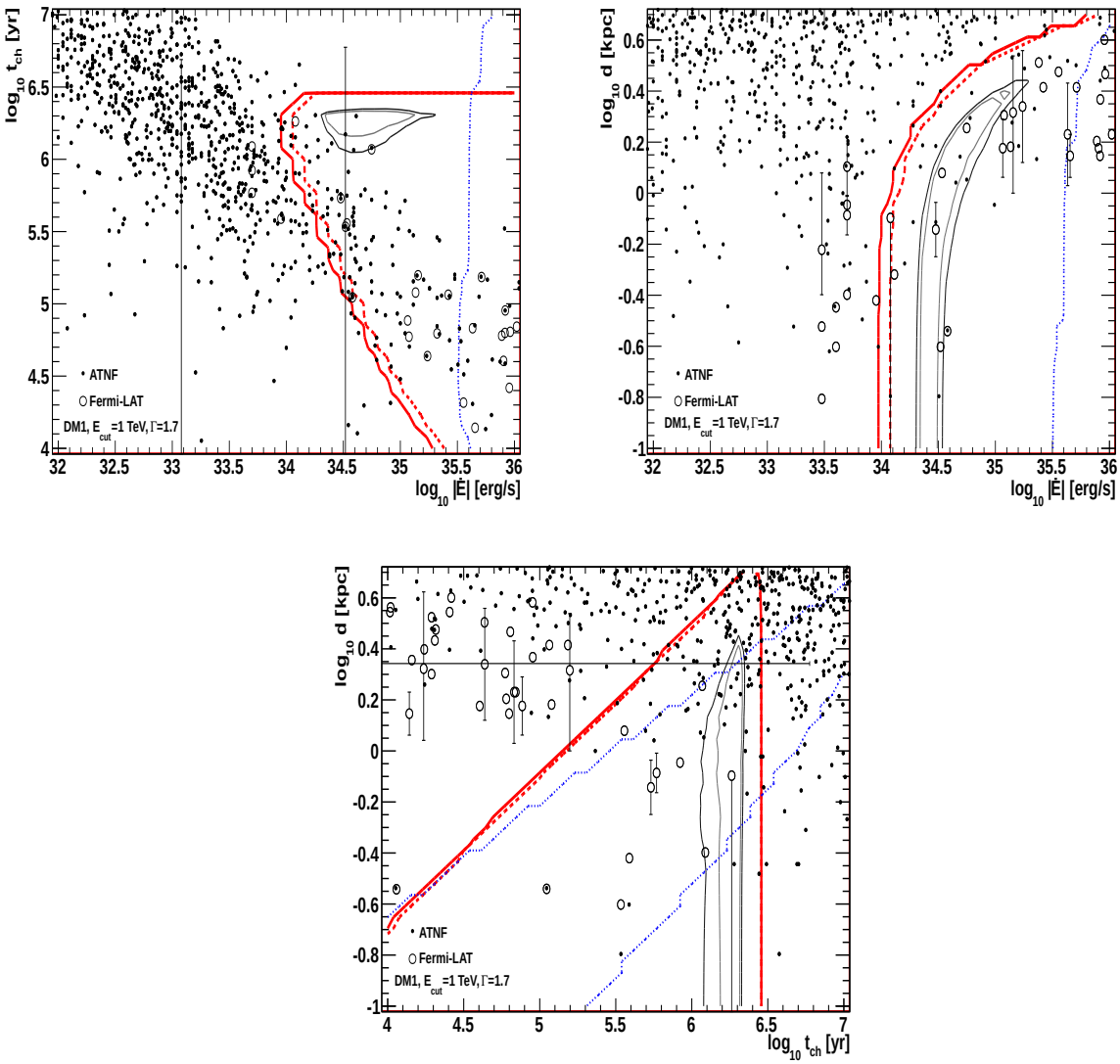

Figure 5.16: Regions in the pulsar parameter space compatible with the mock AMS-02 data shown in the left column of Figure 5.15 corresponding to the fiducial model DM1. The thin inner (outer) solid contour corresponds to an $1-\alpha = 50\%$ (99%) confidence level goodness of fit. The thick solid (dashed) red lines individuate the regions where a single pulsar − plus background − contributes >50% of the positron fraction (flux) at ~ 86 GeV. The dotted blue line delimits the 2σ $e^{\pm}$ anisotropy reach of Fermi-LAT after 5 years. Also shown are the ATNF catalogue [288] (filled dots) and Fermi-LAT pulsars [289, 290] (open circles). Notice that not all pulsars visually within the thin contours are actually inside the corresponding three-dimensional confidence regions since there is a third, hidden dimension.

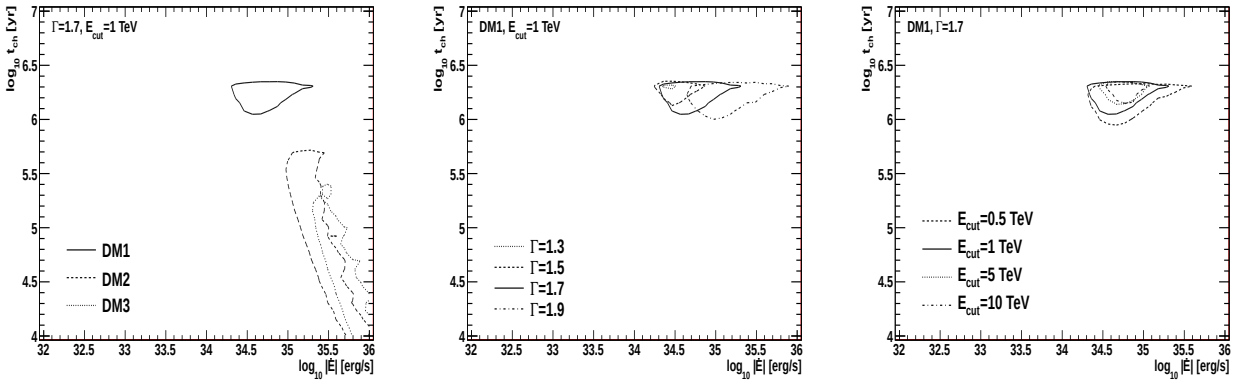

Figure 5.17: The 99% CL region compatible with the mock AMS-02 data in Figure 5.15 for different DM models (left), Γ (central) and E_{cut} (right).

benchmark	Γ	E_{cut} [GeV]	N_1^{50}	N_1^{99}	N_2	N_3
DM1	1.3	1000	0	0	5	3
DM1	1.5	1000	0	0	5	5
DM1	1.7	1000	0	0	5	3
DM1	1.9	1000	0	0	1	1
DM1	1.7	500	0	1	4	4
DM1	1.7	5000	0	0	1	1
DM1	1.7	10^4	0	0	1	1
DM2	1.5	1000	0	0	8	6
DM2	1.7	1000	0	0	6	5
DM2	1.9	1000	0	0	3	1
DM3	1.5	1000	0	0	8	6
DM3	1.7	1000	0	0	8	5
DM3	1.9	1000	0	0	4	2

Table 5.7: The number of known pulsars (from ANTF and Fermi-LAT catalogues) producing good fits to the mock AMS-02 data in Figure 5.15 for different combinations of Γ and E_{cut}. $N_1^{50,99}$ represent the number of catalogue pulsars found within the 50%, 99% CL contours, while N_2 (N_3) is the number of pulsars that contribute individually − plus background − more than 50% of the positron fraction (flux) at ∼86 GeV.

indicated in Table 5.7. In fact, only for the case DM1, $\Gamma = 1.7$, $E_{cut} = 500\,\mathrm{GeV}$ does one find a pulsar setup that can reproduce the mock data in a satisfactory manner. This may be interpreted as an argument against the pulsar hypothesis, even though catalogues are likely incomplete since pulsars emit electromagnetic radiation in a directional fashion and thus only a fraction of these objects may be observed from Earth – therefore the pulsar hypothesis cannot be ruled out on this basis. In order to estimate the incompleteness of catalogues, one may compute the so-called beaming fraction defined as the fraction of sky each pulsar beam sweeps,

$$F(\alpha \neq (0,\pi), \Delta\theta) = \frac{1}{4\pi}\int_{\Delta\Omega} d\Omega = \frac{1}{2}\left[\cos\left(\alpha - \Delta\theta/2\right) - \cos\left(\alpha + \Delta\theta/2\right)\right] \quad ,$$

where α is the angle between rotation and magnetic axes, $\Delta\theta/2$ is the half-width of the beam and we have considered top-hat beams (see e.g. [305]). Assuming an isotropic distribution for α, the mean beaming fraction reads

$$\langle F\rangle(\Delta\theta) = \int_0^{\pi/2} d\alpha\, F(\alpha, \Delta\theta)\sin\alpha = \frac{\pi}{4}\sin\left(\frac{\Delta\theta}{2}\right) \quad .$$

The width of the beam $\Delta\theta$ is, of course, dependent on the emission mechanism. Radio beams, for instance have typical half-openings $\Delta\theta/2 = 5.8^\circ (P/\mathrm{s})^{-1/2}$ [306] which for a fiducial period $P \sim 0.1$ s gives $\Delta\theta/2 \simeq 18^\circ$ and $\langle F_r\rangle \sim 0.24$. However, values $F_r \sim 1$ have been found by studying different populations of detected γ-ray and radio pulsars [305] indicating wide radio emission. As for γ-rays, beaming fractions in the literature vary in the range $F_g \sim 0.1 - 1$ [307]. Now, if the distribution of nearby pulsars is assumed isotropic, the ratio of total to observed numbers of objects should be given by $1/F$, or $\sim$1–4 (1–10) using the above-stated radio (γ-ray) beaming fractions. These figures do not include distance selection effects, but recall that in the present work we are interested in nearby, high-luminosity objects.

Another difficulty with the single pulsar explanation evident from Table 5.7 arises from the fact that at least a few known pulsars should contribute (together with the background) more that 50% of the positron fraction and positron flux at a given energy (~ 86 GeV). Therefore, in order to accommodate the cutoffs of Figure 5.15 with a single pulsar, one also needs to explain why a few known pulsars produce less electron-positron pairs than expected. A caveat to this argument is the fact that a rather high efficiency $\eta_{e^\pm} = 0.4$ is being used. For the reference case DM1, $\Gamma = 1.7$, $E_{cut} = 1$ TeV, we redid the calculations with $\eta_{e^\pm} = 0.04$ and found no known pulsar contributing significantly to the e^+ flux or fraction, which indeed weakens the above-mentioned reasoning.

It has been proposed in the literature that the pulsar origin of the cosmic ray lepton excess could be tested by means of anisotropy measurements. Unfortunately, however, we find no catalogue pulsars producing $e^\pm$ or e^+ anisotropy levels visible to Fermi-LAT in 5 years or AMS-02 in 18 years. This conclusion is clear in Figure 5.18 where the experimental reaches have been plotted along with the maximal anisotropy – attained at energy $E^{e^\pm}_{max}$ or $E^{e^+}_{max}$ – featured by known pulsars with ages $t_{ch} = 10^4 - 10^7$ yr. Obviously it is possible that a low-energy anisotropy is visible while the maximal value goes undetected, but we do not consider such case since it would not be a strong evidence for singling out a particular pulsar. In this figure the references values $\Gamma = 1.7$ and $E_{cut} = 1000$ GeV were assumed, but we have also checked that the expected anisotropies from known pulsars are

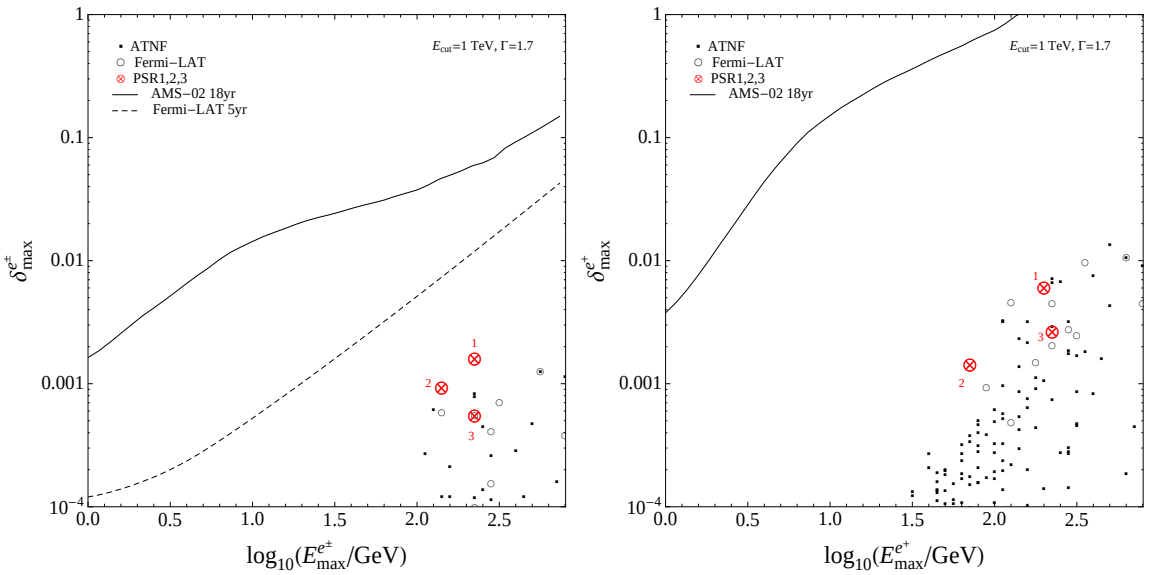

Figure 5.18: The maximal anisotropy produced by ATNF (filled dots) and Fermi-LAT (open circles) pulsars with $t_{ch} = 10^4 - 10^7$ yr as a function of the energy at which such anisotropy is attained. Here, the values $\Gamma = 1.7$, $E_{cut} = 1000$ GeV and $f = 0.9$ (besides $\tau_0 = 10^4$ yr and $\eta_{e^\pm} = 0.4$) were assumed for all catalogue pulsars. The fiducial setups in Table 5.5 are shown by red circled crosses. In the left (right) frame we show the $e^\pm$ (e^+) maximum anisotropy. The AMS-02 18 years (Fermi-LAT 5 years) 2σ anisotropy reach is plotted in solid (dashed). Notice that $E^{e^\pm}_{max}$ and $E^{e^+}_{max}$ are different from the maximal energy allowed by losses, E_{max}.

below the experimental reaches for all the combinations of parameters (Γ, E_{cut}) listed in Table 5.7. Notice that the recent 3σ $e^\pm$ dipole anisotropy upper limits from Fermi-LAT [304] range from $\sim 10^{-2}$ at 100 GeV to $\sim 10^{-1}$ at 500 GeV – somewhat in between the dashed and solid curves in the left frame of Figure 5.18. Note as well that the anisotropies we find are significantly smaller than in other works (see e.g. [308]) because we are using an $e^\pm$ "background" tuned to roughly match Fermi-LAT data and we are not letting the catalogue pulsars output $|\dot{E}|$ vary to explain the lepton excess.

We now turn to the inverse problem: we assume a single pulsar as the source of high-energy electrons and positrons, and evaluate the prospects for distinguishing this scenario from that of DM annihilations. The three fiducial sets of pulsar properties shown in Table 5.5 and Figure 5.13 were adopted, each featuring a different cutoff sharpness. Applying a procedure very similar to the previous case, we generate mock data for the positron fraction and positron flux in the pulsar scenario and test the DM hypothesis. Direct annihilations into $e^\pm$ and democratic annihilations into leptons are both considered, and m_χ and $\langle \sigma_{ann} v \rangle$ are treated as free parameters. The resulting $1 - \alpha = 99\%, 50\%$ contours are presented in Figure 5.19. The shaded regions are excluded at 3σ by present data on the positron fraction (PAMELA) and/or the electron plus positron flux (Fermi-LAT, H.E.S.S.). As evident from Figure 5.19, DM models with direct annihilations into electron-positron pairs can mimic the spectrum produced by the benchmark PSR2, but not the first and third cases that present milder cutoffs. Analogously, democratic DM annihilations into charged leptons cannot be ruled out as explanation of the spectrum induced by PSR1, but do not explain a sharp cutoff as the one produced by PSR2. For the sake of clarity we have not considered further annihilation channels that may ease the fit to mild pulsar-like cutoffs. In any case, for the representative pulsar cases, one can always have well-fit DM spectra either with annihilations into $e^\pm$ or democratic leptons. Of course, as extensively discussed in the literature and already pointed out in Section 5.7.1, the large cross-sections

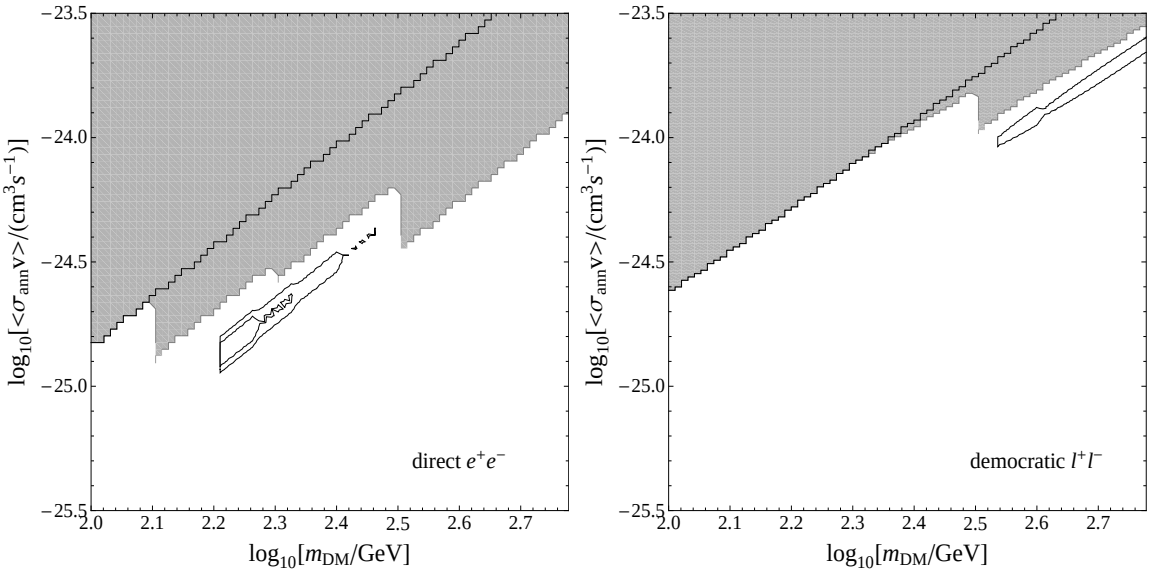

Figure 5.19: The regions in the Dark Matter parameter space compatible with the mock AMS-02 data assuming the three pulsar benchmarks of Table 5.5. The inner (outer) contour corresponds to an $1-\alpha = 50\%$ (99%) confidence level goodness of fit. In the left frame, direct annihilations into e^+e^- are assumed and the solid contours correspond to PSR2; in this case no compatibility is found for PSR1 nor PSR3. In the right frame, democratic annihilations into leptons are assumed and the solid contour ($1-\alpha = 99\%$) corresponds to PSR1; in this case no compatibility is found for PSR2 nor PSR3. In both frames, the shaded region is excluded at 3σ by PAMELA positron fraction or Fermi-LAT/H.E.S.S. electron plus positron flux, being that the portion above the upper solid line is excluded by PAMELA.

highlighted in Figure 5.19 are excluded by or in tension with other data.

Throughout our work we have assumed (almost) "perfect data", i.e. mock data presenting no fluctuations with respect to the "true" observables (but including the smearing due to the energy resolution of the instrument). This is of course a quite optimistic assumption regarding the ability to discriminate different sources and therefore strengthens our conclusions. Nevertheless, for the benchmark DM1 we have generated mock data by drawing the flux in each energy bin from a Gaussian distribution of mean given by the flux corresponding to N_X in equation (5.30) and standard deviation as explained in Section 5.7.3. In that case, for a single realisation, the true model yields a good (but not perfect) fit to the mock data with $\chi^2_{DM}/n_{dof} = 40.7/58$ ($p = 95.6\%$), as opposed to $\chi_{DM} \sim 0$ using "perfect data". On the other hand, fixing $\Gamma = 1.7$ and $E_{cut} = 1$ TeV, we find that the best pulsar parameter set provides a chi-square $\chi^2_{pul}/n_{dof} = 42.1/58$ ($p = 94.2\%$), which cannot be ruled out with any reasonable statistical significance. We have also checked that the 99% CL contour in the pulsar parameter space obtained using mock data with fluctuations encompasses a region similar (but smaller) than the one shown in Figures 5.16 and 5.17. In the future, a dedicated study of the performance of AMS-02 in detecting electrons and positrons may allow a more realistic analysis, but we stress here that such would reinforce the idea that rejecting the pulsar hypothesis in case of a DM-like spectrum (or vice-versa) will be highly challenging.

5.7.5 Conclusions

In this work we have studied the capability of future precision $e^{\pm}$ measurements to constrain possible origins of the cosmic-ray lepton excess, focusing on the Dark Matter and pulsar interpretations. In order to model upcoming experimental capabilities, the perfor-

mance of AMS-02 was estimated in a realistic way, including both systematic and statistical uncertainties. We have considered the case in which a cutoff in the electron/positron spectrum, produced either by DM annihilations or by acceleration in a pulsar, is observed, and quantified the ability of AMS-02 to reject the wrong hypothesis. In particular, the first scenario studied was the case where the excess is due to DM direct annihilations to $e^{\pm}$ pairs, for three different values of the DM mass ($m_\chi = 100, 300, 500\,\mathrm{GeV}$). Even if the DM-induced spectral cutoff is quite sharp, it turns out that it is always possible to find values for the pulsar spin-down luminosity, distance and characteristic age that produce an electron-positron spectrum that would be compatible, within the experimental uncertainties, with the DM one. However, such would require quite specific values of the pulsar luminosity and age. In fact, in nearly all cases, none of the kwown pulsars within the ATNF catalogue, nor of the Fermi-LAT pulsars, satisfies these requirements, although it should be taken into account that catalogues are likely incomplete. Then, we have considered the symmetric case where the excess is produced by a pulsar, and tried to fit the anticipated data with DM directly annihilating either to e^+/e^- pairs or democratically (i.e. 33% of the time each) to e^+/e^-, μ^+/μ^- and τ^+/τ^-. Within the framework of each model, DM was treated in an as much model-independent way as possible, taking the DM mass and annihilation cross-section as independent parameters; nevertheless, the "democratic" case can be seen as somewhat representative of KK and leptophilic DM models. We find that the possibility to reproduce the pulsar-induced spectrum, as well as the volume in the DM parameter space required to do so critically depends on the shape of the cutoff, and thus on the characteristics of the pulsar originating the excess. In any case, generically speaking, it is possible to mimic a pulsar-like spectrum with DM annihilations, even though the required cross-sections are usually in tension with other data as extensively discussed in the literature.

Let us point out that our results were obtained in favourable conditions regarding a possible source discrimination, namely by fixing the propagation setup. Including propagation uncertainties would likely worsen the prospects for discrimination. The main conclusion of our work is therefore that future $e^{\pm}$ data will likely be insufficient to discriminate between the Dark Matter and the single pulsar interpretations of the cosmic-ray lepton excess. One caveat to this statement would be the detection of several bumps in the electron-positron spectrum at high energies that could be associated to the contribution of several nearby pulsars, and that would be difficult to mimic with Dark Matter annihilations or decays (see e.g. [309]). In the future, complementary data, or a better understanding of both sources and cosmic-ray propagation, may contribute to a better discrimination power than presented here.

5.8 Paper VI: Thermal relics in modified cosmologies: bounds on evolution histories of the early Universe and cosmological boosts for PAMELA[6]

Alternative cosmologies, based on extensions of General Relativity, predict modified thermal histories in the early Universe during the pre–BBN era, epoch which is not directly

[6]This Section is based on the article [6], done in collaboration with Riccardo Catena, Nicolao Fornengo, Lidia Pieri and Antonio Masiero.

constrained by cosmological observations. When the expansion rate is enhanced with respect to the standard case, thermal relics typically decouple with larger relic abundances. The correct value of the relic abundance is therefore obtained for larger annihilation cross-sections, as compared to standard cosmology. A direct consequence is that indirect detection rates are enhanced. Extending previous analyses, we derive here updated astrophysical bounds on the Dark Matter annihilation cross-sections and use them to constrain alternative cosmologies in the pre–BBN era. We also determine the characteristics of these alternative cosmologies in order to provide the correct value of relic abundance for a thermal relic with the (large) annihilation cross-section required to explain the PAMELA results on the positron fraction, therefore providing a "cosmological boost" solution to the Dark Matter interpretation of the PAMELA data.

5.8.1 Overview

BBN is the deepest available probe of the early Universe. Its success in explaining the primordial abundances of light elements [11, 32], combined with CMB and large scale structure studies, confirms the standard model of cosmology since the BBN epoch at MeV temperatures. At those temperatures the Universe must have been essentially radiation-dominated. Before, however, a period of very enhanced expansion may have occured. In the Refs. [16, 310] indirect searches for Dark Matter annihilation, namely antiprotons and γ–rays from the Galactic Centre, were used to derive limits on the pre–BBN expansion rate of the Universe. The basic idea is as follows. If DM is composed of WIMPs which thermalise in the early Universe and then freeze–out their abundance before BBN, then the expansion history since freeze–out and the precise measurement of the Dark Matter relic abundance $\Omega^0_{cdm}h^2 = 0.1131 \pm 0.0034$ [311] fix the annihilation cross-section $\langle\sigma_{ann}v\rangle$ (for a given DM mass m_χ). A faster pre–BBN expansion requires a larger annihilation cross-section in order to meet the relic abundance bound, and in turn enhanced DM–induced astrophysical fluxes result. Thus it is possible to draw an upper limit on the Hubble rate $H(T)$ before the BBN epoch [16, 310]. In the present work we revisit this subject mainly motivated by the host of astrophysical data released in the last years, such as cosmic–ray electrons and positrons (PAMELA [241], ATIC [242], Fermi-LAT [243], HESS [269, 245]), antiprotons (PAMELA [198]) and γ-rays (HESS [230], Fermi-LAT [312, 231, 313]). The rising behaviour of the positron fraction observed by PAMELA [241], in particular, has been subject of deep scrutiny, and in addition to astrophysical interpretations [183, 284, 285] it has been discussed the possibility that the rise is due to DM annihilation dominantly occurring into leptons [219]. The DM interpretation requires large values of $\langle\sigma_{ann}v\rangle$, which are then incompatible with a successful thermal relic. Furthermore, results from N–body simulations have been recently presented [220, 85] allowing for a better modelling of dark structure and substructure in our Galaxy.

Consequently, we are now in a position to reassess the constraints on pre–BBN cosmologies by using a rather complete scheme of observables. Besides an update of the previous works [16, 310], we are also interested in the possibility of accommodating the rising positron fraction with annihilations of a thermal DM particle whose properties naturally arise in non–standard cosmologies. Refs. [16, 310, 28, 314, 315], for instance, show that the large annihilation cross-sections required to meet the measured positron fraction or electron spectrum are attainable in the context of non–standard cosmological scenarios such as low reheating temperatures scenarios, scalar–tensor theories of Gravity

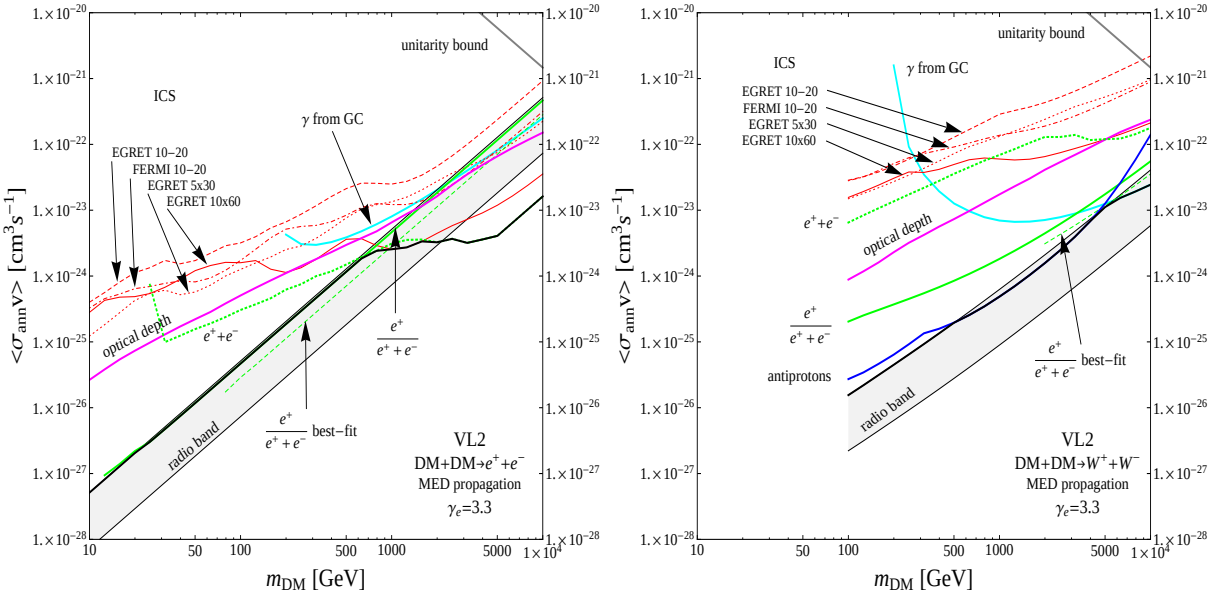

Figure 5.20: Upper limits on the DM annihilation cross-section (versus the DM mass) coming from different astrophysical observations. Here we have considered the Via Lactea II DM distribution, DM annihilations into e^+e^- (left) and W^+W^- (right), the MED propagation model for cosmic rays and an electron spectral index $\gamma_e = 3.3$. The region above the thick black line is excluded by the convolution of all the implemented constraints. The dashed line labelled as "$\frac{e^+}{e^++e^-}$ best–fit" denotes the values of the DM annihilation cross-section required to explain the PAMELA data on the positron fraction. The unitarity bound assuming s-wave annihilations [329] is also shown.

or kination phases. Analyses of phenomenological consequences of modified cosmologies are also discussed in Refs. [316, 317, 318, 319, 320, 22, 23, 321].

5.8.2 Survey of bounds on annihilating Dark Matter

Dark Matter annihilations can in principle be sources of electrons and positrons, antiprotons, antideuterons, photons and neutrinos. Such particles, or their interactions in the surrounding medium, provide a plethora of ways to effectively constrain the intrinsic properties of annihilating DM as discussed earlier in this Chapter. Here we will focus on galactic positrons, antiprotons, γ-rays and radio photons, and on constraints related to the optical depth of CMB photons. Other relevant channels, which are not included in our analysis, are neutrinos from the Galactic Centre (GC) [322, 250, 251] (neutrinos from Sun [323, 324, 325] and Earth [325] do not directly constrain the total annihilation cross-section), and γ-rays from dwarf spheroidal galaxies [326, 55], galaxy clusters [94, 327] and extragalactic halos [260]. For multi-messenger, multi-wavelength analyses see e.g. [55, 328, 54, 210, 4].

In the present work we adopt a model–independent approach and consider generic annihilating DM candidates of masses m_χ in the interval [10 GeV, 10 TeV]. We study the bounds on the velocity–averaged annihilation cross-section $\langle\sigma_{ann}v\rangle$ for each annihilation channel separately: e^+e^-, $\mu^+\mu^-$, $\tau^+\tau^-$, W^+W^- or $\bar{b}b$. This scheme basically captures the essential features of several well–motivated DM particles such as the lightest supersymmetric particle or the lightest Kaluza-Klein particle. We will consider throughout the paper the case of a DM particle which dominantly annihilates as s–wave.

Annihilation signals are proportional to the square of the Dark Matter density, and it is therefore crucial to properly specify the DM distribution in the Milky Way. We rely on the

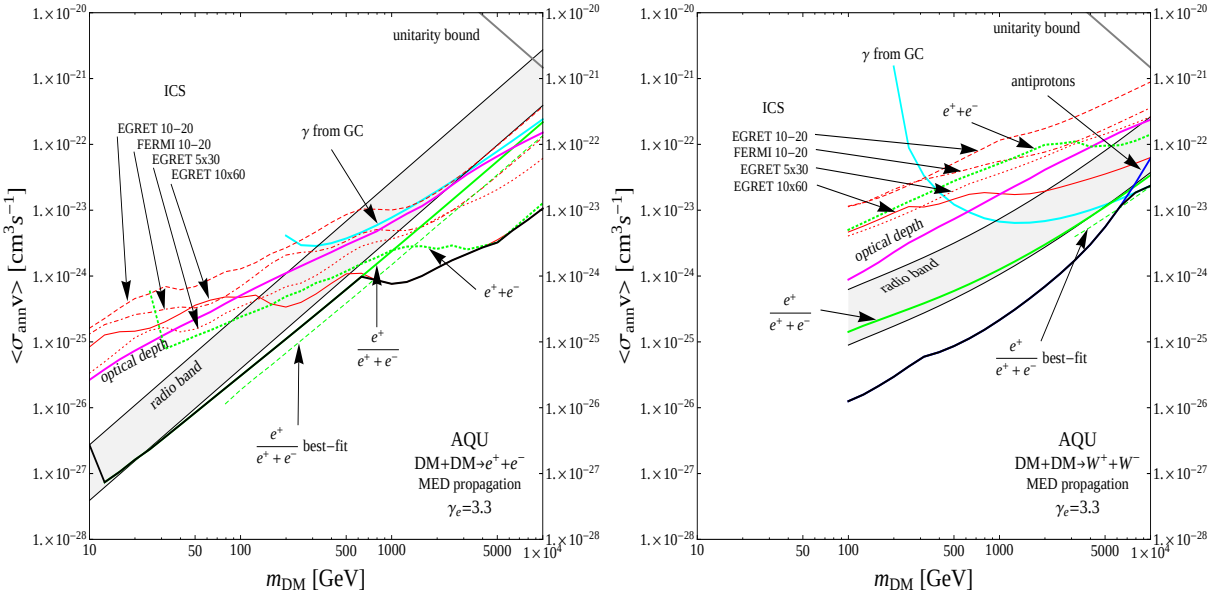

Figure 5.21: The same as in Figure 5.20, for Aquarius DM distribution.

recent results of the high–resolution $N-$body simulations Via Lactea II [220] and Aquarius [85]. In the former, the total DM profile (smooth + clumpy components) is well fitted to a Navarro-Frenk-White profile, while in the latter the density distribution follows an Einasto profile with $\alpha = 0.17$, as explained in detail in 5.1.3. In these setups the local density of the smooth component is $\rho_0^{VL2} = 0.41$ GeV/cm^3 and $\rho_0^{Aq} = 0.58$ GeV/cm^3. Again we use $M_{min} = 10^{-6}$ M$_\odot$ as the minimum subhalo mass. As an additional benchmark for the galactic distribution of DM, we consider the case of a smooth cored isothermal profile with no substructures. Following [76, 63], we set $\rho_\odot^{\rm iso} = 0.4$ GeV/cm^3.

The astrophysical bounds on the Dark Matter annihilation cross-section $\langle\sigma_{ann}v\rangle$, as a function of the Dark Matter mass m_χ, for the different annihilation channels and for the different Dark Matter density profiles, are summarised in Figures 5.20–5.23. Due to the intrinsic complexity of these Figures, we refer the reader to the internal labels and to the captions in order to pin down the various bounds, without excessive comments in the body of the text. We just remark that Figures 5.20–5.22 show the separate impact of all the astrophysical bounds, for specific annihilation final states and specific DM halo profiles. Figure 5.23 represents a summary of the astrophysical bounds on the DM annihilation cross-section vs. the DM mass, for the Via Lactea II, Aquarius and cored isothermal halo profiles, respectively. We notice that the effect of the bounds may be non trivial, depending on the DM mass, the annihilation channels and the halo profile. Clearly, signals which are more sensitive to the Galactic Centre DM shape (like the radio bound or gamma–rays from the Galactic Centre) induce bounds which are more affected by the uncertainty on the DM distribution. Other signals, like e.g. antiprotons, are not very sensitive to the DM halo profile [221], as can be seen by confronting again the right frames of Figures 5.20, 5.21 and 5.22. Instead, signals like antiprotons or positrons are more sensitive to the diffusive region of the galactic environment [221, 181], and therefore will produce bounds which are limited by the uncertainties on the cosmic–ray propagation properties.

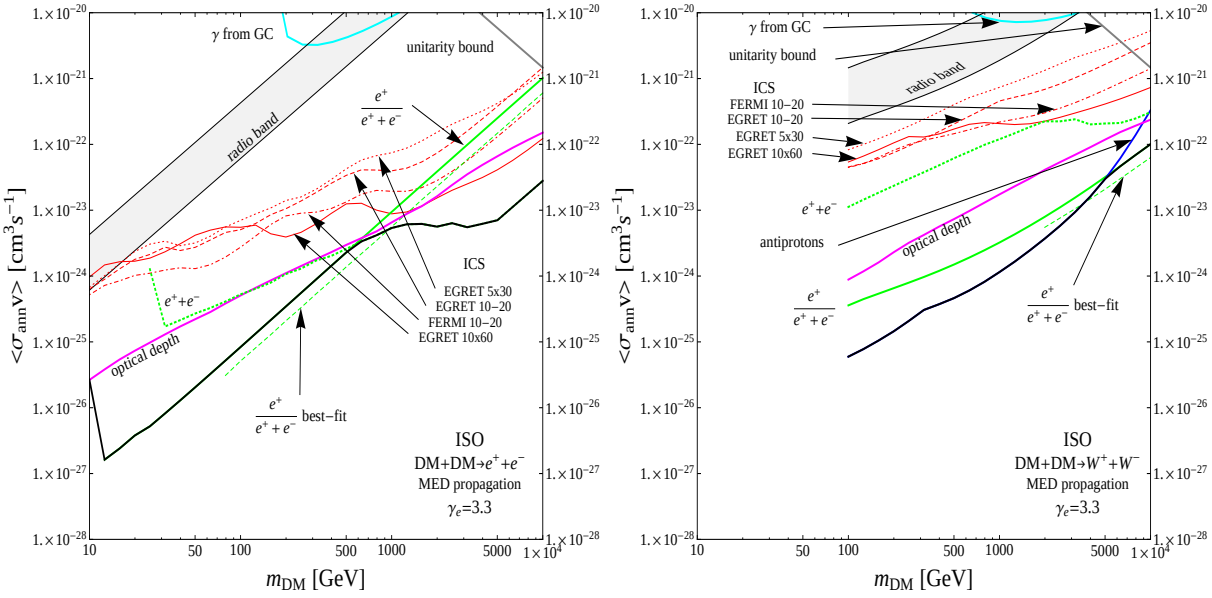

Figure 5.22: The same as in Figure 5.20, for a cored isothermal DM distribution.

Antimatter

To compute antimatter signals induced by Dark Matter annihilations we follow the same procedure as described in Section 5.3 and 5.4.

Electrons and positrons The PAMELA satellite has measured the positron fraction $\phi_{e^+}/(\phi_{e^+} + \phi_{e^-})$ in the energy range 1.5−100 GeV [241]. The data show a steep rise above ~ 7 GeV. Here we restrict ourselves to $E_{e^+} > 10$ GeV and therefore disregard solar modulation. In order to translate the PAMELA positron data into an upper limit on the DM-induced positron flux $\phi_{e^+}^{\rm DM}$, we assume (i) a power-law electron flux $\phi_{e^-} \propto E_{e^-}^{-\gamma_e}$, $\gamma_e = \{3.3, 3.4, 3.5\}$ (in rough agreement with [266]) normalised to the AMS–01 measurement at 10 GeV [240]; and (ii) a secondary positron flux $\phi_{e^+}^{sec}$ produced by the spallation of cosmic rays in the Galaxy [162]. In this scheme, $\phi_{e^+} = \phi_{e^+}^{DM} + \phi_{e^+}^{\rm sec}$. We now require, for fixed m_χ, that no single energy bin of the PAMELA positron data above 10 GeV is exceeded by more than 3σ. This produces an overall upper limit on $\langle\sigma_{ann}v\rangle$. A complementary bound, particularly for multi-TeV leptophilic DM candidates, is motivated by the recent measurements of the electron plus positron flux by Fermi-LAT [243] and HESS [269, 245]. As with PAMELA positron fraction, we disregard solar modulation – Fermi-LAT and HESS cover energies ranging from ~ 25 to ~ 5000 GeV – and, conservatively, draw the 2σ upper limit on $\langle\sigma_{ann}v\rangle$ by only considering electrons and positrons produced by DM annihilations.

On the other hand, we are also interested in studying the feasibility of explaining the PAMELA positron fraction with DM annihilations. So, for fixed m_χ, we fit the data above 10 GeV leaving $\langle\sigma_{ann}v\rangle$ as a free parameter and demand that $\chi^2 < 20$ (7 data points are available). Whenever the positron best–fit values of $\langle\sigma_{ann}v\rangle$ are not in conflict with bounds coming from other astrophysical signals, we consider that value as an acceptable explanation of the PAMELA data in terms of Dark Matter annihilation. More detailed fitting procedures have been presented in other references e.g. [252]. It is well–known that it is possible to obtain good fits to the PAMELA positron data with DM particles which

annihilate preferably into leptons (hadrons) with masses above ~ 100 GeV (a few TeV). Of course, the required annihilation cross-sections are larger than the standard thermal value. We clearly recover these results in our analysis. Differences with respect to Refs. such as [252] are due to a different local Dark Matter density (we are using values greater than the "usual" 0.3 GeV/cm^3), the inclusion of Dark Matter substructure (according to Via Lactea II and Aquarius simulations), and the use of a slightly smaller electron flux (we normalise to AMS-01 at 10 GeV and consider a power-law index 3.3 as a reference value). All such factors play to lower our "PAMELA best-fit" cross-sections with respect to other References.

Note as well that a joint explanation of the PAMELA positron fraction and the Fermi-LAT/HESS electron plus positron flux in terms of DM annihilations favours heavy rather than light DM particles. However, in this work we do not pursue a global fit to PAMELA/Fermi-LAT/HESS but instead use the electron plus positron flux as an astrophysical constraint only.

Antiprotons The comparison of the PAMELA antiproton ratio $\phi_{\bar{p}}/\phi_p$ [198] with theoretical estimates of secondary antiprotons reveals little space for $\bar{p}$ deriving from DM annihilations (or any other primary source) [54]. These considerations disfavour light DM particles decaying prominently into hadrons.

To derive the antiproton bound we use the interstellar proton flux ϕ_p and the interstellar secondary antiproton flux $\phi_{\bar{p}}^{\rm sec}$ as given in Ref. [54], and apply a solar modulation in the force field approximation with $\phi_F = 500$ MV. The 2σ upper bound on $\langle\sigma_{ann}v\rangle$ from antiproton searches is derived by using the whole energy spectrum in the range where PAMELA antiproton measurements are available [198].

γ-rays

In some specific models, DM particles can annihilate directly into photon(s) producing clear spectral γ-ray lines (see e.g. [330]): the branching ratios for such processes are however usually low. We do not consider in this paper such annihilation channels. Instead, we consider γ-rays produced by decays of (or radiation from) final state particles of the annihilation process. These processes lead to a continuous spectrum up to energies close to the mass of the DM particle, as discussed in Section 5.2 (see in particular equation (5.9)). We compute the γ-ray flux in a 10^{-5} sr solid angle towards the Galactic Centre (GC). We compare our predictions with the HESS measurement of the GC source in 2003 and 2004, $\Phi(> 160 \text{ GeV}) = 1.89 \pm 0.38 \times 10^{-11}$ cm^{-2}s^{-1} [230], and derive the bound on the annihilation cross-section requiring that our model does not exceed the measurement by more than 2σ: this is the bound from the Galactic Centre, labelled as "γ from GC" in Figures 5.20–5.22.

Another way for DM annihilations to give rise to γ–ray fluxes is through inverse Compton scattering on electrons and positrons produced by DM annihilation. In fact, low–energy photons, such as those in the CMB, starlight and infrared radiation, may be up–scattered by high–energy electrons and positrons. This channel has gained particular relevance ever since the PAMELA collaboration published their exciting results: if the positron data are due to DM annihilations, then there should exist a large population of electrons and positrons in the Milky Way able to up–scatter low–energy photons. In Ref. [163] the authors computed the ICS γ–ray spectrum towards regions far from the

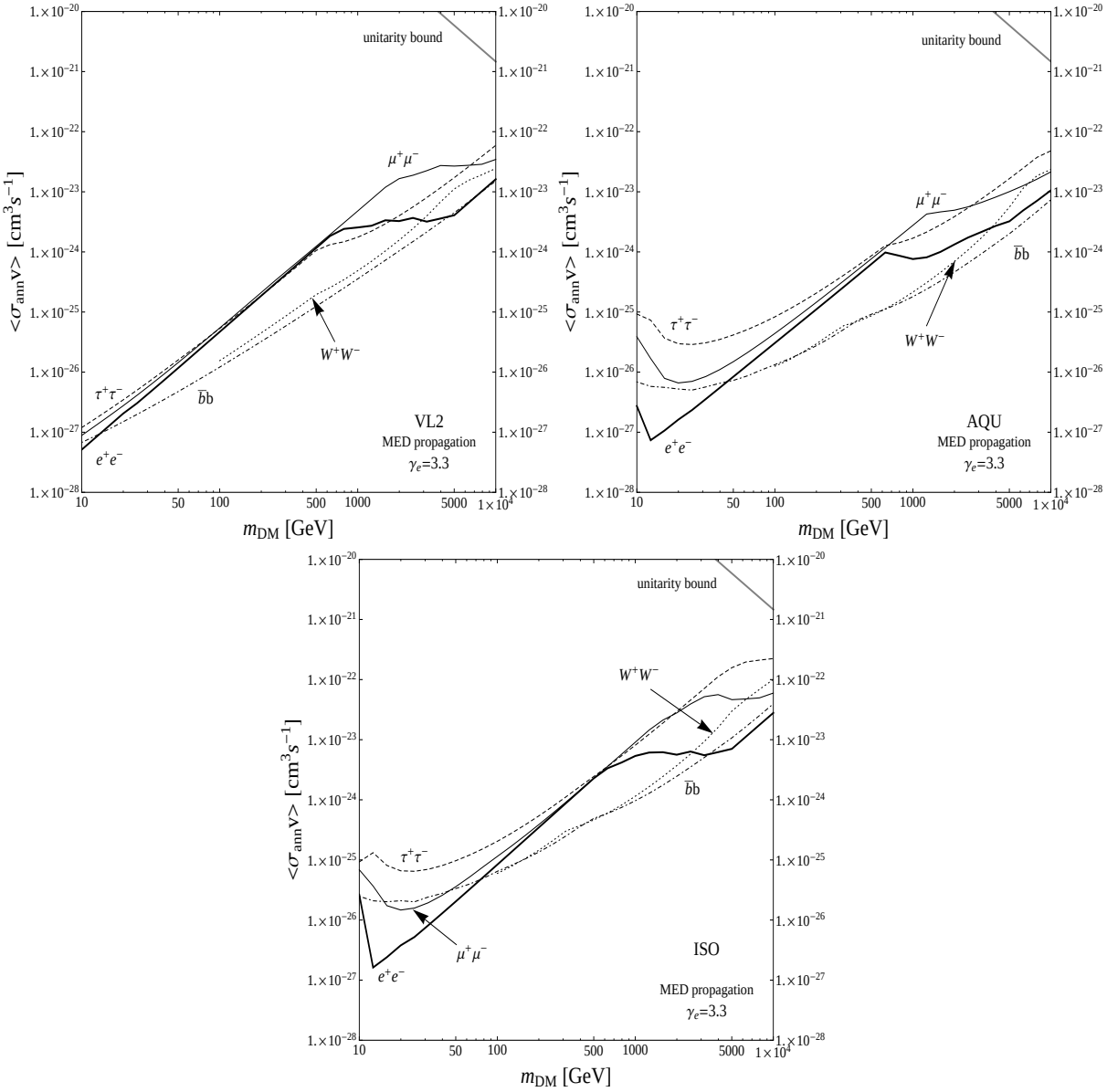

Figure 5.23: Summary of the astrophysical bounds on the DM annihilation cross-section vs. the DM mass, for the Via Lactea II (top left), Aquarius (top right) and cored isothermal (bottom) DM distribution and for different DM annihilation channels: e^+e^-, $\mu^+\mu^-$, $\tau^+\tau^-$, W^+W^- and $\bar{b}b$. Cosmic rays are propagated in the MED model and the electron spectral index is $\gamma_e = 3.3$.

GC. Here we apply the same procedure – see details in Section 4.2.3. Notice that these constraints are especially robust against the DM density profile since the GC region is excluded from the field of view.

Radio photons

The interpretation of the rising positron fraction observed by PAMELA as a signal of DM annihilations would result in a large amount of highly energetic electrons and positrons permeating our Galaxy. This should hold true particularly towards the GC where the DM density is expected to be the highest. Such relativistic electrons and positrons propagating in the galactic magnetic field emit synchrotron radiation in the radio frequency band. As in Section 5.6, we consider a cone with half-aperture 4" pointed toward the GC and $\nu = 0.408$ GHz for which an upper bound of 0.05 Jy has been derived from radio observations [331]. In this way we can determine the constraint on the plane $m_\chi - \langle\sigma_{ann} v\rangle$ given by radio observations of the GC. In order to take into account the different approaches of Refs. [328] and [55], we weaken the bound obtained with equation (5.22) by a factor 7 [7] and consider such rescaled result as an effective constraint. The radio bound is shown as a shaded band in Figures 5.20–5.22.

Optical depth of CMB photons

The optical depth of CMB photons depends on how and when the reionisation of the Universe occured. If DM is annihilating, then a considerable amount of high–energy electrons and positrons may be created after recombination giving rise, by ICS on CMB photons, to a population of (low–energy) γ–rays. These can easily ionise the gas releasing electrons and hence reducing the optical depth of CMB photons [262]. Comparing such effect with the measured optical depth by WMAP, the authors of Ref. [263] have derived upper limits on the annihilation cross-section of DM particles, that we also reproduce in Figures 5.20–5.22. Since there is no dependence on the DM density profile, these constraints are very robust and difficult to avoid. This constraint has also been carefully analysed in Refs. [278] and [332].

Other effects of conspicuous DM annihilations in the early Universe are the heating of the intergalactic medium [263] and the distortion of CMB anisotropies and polarisation [277].

5.8.3 Modified cosmologies

Cosmological models arising in modifications of General Relativity very often predict a cosmological history with an expansion rate $H'(T)$ larger than the Hubble expansion rate $H(T)$ of standard cosmology at early times. Generically, we can encode this enhancement into a temperature–dependent function $A(T)$ as [28, 16, 310]

$$H'(T) \;=\; A(T) H(T) \tag{5.31}$$

with $A(T) > 1$ at large temperatures and with $A(T) \to 1$ just before BBN kicks in, in order not to spoil the successful predictions of BBN on the abundance of primordial

[7] We thank Marco Regis and Marco Taoso for the numerical comparison between Refs. [328, 55].

light elements. In order to be as general as possible, we will perform our analysis by parameterising the temperature–behavior of the enhancement function $A(T)$ as

$$A(T) = 1 + \eta \left(\frac{T}{T_{\rm f}}\right)^{\nu} \tanh\left(\frac{T - T_{\rm re}}{T_{\rm re}}\right) \tag{5.32}$$

for temperatures $T > T_{\rm re}$ and $A(T) = 1$ for $T \leq T_{\rm re}$. This form has been adopted in the Refs. [28, 16]: it is a suitable parameterisation to describe a cosmology where $H' \to H$, at some "re-entering" temperature $T_{\rm re} \gtrsim 1$ MeV. For definiteness we will fix $T_{\rm re} = 1$ MeV in our analysis and take $T_{\rm f}$ to be the temperature at which the WIMP DM candidate freezes out in standard cosmology ($T_{\rm f}$ is therefore DM mass–dependent). Notice that at $T = T_f \gg T_{re}$, $A(T_f) = 1 + \eta$. The freeze–out temperature is determined with the standard procedure, which can be found for instance in Refs. [28, 16].

We will organise our discussion in terms of bounds on η for different cosmological models, characterised by the parameter ν: $\nu = 2$ refers to the Hubble rate evolution in a Randall–Sundrum type II brane cosmology scenario of Ref. [333]; $\nu = 1$ is the typical kination evolution, discussed e.g. in Ref. [24, 25, 26, 27]; $\nu = -1$ is representative of the behaviour found in scalar–tensor cosmologies in Ref. [28]. The trivial case $\nu = 0$ refers to an overall boost of the Hubble rate, like in the case of a large number of additional relativistic degrees of freedom in the thermal plasma.

With an increased expansion rate, thermal relics freeze–out their abundance earlier than in standard cosmology: this implies that a thermal (cold) relic matches the correct relic abundance for annihilation cross-sections $\langle \sigma_{ann} v \rangle$ which are larger than in standard cosmology. A consequence of this is that Dark Matter particles possess today, in the galactic environment, larger annihilation cross-sections and thus enhanced indirect detection signals, as compared to those obtained for a thermal decoupling in standard cosmology. This implies that indirect searches for Dark Matter may have a potential of constraining pre–BBN cosmological histories, under the assumption that Dark Matter is a thermal relic. In Refs. [16, 310] cosmic–ray antiproton and gamma–ray data were used to derive bounds on the admissible enhancement of the expansion rate in the pre–BBN phase. In the current paper we extend these analyses to comprehend all the astrophysical observables discussed in the previous subsection.

Since alternative cosmologies with $A(T) > 1$ imply that the correct relic abundance of a relic particle is obtained with larger annihilation cross-sections, they offer a framework to explain the PAMELA data without requiring specific mechanisms to boost the annihilation rate such as Sommerfeld enhancements [219, 259] or (unlikely) large astrophysical boosts [222]. Alternative cosmologies offer a "cosmological boost" to a thermal relic.

5.8.4 Cosmological boost: PAMELA and bounds on modified cosmologies

Boosts for PAMELA

We start our analysis by studying under what conditions the modified cosmological scenarios can explain the PAMELA data without violating any of the constraints described in subsection 5.8.2. The study is performed as follows: we numerically solve the Boltzmann equation for the evolution of the number density of a thermal relic in a cosmology where the Hubble rate is given by equations (5.31) and (5.32) and we determine the values of

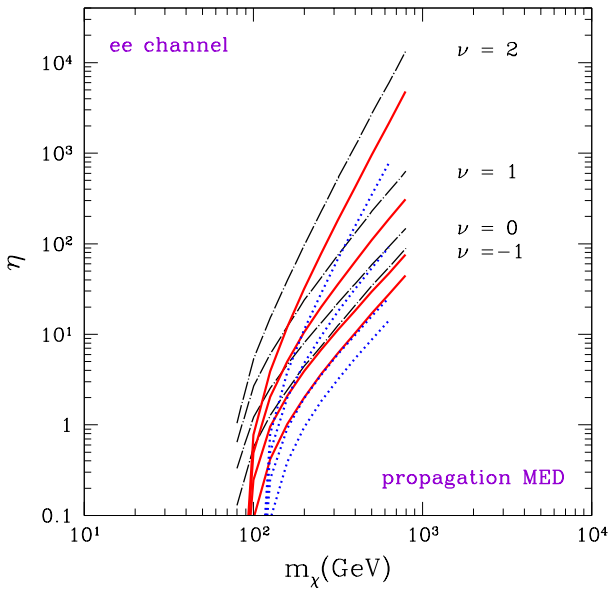

Figure 5.24: Values of the η parameter required to explain the PAMELA data together with $\Omega^0_\chi h^2 = \Omega^0_{cdm} h^2 = 0.11$, in the case of DM annihilation into e^+e^- and for different cosmologies labelled by the values of ν. The DM annihilation cross-section is required to explain the PAMELA data without violating the astrophysical bounds (see Figures 5.20, 5.21 and 5.22) and the values of η are determined, for each DM mass, in order to have the correct DM relic abundance in the modified cosmology, which therefore produces the required cosmological boost. The solid (red) lines refer to the Via Lactea II DM distribution, the dot–dashed (black) lines refer to a cored isothermal sphere and the dotted (blue) lines refer to the Aquarius DM distribution. Propagation parameters are set at the MED case.

the enhancement parameter η which are required, for a given ν, in order to reproduce the correct value $\Omega^0_\chi h^2 = \Omega^0_{cdm} h^2 = 0.11$ for the relic abundance of the Dark Matter particle. The annihilation cross-sections are fixed to explain the PAMELA data (within the implemented astrophysical bounds), and have been derived in subsection 5.8.2. The analysis is performed separately for each of the possibile DM annihilation channels. This is an alternative solution to the PAMELA "anomaly" in terms of Dark Matter annihilation: the compatibility between the large annihilation cross-sections required by the PAMELA data and the WMAP value of the relic abundance are obtained by means of modified cosmologies.

Figure 5.24 refers to the case of annihilation into an e^+e^- final state, and the annihilation cross-sections used to obtain Figure 5.24 are those shown in Figures 5.20, 5.21 and 5.22 which refer to the "$\frac{e^+}{e^+ + e^-}$ best–fit" curve restricted to the range where it is not excluded by any of the considered constraints. The values of η required to explain the PAMELA positron fraction (and compatible with the other bounds) change significantly with the cosmological scenario: they are confined to the range between 0.1 and 100 for $\nu = -1$, while for $\nu = 2$ they are in an interval from $\mathcal{O}(1)$ to about 10^4, depending on the Dark Matter mass and on the Dark Matter halo profile. The values of η increase with m_χ because the PAMELA data require larger annihilation cross-sections for larger masses, as seen in Figure 5.20: in this case, in order to match the WMAP value for the relic abundance, larger cross-sections require earlier decoupling of the Dark Matter particle,

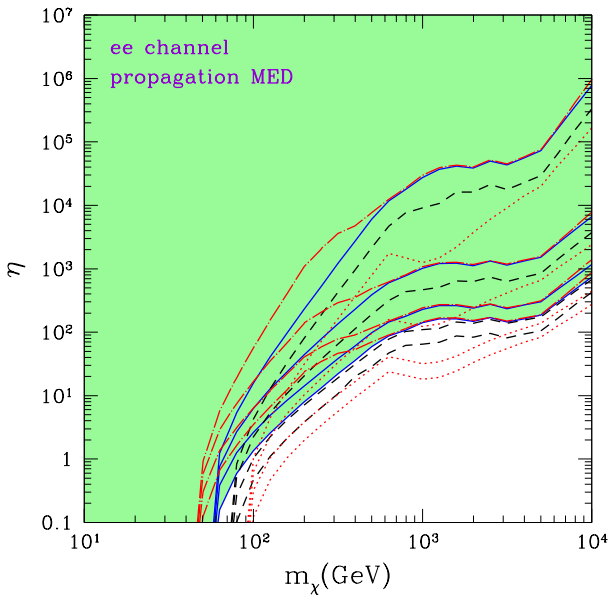

Figure 5.25: Upper bound on the η parameter for different cosmological models and for the case of DM annihilation into e^+e^-. The bounds arise from the astrophysical constraints on the DM annihilation cross-section and from the requirement that the DM relic abundance matches the WMAP value for CDM. The solid (blue) lines refer to a cored isothermal DM distribution, the dashed (black) lines to the Via Lactea II DM distribution and the dotted (red) lines to the Aquarius DM profile. Propagation parameters are set at the MED case. The set of solid, dashed and dotted lines refers to cosmologies with $\nu = -1, 0, 1, 2$ going from the lower to the upper curves. For each cosmology, the excluded values of η are those above the corresponding line. The red dot–dashed lines refer to a cored isothermal DM distribution and the MIN set of propagation parameters.

and this in turn requires a faster expansion of the Universe, hence larger η. In addition, from Figure 5.24 we notice that the enhancement factors are significantly larger for larger values of ν. Figure 5.24 also shows that the uncertainty arising from different choices of the Dark Matter distribution in the halo may be relevant: the solid lines refer to the case of the Via Lactea II Dark Matter distribution, the dot–dashed lines to a cored isothermal sphere and the dotted lines to the Aquarius simulation. The results shown in Figure 5.24 have been obtained for the MED set of astrophysical parameters governing cosmic–ray diffusion.

Astrophysical bounds on modified cosmologies

The astrophysical bounds on the Dark Matter annihilation cross-section discussed in subsection 5.8.2 may be alternatively used to set constraints on the cosmological histories, as it was done in Refs. [16, 310], where antiproton and gamma–ray data were used and a Dark Matter particle annihilating dominantly into a quark–antiquark final state (namely $\bar{b}b$) was assumed. We now extend that analyses by considering the whole host of experimental data of subsection 5.8.2 and by including the whole set of annihilation final states of a cold Dark Matter particle.

The results are shown in Figure 5.25 for the e^+e^- annihilation channel. The solid lines refer to a cored Dark Matter distribution, the dashed lines to Via Lactea II and the dotted lines to Aquarius. Propagation parameters are set to the MED configuration.

The bound for each cosmology ($\nu = -1, 0, 1, 2$, from bottom to top) is the area above the corresponding line. We notice that, depending on the Dark Matter mass and on the annihilation channel, the bounds may be quite restrictive. This is an interesting result, since it imposes strong bounds on the cosmological histories of the Universe at the time of Dark Matter freeze–out (from $T \sim 400$ MeV to $T \sim 400$ GeV for the mass range considered here), under the hypothesis that Dark Matter is a thermal relic. The bounds are typically stronger for lighter Dark Matter, since for lighter Dark Matter the astrophysical bounds are stronger. The dependence on the Dark Matter profile may be large and the size of the difference depends also on the annihilation final state of the DM particle. Figure 5.25 also shows the effect of cosmic-ray propagation uncertainties: the red dot-dashed lines refer to the MIN propagation set for the cored isothermal DM profile.

5.8.5 Conclusions

Alternative cosmologies feature modified expansion rates of the Universe before BBN, $T \gtrsim$ MeV. A typical prediction is that the expansion rate is enhanced with respect to the General Relativity case: this, in turn, implies that thermal relics decouple earlier resulting in larger relic abundances. The correct value of the relic abundance for a thermal relic, value which cannot exceed the cosmological determination of the Dark Matter content of the Universe, is therefore obtained for larger annihilation cross-sections, as compared to standard cosmology. Indirect detection rates of Dark Matter directly depend on the current value of $\langle \sigma_{ann} v \rangle$ in the galactic halo. In the case of a dominant s–wave annihilation, which is typical for most of the cold Dark Matter candidates in large portions of the parameter space of new physics models, the larger values of $\langle \sigma_{ann} v \rangle$ required to match the WMAP Dark Matter abundance in modified cosmologies imply larger signals in the Galaxy. We have exploited this feature in a twofold way.

Firstly, the recent results on the measurement of the positron fraction provided by the PAMELA detector have shown a clear and steady rise at energies above 10 GeV. This behaviour, which is currently under deep scrutiny, has one of its interpretations in terms of Dark Matter annihilation in our Galaxy. The theoretical analyses which have discussed this possibility show that, in order to explain the PAMELA "excess", the annihilation cross-sections need to be orders of magnitude larger than those required in standard cosmology to explain the observed amount of cold Dark Matter. This fact poses a problem for a thermal relic, and various mechanisms have been invoked to boost the positron signal without spoiling the correct value of relic abundance (e.g. astrophysical boosts and Sommerfeld enhanced cross-sections). Since in cosmologies with an enhanced expansion rate we naturally require larger annihilation cross-sections, we have discussed the properties of these alternative cosmologies in order to be able to explain the PAMELA "puzzle" without violating other observations. We have derived the required amount of enhancement for different cosmologies.

Secondly, we have used the large host of independent results on the search for indirect signals of Dark Matter to set bounds on the enhancement of the Hubble rate in the pre–BBN era: this idea was introduced in Ref. [16], and there pursued by using exotic antiproton searches in cosmic–rays. A first attempt to use the gamma–ray signal was done in Ref. [310]. In the current paper we extend these analyses by introducing a whole set of indirect detection signals, which became increasingly relevant in the last months with the recent results from detectors like PAMELA, Fermi-LAT and HESS. We have classified

cathegories of cosmological models with an enhanced expansion rate and we have derived bounds on them under the hypothesis that the Dark Matter is a thermal relic.

Chapter 6

Final remarks

In this thesis, the present panorama and the prospects of Dark Matter searches were carefully analysed in a model-independent way with special focus on direct and indirect detection. As for direct detection, present and upcoming experiments seem very promising in probing the presence of Dark Matter in the solar neighbourhood. After evaluating the systematic uncertainties pertaining the local Dark Matter density in Chapter 2, we studied in detail the impact of astrophysical uncertainties on direct detection signals in Chapter 3. It was found that the reconstruction of the Dark Matter mass and spin-independent scattering cross-section is significantly degraded by astrophysical unknowns. However, the combination of different targets in the next generation of underground detectors enhances the reconstruction accuracy and can even be used to extract some quantities regardless of the astrophysical details. This will be of particular importance when combining direct detection results and LHC data.

Regarding indirect detection, we exemplified in Chapter 5 the importance of pursuing a multi-messenger approach to test the Dark Matter interpretation of the electron/positron excess. Generically speaking, Dark Matter annihilations do not provide very predictive signatures. Instead, due to the large freedom in choosing the mass, annihilation channels and cross-section and the uncertainties associated to the Dark Matter distribution and propagation of cosmic rays, there is a high degree of flexibility in every DM-induced flux. It is in fact possible to explain almost any astrophysical signal by tuning appropriately the numerous parameters at play. Therefore, the different mechanisms put forward to justify the large Dark Matter annihilation cross-sections needed to explain the rise in the positron fraction should always be cross-checked against other astrophysical channels. The origin of the electron/positron excess lies today on the front line of research in astroparticle physics. As shown in Chapter 5, upcoming precise $e^{\pm}$ measurements will not suffice to distinguish between different sources – complementary data are needed. Thus, it will be important to use current and future γ-ray observations of supernova remnants and pulsar wind nebulae to build a more accurate understanding of how electrons and positrons are produced, accelerated and escape astrophysical sources. This will certainly help to quantify the astrophysical contribution to the cosmic ray electronic component, but large uncertainties are inevitably introduced by our lack of knowledge about cosmic-ray propagation. Superior measurements of cosmic-ray nuclei – hopefully provided soon by AMS-02 – will reduce those uncertainties as we have shown in Chapter 4. For instance, already a few precise high-energy data points on the ratio ^{10}Be/^{9}Be would be invaluable. Nevertheless, AMS-02 data will likely be insufficient to distinguish between assumptions

regarding e.g. source distribution or source abundances.

Dark Matter searches stand today at a turning point. Present experimental results are already probing the theoretically motivated ballpark of WIMP properties, providing in some cases very stringent bounds. Moreover, precise, long-awaited data will be collected soon, allowing to check theoretical ideas developed decades ago. In particular, collider data from the LHC, cosmic-ray measurements from AMS-02, and direct detection results from the next generation of underground detectors are awaited eagerly. Future Dark Matter studies should pursue a multi-messenger approach where the interplay between direct, indirect and collider signals is explored without neglecting the underlying uncertainties. Most probably, the discovery of Dark Matter will imply multiple signatures detected with different experiments.

Bibliography

[1] Miguel Pato, Oscar Agertz, Gianfranco Bertone, Ben Moore, and Romain Teyssier. Systematic uncertainties in the determination of the local dark matter density. *Phys. Rev.*, D82:023531, 2010, 1006.1322.

[2] Miguel Pato et al. Complementarity of Dark Matter Direct Detection Targets. 2010, 1012.3458.

[3] Miguel Pato, Dan Hooper, and Melanie Simet. Pinpointing Cosmic Ray Propagation With The AMS-02 Experiment. *JCAP*, 1006:022, 2010, 1002.3341.

[4] Miguel Pato, Lidia Pieri, and Gianfranco Bertone. Multi-messenger constraints on the annihilating dark matter interpretation of the positron excess. *Phys. Rev.*, D80:103510, 2009, 0905.0372.

[5] Miguel Pato, Massimiliano Lattanzi, and Gianfranco Bertone. Discriminating the source of high-energy positrons with AMS-02. *JCAP*, 1012:020, 2010, 1010.5236.

[6] R. Catena, N. Fornengo, M. Pato, L. Pieri, and A. Masiero. Thermal Relics in Modified Cosmologies: Bounds on Evolution Histories of the Early Universe and Cosmological Boosts for PAMELA. *Phys. Rev.*, D81:123522, 2010, 0912.4421.

[7] P. Binetruy. Supersymmetry: Theory, experiment and cosmology. Oxford, UK: Oxford Univ. Pr. (2006) 520 p.

[8] W. N. Cottingham and D. A. Greenwood. An introduction to the standard model of particle physics. Cambridge, UK: Univ. Pr. (2007) 272 p.

[9] L. Bergstrom and A. Goobar. Cosmology and particle astrophysics. Berlin, Germany: Springer (2004) 364 p.

[10] Edward W. Kolb and Michael S. Turner. The Early universe. *Front. Phys.*, 69:1–547, 1990.

[11] K Nakamura et al. Review of particle physics. *J. Phys.*, G37:075021, 2010.

[12] Bernard F. Schutz. A first course in general relativity. Cambridge, UK: Cambridge University Press (1985).

[13] Steven Weinberg. Cosmology. Oxford, UK: Oxford Univ. Pr. (2008) 593 p.

[14] Andrew H. Jaffe. Cosmology lectures notes. 2010.

[15] E. Komatsu et al. Seven-Year Wilkinson Microwave Anisotropy Probe (WMAP) Observations: Cosmological Interpretation. 2010, 1001.4538.

[16] Mia Schelke, Riccardo Catena, Nicolao Fornengo, Antonio Masiero, and Massimo Pietroni. Constraining pre big-bang nucleosynthesis expansion using cosmic antiprotons. *Phys. Rev.*, D74:083505, 2006, hep-ph/0605287.

[17] Gianfranco Bertone, Dan Hooper, and Joseph Silk. Particle dark matter: Evidence, candidates and constraints. *Phys. Rept.*, 405:279–390, 2005, hep-ph/0404175.

[18] Anne M. Green, Stefan Hofmann, and Dominik J. Schwarz. The first WIMPy halos. *JCAP*, 0508:003, 2005, astro-ph/0503387.

[19] P. Gondolo et al. DarkSUSY: Computing supersymmetric dark matter properties numerically. *JCAP*, 0407:008, 2004, astro-ph/0406204.

[20] Gian Francesco Giudice, Edward W. Kolb, and Antonio Riotto. Largest temperature of the radiation era and its cosmological implications. *Phys. Rev.*, D64:023508, 2001, hep-ph/0005123.

[21] N. Fornengo, A. Riotto, and S. Scopel. Supersymmetric dark matter and the reheating temperature of the universe. *Phys. Rev.*, D67:023514, 2003, hep-ph/0208072.

[22] Graciela B. Gelmini and Paolo Gondolo. Neutralino with the right cold dark matter abundance in (almost) any supersymmetric model. *Phys. Rev.*, D74:023510, 2006, hep-ph/0602230.

[23] Graciela Gelmini, Paolo Gondolo, Adrian Soldatenko, and Carlos E. Yaguna. The effect of a late decaying scalar on the neutralino relic density. *Phys. Rev.*, D74:083514, 2006, hep-ph/0605016.

[24] Pierre Salati. Quintessence and the Relic Density of Neutralinos. *Phys. Lett.*, B571:121–131, 2003, astro-ph/0207396.

[25] Francesca Rosati. Quintessential enhancement of dark matter abundance. *Phys. Lett.*, B570:5–10, 2003, hep-ph/0302159.

[26] Stefano Profumo and Piero Ullio. SUSY dark matter and quintessence. *JCAP*, 0311:006, 2003, hep-ph/0309220.

[27] C. Pallis. Quintessential kination and cold dark matter abundance. *JCAP*, 0510:015, 2005, hep-ph/0503080.

[28] Riccardo Catena, N. Fornengo, A. Masiero, Massimo Pietroni, and Francesca Rosati. Dark matter relic abundance and scalar-tensor dark energy. *Phys. Rev.*, D70:063519, 2004, astro-ph/0403614.

[29] Lars Bergstrom. Non-baryonic dark matter: Observational evidence and detection methods. *Rept. Prog. Phys.*, 63:793, 2000, hep-ph/0002126.

[30] Carlos Munoz. Dark matter detection in the light of recent experimental results. *Int. J. Mod. Phys.*, A19:3093–3170, 2004, hep-ph/0309346.

[31] Gianfranco ed. Bertone. Particle Dark Matter: Observations, Models and Searches. Cambridge, UK: Cambridge University Press (2010).

[32] Gary Steigman. Primordial Nucleosynthesis in the Precision Cosmology Era. *Ann. Rev. Nucl. Part. Sci.*, 57:463–491, 2007, 0712.1100.

[33] R. Amanullah et al. Spectra and Light Curves of Six Type Ia Supernovae at $0.511 < z < 1.12$ and the Union2 Compilation. *Astrophys. J.*, 716:712–738, 2010, 1004.1711.

[34] Robert P. Kirshner. Foundations of Supernova Cosmology. 2009, 0910.0257.

[35] T. Padmanabhan. Structure Formation in the Universe. Cambridge, UK: Cambridge University Press (1993) 499 p.

[36] George F. Smoot and D. Scott. Cosmic background radiation: in Review of Particle Physics (RPP 2000). *Eur. Phys. J.*, C15:145–149, 2000.

[37] Torsten Bringmann. Particle Models and the Small-Scale Structure of Dark Matter. *New J. Phys.*, 11:105027, 2009, 0903.0189.

[38] Max Tegmark et al. The 3D power spectrum of galaxies from the SDSS. *Astrophys. J.*, 606:702–740, 2004, astro-ph/0310725.

[39] Max Tegmark. Cosmological neutrino bounds for non-cosmologists. *Phys. Scripta*, T121:153–155, 2005, hep-ph/0503257.

[40] Daniel J. Eisenstein et al. Detection of the Baryon Acoustic Peak in the Large-Scale Correlation Function of SDSS Luminous Red Galaxies. *Astrophys. J.*, 633:560–574, 2005, astro-ph/0501171.

[41] Douglas Clowe et al. A direct empirical proof of the existence of dark matter. *Astrophys. J.*, 648:L109–L113, 2006, astro-ph/0608407.

[42] Maxim Markevitch et al. Direct constraints on the dark matter self-interaction cross-section from the merging galaxy cluster 1E0657-56. *Astrophys. J.*, 606:819–824, 2004, astro-ph/0309303.

[43] James Binney and Tremaine Scott. Galactic Dynamics. Princeton, USA: Princeton University Press (2008).

[44] K. G. Begeman, A. H. Broeils, and R. H. Sanders. Extended rotation curves of spiral galaxies - Dark haloes and modified dynamics. *Mon. Not. Roy. Astron. Soc.*, 249:523–537, April 1991.

[45] Gerard Jungman, Marc Kamionkowski, and Kim Griest. Supersymmetric dark matter. *Phys. Rept.*, 267:195–373, 1996, hep-ph/9506380.

[46] Nicolao Fornengo. Status and perspectives of indirect and direct dark matter searches. *Adv. Space Res.*, 41:2010–2018, 2008, astro-ph/0612786.

[47] John Ellis and Keith A. Olive. Supersymmetric Dark Matter Candidates. 2010, 1001.3651.

[48] Konrad Kuijken. The Maximum Optical Depth Towards Bulge Stars From Axisymmetric Models of the Milky Way. 1997, astro-ph/9706054.

[49] E. W. Otten and C. Weinheimer. Neutrino mass limit from tritium beta decay. *Rept. Prog. Phys.*, 71:086201, 2008, 0909.2104.

[50] S. Tremaine and J. E. Gunn. Dynamical role of light neutral leptons in cosmology. *Phys. Rev. Lett.*, 42:407–410, 1979.

[51] Marco Taoso, Gianfranco Bertone, and Antonio Masiero. Dark Matter Candidates: A Ten-Point Test. *JCAP*, 0803:022, 2008, 0711.4996.

[52] J. Abraham et al. Upper limit on the cosmic-ray photon fraction at EeV energies from the Pierre Auger Observatory. *Astropart. Phys.*, 31:399–406, 2009, 0903.1127.

[53] Lars Bergstrom, Piero Ullio, and James H. Buckley. Observability of gamma rays from dark matter neutralino annihilations in the Milky Way halo. *Astropart. Phys.*, 9:137–162, 1998, astro-ph/9712318.

[54] F. Donato, D. Maurin, P. Brun, T. Delahaye, and P. Salati. Constraints on WIMP Dark Matter from the High Energy PAMELA $\bar{p}/p$ data. *Phys. Rev. Lett.*, 102:071301, 2009, 0810.5292.

[55] Gianfranco Bertone, Marco Cirelli, Alessandro Strumia, and Marco Taoso. Gamma-ray and radio tests of the e+e- excess from DM annihilations. *JCAP*, 0903:009, 2009, 0811.3744.

[56] Marco Taoso, Gianfranco Bertone, Georges Meynet, and Sylvia Ekstrom. Dark Matter annihilations in Pop III stars. *Phys. Rev.*, D78:123510, 2008, 0806.2681.

[57] Marco Taoso, Fabio Iocco, Georges Meynet, Gianfranco Bertone, and Patrick Eggenberger. Effect of low mass dark matter particles on the Sun. *Phys. Rev.*, D82:083509, 2010, 1005.5711.

[58] Gianfranco Bertone. The moment of truth for WIMP Dark Matter. *Nature*, 468:389–393, 2010, 1011.3532.

[59] Stefano Profumo, Kris Sigurdson, and Marc Kamionkowski. What mass are the smallest protohalos? *Phys. Rev. Lett.*, 97:031301, 2006, astro-ph/0603373.

[60] A. M. Ghez, B. L. Klein, M. Morris, and E. E. Becklin. High Proper Motion Stars in the Vicinity of Sgr A*: Evidence for a Supermassive Black Hole at the Center of Our Galaxy. *Astrophys. J.*, 509:678–686, 1998, astro-ph/9807210.

[61] A. M. Ghez et al. Stellar Orbits Around the Galactic Center Black Hole. *Astrophys. J.*, 620:744–757, 2005, astro-ph/0306130.

[62] HongSheng Zhao. A Self-Consistent Dynamical Model for the COBE Detected Galactic Bar. *Mon. Not. Roy. Astron. Soc.*, 283:149–166, 1996, astro-ph/9512064.

[63] Riccardo Catena and Piero Ullio. A novel determination of the local dark matter density. *JCAP*, 1008:004, 2010, 0907.0018.

[64] M. S. Longair. High-energy astrophysics. Vol. 2: Stars, the galaxy and the interstellar medium. Cambridge, UK: Univ. Pr. (1994) 393 p.

[65] S. Malhotra. The vertical equilibrium of molecular gas in the Galactic disk. *Astrophys. J.*, 433:687–704, October 1994, arXiv:astro-ph/9404028.

[66] Walter Dehnen and James Binney. Mass models of the Milky Way. *Mon. Not. Roy. Astron. Soc.*, 294:429, 1998, astro-ph/9612059.

[67] Tsuyoshi Sakamoto, Masashi Chiba, and Timothy C. Beers. The Mass of the Milky Way: Limits from a Newly Assembled Set of Halo Objects. *Astron. Astrophys.*, 397:899–912, 2003, astro-ph/0210508.

[68] K. Kuijken and G. Gilmore. The galactic disk surface mass density and the Galactic force K(z) at Z = 1.1 kiloparsecs. *Astrophys. J. Lett.*, 367:L9–L13, January 1991.

[69] K. Kuijken and G. Gilmore. The Mass Distribution in the Galactic Disc - Part Two - Determination of the Surface Mass Density of the Galactic Disc Near the Sun. *Mon. Not. Roy. Astron. Soc.*, 239:605, 1989.

[70] J. J. Binney and N. W. Evans. Cuspy Dark-Matter Haloes and the Galaxy. *Mon. Not. Roy. Astron. Soc.*, 327:L27, 2001, astro-ph/0108505.

[71] E. Kerins, A. C. Robin, and D. J. Marshall. High precision microlensing maps of the Galactic bulge. 2008, 0805.4626.

[72] J. A. R. Caldwell and J. P. Ostriker. The Mass distribution within our Galaxy: A Three component model. *Astrophys. J.*, 251:61–87, 1981.

[73] P. Salucci, F. Nesti, G. Gentile, and C. F. Martins. The dark matter density at the Sun's location. *Astron. Astrophys.*, 523:A83, 2010, 1003.3101.

[74] Evalyn I. Gates, Geza Gyuk, and Michael S. Turner. The Local halo density. *Astrophys. J.*, 449:L123–L126, 1995, astro-ph/9505039.

[75] Ben Moore et al. Dark matter in Draco and the Local Group: Implications for direct detection experiments. *Phys. Rev.*, D64:063508, 2001, astro-ph/0106271.

[76] P. Belli, R. Cerulli, N. Fornengo, and S. Scopel. Effect of the galactic halo modeling on the DAMA/NaI annual modulation result: an extended analysis of the data for WIMPs with a purely spin-independent coupling. *Phys. Rev.*, D66:043503, 2002, hep-ph/0203242.

[77] Markus Weber and Wim de Boer. Determination of the Local Dark Matter Density in our Galaxy. *Astron. Astrophys.*, 509:A25, 2010, 0910.4272.

[78] Mariangela Lisanti, Louis E. Strigari, Jay G. Wacker, and Risa H. Wechsler. The Dark Matter at the End of the Galaxy. 2010, 1010.4300.

[79] Jurg Diemand, Ben Moore, and Joachim Stadel. Earth-mass dark-matter haloes as the first structures in the early universe. *Nature.*, 433:389–391, 2005, astro-ph/0501589.

[80] Julio F. Navarro, Carlos S. Frenk, and Simon D. M. White. The Structure of Cold Dark Matter Halos. *Astrophys. J.*, 462:563–575, 1996, astro-ph/9508025.

[81] Julio F. Navarro, Carlos S. Frenk, and Simon D. M. White. A Universal Density Profile from Hierarchical Clustering. *Astrophys. J.*, 490:493–508, 1997, astro-ph/9611107.

[82] Gianfranco Bertone and David Merritt. Time-dependent models for dark matter at the Galactic center. *Phys. Rev.*, D72:103502, 2005, astro-ph/0501555.

[83] F. S. Ling, E. Nezri, E. Athanassoula, and R. Teyssier. Dark Matter Direct Detection Signals inferred from a Cosmological N-body Simulation with Baryons. *JCAP*, 1002:012, 2010, 0909.2028.

[84] Mark Vogelsberger et al. Phase-space structure in the local dark matter distribution and its signature in direct detection experiments. 2008, 0812.0362.

[85] Volker Springel et al. The Aquarius Project: the subhalos of galactic halos. *Mon. Not. Roy. Astron. Soc.*, 391:1685–1711, 2008, 0809.0898.

[86] George R. Blumenthal, S. M. Faber, Ricardo Flores, and Joel R. Primack. Contraction of Dark Matter Galactic Halos Due to Baryonic Infall. *Astrophys. J.*, 301:27, 1986.

[87] Oleg Y. Gnedin, Andrey V. Kravtsov, Anatoly A. Klypin, and Daisuke Nagai. Response of dark matter halos to condensation of baryons: cosmological simulations and improved adiabatic contraction model. *Astrophys. J.*, 616:16–26, 2004, astro-ph/0406247.

[88] Michael Gustafsson, Malcolm Fairbairn, and Jesper Sommer-Larsen. Baryonic Pinching of Galactic Dark Matter Haloes. *Phys. Rev.*, D74:123522, 2006, astro-ph/0608634.

[89] Patricia B. Tissera, Simon D. M. White, Susana Pedrosa, and Cecilia Scannapieco. Dark matter response to galaxy formation. 2009, 0911.2316.

[90] Mario G. Abadi, Julio F. Navarro, Mark Fardal, Arif Babul, and Matthias Steinmetz. Galaxy-Induced Transformation of Dark Matter Halos. 2009, 0902.2477.

[91] Victor P. Debattista et al. The Causes of Halo Shape Changes Induced by Cooling Baryons: Disks Versus Substructures. 2007, 0707.0737.

[92] J. I. Read, G. Lake, O. Agertz, and Victor P. Debattista. Thin, thick and dark discs in LCDM. 2008, 0803.2714.

[93] Tobias Bruch, Annika H. G. Peter, Justin Read, Laura Baudis, and George Lake. Dark Matter Disc Enhanced Neutrino Fluxes from the Sun and Earth. *Phys. Lett.*, B674:250–256, 2009, 0902.4001.

[94] Sergio Colafrancesco, S. Profumo, and P. Ullio. Multi-frequency analysis of neutralino dark matter annihilations in the Coma cluster. *Astron. Astrophys.*, 455:21, 2006, astro-ph/0507575.

[95] Piero Ullio, Lars Bergstrom, Joakim Edsjo, and Cedric G. Lacey. Cosmological dark matter annihilations into gamma-rays: A closer look. *Phys. Rev.*, D66:123502, 2002, astro-ph/0207125.

[96] A. A. Abdo et al. Constraints on Cosmological Dark Matter Annihilation from the Fermi-LAT Isotropic Diffuse Gamma-Ray Measurement. *JCAP*, 1004:014, 2010, 1002.4415.

[97] Gianfranco Bertone, David G. Cerdeno, Mattia Fornasa, Roberto Ruiz de Austri, and Roberto Trotta. Identification of Dark Matter particles with LHC and direct detection data. *Phys. Rev.*, D82:055008, 2010, 1005.4280.

[98] Louis E. Strigari and Roberto Trotta. Reconstructing WIMP Properties in Direct Detection Experiments Including Galactic Dark Matter Distribution Uncertainties. *JCAP*, 0911:019, 2009, 0906.5361.

[99] Marcel Zemp et al. The Graininess of Dark Matter Haloes. 2008, 0812.2033.

[100] Oscar Agertz, Romain Teyssier, and Ben Moore. The formation of disc galaxies in a LCDM universe. 2010, 1004.0005.

[101] Aurel Schneider, Lawrence Krauss, and Ben Moore. Impact of Dark Matter Microhalos on Signatures for Direct and Indirect Detection. *Phys. Rev.*, D82:063525, 2010, 1004.5432.

[102] X. X. Xue et al. The Milky Way's Circular Velocity Curve to 60 kpc and an Estimate of the Dark Matter Halo Mass from Kinematics of 2400 SDSS Blue Horizontal Branch Stars. *Astrophys. J.*, 684:1143–1158, 2008, 0801.1232.

[103] Qi Guo, Simon White, Cheng Li, and Michael Boylan-Kolchin. How do galaxies populate Dark Matter halos? *Mon. Not. Roy. Astron. Soc.*, 404:1111, 2010, 0909.4305.

[104] N. Katz. Dissipationless collapse in an expanding universe. *Astrophys. J.*, 368:325–336, February 1991.

[105] Susana E. Pedrosa, Patricia B. Tissera, and Cecilia Scannapieco. The impact of baryons on dark matter haloes. 2009, 0902.2100.

[106] David G. Cerdeno and Anne M. Green. Direct detection of WIMPs. 2010, 1002.1912.

[107] John R. Ellis, Keith A. Olive, and Christopher Savage. Hadronic Uncertainties in the Elastic Scattering of Supersymmetric Dark Matter. *Phys. Rev.*, D77:065026, 2008, 0801.3656.

[108] J. D. Lewin and P. F. Smith. Review of mathematics, numerical factors, and corrections for dark matter experiments based on elastic nuclear recoil. *Astropart. Phys.*, 6:87–112, 1996.

[109] Laura Baudis. Underground searches for cold relics of the early universe. 2005, astro-ph/0503549.

[110] Laura Baudis. Direct Detection of Cold Dark Matter. 2007, 0711.3788.

[111] Christopher Savage, Graciela Gelmini, Paolo Gondolo, and Katherine Freese. Compatibility of DAMA/LIBRA dark matter detection with other searches. *JCAP*, 0904:010, 2009, 0808.3607.

[112] Christopher McCabe. The Astrophysical Uncertainties Of Dark Matter Direct Detection Experiments. *Phys. Rev.*, D82:023530, 2010, 1005.0579.

[113] Eric Armengaud. Gif Lectures on direct detection of Dark Matter. 2010, 1003.2380.

[114] E. Aprile et al. First Dark Matter Results from the XENON100 Experiment. *Phys. Rev. Lett.*, 105:131302, 2010, 1005.0380.

[115] J. Angle et al. Limits on spin-dependent WIMP-nucleon cross-sections from the XENON10 experiment. *Phys. Rev. Lett.*, 101:091301, 2008, 0805.2939.

[116] R. Bernabei et al. New results from DAMA/LIBRA. *Eur. Phys. J.*, C67:39–49, 2010, 1002.1028.

[117] C. E. Aalseth et al. Results from a Search for Light-Mass Dark Matter with a P-type Point Contact Germanium Detector. 2010, 1002.4703.

[118] Christopher Savage, Graciela Gelmini, Paolo Gondolo, and Katherine Freese. XENON10/100 dark matter constraints in comparison with CoGeNT and DAMA: examining the Leff dependence. 2010, 1006.0972.

[119] Z. Ahmed et al. Dark Matter Search Results from the CDMS II Experiment. *Science*, 327:1619–1621, 2010, 0912.3592.

[120] Fedor Bezrukov, Felix Kahlhoefer, and Manfred Lindner. Interplay between scintillation and ionization in liquid xenon Dark Matter searches. 2010, 1011.3990.

[121] Z. Ahmed et al. Results from a Low-Energy Analysis of the CDMS II Germanium Data. 2010, 1011.2482.

[122] V. N. Lebedenko et al. Result from the First Science Run of the ZEPLIN-III Dark Matter Search Experiment. *Phys. Rev.*, D80:052010, 2009, 0812.1150.

[123] Anne M. Green. Determining the WIMP mass from a single direct detection experiment, a more detailed study. *JCAP*, 0807:005, 2008, 0805.1704.

[124] Anne M. Green. Dependence of direct detection signals on the WIMP velocity distribution. *JCAP*, 1010:034, 2010, 1009.0916.

[125] Patrick J. Fox, Jia Liu, and Neal Weiner. Integrating Out Astrophysical Uncertainties. 2010, 1011.1915.

[126] Patrick J. Fox, Graham D. Kribs, and Tim M. P. Tait. Interpreting Dark Matter Direct Detection Independently of the Local Velocity and Density Distribution. 2010, 1011.1910.

[127] Annika H. G. Peter. Getting the astrophysics and particle physics of dark matter out of next-generation direct detection experiments. *Phys. Rev.*, D81:087301, 2010, 0910.4765.

[128] M. Cannoni, J. D. Vergados, and M. E. Gomez. Extraction of neutralino-nucleon scattering cross sections from total rates. 2010, 1011.6108.

[129] G. Bertone, David G. Cerdeno, J. I. Collar, and Brian C. Odom. WIMP identification through a combined measurement of axial and scalar couplings. *Phys. Rev. Lett.*, 99:151301, 2007, 0705.2502.

[130] Yashar Akrami, Christopher Savage, Pat Scott, Jan Conrad, and Joakim Edsjo. How well will ton-scale dark matter direct detection experiments constrain minimal supersymmetry? 2010, 1011.4318.

[131] Yashar Akrami, Christopher Savage, Pat Scott, Jan Conrad, and Joakim Edsjo. Statistical coverage for supersymmetric parameter estimation: a case study with direct detection of dark matter. 2010, 1011.4297.

[132] Roberto Ruiz de Austri, Roberto Trotta, and Leszek Roszkowski. A Markov chain Monte Carlo analysis of the CMSSM. *JHEP*, 05:002, 2006, hep-ph/0602028.

[133] E. Aprile et al. XENON1T at LNGS, Proposal, April 2010.

[134] E. Aprile et al. Technical Design Report, October 2010.

[135] http://darwin.physik.uzh.ch/.

[136] http://www.eureca.ox.ac.uk/.

[137] Laura Baudis. DARWIN: dark matter WIMP search with noble liquids. 2010, 1012.4764.

[138] http://www.cresst.de/.

[139] http://edelweiss.in2p3.fr/.

[140] Roberto Trotta. Bayes in the sky: Bayesian inference and model selection in cosmology. *Contemp. Phys.*, 49:71–104, 2008, 0803.4089.

[141] Farhan Feroz and M. P. Hobson. Multimodal nested sampling: an efficient and robust alternative to MCMC methods for astronomical data analysis. 2007, 0704.3704.

[142] F. Feroz, M. P. Hobson, and M. Bridges. MultiNest: an efficient and robust Bayesian inference tool for cosmology and particle physics. 2008, 0809.3437.

[143] Roberto Trotta, Farhan Feroz, Mike P. Hobson, Leszek Roszkowski, and Roberto Ruiz de Austri. The Impact of priors and observables on parameter inferences in the Constrained MSSM. *JHEP*, 12:024, 2008, 0809.3792.

[144] M. Kuhlen et al. Dark Matter Direct Detection with Non-Maxwellian Velocity Structure. *JCAP*, 1002:030, 2010, 0912.2358.

[145] Martin C. Smith et al. The RAVE Survey: Constraining the Local Galactic Escape Speed. *Mon. Not. Roy. Astron. Soc.*, 379:755–772, 2007, astro-ph/0611671.

[146] Yoshiaki Sofue. Pseudo Rotation Curve connecting the Galaxy, Dark Halo, and Local Group. 2008, 0811.0860.

[147] M. J. Reid et al. Trigonometric Parallaxes of Massive Star Forming Regions: VI. Galactic Structure, Fundamental Parameters and Non- Circular Motions. *Astrophys. J.*, 700:137–148, 2009, 0902.3913.

[148] Jo Bovy, David W. Hogg, and Hans-Walter Rix. Galactic masers and the Milky Way circular velocity. *Astrophys. J.*, 704:1704–1709, 2009, 0907.5423.

[149] Paul J. McMillan and James J. Binney. The uncertainty in Galactic parameters. 2009, 0907.4685.

[150] Pasquale Blasi. Direct Measurements, Acceleration and Propagation of Cosmic Rays. 2008, 0801.4534.

[151] Andrew W. Strong, Igor V. Moskalenko, and Vladimir S. Ptuskin. Cosmic-ray propagation and interactions in the Galaxy. *Ann. Rev. Nucl. Part. Sci.*, 57:285–327, 2007, astro-ph/0701517.

[152] U. Heinbach and M. Simon. Propagation of galactic cosmic rays under diffusive reacceleration. *Astrophys. J.*, 441:209–221, March 1995.

[153] A. W. Strong and I. V. Moskalenko. Propagation of cosmic-ray nucleons in the Galaxy. *Astrophys. J.*, 509:212–228, 1998, astro-ph/9807150.

[154] M. S. Longair, (ed.). High-energy astrophysics. Vol. 1: Particles, photons and their detection. Cambridge, UK: Univ. Pr. (1992) 418 p.

[155] L. C. Tan and L. K. Ng. Parameterization of antiproton invariant cross-section in pp collisions using a new scaling variable. *Phys. Rev.*, D26:1179–1182, 1982.

[156] L. C. Tan and L. K. Ng. Calculation of the equilibrium antiproton spectrum. *Journal of Physics G Nuclear Physics*, 9:227–242, February 1983.

[157] A. Bottino, F. Donato, N. Fornengo, and P. Salati. Which fraction of the measured cosmic ray antiprotons might be due to neutralino annihilation in the galactic halo? *Phys. Rev.*, D58:123503, 1998, astro-ph/9804137.

[158] Lars Bergstrom, Joakim Edsjo, and Piero Ullio. Cosmic antiprotons as a probe for supersymmetric dark matter? *Astrophys. J.*, 526:215–235, 1999, astro-ph/9902012.

[159] R. J. Protheroe. Cosmic ray anti-protons in the closed galaxy model. *Astrophys. J.*, 251:387–392, 1981.

[160] Junji Hisano, Shigeki Matsumoto, Osamu Saito, and Masato Senami. Heavy Wino-like neutralino dark matter annihilation into antiparticles. *Phys. Rev.*, D73:055004, 2006, hep-ph/0511118.

[161] F. Donato et al. Antiprotons from spallation of cosmic rays on interstellar matter. *Astrophys. J.*, 563:172–184, 2001, astro-ph/0103150.

[162] T. Delahaye et al. Galactic secondary positron flux at the Earth. *Astron. Astrophys.*, 501:821–833, 2009, 0809.5268.

[163] Marco Cirelli and Paolo Panci. Inverse Compton constraints on the Dark Matter e+e- excesses. *Nucl. Phys.*, B821:399–416, 2009, 0904.3830.

[164] D. Maurin, F. Donato, R. Taillet, and P. Salati. Cosmic Rays below Z=30 in a diffusion model: new constraints on propagation parameters. *Astrophys. J.*, 555:585–596, 2001, astro-ph/0101231.

[165] David Maurin et al. Galactic cosmic ray nuclei as a tool for astroparticle physics. 2002, astro-ph/0212111.

[166] Richard Taillet and David Maurin. Spatial Origin of Galactic Cosmic Rays in Diffusion Models: I- Standard sources in the Galactic disk. *Astron. Astrophys.*, 402:971, 2003, astro-ph/0212112.

[167] http://galprop.stanford.edu/web_galprop/galprop_home.html.

[168] C. Evoli, D. Gaggero, D. Grasso, and L. Maccione. Cosmic-Ray Nuclei, Antiprotons and Gamma-rays in the Galaxy: a New Diffusion Model. *JCAP*, 0810:018, 2008, 0807.4730.

[169] Giuseppe Di Bernardo, Carmelo Evoli, Daniele Gaggero, Dario Grasso, and Luca Maccione. Unified interpretation of cosmic-ray nuclei and antiproton recent measurements. *Astropart. Phys.*, 34:274–283, 2010, 0909.4548.

[170] L. J. Gleeson and W. I. Axford. Solar Modulation of Galactic Cosmic Rays. *Astrophys. J.*, 154:1011, 1968.

[171] R. U. Abbasi et al. Observation of the GZK cutoff by the HiRes experiment. *Phys. Rev. Lett.*, 100:101101, 2008, astro-ph/0703099.

[172] J. Abraham et al. Observation of the suppression of the flux of cosmic rays above 4×10^{19}eV. *Phys. Rev. Lett.*, 101:061101, 2008, 0806.4302.

[173] A. Putze, L. Derome, and D. Maurin. A Markov Chain Monte Carlo technique to sample transport and source parameters of Galactic cosmic rays: II. Results for the diffusion model combining B/C and radioactive nuclei. *Astron. Astrophys.*, 516:A66, 2010, 1001.0551.

[174] Alexander D. Panov et al. The results of ATIC-2 experiment for elemental spectra of cosmic rays. 2006, astro-ph/0612377.

[175] H. S. Ahn et al. Discrepant hardening observed in cosmic-ray elemental spectra. *Astrophys. J.*, 714:L89–L93, 2010, 1004.1123.

[176] Julien Lavalle. Impact of the spectral hardening of TeV cosmic rays on the prediction of the secondary positron flux. 2010, 1011.3063.

[177] A. Putze, D. Maurin, and F. Donato. p, He, and C to Fe cosmic-ray primary fluxes in diffusion models: Source and transport signatures on fluxes and ratios. 2010, 1011.0989.

[178] Fiorenza Donato and Pasquale D. Serpico. 'Discrepant hardenings' in cosmic ray spectra: a first estimate of the effects on secondary antiproton and diffuse gamma-ray yields. 2010, 1010.5679.

[179] http://www.ams02.org.

[180] Melanie Simet and Dan Hooper. Astrophysical Uncertainties in the Cosmic Ray Electron and Positron Spectrum From Annihilating Dark Matter. *JCAP*, 0908:003, 2009, 0904.2398.

[181] T. Delahaye, R. Lineros, F. Donato, N. Fornengo, and P. Salati. Positrons from dark matter annihilation in the galactic halo: theoretical uncertainties. *Phys. Rev.*, D77:063527, 2008, 0712.2312.

[182] Alejandro Ibarra and David Tran. Antimatter Signatures of Gravitino Dark Matter Decay. *JCAP*, 0807:002, 2008, 0804.4596.

[183] Dan Hooper, Pasquale Blasi, and Pasquale Dario Serpico. Pulsars as the Sources of High Energy Cosmic Ray Positrons. *JCAP*, 0901:025, 2009, 0810.1527.

[184] P. Zuccon. Prepared for 31st International Cosmic Ray Conferences (ICRC 2009), Łódź, Poland, 7-15 Jul 2009.

[185] A. G. Malinin. Astroparticle physics with AMS-02. *Phys. Atom. Nucl.*, 67:2044–2049, 2004.

[186] Behcet Alpat. Alpha Magnetic Spectrometer (AMS02) experiment on the International Space Station (ISS). 2003, astro-ph/0308487.

[187] J. Casaus. Cosmic-ray astrophysics with AMS-02. Prepared for 28th International Cosmic Ray Conferences (ICRC 2003), Tsukuba, Japan, 31 Jul - 7 Aug 2003.

[188] Behcet Alpat. Astroparticle Physics with AMS02. 2007, 0707.3605.

[189] L. Arruda et al. Isotope separation with the RICH detector of the AMS Experiment. 2005, 0710.0846.

[190] Pierre Brun. Indirect Searches for Dark Matter with AMS-02. *Eur. Phys. J.*, C56:27–31, 2008, 0710.2458.

[191] Diego Casadei. Cosmic ray astrophysics with AMS-02. 2004, astro-ph/0404529.

[192] http://pamela.roma2.infn.it.

[193] Chih-Hsun Lin. Cosmic-ray astrophysics with AMS-02. Prepared for 32nd International Conference on High-Energy Physics (ICHEP 04), Beijing, China, 16-22 Aug 2004.

[194] A. Oliva. High Charge Cosmic Rays Measurement with the AMS-02 Silicon Tracker. PhD thesis, 2007.

[195] S. Rosier-Lees. Prepared for 30th International Cosmic Ray Conferences (ICRC 2007), Mérida, México, 3-11 Jul 2007.

[196] F. Spada. The Physics of AMS-02. talk at the Tenth European Meeting From the Planck Scale to the Electroweak Scale (Planck 07), Warsaw, Poland, 9-13 Jun 2007.

[197] Rui Pereira. Astrophysics with the AMS-02 experiment. 2007, 0710.0984.

[198] O. Adriani et al. A new measurement of the antiproton-to-proton flux ratio up to 100 GeV in the cosmic radiation. *Phys. Rev. Lett.*, 102:051101, 2009, 0810.4994.

[199] M. E. Wiedenbeck et al. The Level of Solar Modulation of Galactic Cosmic Rays from 1997 to 2005 as Derived from ACE Measurements of Elemental Energy Spectra. Prepared for 29th International Cosmic Ray Conferences (ICRC 2005), Pune, India, 3-11 Aug 2005.

[200] S. J. Sturner, J. G. Skibo, C. D. Dermer, and J. R. Mattox. Temporal Evolution of Nonthermal Spectra from Supernova Remnants. *Astrophys. J.*, 490:619–+, December 1997.

[201] A. W. Strong and I. V. Moskalenko. New developments in the GALPROP CR propagation model. 2001, astro-ph/0106504.

[202] A. W. Strong and I. V. Moskalenko. A 3D time-dependent model for galactic cosmic rays and gamma-rays. 2001, astro-ph/0106505.

[203] P. Picozza. talk at the TeV Particle Astrophysics 2009, Menlo Park, California, USA, 13-17 Jul 2009.

[204] http://www.darksusy.org.

[205] Marco Cirelli et al. PPPC 4 DM ID: A Poor Particle Physicist Cookbook for Dark Matter Indirect Detection. 2010, 1012.4515.

[206] Torbjorn Sjostrand et al. High-energy physics event generation with PYTHIA 6.1. *Comput. Phys. Commun.*, 135:238–259, 2001, hep-ph/0010017.

[207] Torbjorn Sjostrand, Stephen Mrenna, and Peter Z. Skands. PYTHIA 6.4 Physics and Manual. *JHEP*, 05:026, 2006, hep-ph/0603175.

[208] Torbjorn Sjostrand, Stephen Mrenna, and Peter Z. Skands. A Brief Introduction to PYTHIA 8.1. *Comput. Phys. Commun.*, 178:852–867, 2008, 0710.3820.

[209] Torsten Bringmann, Lars Bergstrom, and Joakim Edsjo. New Gamma-Ray Contributions to Supersymmetric Dark Matter Annihilation. *JHEP*, 01:049, 2008, 0710.3169.

[210] Lars Bergstrom, Gianfranco Bertone, Torsten Bringmann, Joakim Edsjo, and Marco Taoso. Gamma-ray and Radio Constraints of High Positron Rate Dark Matter Models Annihilating into New Light Particles. *Phys. Rev.*, D79:081303, 2009, 0812.3895.

[211] M. Kachelriess, P. D. Serpico, and M. Aa. Solberg. On the role of electroweak bremsstrahlung for indirect dark matter signatures. *Phys. Rev.*, D80:123533, 2009, 0911.0001.

[212] Paolo Ciafaloni et al. Weak Corrections are Relevant for Dark Matter Indirect Detection. 2010, 1009.0224.

[213] Gianfranco Bertone, Wilfried Buchmuller, Laura Covi, and Alejandro Ibarra. Gamma-Rays from Decaying Dark Matter. *JCAP*, 0711:003, 2007, 0709.2299.

[214] Alejandro Ibarra and David Tran. Decaying Dark Matter and the PAMELA Anomaly. *JCAP*, 0902:021, 2009, 0811.1555.

[215] Wilfried Buchmuller, Alejandro Ibarra, Tetsuo Shindou, Fumihiro Takayama, and David Tran. Probing Gravitino Dark Matter. *JCAP*, 0909:021, 2009, 0906.1187.

[216] A. Sommerfeld. *Ann. Phys.*, 11:257, 1931.

[217] Junji Hisano, Shigeki Matsumoto, and Mihoko M. Nojiri. Explosive dark matter annihilation. *Phys. Rev. Lett.*, 92:031303, 2004, hep-ph/0307216.

[218] Junji Hisano, Shigeki Matsumoto, Mihoko M. Nojiri, and Osamu Saito. Direct detection of the Wino- and Higgsino-like neutralino dark matters at one-loop level. *Phys. Rev.*, D71:015007, 2005, hep-ph/0407168.

[219] Nima Arkani-Hamed, Douglas P. Finkbeiner, Tracy R. Slatyer, and Neal Weiner. A Theory of Dark Matter. *Phys. Rev.*, D79:015014, 2009, 0810.0713.

[220] J. Diemand et al. Clumps and streams in the local dark matter distribution. *Nature*, 454:735–738, 2008, 0805.1244.

[221] F. Donato, Nicolao Fornengo, D. Maurin, and P. Salati. Antiprotons in cosmic rays from neutralino annihilation. *Phys. Rev.*, D69:063501, 2004, astro-ph/0306207.

[222] J. Lavalle, Q. Yuan, D. Maurin, and X. J. Bi. Full Calculation of Clumpiness Boost factors for Antimatter Cosmic Rays in the light of ΛCDM N-body simulation results. *Astron. Astrophys.*, 479:427–452, 2008, 0709.3634.

[223] David Maurin, R. Taillet, and C. Combet. Approximate formulae for exotic GCR anti-p and anti-d: Fluxes and astrophysical uncertainties. 2006, astro-ph/0609522.

[224] http://heasarc.gsfc.nasa.gov/docs/cgro/egret/.

[225] http://www glast.stanford.edu/.

[226] http://wwwmagic.mppmu.mpg.de/.

[227] http://veritas.sao.arizona.edu/.

[228] http://www.mpi hd.mpg.de/hfm/HESS/.

[229] http://www.cta observatory.org/CTA_home.html.

[230] F. Aharonian et al. HESS observations of the galactic center region and their possible dark matter interpretation. *Phys. Rev. Lett.*, 97:221102, 2006, astro-ph/0610509.

[231] A. A. Abdo et al. Fermi Large Area Telescope Measurements of the Diffuse Gamma-Ray Emission at Intermediate Galactic Latitudes. *Phys. Rev. Lett.*, 103:251101, 2009, 0912.0973.

[232] A. A. Abdo et al. Fermi LAT Search for Photon Lines from 30 to 200 GeV and Dark Matter Implications. *Phys. Rev. Lett.*, 104:091302, 2010, 1001.4836.

[233] A. A. Abdo et al. Observations of Milky Way Dwarf Spheroidal galaxies with the Fermi-LAT detector and constraints on Dark Matter models. *Astrophys. J.*, 712:147–158, 2010, 1001.4531.

[234] A. Abramowski et al. H.E.S.S. constraints on Dark Matter annihilations towards the Sculptor and Carina Dwarf Galaxies. 2010, 1012.5602.

[235] M. Ackermann et al. Constraints on Dark Matter Annihilation in Clusters of Galaxies with the Fermi Large Area Telescope. *JCAP*, 1005:025, 2010, 1002.2239.

[236] F. Aharonian. Very high energy gamma-ray observations of the galaxy clusters Abell 496 and Abell 85 with H.E.S.S. 2008, 0812.1638.

[237] O. Adriani et al. PAMELA results on the cosmic-ray antiproton flux from 60 MeV to 180 GeV in kinetic energy. *Phys. Rev. Lett.*, 105:121101, 2010, 1007.0821.

[238] S. W. Barwick et al. Measurements of the cosmic-ray positron fraction from 1- GeV to 50-GeV. *Astrophys. J.*, 482:L191–L194, 1997, astro-ph/9703192.

[239] M. Boezio et al. The Cosmic-Ray Electron and Positron Spectra Measured at 1 AU during Solar Minimum Activity. *Astrophys. J.*, 532:653–669, March 2000.

[240] M. Aguilar et al. Cosmic-ray positron fraction measurement from 1-GeV to 30- GeV with AMS-01. *Phys. Lett.*, B646:145–154, 2007, astro-ph/0703154.

[241] Oscar Adriani et al. An anomalous positron abundance in cosmic rays with energies 1.5-100 GeV. *Nature*, 458:607–609, 2009, 0810.4995.

[242] J. Chang et al. An excess of cosmic ray electrons at energies of 300-800 GeV. *Nature*, 456:362–365, 2008.

[243] A. Abdo et al. Measurement of the Cosmic Ray e+ plus e- spectrum from 20 GeV to 1 TeV with the Fermi Large Area Telescope. *Phys. Rev. Lett.*, 102:181101, 2009, 0905.0025.

[244] M. Ackermann et al. Fermi LAT observations of cosmic-ray electrons from 7 GeV to 1 TeV. *Phys. Rev.*, D82:092004, 2010, 1008.3999.

[245] F. Aharonian et al. Probing the ATIC peak in the cosmic-ray electron spectrum with H.E.S.S. *Astron. Astrophys.*, 508:561, 2009, 0905.0105.

[246] Stephane Coutu et al. Cosmic-ray positrons: Are there primary sources? *Astropart. Phys.*, 11:429–435, 1999, astro-ph/9902162.

[247] J. J. Beatty et al. New measurement of the cosmic-ray positron fraction from 5-GeV to 15-GeV. *Phys. Rev. Lett.*, 93:241102, 2004, astro-ph/0412230.

[248] S. Desai et al. Study of TeV Neutrinos with Upward Showering Muons in Super-Kamiokande. *Astropart. Phys.*, 29:42–54, 2008, 0711.0053.

[249] J. Ahrens et al. Sensitivity of the IceCube detector to astrophysical sources of high energy muon neutrinos. *Astropart. Phys.*, 20:507–532, 2004, astro-ph/0305196.

[250] Junji Hisano, Kazunori Nakayama, and Masaki J. S. Yang. Upward muon signals at neutrino detectors as a probe of dark matter properties. *Phys. Lett.*, B678:101–106, 2009, 0905.2075.

[251] Douglas Spolyar, Matthew R. Buckley, Katherine Freese, Dan Hooper, and Hitoshi Murayama. High Energy Neutrinos As A Test of Leptophilic Dark Matter. 2009, 0905.4764.

[252] Marco Cirelli, Mario Kadastik, Martti Raidal, and Alessandro Strumia. Model-independent implications of the e+, e-, anti-proton cosmic ray spectra on properties of Dark Matter. *Nucl. Phys.*, B813:1–21, 2009, 0809.2409.

[253] Yasunori Nomura and Jesse Thaler. Dark Matter through the Axion Portal. *Phys. Rev.*, D79:075008, 2009, 0810.5397.

[254] Marco Cirelli, Roberto Franceschini, and Alessandro Strumia. Minimal Dark Matter predictions for galactic positrons, anti-protons, photons. *Nucl. Phys.*, B800:204–220, 2008, 0802.3378.

[255] Junji Hisano, Shigeki Matsumoto, Minoru Nagai, Osamu Saito, and Masato Senami. Non-perturbative Effect on Thermal Relic Abundance of Dark Matter. *Phys. Lett.*, B646:34–38, 2007, hep-ph/0610249.

[256] Lars Bergstrom, Joakim Edsjo, and Gabrijela Zaharijas. Dark matter interpretation of recent electron and positron data. *Phys. Rev. Lett.*, 103:031103, 2009, 0905.0333.

[257] M. Cirelli. talk at TANGO in PARIS, 4-6 May 2009, Paris, France.

[258] Jeremy Mardon, Yasunori Nomura, Daniel Stolarski, and Jesse Thaler. Dark Matter Signals from Cascade Annihilations. *JCAP*, 0905:016, 2009, 0901.2926.

[259] Brant Robertson and Andrew Zentner. Dark Matter Annihilation Rates with Velocity-Dependent Annihilation Cross Sections. *Phys. Rev.*, D79:083525, 2009, 0902.0362.

[260] Stefano Profumo and Tesla E. Jeltema. Extragalactic Inverse Compton Light from Dark Matter Annihilation and the Pamela Positron Excess. *JCAP*, 0907:020, 2009, 0906.0001.

[261] Alexander V. Belikov and Dan Hooper. The Contribution Of Inverse Compton Scattering To The Diffuse Extragalactic Gamma-Ray Background From Annihilating Dark Matter. *Phys. Rev.*, D81:043505, 2010, 0906.2251.

[262] Alexander V. Belikov and Dan Hooper. How Dark Matter Reionized The Universe. *Phys. Rev.*, D80:035007, 2009, 0904.1210.

[263] Marco Cirelli, Fabio Iocco, and Paolo Panci. Constraints on Dark Matter annihilations from reionization and heating of the intergalactic gas. *JCAP*, 0910:009, 2009, 0907.0719.

[264] Juan Zhang et al. Discriminating different scenarios to account for the cosmic e + /- excess by synchrotron and inverse Compton radiation. *Phys. Rev.*, D80:023007, 2009, 0812.0522.

[265] Gianfranco Bertone, Geraldine Servant, and Guenter Sigl. Indirect detection of Kaluza-Klein dark matter. *Phys. Rev.*, D68:044008, 2003, hep-ph/0211342.

[266] D. Casadei and V. Bindi. The origin of cosmic ray electrons and positrons. *Astrophys. J.*, 612:262–267, 2004.

[267] S. Torii et al. High-energy electron observations by PPB-BETS flight in Antarctica. 2008, 0809.0760.

[268] O. Adriani et al. A statistical procedure for the identification of positrons in the PAMELA experiment. *Astropart. Phys.*, 34:1–11, 2010, 1001.3522.

[269] F. Aharonian et al. The energy spectrum of cosmic-ray electrons at TeV energies. *Phys. Rev. Lett.*, 101:261104, 2008, 0811.3894.

[270] Pasquale Dario Serpico. On the possible causes of a rise with energy of the cosmic ray positron fraction. *Phys. Rev.*, D79:021302, 2009, 0810.4846.

[271] A. M. Atoyan, F. A. Aharonian, and H. J. Völk. Electrons and positrons in the galactic cosmic rays. *Phys. Rev.*, D52:3265–3275, September 1995.

[272] Junji Hisano, Shigeki. Matsumoto, Mihoko M. Nojiri, and Osamu Saito. Non-perturbative effect on dark matter annihilation and gamma ray signature from galactic center. *Phys. Rev.*, D71:063528, 2005, hep-ph/0412403.

[273] Marco Cirelli, Alessandro Strumia, and Matteo Tamburini. Cosmology and Astrophysics of Minimal Dark Matter. *Nucl. Phys.*, B787:152–175, 2007, 0706.4071.

[274] Maxim Pospelov and Adam Ritz. Astrophysical Signatures of Secluded Dark Matter. *Phys. Lett.*, B671:391–397, 2009, 0810.1502.

[275] Massimiliano Lattanzi and Joseph I. Silk. Can the WIMP annihilation boost factor be boosted by the Sommerfeld enhancement? *Phys. Rev.*, D79:083523, 2009, 0812.0360.

[276] John David March-Russell and Stephen Mathew West. WIMPonium and Boost Factors for Indirect Dark Matter Detection. *Phys. Lett.*, B676:133–139, 2009, 0812.0559.

[277] Silvia Galli, Fabio Iocco, Gianfranco Bertone, and Alessandro Melchiorri. CMB constraints on Dark Matter models with large annihilation cross-section. *Phys. Rev.*, D80:023505, 2009, 0905.0003.

[278] Tracy R. Slatyer, Nikhil Padmanabhan, and Douglas P. Finkbeiner. CMB Constraints on WIMP Annihilation: Energy Absorption During the Recombination Epoch. *Phys. Rev.*, D80:043526, 2009, 0906.1197.

[279] I. Buesching, O. C. de Jager, M. S. Potgieter, and C. Venter. A Cosmic Ray Positron Anisotropy due to Two Middle-Aged, Nearby Pulsars? 2008, 0804.0220.

[280] Stefano Profumo. Dissecting Pamela (and ATIC) with Occam's Razor: existing, well-known Pulsars naturally account for the 'anomalous' Cosmic-Ray Electron and Positron Data. 2008, 0812.4457.

[281] T. Delahaye, J. Lavalle, R. Lineros, F. Donato, and N. Fornengo. Galactic electrons and positrons at the Earth:new estimate of the primary and secondary fluxes. *Astron. Astroph.*, 524:A51, 2010, 1002.1910.

[282] Leo Gendelev, Stefano Profumo, and Michael Dormody. The Contribution of Fermi Gamma-Ray Pulsars to the local Flux of Cosmic-Ray Electrons and Positrons. *JCAP*, 1002:016, 2010, 1001.4540.

[283] T. Kamae et al. Cosmic Ray $e^+/(e^- + e^+)$ and pbar/p Ratios Explained by an Injection Model Based on Gamma-ray Observations. 2010, 1010.3477.

[284] Pasquale Blasi. The origin of the positron excess in cosmic rays. *Phys. Rev. Lett.*, 103:051104, 2009, 0903.2794.

[285] Pasquale Blasi and Pasquale D. Serpico. High-energy antiprotons from old supernova remnants. *Phys. Rev. Lett.*, 103:081103, 2009, 0904.0871.

[286] Philipp Mertsch and Subir Sarkar. Testing astrophysical models for the PAMELA positron excess with cosmic ray nuclei. *Phys. Rev. Lett.*, 103:081104, 2009, 0905.3152.

[287] Jeter Hall and Dan Hooper. Distinguishing Between Dark Matter and Pulsar Origins of the ATIC Electron Spectrum With Atmospheric Cherenkov Telescopes. *Phys. Lett.*, B681:220–223, 2009, 0811.3362.

[288] R N Manchester, G B Hobbs, A Teoh, and M Hobbs. The ATNF Pulsar Catalogue. *Astron. J.*, 129:1993, 2005, astro-ph/0412641.

[289] A. A. Abdo et al. The First Fermi Large Area Telescope Catalog of Gamma-ray Pulsars. *Astrophys. J. Suppl.*, 187:460–494, 2010, 0910.1608.

[290] P. M. Saz Parkinson et al. Eight gamma-ray pulsars discovered in blind frequency searches of Fermi LAT data. *Astrophys. J.*, 725:571–584, 2010, 1006.2134.

[291] M. A. DuVernois et al. Cosmic ray electrons and positrons from 1-GeV to 100-GeV: Measurements with HEAT and their interpretation. *Astrophys. J.*, 559:296–303, 2001.

[292] M. Aguilar et al. The Alpha Magnetic Spectrometer (AMS) on the International Space Station. I: Results from the test flight on the space shuttle. *Phys. Rept.*, 366:331–405, 2002.

[293] S. Torii et al. The energy spectrum of cosmic ray electrons from 10-GeV to 100-GeV observed with a highly granulated imaging calorimeter. *Astrophys. J.*, 559:973–984, 2001.

[294] D. Grasso et al. On possible interpretations of the high energy electron- positron spectrum measured by the Fermi Large Area Telescope. *Astropart. Phys.*, 32:140–151, 2009, 0905.0636.

[295] Patrick J. Fox and Erich Poppitz. Leptophilic Dark Matter. *Phys. Rev.*, D79:083528, 2009, 0811.0399.

[296] Eung Jin Chun, Jong-Chul Park, and Stefano Scopel. Dirac gaugino as leptophilic dark matter. *JCAP*, 1002:015, 2010, 0911.5273.

[297] Dan Hooper and Kathryn M. Zurek. The PAMELA and ATIC Signals From Kaluza-Klein Dark Matter. *Phys. Rev.*, D79:103529, 2009, 0902.0593.

[298] Pasquale Blasi and Elena Amato. Positrons from pulsar winds. 2010, 1007.4745.

[299] A. Kounine. Status of the AMS Experiment. 2010, 1009.5349.

[300] P. Maestro. Indirect Search for Dark Matter by Measurements of the Cosmic Ray Positron Spectrum with the AMS-02 experiment. PhD thesis, 2003.

[301] Sadakazu Haino et al. Measurements of primary and atmospheric cosmic-ray spectra with the BESS-TeV spectrometer. *Phys. Lett.*, B594:35–46, 2004, astro-ph/0403704.

[302] M. Schmanau. The performance of the AMS-02 Transition Radiation Detector. Prepared for the 29th International Cosmic Ray Conference (ICRC 2005), Pune, India, 3-11 Aug 2005.

[303] Jorge Casaus. The AMS-02 experiment on the ISS. *J. Phys. Conf. Ser.*, 171:012045, 2009.

[304] M. Ackermann et al. Searches for Cosmic-Ray Electron Anisotropies with the *Fermi* Large Area Telescope. *Phys. Rev.*, D82:092003, 2010, 1008.5119.

[305] V. Ravi, R. N. Manchester, and G. Hobbs. Wide radio beams from gamma-ray pulsars. 2010, 1005.1966.

[306] J. M. Rankin. Toward an empirical theory of pulsar emission. VI - The geometry of the conal emission region. *Astrophys. J.*, 405:285–297, March 1993.

[307] Kyle P. Watters, Roger W. Romani, Patrick Weltevrede, and Simon Johnston. An Atlas For Interpreting Gamma-Ray Pulsar Light Curves. *Astrophys. J.*, 695:1289–1301, 2009, 0812.3931.

[308] Giuseppe Di Bernardo et al. Implications of the Cosmic Ray Electron Spectrum and Anisotropy measured with Fermi-LAT. 2010, 1010.0174.

[309] Dmitry Malyshev, Ilias Cholis, and Joseph Gelfand. Pulsars versus Dark Matter Interpretation of ATIC/PAMELA. *Phys. Rev.*, D80:063005, 2009, 0903.1310.

[310] F. Donato, N. Fornengo, and M. Schelke. Additional bounds on the pre Big–Bang–Nucleosynthesis Expansion by means of γ-rays from the Galactic Center. *JCAP*, 0703:021, 2007, hep-ph/0612374.

[311] E. Komatsu et al. Five-Year Wilkinson Microwave Anisotropy Probe WMAP Observations:Cosmological Interpretation. *Astrophys. J. Suppl.*, 180:330–376, 2009, 0803.0547.

[312] T. A. Porter and for the Fermi LAT Collaboration. Fermi LAT Measurements of the Diffuse Gamma-Ray Emission at Intermediate Galactic Latitudes. 2009, 0907.0294.

[313] A. A. Abdo et al. Fermi LAT Observation of Diffuse Gamma-Rays Produced Through Interactions between Local Interstellar Matter and High Energy Cosmic Rays. *Astrophys. J.*, 703:1249–1256, 2009, 0908.1171.

[314] A. A. El-Zant, S. Khalil, and H. Okada. Dark Matter Annihilation and the PAMELA, FERMI and ATIC Anomalies. *Phys. Rev.*, D81:123507, 2010, 0903.5083.

[315] C. Pallis. Cold Dark Matter in non-Standard Cosmologies, PAMELA, ATIC and Fermi LAT. *Nucl. Phys.*, B831:217–247, 2010, 0909.3026.

[316] Graciela B. Gelmini. Experimental signatures of non-standard pre-BBN cosmologies. *Nucl. Phys. Proc. Suppl.*, 194:63–68, 2009, 0907.1694.

[317] Graciela B. Gelmini and Paolo Gondolo. Ultra-cold WIMPs: relics of non-standard pre-BBN cosmologies. *JCAP*, 0810:002, 2008, 0803.2349.

[318] A. Arbey and F. Mahmoudi. SUSY constraints from relic density: high sensitivity to pre-BBN expansion rate. *Phys. Lett.*, B669:46–51, 2008, 0803.0741.

[319] Gabriela Barenboim and Joseph D. Lykken. Minimal noncanonical cosmologies. *JHEP*, 07:016, 2006, astro-ph/0604528.

[320] Gabriela Barenboim and Joseph D. Lykken. Quintessence, inflation and baryogenesis from a single pseudo-Nambu-Goldstone boson. *JHEP*, 10:032, 2007, 0707.3999.

[321] John D. Barrow. Massive particles as a probe of the early Universe. *Nucl. Phys.*, B208:501–508, 1982.

[322] Gianfranco Bertone, Emmanuel Nezri, Jean Orloff, and Joseph Silk. Neutrinos from dark matter annihilations at the galactic centre. *Phys. Rev.*, D70:063503, 2004, astro-ph/0403322.

[323] R. Abbasi et al. Limits on a muon flux from neutralino annihilations in the Sun with the IceCube 22-string detector. *Phys. Rev. Lett.*, 102:201302, 2009, 0902.2460.

[324] G. Wikstrom and J. Edsjo. Limits on the WIMP-nucleon scattering cross-section from neutrino telescopes. *JCAP*, 0904:009, 2009, 0903.2986.

[325] V. Berezinsky et al. Searching for relic neutralinos using neutrino telescopes. *Astropart. Phys.*, 5:333–352, 1996, hep-ph/9603342.

[326] L. Pieri, A. Pizzella, E. M. Corsini, E. Dalla Bonta', and F. Bertola. Could the Fermi-LAT detect gamma-rays from dark matter annihilation in the dwarf galaxies of the Local Group? *Astron. Astrophys.*, 496:351, 2009, 0812.1494.

[327] Tesla E. Jeltema, John Kehayias, and Stefano Profumo. Gamma Rays from Clusters and Groups of Galaxies: Cosmic Rays versus Dark Matter. *Phys. Rev.*, D80:023005, 2009, 0812.0597.

[328] Marco Regis and Piero Ullio. Multi-wavelength signals of dark matter annihilations at the Galactic center. *Phys. Rev.*, D78:043505, 2008, 0802.0234.

[329] John F. Beacom, Nicole F. Bell, and Gregory D. Mack. General upper bound on the dark matter total annihilation cross section. *Phys. Rev. Lett.*, 99:231301, 2007, astro-ph/0608090.

[330] Michael Gustafsson, Erik Lundstrom, Lars Bergstrom, and Joakim Edsjo. Significant gamma lines from inert Higgs dark matter. *Phys. Rev. Lett.*, 99:041301, 2007, astro-ph/0703512.

[331] R. D. Davies, D. Walsh, and R. S. Booth. The radio source at the galactic nucleus. *Mon. Not. Roy. Astron. Soc.*, 177:319–333, November 1976.

[332] Gert Huetsi, Andi Hektor, and Martti Raidal. Constraints on leptonically annihilating Dark Matter from reionization and extragalactic gamma background. *Astron. Astrophys.*, 505:999–1005, 2009, 0906.4550.

[333] Lisa Randall and Raman Sundrum. An alternative to compactification. *Phys. Rev. Lett.*, 83:4690–4693, 1999, hep-th/9906064.